The Dissertation Committee for Zeyu Zhao certifies that this is the approved version of the following dissertation:

Efficient Seismic Imaging with the Double Plane Wave Data

Committee:

Mrinal K. Sen, Supervisor

Paul L. Stoffa, Co-Supervisor

Clifford A. Frohlich

Stephen P. Grand

Robert H. Tatham

Yosio Nakamura

Efficient Seismic Imaging with the Double Plane Wave Data

by

Zeyu Zhao, B.E.

DISSERTATION

Presented to the Faculty of the Graduate School of

The University of Texas at Austin

in Partial Fulfillment

of the Requirements

for the Degree of

DOCTOR OF PHILOSOPHY

The University of Texas at Austin

December 2015

Dedication

To my family

Acknowledgements

Being persistent, optimistic and confident are the greatest things that I have learned during my Ph.D. study. Persistence is the key to stay active in research. There are always times of frustrations and even loneliness, keeping optimistic and confident, however, helped me navigate through hurdles in the path and get through those tough times. The moment that I was able to solve a scientific program gives the most rewarding and exciting feeling in my life, and it makes all of the hard-working days and nights worthwhile. The lessons I have learned are valuable life experiences.

I am fortunate to work with my supervisor Dr. Mrinal Sen and my co-supervisor Dr. Paul Stoffa, and I was fortunate to be able to stand on the shoulders of giants. It is my greatest pleasure to work with two of the most respected geophysicists in the world. I was given lots of freedom to pursue my research interests, and Mrinal and Paul were always there to help. It is always inspiring to talk with them about my research. More importantly, the majority of the theory in this dissertation came from the long discussions with Mrinal and Paul during my qualifying exam. I am more than grateful to their patience, encouragement, endless support and stimulating suggestions. The dissertation would never been finished without their guidance. I give my deepest gratitude to Mrinal and Paul who have been not only great supervisors, but also my friends.

I would like to express my gratitude to my committee members, Dr. Robert Tatham, who taught me seismic lithology and gave me exciting insights on plane wave domain, Dr. Stephen Grand, who gave me great lectures on seismology and potential

fields, Dr. Yosio Nakamura and Dr. Clifford Frohlich, who provided me valuable suggestions on my dissertation.

Now, I want to write in a less formal tone to thank the people who do not have their name on the title page of this dissertation.

I need to thank Dr. Kyle Spikes, who looks intimidating, and indeed he could be really intimidating under some circumstances. Kyle gave me the very first lecture in my graduate school, and I was glad that I did not do too bad. I thank Dr. Clark Wilson and Dr. Luc Lavier who are really helpful in helping me debugging my Matlab codes. Within Jackson School of Geosciences, my acknowledgements also go to Dr. Bob Hardage, Dr. Hongliu Zeng and Dr. Omar Ghattas, whose courses really benefited my research from all perspectives of geosciences. I am also grateful that I worked with the best administrators: Philip Guerrero, Margo Grace, Judy Sansom, Nancy Hard, Eric Aiello and Rosalind Gamble. I want to thank Thomas Hess for his endless and generous help on using seismic processing software, correcting my grammars, reviewing my papers and even recovering my dead SSD. I also want to thank Mark Wiederspahn for his technical support in UTIG. Mark has always been an incredible problem solver for all technical problems. I would like to thank Roustam Seif for teaching me MPI and for tolerating me when I was using all computing powers in pls8 and pls9. I also need to thank all my colleagues in UTIG for allowing me to have the biggest office (i.e., the commons) within the department, or maybe even within the entire university.

I would like to sincerely thank WesternGeco, Repsol and Statoil for providing me the internship opportunities. I would like to thank my mentors Qinglin Liu, Sheng Xu and

Hongbo Zhou, and my co-workers Lisheng Li, Dingxue Wang, Luxin Zhang, Lianping Zhang, Jiao He, Meixia Wang, Daoliu Wang, Jun Mu, Bing Tang, Po Zhang, Jinjun Liu, Jungmin Kwon, Hyunggu Jun and Mike Cogan.

I would like to acknowledge the help from Reynam Pestana at Universidade Federal Da Bahia, Jacob Fokkema at Delft, Hillel Tal-Ezer at The Academic College of Tel-Aviv Yaffo., Jiongbing Cheng at Tongji University, Yu Zhang at ConocoPhillips, Faqi Liu at Hess, Chunlei Chu at BP, Junru Jiao and Qunshan Zhang at Respol, Hongwei Liu at Saudi Aramco, Jerry Guo at GeoApex, Ning Guo.

The help from Xingyao Yin, Jianping Huang, Guochen Wu, Junhua Zhang, Zhenchun Li, Fang Gang, Zhaoyun Zong and Xiaolong Zhao, Yang Liu at China University of Petroleum are also acknowledged.

My research was support by the EDGER Forum and the GeoApex scholarship, and I thank all of the EDGER Forum's sponsors for supporting us. For my dissertation, a special thanks to Hess for providing the VTI model and the dataset.

Here we go the longest list for my former and current colleagues at Jackson School of Geosciences: Rui Zhang, Samik Sil, Mohammed Alhussian, Qi Ren, Reetam Biswas, Datta Debanjan, Badr Alulaiw, Jingwei Hu, Xiao Zhu, Xiaolei Song, Siwei Li, Russel Cater, Meijuan Jiang, Yu Xia, Gang Luo, Kwon Taek Oh, Junzhe Sun, Yangkang Chen, Han Liu, Bei Pan, AJ Yanke, Anthony Barone, Barry Borgman, David Tang, Elliot Dahl, Kelly Regimbal, Chang Lu, Tieyuan Zhu, Hejun Zhu, Yatong Zhou, Yawen He,

Zhiguang Xue, Yanadet Sripanich, Sarah Coyle, Lauren Becker… It is my great pleasure to meet you guys.

Thanks also go to my special one Lisa H., your endless support and encouragement will always be appreciated. Thanks for being my personal cheerleader when I was writing, writing, writing. It is probably not difficult for you to pretend to be a geophysicist after going over ALL my writings countless times, but do not do that!

Finally, I saved the most important acknowledgements to my Family, especially my parents. I simply can not achieve anything without your support. Took me to fieldtrips, decorated rooms with rocks… Hm... I now understand why I became a geophysicist.

Grad school and life in Austin would always be my most cherished memories.

At Institute for Geophysics
The University of Texas at Austin
December 3rd, 2015 (The night before it is due.)

Efficient Seismic Imaging with the Double Plane Wave Data

Zeyu Zhao, Ph. D.

The University of Texas at Austin, 2015

Supervisor: Mrinal K. Sen

Co-supervisor: Paul L. Stoffa

Seismic imaging is critical in providing the image of the Earth's subsurface, and it plays an important role in hydrocarbon explorations. Obtaining high resolution images with accurate reflectivities and accurate positions of subsurface structures is the goal for exploration geophysicists. Reverse time migration (RTM), which solves the two-way wave equation, can resolve all wavefield propagation phenomena. In geologically complex regions, RTM has been proven to outperform other imaging methods in correctly revealing the subsurface structures. However, implementing the traditional pre-stack shot profile RTM is computationally expensive. Time consuming wavefield propagation processes need to be performed for each shot gather to obtain high resolution images. The traditional RTM can become extremely expensive with increasing shot numbers. In this dissertation, I focus on improving the migration efficiency of the RTM using the double plane wave (DPW) data, which are the fully decomposed plane wave data. Three RTM methods are developed to migrate the DPW data, all of which can improve the migration efficiency comparing to the traditional shot profile RTM. Two of the methods utilize the adjoint state method, and they are known as the time domain DPW-based RTM and the frequency domain DPW-based RTM. A third migration method using the DPW data is derived under the Born approximation. This method

employs the frequency domain plane wave Green's functions for imaging, and it is named as frequency domain DPW RTM. Among the three proposed RTM methods, the frequency domain DPW RTM is the most efficient. Comparing to the traditional shot profile pre-stack RTM, the frequency domain DPW RTM can increase migration efficiency of RTM by an order of magnitude, making the frequency domain DPW RTM a preferable option for migrating large seismic datasets. All of the three proposed migration methods can image subsurface structures with given dips, which makes them target-oriented imaging methods. The proposed methods are beneficial to migration velocity analysis. To improve the resolution of migration results, a least squares RTM method using the DPW data is proposed. A Born modeling operator that predict the DPW data at the surface and its adjoint operator, which is a migration operator, are derived to implement the least squares RTM. Both of the operators require only a limited number of plane wave Green's functions for the modeling and the migration processes. The proposed least squares RTM substantially increases the efficiency of the least squares migration. In the DPW domain, the applicability of the reciprocity principle is also investigated. The reciprocity principle can be applied to the seismic data that are processed with proper seismic processing flow. Utilizing the reciprocity principle, a DPW dataset transformed from one-sided shot gathers can approximate a DPW dataset transformed from split-spread shot gathers. Therefore, I suggest that one-sided acquisition geometries should be extended to the largest possible offsets, and the reciprocity principle should be invoked to improve subsurface illumination. Migration efficiency can be further improved with the help of the reciprocity principle.

Table of Contents

List of Tables

List of Figures

Chapter 1: Introduction

1.1. MIGRATION

The objective of migration is to recover subsurface structures using post-stack or pre-stack seismic data. Migration methods, such as Kirchhoff migration (Schneider, 1978), Gaussian Beam migration (Hill 1990, 2001), one-way wave equation (Claerbout 1985) and reverse time migration (RTM) (Baysal et al., 1983; McMechan 1983; Whitmore 1983), have been developed based on different approximations of the acoustic wave equation. By solving the two-way wave equation, RTM can resolve all wavefield propagation phenomena, which makes RTM by far the most accurate seismic migration method, given a sufficiently accurate velocity model. In geologically complex regions, RTM has been proven to outperform other migration methods (Farmer et al., 2006; Xu et al., 2011).

RTM can be performed in the time (Baysal et al., 1983; McMechan 1983; Whitmore 1983) and the frequency domains (Xu et al., 2010; Kim et al., 2011). In the time domain, the RTM requires forward and backward propagated wavefields at each time step to apply imaging conditions. Wavefields can be obtained by solving the two-way wave equation with explicit time marching (Tal-Ezer 1986; Tal-Ezer et al., 1987; Kosloff et al., 1989; Etgen and Brandsberg‐Dahl 2009; Zhang and Zhang 2009; Pestana and Stoffa 2010; Fomel et al., 2013). Recently, performing RTM in the frequency domain has been investigated as an alternative to the time domain RTM. In the frequency domain, the two-way wave equation becomes the Helmholtz equation (Marfurt 1984). Several researchers (Shin et al., 2001; Xu et al., 2010; Kim et al., 2011) have successfully

demonstrated the effectiveness of the frequency domain RTM via solving the linear system of the Helmholtz equation.

Although powerful computers have made the traditional pre-stack shot profile RTM a practical migration procedure, pre-stack shot profile RTM is still computationally intensive. The traditional pre-stack shot profile RTM in the time domain requires to computing wavefields at different time steps and store those wavefields, which requires considerable memory or disk space for large models. Wavefield reconstruction methods (Clapp 2009; Liu et al., 2013; Tan and Huang 2014) and optimal checkpointing technique (Symes 2007) were introduced to mitigate the memory requirement issue. Additionally, extensive efforts were made to increase pre-stack RTM efficiency by reducing the number of wavefield propagations. Phase encoding migration strategies (Whitmore 1995; Zhang et al., 2005; Liu et al., 2006) were applied to impelement the RTM by several researchers (Zhang et al., 2007; Zhang and Sun 2008). Phase encoding migration or delayed shot migration strategies were initially implemented for the one-way wave equation migration to migrate a combination of shot profiles in one migration process (Scott and Curtis 1998; Romero et al., 2000). Phase encoding migration strategies, however, often generate undesirable artifacts, known as the crosstalk artifacts (Romero et al., 2000; Liu et al., 2006). The plane wave migration, a special form of phase encoding migration strategies, is the most straightforward method to reduce the crosstalk artifacts (Liu et al., 2006). Plane wave RTM (Vigh and Starr 2006) was shown to be efficient compared to the shot profile RTM due to significant reduction in the number of wavefield propagations during the migration. And it is able to generate images that are equivalent to those of the pre-stack shot profile RTM.

Plane wave migration technique was introduced by Taner (1976). Several imaging methods were developed to migrate plane wave data decomposed from common source

data (Taner 1976; Yilmaz and Taner 1987). Offset plane wave sections can be downward continued (Ottolini and Claerbout 1984; Mosher et al., 1996), and velocity estimation can be performed after the migration (Ottolini and Claerbout 1984). Expanding the traveltime of asymptotic ray theory (ART) receiver Green's functions into plane wave delay time, receiver plane wave data can be migrated (Hildebrand and Carroll 1993; Akbar et al., 1996). Plane wave migration methods are able to improve the migration efficiency.

Images obtained by performing migration can be improved substantially by employing the least squares migration (Schuster 1993; Nemeth et al., 1999). This approach, however, is computationally very expensive. The least squares migration is often performed in the data space that requires a great number of iterations to update reflectivity models. For large seismic datasets, a large amount of forward modeling and migration operations are needed in each iteration, which makes the least square migration a time consuming procedure.

1.2. PLANE WAVE DOMAIN

1.2.1. Overview

Seismic data can be decomposed into plane wave components by slant stacking a seismic profile, which is also known as the $\tau - \mathbf{p}$ transform (Diebold and Stoffa 1981; Stoffa et al., 1981; Brysk and McCowan 1986; Claerbout 1986; Foster and Mosher 1992). The plane wave domain has lots of advantages (Stoffa 1989). Interval velocities can be better estimated in the plane wave domain for wide-angle seismic data (Stoffa and Buhl 1979; Stoffa et al., 1981). Different seismic arrivals, such as reflections, refractions, compressional and shear waves, can be better separated in the plane wave domain (Tatham and Goolsbee 1984). Multiple removal was successfully performed using plane

wave transformed data (Brysk et al., 1987; Liu et al., 2000). The plane wave domain is also the ideal domain for analyzing anisotropy of layers (Sen and Mukherjee 2003; Sil and Sen 2009a, 2009b). Inversion technique was also successfully implemented in the plane wave domain (Diebold and Stoffa 1981).

Migration using plane wave data was introduced by Taner (1976). Conventionally, plane wave decomposed common source data was used in migration (Taner 1976; Taner et al., 1987; Yilmaz and Taner 1987; Akbar et al., 1996; Liu et al., 2002). Plane wave full waveform inversion (FWI) (Vigh and Starr 2008; Zhang and Wang 2009; Tao and Sen 2013), which also employs plane wave data decomposed from common source gathers, was shown to improve computation efficiency.

Recently, a coupled plane wave domain, which is known as the double radon transformed domain (Tatalovic et al., 1991b; Borselen et al., 1992) or the double plane wave (DPW) domain (Zhao, Sen, et al., 2014; Zhao, Stoffa, et al., 2014), was introduced to process seismic data. Simultaneously slant stacking of shot gathers over source and receiver locations can decompose seismic data to the coupled plane wave domain. This double slant stacking procedure is known as the DPW transform (Seifoullaev et al., 2005), and the corresponding plane wave data are known as the DPW data (Zhao, Sen, et al., 2015b). By performing the DPW transform, seismic data can be fully decomposed into plane wave components. The coupled plane wave pre-stack modeling methods (Sen and Frazer 1991; Sen and Pal 2009) were introduced to compute those coupled plane wave data at the surface. Surface-related wave separations can be implemented in the DPW domain (Borselen et al., 1992). A migration method using the DPW data was first implemented by a phase shift migration method in the frequency domain (Tatalovic et al., 1991b; Fokkema and van den Berg 1992). The DPW data can be migrated with a Kirchhoff type depth migration method (Stoffa et al., 2006). An RTM strategy using the

DPW data was introduced to improve the accuracy of the DPW migration, and it was implemented in both the time and the frequency domains (Zhao, Sen, et al., 2014; Zhao, Stoffa, et al., 2014). In the frequency domain, plane wave Green's functions can be used to migrate the DPW data (Zhao, Sen, et al., 2015a). This method substantially improves the efficiency of the RTM.

In the following sections, I will briefly review the traditional plane wave domain, the DPW domain and the DPW Kirchhoff-based migration proposed by Stoffa et al. (2006).

1.2.2. Traditional plane wave domain

1.2.2.1. $\tau - \mathbf{p}$ transform

Slant stacking, known as the $\tau - \mathbf{p}$ transform (Diebold and Stoffa 1981; Stoffa et al., 1981; Claerbout 1986; Foster and Mosher 1992), performs plane wave decomposition. Typically, the $\tau - \mathbf{p}$ transform is performed on seismic record. In the frequency domain, the $\tau - \mathbf{p}$ transform for seismic record $P(\mathbf{x},\omega)$ has a simple form:

$$P(\mathbf{p},\omega) = \int P(\mathbf{x},\omega)\exp(-i\omega\mathbf{p}\cdot\mathbf{x})d\mathbf{x}, \tag{1.1}$$

where $P(\mathbf{p},\omega)$ represents the corresponding frequency domain plane wave seismic profile, ω is the angular frequency, $\mathbf{p} = (p_x, p_y)$ is the ray-parameter (or can be called the slowness vector), and $\mathbf{x} = (x, y, z = 0)$ is the surface location. Typically, a ray-parameter $\mathbf{p}$ is defined as $\mathbf{p} = (\sin\theta_x / v, \sin\theta_y / v)$, where v is the velocity, θ_x and θ_y are the opening angles of the ray-parameter in x and y directions with respect to the

vertical axis, respectively. Therefore, a ray-parameter is a vector that has a direction defined by the opening angle and a length defined by the velocity. Equation (1.1) implies that for a given frequency ω and a ray-parameter $\mathbf{p}$, the seismic data along the phase line $-i\omega\mathbf{p}\cdot\mathbf{x}$ are stacked into one point in the corresponding plane wave domain. The stacked point in the plane wave domain indicates that there is a plane wave component with ray-parameter $\mathbf{p}$ incident at the surface with incident angle θ_x and θ_y. Plane wave data in the $\tau-\mathbf{p}$ domain (i.e., $P(\mathbf{p},\tau)$) are obtained by transforming the $P(\mathbf{p},\omega)$ into the time domain.

Slant stacking is a linear process, and its inverse is given by (Claerbout 1986; Stoffa et al., 2006)

$$P(\mathbf{x},\omega)=\omega^2\int P(\mathbf{p},\omega)\exp(+i\omega\mathbf{p}\cdot\mathbf{x})d\mathbf{p}, \tag{1.2}$$

where ω^2 is the frequency filter.

Typically, slant stacking is performed for a seismic gather, such as a shot gather, a receiver gather or a common mid-point (CMP) gather. For multi-coverage seismic dataset in source-receiver coordinates, $P(\mathbf{s},\mathbf{r},\omega)$, slant stacking can be performed over either source **s** or receiver **r** locations. The corresponding forward slant stacking formulas can be written as

$$P(\mathbf{p}_s,\mathbf{r},\omega)=\int P(\mathbf{s},\mathbf{r},\omega)\exp[-i\omega\mathbf{p}_s\cdot(\mathbf{s}-\mathbf{x}_{ref})]d\mathbf{s}, \tag{1.3}$$

and

$$P(\mathbf{s},\mathbf{p}_r,\omega)=\int P(\mathbf{s},\mathbf{r},\omega)\exp[-i\omega\mathbf{p}_r\cdot(\mathbf{r}-\mathbf{x}_{ref})]d\mathbf{r}, \tag{1.4}$$

for stacking over $\mathbf{s}$ and $\mathbf{r}$, respectively. In equations (1.3) and (1.4), $\mathbf{x}_{ref}$ is the reference point for slant stacking, $\mathbf{p}_s$ and $\mathbf{p}_r$ are source and receiver plane wave ray-parameters, respectively.

If seismic gathers are in the source-offset coordinates (i.e., $P(\mathbf{s}',\mathbf{o},\omega)$), we can perform slant stacking for $\mathbf{o}$, where $\mathbf{o}=\mathbf{s}'-\mathbf{r}$, according to

$$P(\mathbf{s}',\mathbf{p}_o,\omega)=\int P(\mathbf{s}',\mathbf{o},\omega)\exp(-i\omega\mathbf{p}_o\cdot\mathbf{o})d\mathbf{o}, \tag{1.5}$$

where $P(\mathbf{s},\mathbf{p}_o,\omega)$ is the corresponding plane wave data with an offset ray-parameter $\mathbf{p}_o$, and $\mathbf{s}'=\mathbf{s}$. Ray-parameters $\mathbf{p}_s$, $\mathbf{p}_r$ and $\mathbf{p}_o$ are ray-parameters measured at the surface.

According to equation (1.2), the inverse slant stacking formulas for equations (1.3), (1.4) and (1.5) can be written as

$$P(\mathbf{s},\mathbf{r},\omega)=\omega^2\int P(\mathbf{p}_s,\mathbf{r},\omega)\exp[+i\omega\mathbf{p}_s\cdot(\mathbf{s}-\mathbf{x}_{ref})]d\mathbf{p}_s, \tag{1.6}$$

$$P(\mathbf{s},\mathbf{r},\omega)=\omega^2\int P(\mathbf{s},\mathbf{p}_r,\omega)\exp[+i\omega\mathbf{p}_r\cdot(\mathbf{r}-\mathbf{x}_{ref})]d\mathbf{p}_r, \tag{1.7}$$

and

$$P(\mathbf{s}',\mathbf{o},\omega)=\omega^2\int P(\mathbf{s}',\mathbf{p}_o,\omega)\exp(+i\omega\mathbf{p}_o\cdot\mathbf{o})d\mathbf{p}_o, \tag{1.8}$$

respectively.

By performing the traditional $\tau - \mathbf{p}$ transform, seismic data recorded on the surface are decomposed into plane wave components for given locations. Hyperbolic moveout curves in the t-$\mathbf{x}$ domain were transformed into elliptical moveout curves in the $\tau - \mathbf{p}$ domain.

1.2.3. Double plane wave domain

1.2.3.1. Double plane wave transform

Previously introduced $\tau - \mathbf{p}$ transforms perform slant stacking over $\mathbf{o}$, $\mathbf{s}$ or $\mathbf{r}$ and decompose seismic data into $\mathbf{p}_o$, $\mathbf{p}_s$ or $\mathbf{p}_r$ plane wave components, respectively. The recorded seismic data $P(\mathbf{s},\mathbf{r},\omega)$, however, can be fully decomposed into a coupled plane wave domain by performing the slant stacking for $\mathbf{s}$ and $\mathbf{r}$ simultaneously (Stoffa et al., 2006). The corresponding coupled plane wave domain is known as the double radon transformed domain (Fokkema and van den Berg 1992) or the DPW domain (Zhao, Stoffa, et al., 2014). The double slant stacking procedure is called the DPW transform. Given densely spatial sampled seismic data, the DPW transformed data can be obtained with minimal slant stacking artifacts. The forward and inverse DPW transforms (Stoffa et al., 2006) for the recorded data $P(\mathbf{s},\mathbf{r},\omega)$ in the source-receiver coordinates can be written as

$$P(\mathbf{p}_s,\mathbf{p}_r,\omega) = \iint P(\mathbf{s},\mathbf{r},\omega)\exp(-i\omega[\mathbf{p}_s\cdot(\mathbf{s}-\mathbf{x}_{ref})+\mathbf{p}_r\cdot(\mathbf{r}-\mathbf{x}_{ref})])d\mathbf{s}\,d\mathbf{r}, \qquad (1.9)$$

and

$$P(\mathbf{s},\mathbf{r},\omega) = \omega^4\iint P(\mathbf{p}_s,\mathbf{p}_r,\omega)\exp(+i\omega[\mathbf{p}_s\cdot(\mathbf{s}-\mathbf{x}_{ref})+\mathbf{p}_r\cdot(\mathbf{r}-\mathbf{x}_{ref})])d\mathbf{p}_s\,d\mathbf{p}_r, \qquad (1.10)$$

respectively. For simplicity, $\mathbf{x}_{ref}$ is always chosen to be the same for stacking over $\mathbf{s}$ and stacking over $\mathbf{r}$. Each trace in this DPW domain is indexed by $\mathbf{p}_s$ and $\mathbf{p}_r$, meaning that a receiver plane wave arriving at the surface with a ray-parameter $\mathbf{p}_r$ is introduced by a source plane wave initiated at the surface with a ray-parameter $\mathbf{p}_s$.

The DPW transform can also be performed for the recorded data $P(\mathbf{s},\mathbf{o},\omega)$ in the source-offset coordinates (Tatalovic et al., 1991b; Stoffa et al., 2006), and the corresponding forward and inverse DPW transforms can be written as

$$P(\mathbf{p}_{s'},\mathbf{p}_o,\omega)=\iint P(\mathbf{s}',\mathbf{o},\omega)\exp(-i\omega[\mathbf{p}_{s'}\cdot(\mathbf{s}'-\mathbf{x}_{ref})+\mathbf{p}_o\cdot\mathbf{o}])d\mathbf{s}'d\mathbf{o}, \qquad (1.11)$$

and

$$P(\mathbf{s}',\mathbf{o},\omega)=\omega^4\iint P(\mathbf{p}_{s'},\mathbf{p}_o,\omega)\exp(+i\omega[\mathbf{p}_{s'}\cdot(\mathbf{s}'-\mathbf{x}_{ref})+\mathbf{p}_o\cdot\mathbf{o}])d\mathbf{p}_{s'}d\mathbf{p}_o, \qquad (1.12)$$

respectively. For brevity, I will use Ps-Pr to represent the $P(\mathbf{p}_s,\mathbf{p}_r,\omega)$ DPW data and use Ps-Po to represent the $P(\mathbf{p}_{s'},\mathbf{p}_o,\omega)$ DPW data. $\mathbf{p}_{s'}$ plane waves in the Ps-Po DPW data carry dips information of subsurface interfaces (Detailed discussions is in the next section). $\mathbf{p}_o$ in the Ps-Po DPW data is analogous to $\mathbf{p}_r$ in the Ps-Pr DPW data, and it represents offset plane waves introduced by reflectors whose measured dips at surfaces are $\mathbf{p}_{s'}$.

Equations (1.9) and (1.11) use different variables and different references during double slant stacking, so the corresponding DPW datasets are expected to be visually different. However, $P(\mathbf{p}_s,\mathbf{p}_r,\omega)$ and $P(\mathbf{p}_{s'},\mathbf{p}_o,\omega)$ represent an identical seismic dataset. Because wavefields are invariant for different coordinate systems, recorded shot gathers and the transformed DPW data have relationships as follow:

$$P'(\mathbf{s}',\mathbf{o},\omega) = P(\mathbf{s},\mathbf{r},\omega), \tag{1.13}$$

$$P'(\mathbf{p}_{s'},\mathbf{p}_o,\omega) = P(\mathbf{p}_s,\mathbf{p}_r,\omega). \tag{1.14}$$

The above analyses are in 3D. For simplicity, 2D illustrations are used to demonstrate the DPW transform and the corresponding DPW dataset. In a 2D case, shot gathers in the source-receiver and the source-offset coordinates are shown in Figure 1.1 and 1.2, respectively.

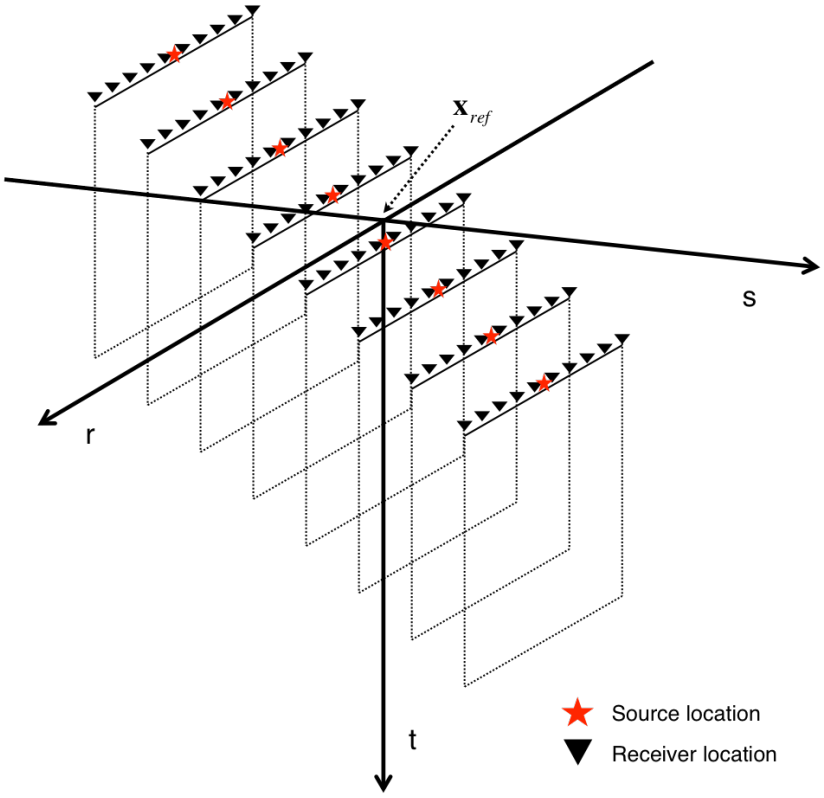

Figure 1.1. An illustration of 2D shot gathers in the source-receiver coordinates. $\mathbf{x}_{ref}$ is the reference point for the DPW transform.

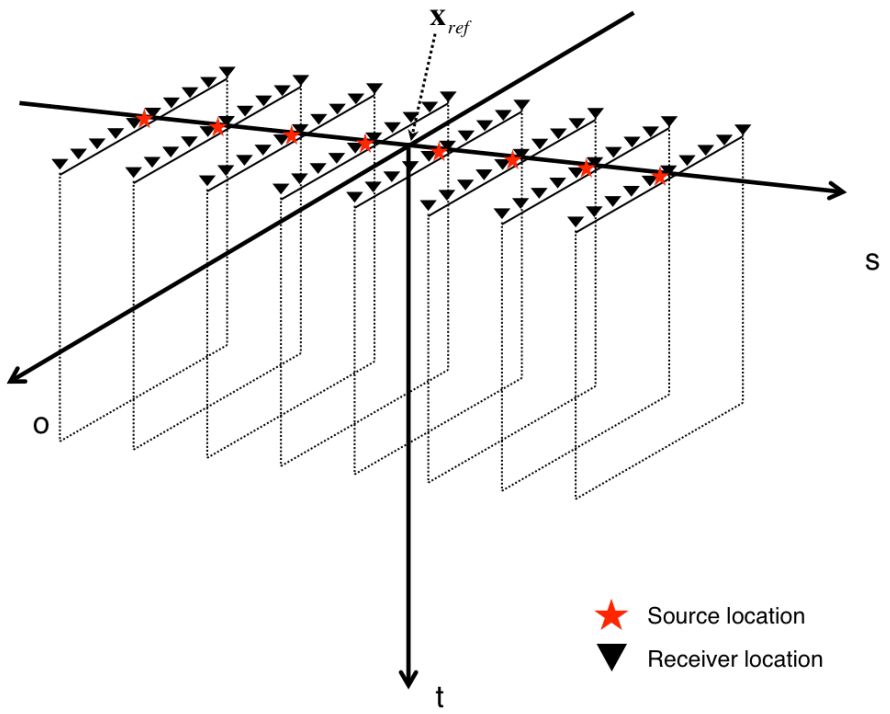

Figure 1.2. An illustration of 2D shot gathers in the source-offset coordinates. $\mathbf{x}_{ref}$ is the reference point for the DPW transform.

By performing the DPW transform using equation (1.9), a Ps-Pr DPW dataset can be obtained in a 3D volume as shown in Figure 1.3a). The horizontal plane of the 3D volume is shown in Figure 1.3b), where two horizontal axes of the plane are indexed by $\mathbf{p}_s$ and $\mathbf{p}_r$. The vertical axis of the 3D volume is either vertical delay time τ or frequency ω, depending upon the domain of the dataset. A Ps-Po DPW dataset is similar to a Ps-Pr DPW dataset, whereas the two horizontal axes of the 3D volume are indexed by $\mathbf{p}_{s'}$ and $\mathbf{p}_o$.

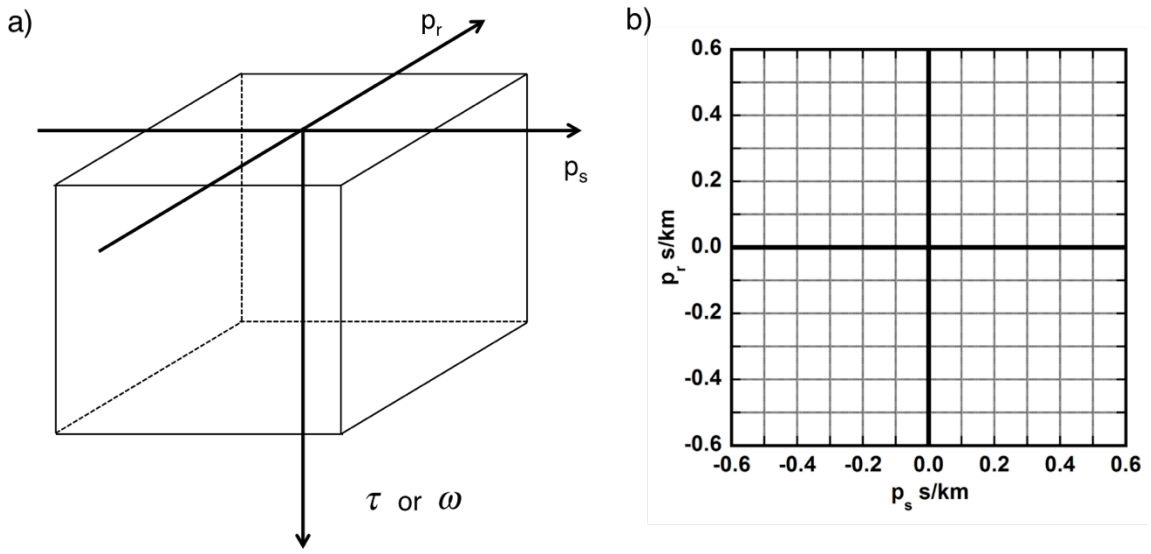

Figure 1.3. a) An illustration of a 3D volume of a Ps-Pr DPW dataset transformed from 2D gathers shown in Figure 1.1. b) An illustration of the horizontal plane of the 3D volume shown in a).

1.2.3.2. Relationships between the Ps-Pr DPW data and the Ps-Po DPW data

Simple relationships between different ray-parameters $\mathbf{p}_s$, $\mathbf{p}_r$ and $\mathbf{p}_o$ were derived by Stoffa et al. (2006). They started with the basic relationships between the source-receiver coordinates and the source-offset coordinates:

$$\mathbf{o} = \mathbf{r} - \mathbf{s}, \tag{1.15}$$

$$\mathbf{s}' = \mathbf{s}, \tag{1.16}$$

Equations (1.15) and (1.16) explain changes of variables from the source-receiver coordinates to the source-offset coordinates. Taking the derivative for t with respect to $\mathbf{s}$

and $\mathbf{r}$, and using the chain rule, following relationships can be derived (Stoffa et al., 2006):

$$\mathbf{p}_r = \frac{\partial t}{\partial \mathbf{r}} = \frac{\partial t}{\partial \mathbf{o}}\frac{\partial \mathbf{o}}{\partial \mathbf{r}} + \frac{\partial t}{\partial \mathbf{s}'}\frac{\partial \mathbf{s}'}{\partial \mathbf{r}} = \frac{\partial t}{\partial \mathbf{o}} = \mathbf{p}_o, \tag{1.17}$$

$$\mathbf{p}_s = \frac{\partial t}{\partial \mathbf{s}} = \frac{\partial t}{\partial \mathbf{s}'}\frac{\partial \mathbf{s}'}{\partial \mathbf{s}} + \frac{\partial t}{\partial \mathbf{o}}\frac{\partial \mathbf{o}}{\partial \mathbf{s}} = \frac{\partial t}{\partial \mathbf{s}'} - \frac{\partial t}{\partial \mathbf{o}} = \mathbf{p}_{s'} - \mathbf{p}_o, \tag{1.18}$$

$$d\mathbf{p}_s d\mathbf{p}_r = d\mathbf{p}_{s'} d\mathbf{p}_o, \tag{1.19}$$

where $\frac{\partial t}{\partial \mathbf{r}}$, $\frac{\partial t}{\partial \mathbf{s}}$, and etc., are partial derivatives. According to equations (1.17) and (1.18), we can have

$$\mathbf{p}_{s'} = \mathbf{p}_s + \mathbf{p}_r. \tag{1.20}$$

Relationships between $\mathbf{p}_s$, $\mathbf{p}_r$ and $\mathbf{p}_{s'}$ are illustrated in Figure 1.4, 1.5 and 1.6.

Figure 1.4a) shows a raypath in a 2D homogenous medium, where the background velocity is constant. A ray with ray-parameter $\mathbf{p}_s$ initiated at the surface hits a reflector and bounces to the surface with ray-parameter $\mathbf{p}_r$. θ_1 and θ_2 are the opening angles of the incident ray and the outgoing ray with respect to the vertical axis, respectively. θ_1 is defined to be negative, and θ_2 is defined to be positive. θ_r represents the dipping angle of the reflector with respect to the horizontal axis. At the surface, according to equation (1.20), vector addition can be performed between ray-parameters $\mathbf{p}_s$ and $\mathbf{p}_r$ with a resultant ray-parameter $\mathbf{p}_{s'}$, as shown in Figure 1.4b). In Figure 1.4b), θ_3 is the opening angle of $\mathbf{p}_{s'}$ with respect to the vertical axis. Because

the background velocity is constant, the values of ray-parameters $\mathbf{p}_s$ and $\mathbf{p}_r$ remain constant along the entire ray. As a result, θ_3 is equal to the dipping angle θ_r of the reflector. In this case, ray-parameter $\mathbf{p}_{s'}$ measured at the surface represents the dipping angle of the subsurface interface.

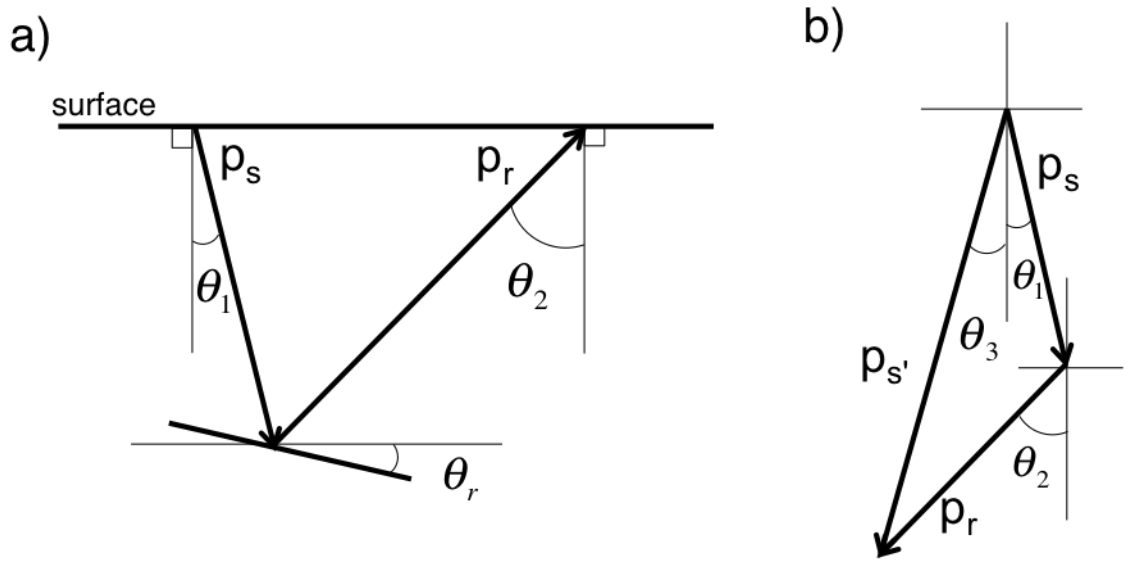

Figure 1.4. a) An illustration of a raypath in a homogeneous medium, where $\mathbf{p}_s$ is the ray-parameter of the incident ray, and $\mathbf{p}_r$ is the ray-parameter of the ray arriving at the surface. b) An illustration of vector addition for $\mathbf{p}_s$ and $\mathbf{p}_r$ at the surface.

Figure 1.5a) shows a raypath in an inhomogeneous medium with velocity variations. $\mathbf{p}_s$ is the ray-parameter of the ray initiated at the surface, and $\mathbf{p}_r$ is the ray-parameter of the ray received at the surface. θ_1 and θ_2 are again the opening angles of the incident ray and the outgoing ray at the surface with respect to the vertical axis, respectively. Assuming constant velocity at the surface, vector addition can be performed

at the surface, as shown in Figure 1.5b). Because the medium is inhomogeneous, the values of ray-parameters $\mathbf{p}_s$ and $\mathbf{p}_r$ measured at the surface are not necessarily equal to those measured at the reflection point. As a result, the opening angle θ_3 of the ray-parameter $\mathbf{p}_{s'}$ measured at the surface might not be equal to the dipping angle θ_r of the reflector. Although the dip of the interface cannot be directly obtained by measuring ray-parameter $\mathbf{p}_{s'}$ at the surface, $\mathbf{p}_{s'}$ plane wave carries the information of the dipping interface. In fact, ray-parameter $\mathbf{p}_{s'}$ is the time dips of the subsurface interfaces in a seismic profile, and $\mathbf{p}_{s'}$ plane waves need to be migrated to recover the true dips of the interfaces.

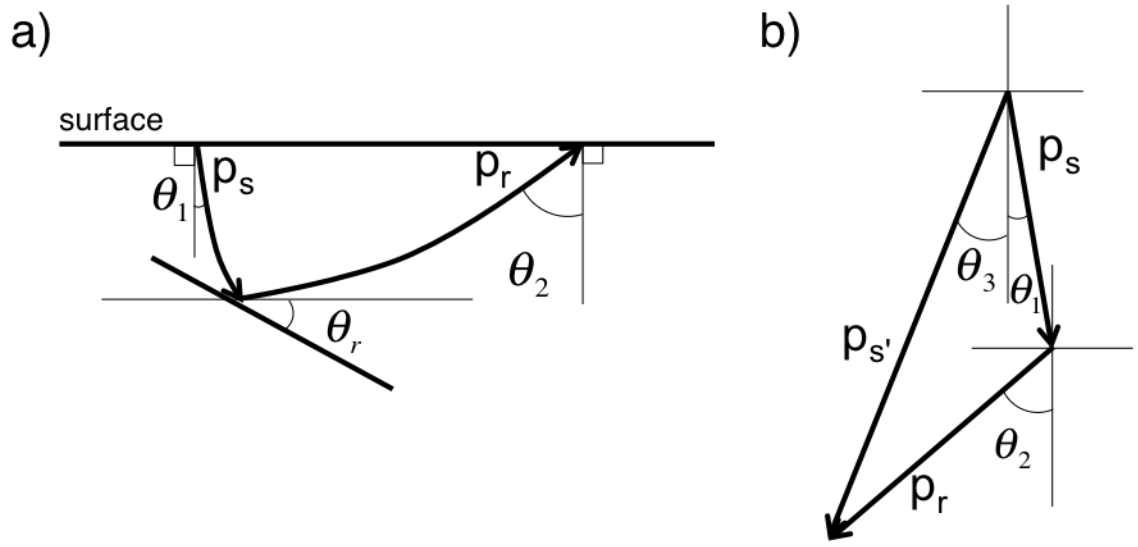

Figure 1.5. a) An illustration of a raypath in an inhomogeneous medium, where $\mathbf{p}_s$ is the ray-parameter of the incident ray, and $\mathbf{p}_r$ is the ray-parameter of the ray arriving at the surface. b) An illustration of vector addition for $\mathbf{p}_s$ and $\mathbf{p}_r$ at the surface.

A plane wave incident at the surface with ray-parameter $\mathbf{p}_s$ can generate a spherical wave when it hits a diffractor, as shown in Figure 1.6. The scattered spherical wave can be viewed as a composite of plane waves propagating at all directions with different $\mathbf{p}_r$ ray-parameters. Introduced by the same $\mathbf{p}_s$ plane wave, each $\mathbf{p}_r$ plane wave carries a part of the scattered energy. At the surface, by applying the vector addition shown in Figure 1.4b), each $\mathbf{p}_s$ and $\mathbf{p}_r$ combination can form one $\mathbf{p}_{s'}$ plane wave. Because the number of $\mathbf{p}_r$ plane waves is large, the same number of $\mathbf{p}_{s'}$ plane waves can be generated, as if there were a great number of interfaces with different dips at the subsurface. As I will demonstrate in following chapters, when all combinations of $\mathbf{p}_s$ and $\mathbf{p}_r$ plane waves or all $\mathbf{p}_{s'}$ plane waves are migrated, only at the diffraction point can migrated energy be constructively stacked. As a result, the diffractor can be fully recovered.

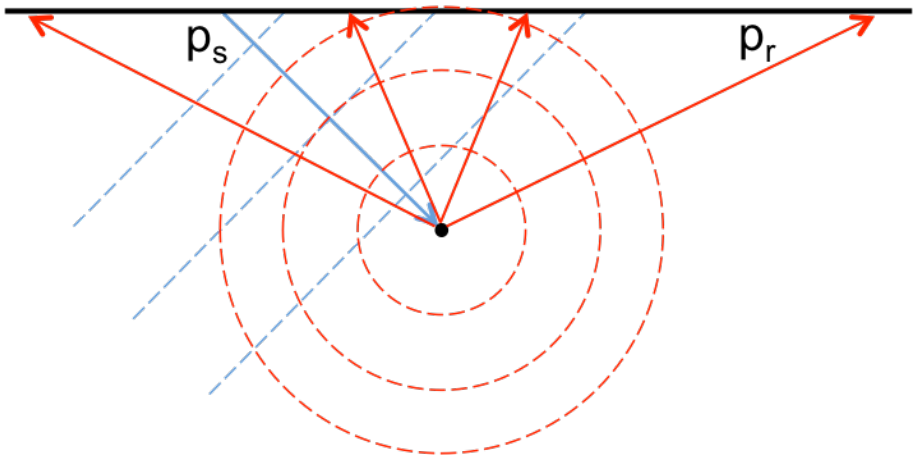

Figure 1.6. An illustration of raypaths and wavefronts, when a plane wave hits a diffractor in a homogeneous medium. The solid blue line and the solid red lines with the arrow indicate the raypaths of incident $\mathbf{p}_s$ plane wave and scattered $\mathbf{p}_r$ plane waves, respectively. The dashed blue line and the dashed red circles indicate the plane and the spherical wavefronts, respectively.

In the real world, a combination of ray-parameters $\mathbf{p}_s$ and $\mathbf{p}_r$ or a ray-parameter $\mathbf{p}_{s'}$ rarely represents the true dips of a subsurface interface. Nonetheless, selected plane waves can be used to perform migration. Therefore, subsurface interfaces with specific dips can be recovered independently. Plane waves in DPW datasets (either Ps-Po datasets or Ps-Pr datasets) carry intuitive geological structure information that cannot be easily identified in traditional gathers. As a result, when migration is performed using the DPW data, subsurface structures can be imaged in a target-oriented way. This might help velocity building and seismic interpretation processes.

1.2.3.3. Kirchhoff-based DPW depth migration

Migrating the DPW data was first implemented with phase shift migration method (Tatalovic et al., 1991b; Fokkema and van den Berg 1992). Stoffa et al. (2006) introduced a Kirchhoff type migration to migrate the DPW data.

Based on the double downward-continuation integral (Clayton and Stolt 1981; Stolt and Weglein 1985; Hildebrand and Carroll 1993), the Kirchhoff-based DPW depth migration downward continues the DPW data from the surface by calculating plane wave vertical delay times. In the frequency domain, the double downward-continuation integral is given by

$$I(\mathbf{x},\omega) = \int \partial_n G(\mathbf{x},\mathbf{s},\omega) \int \partial_n G(\mathbf{x},\mathbf{r},\omega) P(\mathbf{s},\mathbf{r},\omega)\, d\mathbf{r}\, d\mathbf{s}, \tag{1.21}$$

where $P(\mathbf{s},\mathbf{r},\omega)$ is the recorded seismic data at the surface, $I(\mathbf{x},\omega)$ represents the subsurface image for imaging point $\mathbf{x}$ given a specific frequency ω, $G(\mathbf{x},\mathbf{s},\omega)$ and $G(\mathbf{x},\mathbf{r},\omega)$ are Green's functions from $\mathbf{s}$ and from $\mathbf{r}$ to the $\mathbf{x}$, respectively, and $\partial_n G$ is the surface normal derivative of the Green's function.

Green's functions need to be constructed to predict wavefields in the subsurface. Under the high frequency approximation, ART Green's functions given by

$$G(\mathbf{x},\mathbf{r},\omega) \approx A(\mathbf{x},\mathbf{s}) \exp(-i\omega t(\mathbf{x},\mathbf{s})) \tag{1.22}$$

where $A(\mathbf{x},\mathbf{s})$ and $t(\mathbf{x},\mathbf{s})$ are the amplitude and traveltime terms from $\mathbf{s}$ to $\mathbf{x}$, respectively. Receiver ART Green's functions are in a form similar to that of equation (1.22), except that $\mathbf{s}$ in equation (1.22) is replaced by an $\mathbf{r}$.

By substituting ART Green's functions into equation (1.21) and assuming that the amplitude terms of Green's functions are slowly varying functions of space (Hildebrand and Carroll 1993), the pre-stack Kirchhoff depth migration imaging condition for a given frequency can be derived as

$$I(\mathbf{x},\omega) = -\omega^2 \int\int W(\mathbf{x},\mathbf{s},\mathbf{r}) \exp(-i\omega[t(\mathbf{x},\mathbf{s}) + t(\mathbf{x},\mathbf{r})]) P(\mathbf{s},\mathbf{r},\omega)\, d\mathbf{r}\, d\mathbf{s}, \tag{1.23}$$

where $W(\mathbf{x},\mathbf{s},\mathbf{r})$ is the amplitude weighting term, and it can be written as

$$W(\mathbf{x},\mathbf{s},\mathbf{r}) = \partial_n t(\mathbf{x},\mathbf{s}) A(\mathbf{x},\mathbf{s}) \partial_n t(\mathbf{x},\mathbf{r}) A(\mathbf{x},\mathbf{r}). \tag{1.24}$$

Substituting equation (1.10) can into equation (1.23) (Stoffa et al., 2006), equation (1.23) becomes

$$\begin{aligned} I(\mathbf{x},\omega) = -\omega^6 \iint\iint W(\mathbf{x},\mathbf{s},\mathbf{r}) \exp(-i\omega[t(\mathbf{x},\mathbf{s}) + t(\mathbf{x},\mathbf{r})]) \\ \times P(\mathbf{p}_s,\mathbf{p}_r,\omega) \exp(+i\omega[\mathbf{p}_s \cdot (\mathbf{s} - \mathbf{x}_{ref}) + \mathbf{p}_r \cdot (\mathbf{r} - \mathbf{x}_{ref})]) d\mathbf{p}_s d\mathbf{p}_r d\mathbf{r} d\mathbf{s}. \end{aligned} \tag{1.25}$$

Rearranging terms, equation (1.25) becomes

$$\begin{aligned} I(\mathbf{x},\omega) = -\omega^6 \iint\iint W(\mathbf{x},\mathbf{s},\mathbf{r}) P(\mathbf{p}_s,\mathbf{p}_r,\omega) \\ \times \exp(-i\omega[t(\mathbf{x},\mathbf{s}) - \mathbf{p}_s \cdot (\mathbf{s} - \mathbf{x}_{ref}) + t(\mathbf{x},\mathbf{r}) - \mathbf{p}_r \cdot (\mathbf{r} - \mathbf{x}_{ref})]) d\mathbf{p}_s d\mathbf{p}_r d\mathbf{r} d\mathbf{s}. \end{aligned} \tag{1.26}$$

According to the relationship between the plane wave vertical delay time τ and the traveltime t (Diebold and Stoffa 1981):

$$\tau = t - \mathbf{p} \cdot \mathbf{x}, \tag{1.27}$$

the traveltime term $t(\mathbf{x},\mathbf{s}) - \mathbf{p}_s \cdot (\mathbf{s} - \mathbf{x}_{ref})$ in equation (1.26) can be written as

$$\tau_{\mathbf{x}_{ref}}(\mathbf{x},\mathbf{p}_s) = t(\mathbf{x},\mathbf{s}) - \mathbf{p}_s \cdot (\mathbf{s} - \mathbf{x}_{ref}), \tag{1.28}$$

where $\tau_{\mathbf{x}_{ref}}(\mathbf{x},\mathbf{p}_s)$ is the vertical delay time of ray-parameter $\mathbf{p}_s$ with respect to the reference point $\mathbf{x}_{ref}$. Equation (1.28) can also be written as

$$\tau_{\mathbf{x}_{ref}}(\mathbf{x},\mathbf{p}_s) = \tau_h(\mathbf{x},\mathbf{p}_s) - \mathbf{p}_s \cdot (\mathbf{x}_h - \mathbf{x}_{ref}), \tag{1.29}$$

where $\mathbf{x}_h$ is the horizontal location of $\mathbf{x}$, and $\tau_h(\mathbf{x},\mathbf{p}_s)$ is the vertical delay time of ray-parameter $\mathbf{p}_s$ with respect to $\mathbf{x}_h$. Equation (1.29) can be explained in Figure 1.7 where we have a homogenous velocity model with v=1. In this case, the length of a raypath can represent the traveltime for a ray.

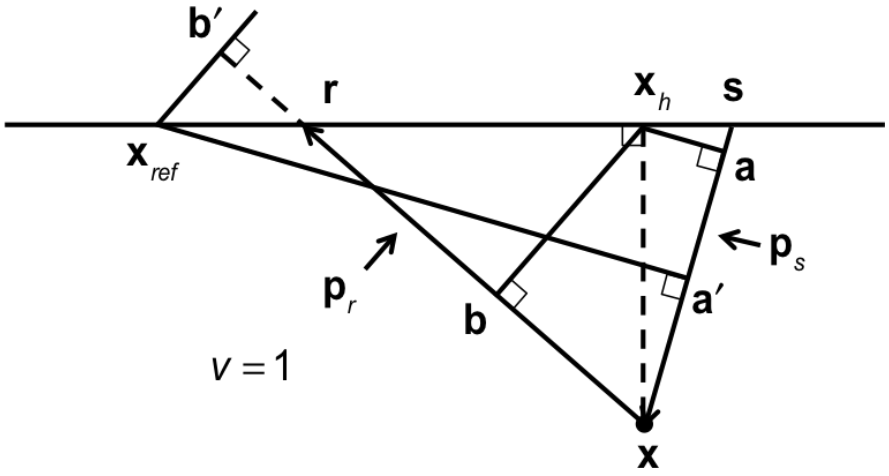

Figure 1.7. An illustration of a homogenous velocity model with raypath drawn. $\mathbf{s} = (s_x, s_y = 0, s_z = 0)$ is the source location, $\mathbf{r} = (r_x, r_y = 0, r_z = 0)$ is the receiver location, $\mathbf{x} = (x, y = 0, z)$ is an image point, $\mathbf{x}_h = (x_h, y_h = 0, z_h = 0)$ is the horizontal position of $\mathbf{x}$, and $\mathbf{x}_{ref} = (x_{ref}, y_{ref} = 0, z_{ref} = 0)$ is the reference point of the DPW transform. $\mathbf{p}_s = (p_{sx}, 0)$ and $\mathbf{p}_r = (p_{rx}, 0)$ are ray-parameters for the incident ray and the received ray, respectively. $\mathbf{a}$, $\mathbf{a}'$, $\mathbf{b}$ and $\mathbf{b}'$ have geometrical meanings as shown in the figure.

In Figure 1.7, a ray initiated from **s** with ray-parameter $\mathbf{p}_s$ hits an image point **x**. A ray with ray-parameter $\mathbf{p}_r$ and received by **r** was selected to form a full raypath from the source to the receiver. Because the ray traveltime can be represented by the raypath, for the ray initiated from the source, we have

$$\tau_{\mathbf{x}_{ref}}(\mathbf{x}, \mathbf{p}_s) = t(\mathbf{x}, \mathbf{s}) - \mathbf{p}_s \cdot (\mathbf{s} - \mathbf{x}_{ref}) = \mathbf{sx} - \mathbf{sa}' = \mathbf{a}'\mathbf{x}, \tag{1.30}$$

$$\tau_{\mathbf{x}_h}(\mathbf{x}, \mathbf{p}_s) = t(\mathbf{x}, \mathbf{s}) - \mathbf{p}_s \cdot (\mathbf{s} - \mathbf{x}_h) = \mathbf{sx} - \mathbf{sa} = \mathbf{ax}, \tag{1.31}$$

where $t_{\mathbf{sx}}$ is the traveltime from **s** to **x**, $\mathbf{x}_h$ is the horizontal position of **x**, $\tau_{\mathbf{x}_{ref}}$ is the plane wave vertical delay time with respect to $\mathbf{x}_{ref}$, and $\tau_{\mathbf{x}_h}$ is the plane wave vertical delay time with respect to $\mathbf{x}_h$. According to Figure 1.7, the $\tau_{\mathbf{x}_{ref}}$ can also be represented by

$$\begin{aligned} \tau_{\mathbf{x}_{ref}}(\mathbf{x},\mathbf{p}_s) &= \mathbf{sx} - \mathbf{sa}' \\ &= \mathbf{sx} - \mathbf{sa} - \mathbf{aa}' \\ &= \mathbf{ax} - \mathbf{aa}'. \end{aligned} \tag{1.32}$$

Substituting $\mathbf{ax} = \tau_h(\mathbf{x},\mathbf{p}_s)$ and $\mathbf{aa}' = \mathbf{p}_s \cdot (\mathbf{x}_h - \mathbf{x}_{ref})$ into equation (1.32), we can obtain

$$\tau_{\mathbf{x}_{ref}}(\mathbf{x},\mathbf{p}_s) = \tau_h(\mathbf{x},\mathbf{p}_s) - \mathbf{p}_s \cdot (\mathbf{x}_h - \mathbf{x}_{ref}). \tag{1.33}$$

Equation (1.33) suggests that the vertical delay time $\tau_{\mathbf{x}_{ref}}$ with respect to $\mathbf{x}_{ref}$ can be obtained from the vertical delay time τ_h with respect to $\mathbf{x}_h$ plus a time correction term $-\mathbf{p}_s \cdot (\mathbf{x}_h - \mathbf{x}_{ref})$.

Following the above developments, for a ray received by the receiver with ray-parameter $\mathbf{p}_r$, we can obtain

$$\tau_{\mathbf{x}_{ref}}(\mathbf{x},\mathbf{p}_r) = \tau_h(\mathbf{x},\mathbf{p}_r) - \mathbf{p}_r \cdot (\mathbf{x}_h - \mathbf{x}_{ref}). \tag{1.34}$$

Substituting equations (1.29) and (1.34) into equation (1.26) with subscript *h* dropped for $\tau_h(\mathbf{x},\mathbf{p}_s)$ and $\tau_h(\mathbf{x},\mathbf{p}_r)$, and summing over frequencies (Stoffa et al., 2006), the Kirchhoff-based DPW depth migration imaging condition can be written as

$$I(\mathbf{x}) = L(\mathbf{x})\iint P(\mathbf{p}_s,\mathbf{p}_r,\tau(\mathbf{x},\mathbf{p}_s)+\tau(\mathbf{x},\mathbf{p}_r)-(\mathbf{p}_s+\mathbf{p}_r)\cdot(\mathbf{x}_h-\mathbf{x}_{ref}))d\mathbf{p}_s d\mathbf{p}_r, \qquad (1.35)$$

where $\tau(\mathbf{x},\mathbf{p}_s)$ and $\tau(\mathbf{x},\mathbf{p}_r)$ are $\mathbf{p}_s$ and $\mathbf{p}_r$ plane wave vertical delay times with respect to $\mathbf{x}_h$, respectively, and $L(\mathbf{x}) = \dfrac{\partial^2}{\partial\tau^2}\iint W(\mathbf{x},\mathbf{s},\mathbf{r})d\mathbf{s}\,d\mathbf{r}$.

Focusing on the kinematic aspect of equation (1.35), the amplitude weighting term $L(\mathbf{x})$ can be ignored, and equation (1.35) becomes

$$I(\mathbf{x}) = \iint P(\mathbf{p}_s,\mathbf{p}_r,\tau(\mathbf{x},\mathbf{p}_s)+\tau(\mathbf{x},\mathbf{p}_r)-(\mathbf{p}_s+\mathbf{p}_r)\cdot(\mathbf{x}_h-\mathbf{x}_{ref}))d\mathbf{p}_s d\mathbf{p}_r, \qquad (1.36)$$

Equation (1.36) suggests that for a given $\mathbf{p}_s$ and $\mathbf{p}_r$ combination, the image at $\mathbf{x}$ can be obtained by finding the DPW data whose total vertical delay time equals to $\tau(\mathbf{x},\mathbf{p}_s)+\tau(\mathbf{x},\mathbf{p}_r)-(\mathbf{p}_s+\mathbf{p}_r)\cdot(\mathbf{x}_h-\mathbf{x}_{ref})$, and then positioning the corresponding DPW data at the image point $\mathbf{x}$.

In equation (1.36), $\tau(\mathbf{x},\mathbf{p}_s)$ and $\tau(\mathbf{x},\mathbf{p}_s)$, which are vertical delay times with respect to $\mathbf{x}_h$, are required to predict plane wavefields. At each $\mathbf{x}_h$ position, the DPW data in vertical delay times with respect to $\mathbf{x}_h$ are required. However, the DPW data transformed from shot gathers are in vertical delay times with respect to $\mathbf{x}_{ref}$. Therefore, at each $\mathbf{x}_h$ position, the term $-(\mathbf{p}_s+\mathbf{p}_r)\cdot(\mathbf{x}_h-\mathbf{x}_{ref})$ in equation (1.36) shift the original

vertical delay time of the DPW data, which is with respect to $\mathbf{x}_{ref}$, to a new vertical delay time, which is with respect to $\mathbf{x}_h$.

Figure 1.8 shows the migration results obtained by implementing the Kirchhoff-based DPW depth migration. The image is reasonablely good, and ray-parameter common image gathers (CIGs), as shown in Figure 1.9, can be easily obtained.

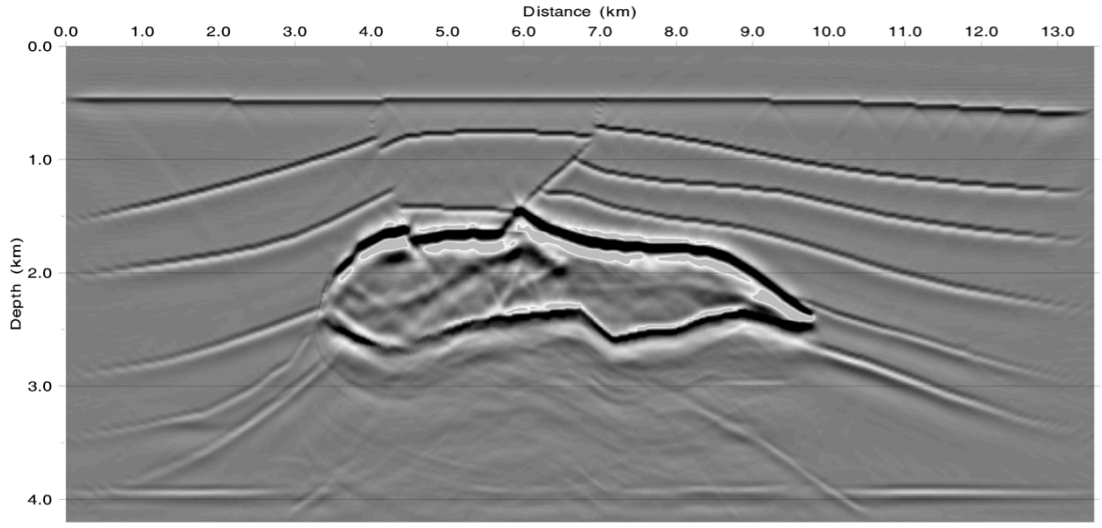

Figure 1.8. The migration result obtained by the Kirchhoff-based DPW depth migration.

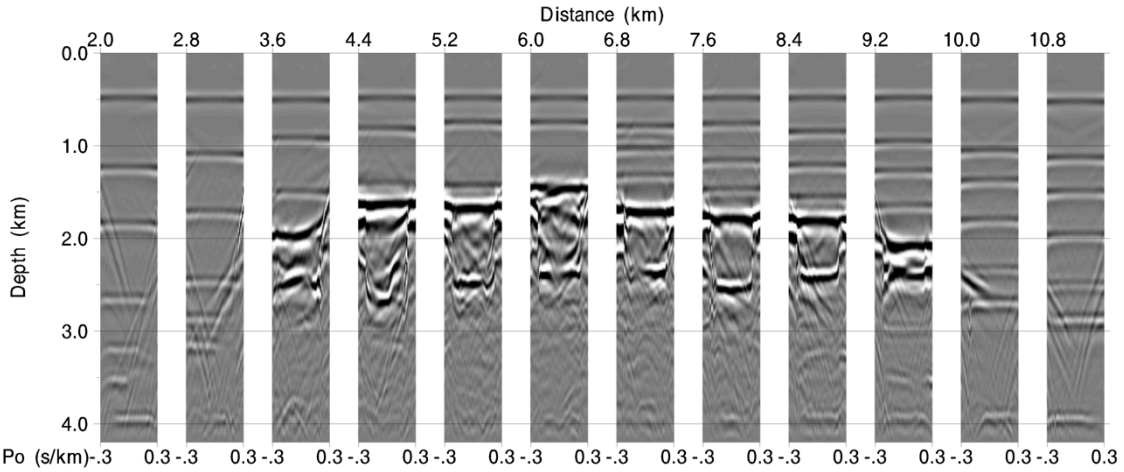

Figure 1.9. The Ray-parameter CIGs of the migration result shown in Figure 1.8.

The Kirchhoff-based DPW depth migration imaging condition has a similar form to that of the pre-stack shot profile Kirchhoff depth migration where traveltimes from source and receiver locations to different subsurface locations are needed (Schneider et al., 1992; Akbar et al., 1996). However, the Kirchhoff-based DPW depth migration requires the plane wave vertical delay time for a given combination of ray-parameters, $\mathbf{p}_s$ and $\mathbf{p}_r / \mathbf{p}_o$. The number of vertical delay times required by the Kirchhoff-based DPW migration is much smaller than the number of traveltimes required by the shot profile Kirchhoff migration (Stoffa et al., 2006). In addition, the same vertical delay time can be used for source and receiver plane waves, both of which have a same incident angle at the surface. Therefore, the Kirchhoff-based DPW depth migration has the potential to achieve much better efficiency than shot profile Kirchhoff depth migration. As previously introduced, different plane waves in a DPW dataset can be selected for migration, so that subsurface interfaces can be imaged according to their dips, making the method target-oriented. Additionally, trial images, as well as CIGs, can be obtained

promptly by migrating small portions of plane waves, and they can be used to verify velocity models. As more $\mathbf{p}_s$ plane waves are migrated, more detailed structures can be imaged. Therefore, when the velocity model is not well defined, small portions of a DPW dataset should be migrated to generate trial and intermediate images and CIGs. The velocity model can be updated rapidly according to the images and the CIGs. More plane waves should be migrated as better velocity models become available. The strategy of staging over plane wave apertures can be a useful tool for migration velocity analysis

It is worth noting that the Kirchhoff-based DPW migration requires traveltime computations, which can be inaccurate if the velocity models have complex variations (Farmer et al., 2006; Xu et al., 2011). As a result, images generated by the Kirchhoff-based DPW migration in complex subsurface regions might be kinematically incorrect. Better results are expected if the DPW data can be migrated using a RTM algorithm.

1.3. DISSERTATION OUTLINE

My dissertation focuses on developing migration algorithms that can improve the migration efficiency using the DPW data. The concepts of the DPW transform and the DPW data are used throughout the dissertation. The next four chapters are briefly introduced:

- Chapter 2: Double Plane Wave-Based Reverse Time Migration in the Time Domain

  In this chapter, I introduce a new time domain RTM strategy, which uses plane wave transformed gathers, called the time domain DPW-based RTM method. The range of plane wave components needed for migration can be determined by estimating the maximum time dips present in seismic shot gathers.

This reduces the total number of input traces for migration and increases migration efficiency. Unlike the pre-stack shot profile RTM where the number of forward propagation is proportional to the number of shots, the number of forward propagations needed for the time domain DPW-based RTM remains constant and is relatively small even for large seismic datasets. Therefore, the proposed method can improve RTM efficiency and be suitable for migrating large datasets. Similar to the Kirchhoff-based DPW depth migration, the time domain DPW-based RTM can be performed for selected plane wave components to obtain subsurface interfaces with different dips. This feature makes the method a useful tool for migration velocity analysis. An illumination compensation imaging condition for the time domain DPW-based RTM is also proposed to improve images in the deeper parts of the sections.

- Chapter 3: Double Plane Wave Migration in the Frequency Domain

  Two migration methods by which the DPW data can be migrated in the frequency domain are investigated. A frequency domain DPW-based RTM using the adjoint state method is briefly discussed. Then, a new DPW migration algorithm is derived under the Born approximation, and it is referred to as the frequency domain DPW RTM. Frequency plane wave Green's functions need to be constructed for the frequency domain DPW RTM. The number of frequency plane wave Green's functions required for migration is limited. In most cases, that number is 100 ~ 400 even for the seismic datasets that have thousands of shots. Furthermore, frequency plane wave Green's functions can be used for imaging each set of plane waves - either source or receiver/offset plane waves. As a result, the migration efficiency can be substantially improved. The proposed frequency

domain DPW RTM can also include anisotropy by constructing plane wave Green's functions in anisotropic media.

- Chapter 4: Reciprocity and Double Plane Wave Migration

  In this chapter, the applicability of the reciprocity principle in the DPW domain is investigated. Implementation issues of plane wave migration associated with one-sided or end-on gathers are discussed. Utilizing the reciprocity principle, a DPW dataset transformed from one-sided gathers can approximate a DPW dataset generated from split-spread shot gathers. Therefore, split-spread gathers are not required to optimally implement the DPW migration methods. Two methods are demonstrated to obtain optimal DPW datasets. Based on this study, under the ideal acquisition conditions, I suggest that one-sided acquisition geometries should be extended to the largest possible offsets, and reciprocity should be invoked to improve subsurface illumination. Migration efficiency can also be improved for the DPW migrations with the help of the reciprocity principle.

- Chapter 5: Double Plane Wave Least Squares Reverse Time Migration

  A least squares migration method using plane wave data in a fully decomposed DPW-frequency domain is proposed. I call this approach the DPW least squares RTM. The proposed method is an iterative updating method that requires forward modeling and migration for the DPW data. A Born modeling operator is derived based on the shot profile Born modeling operator in the frequency domain to predict the DPW data. The adjoint operator of the DPW Born modeling operator is shown to be kinematically equivalent to the frequency domain DPW RTM operator. Both the DPW Born modeling and its adjoint operators require plane wave Green's functions, which are only on an order of

hundreds even for datasets with thousands of shots. Additionally, once the plane wave Green's functions have been calculated, they can be used for both the modeling and the migration processes throughout the iterative updating process. Wavefield propagations are not needed during iterations. Therefore, the DPW least squares RTM requires much fewer wavefield calculations than that required by the traditional shot profile least squares RTM. The efficiency of the least squares RTM can be significantly improved. An approximate Hessian matrix for the misfit function for the DPW data is also derived. Its diagonal matrix can be implemented as a pre-conditioner to the gradient of the misfit function to improve the convergence rate of the least squares RTM.

Chapter 2: Double Plane Wave-Based Reverse Time Migration in the Time Domain

2.1. INTRODUCTION

Reverse time migration (RTM) (Baysal et al., 1983; McMechan 1983; Whitmore 1983) has become a workhorse for pre-stack depth imaging. By solving the two-way wave equation, RTM can resolve all wavefield propagation phenomenon, which makes RTM by far the most accurate seismic migration method given a sufficiently accurate velocity model. In geologically complex regions, RTM has been proven to outperform other imaging methods, such as Kirchhoff migration (Schneider 1978), Gaussian Beam migration (Hill 1990, 2001) and one-way wave equation (Claerbout 1985).

Implementation of the traditional pre-stack shot profile RTM in the time domain requires two wavefield propagation processes: a forward propagation process for a synthetic source and a backward propagation process for the corresponding recorded shot gather. Both wavefield propagation processes need to be performed for each shot gather to obtain high resolution images. Wavefield propagation itself is computationally intensive. Typically, seismic data have a large number of shots, and therefore, a large number of wavefield propagations are required for the traditional pre-stack shot profile RTM at a very high computational expense.

Several approaches, such as phase encoding and delayed-shot RTM (Zhang et al., 2003; Zhang et al., 2005; Zhang et al., 2006), were investigated to reduce the computational cost of the pre-stack shot profile RTM. Most of those approaches focus on reducing the number of wavefield propagations. Phase encoding migration strategies (Whitmore 1995; Scott and Curtis 1998; Liu et al., 2002; Sun et al., 2002; Liu et al.,

2006) utilize the linearity of the wave equation to reduce the number of wavefield extrapolations. They were initially implemented for the one-way wave equation migration to migrate a combination of shot profiles in one migration process. Phase encoding migration strategies, however, often generate undesirable artifacts, known as the crosstalk artifacts (Liu et al., 2006). Those artifacts are generated due to the i-th source wavefield cross-correlating with the j-th receiver wavefield (where $j \neq i$) extrapolated from the composite shot profile. Plane wave migration, a special form of phase encoding migration strategies, is the most straightforward method to reduce the crosstalk artifacts. Plane wave RTM was investigated by several researchers to improve the overall efficiency of the RTM (Vigh and Starr 2006), and it was shown to be able to generate images that are equivalent to those of the pre-stack shot profile RTM (Zhang et al., 2007).

The plane wave RTM requires seismic data in the plane wave domain. Slant stacking, known as the $\tau - \mathbf{p}$ transform (Stoffa et al., 1981; Claerbout 1986), transforms shot gathers from the $t - \mathbf{x}$ domain to the plane wave domain. The traditional plane wave RTM utilizes plane wave data that are slant stacked over source locations only. In this research, plane wave RTM is performed with plane wave data that are slant stacked over both source and receiver locations. Simultaneously slant stacking over source and receiver locations is called a double slant stack or double plane wave (DPW) transform. The DPW transform fully decomposes seismic data into a coupled plane wave domain, which is known as the DPW domain (Zhao, Sen, et al., 2014; Zhao, Stoffa, et al., 2014) or the double radon-transformed domain (Tatalovic et al., 1991a; Fokkema and van den Berg 1992). DPW modeling (Sen and Frazer 1991) was introduced to simulate DPW data at the surface. A phase shifted migration method utilizing DPW data was introduced by Tatalovic et al. (1991). Stoffa et al. (2006) implemented a Kirchhoff-based DPW depth

migration method. The RTM using the DPW data was first introduced by Zhao, Sen, et al. (2014) and Zhao, Stoffa, et al. (2014).

In this chapter, I briefly analyze the relationship between the imaging condition of the pre-stack shot profile Kirchhoff depth migration and that of the pre-stack shot profile RTM. Carrying out the same analysis for the Kirchhoff-based DPW depth migration, I introduce the DPW-based RTM imaging condition in the time domain. The proposed method requires plane wavefield propagation similar to the traditional plane wave RTM. However, the proposed method differs substantially from all existing plane wave RTMs in that the DPW-based RTM makes use of the fully decomposed plane wave data (i.e., the DPW data). Each plane wave component can be migrated independently and in parallel. By limiting or specifying particular plane wave apertures, the proposed method can image subsurface interfaces according to their dips and produce target-oriented migration results. Consequently, the DPW-based RTM has the potential to become a tool for migration velocity analysis. Illumination compensation imaging conditions are also described for the proposed method. I demonstrate that the proposed DPW-based RTM method can reduce computational cost for large datasets.

2.2. SHOT PROFILE KIRCHHOFF DEPTH MIGRATION

The Kirchhoff migration (Schneider 1978) was first introduced to migrate zero offset data. As introduced in the previous chapter, the pre-stack Kirchhoff depth migration can be derived from the double downward-continuation integral (Clayton and Stolt 1981; Stolt and Weglein 1985; Hildebrand and Carroll 1993). Subsurface areas are imaged by downward continuing source and receiver wavefields. In the frequency domain the double downward-continuation integral is given by

$$I(\mathbf{x},\omega) = \int \partial_n G(\mathbf{x},\mathbf{s},\omega) \int \partial_n G(\mathbf{x},\mathbf{r},\omega) P(\mathbf{s},\mathbf{r},\omega)\, d\mathbf{r}\, d\mathbf{s}, \tag{2.1}$$

where $P(\mathbf{s},\mathbf{r},\omega)$ is the recorded seismic data at the surface, $I(\mathbf{x},\omega)$ represents the subsurface image for imaging point $\mathbf{x}$ given a specific frequency ω, $G(\mathbf{x},\mathbf{s},\omega)$ and $G(\mathbf{x},\mathbf{r},\omega)$ are Green's functions from $\mathbf{s}$ and from $\mathbf{r}$ to $\mathbf{x}$, respectively, and $\partial_n G$ is the surface normal derivative of the Green's function.

Under the high frequency assumption, Green's functions are given by (Stoffa et al., 2006)

$$G(\mathbf{x},\mathbf{s},\omega) \approx \mathrm{A}(\mathbf{x},\mathbf{s}) \exp(i\omega t(\mathbf{x},\mathbf{s})), \tag{2.2}$$

where $\mathrm{A}(\mathbf{x},\mathbf{s})$ and $t(\mathbf{x},\mathbf{s})$ are the amplitude and traveltime terms from $\mathbf{s}$ to $\mathbf{x}$, respectively. Receiver asymptotic ray theory (ART) Green's functions are in a form similar to that of equation (2.2), except that the $\mathbf{s}$ in equation (2.2) is replaced by an $\mathbf{r}$.

Substituting ART Green's functions into equation (2.1) and assuming that amplitude terms of Green's functions are slowly varying functions of space (Hildebrand and Carroll 1993), we can obtain pre-stack Kirchhoff depth migration imaging condition for a given frequency:

$$I(\mathbf{x},\omega) = -\omega^2 \int\int W(\mathbf{x},\mathbf{s},\mathbf{r}) \exp(i\omega[t(\mathbf{x},\mathbf{s}) + t(\mathbf{x},\mathbf{r})]) P(\mathbf{s},\mathbf{r},\omega)\, d\mathbf{r}\, d\mathbf{s}, \tag{2.3}$$

where $W(\mathbf{x},\mathbf{s},\mathbf{r})$ is the amplitude term, and it is defined as

$$W(\mathbf{x},\mathbf{s},\mathbf{r}) = \partial_n t(\mathbf{x},\mathbf{s}) A(\mathbf{x},\mathbf{s}) \partial_n t(\mathbf{x},\mathbf{r}) A(\mathbf{x},\mathbf{r}). \tag{2.4}$$

Summing over frequencies in equation (2.4), the pre-stack shot profile Kirchhoff depth migration integral becomes

$$I(\mathbf{x}) = -\frac{\partial^2}{\partial t^2} \iint W(\mathbf{x},\mathbf{s},\mathbf{r}) P(\mathbf{s},\mathbf{r},t(\mathbf{x},\mathbf{s}) + t(\mathbf{x},\mathbf{r})) d\mathbf{r}\, d\mathbf{s}, \tag{2.5}$$

where $t(\mathbf{x},\mathbf{s}) + t(\mathbf{x},\mathbf{r})$ is the traveltime term. Subsurface wavefields are predicted by computing traveltime in the Kirchhoff depth migration. For a subsurface image point $\mathbf{x}$, the total travel time from a source and receiver pair equals to the traveltime from the source point to the image point plus the traveltime from the image point to the receiver, (i.e., $T_{total} = t(\mathbf{x},\mathbf{s}) + t(\mathbf{x},\mathbf{r})$).

2.3. SHOT PROFILE RTM IN THE TIME DOMAIN

The pre-stack Kirchhoff depth migration can be interpreted as the imaging condition for the pre-stack shot profile RTM. The well-known imaging condition for the pre-stack shot profile RTM (Chattopadhyay and McMechan 2008) can be expressed as

$$I(\mathbf{x}) = \sum_{\mathbf{s}} \sum_{t} \frac{\partial^2 U_s(\mathbf{x},t;\mathbf{s})}{\partial t^2} U_r(\mathbf{x},t;\mathbf{s}), \tag{2.6}$$

where $U_s(\mathbf{x},t;\mathbf{s})$ and $U_r(\mathbf{x},t;\mathbf{s})$ are the forward propagated source wavefield and the backward propagated receiver wavefield for a given shot, respectively. Under the constant density assumption, $U_s(\mathbf{x},t;\mathbf{s})$ can be obtained by performing forward time marching for the time domain constant desnsity two-way wave equation

$$(\frac{1}{v^2(\mathbf{x})}\frac{\partial^2}{\partial t^2}-\nabla^2)U_s(\mathbf{x},t;\mathbf{s})=f(t;\mathbf{s}), \tag{2.7}$$

where $v(\mathbf{x})$ is the velocity at the subsurface, ∇^2 is the Laplace operator, and $f(t;\mathbf{s})$ is the source time series at a given shot location $\mathbf{s}$. $U_r(\mathbf{x},t;\mathbf{s})$ can be obtained by performing backward time marching for the two-way wave equation

$$(\frac{1}{v^2(\mathbf{x})}\frac{\partial^2}{\partial t^2}-\nabla^2)U_r(\mathbf{x},t;\mathbf{s})=0, \tag{2.8}$$

with the initial condition

$$U_r(\mathbf{r},t;\mathbf{s})=d_{obs}(\mathbf{r},t;\mathbf{s}), \tag{2.9}$$

where $d_{obs}(\mathbf{r},t;\mathbf{s})$ is the shot gather for a given shot location $\mathbf{s}$.

2.4. RELATIONSHIP BETWEEN THE KIRCHHOFF DEPTH MIGRATION AND THE RTM

Equations (2.5) and (2.6) both indicate that the total traveltime for $\mathbf{x}$ with a given $\mathbf{s}$ and $\mathbf{r}$ pair is equal to the traveltime from the $\mathbf{s}$ to $\mathbf{x}$ plus the traveltime the $\mathbf{x}$ to $\mathbf{r}$. The final image is obtained by summing over images obtained from each shot.

In post-stack cases, the Kirchhoff migration is a solution of the wave equation in an integral form. Wavefields at subsurface can be downward continued by calculating a surface integral. The same wave equation can be solved by the explicit time marching with given initial conditions, which are zero offset sections in post-stack cases (Baysal et al., 1983; McMechan 1983). The Kirchhoff migration in the pre-stack case still employs the solution to the wave equation in an integral form. The pre-stack shot profile RTM performs the forward and backward wavefield propagations separately via solving the wave equation with the explicit time marching. In fact, both the Kirchhoff migration and the RTM solve the wave equation, but in different ways. Based on this analysis, the imaging condition for the DPW-based RTM in the time domain is introduced in the next section.

2.5. IMAGING CONDITIONS FOR THE DPW-BASED RTM IN THE TIME DOMAIN

As shown in the previous chapter, the imaging condition for the Kirchhoff-based DPW depth migration can be written as

$$I(\mathbf{x}) = L(\mathbf{x}) \iint P(\mathbf{p}_s, \mathbf{p}_r, \tau(\mathbf{x}, \mathbf{p}_s) + \tau(\mathbf{x}, \mathbf{p}_r) - (\mathbf{p}_s + \mathbf{p}_r) \cdot (\mathbf{x}_h - \mathbf{x}_{ref})) d\mathbf{p}_s d\mathbf{p}_r, \qquad (2.10)$$

where $\mathbf{x}_h$ is the horizontal position of $\mathbf{x}$, $\tau(\mathbf{x}, \mathbf{p}_s)$ and $\tau(\mathbf{x}, \mathbf{p}_r)$ are $\mathbf{p}_s$ and $\mathbf{p}_r$ plane wave vertical delay times with respect to $\mathbf{x}_h$, respectively, and the term $L(\mathbf{x}) = \dfrac{\partial^2}{\partial \tau^2} \iint W(\mathbf{x}, \mathbf{s}, \mathbf{r}) d\mathbf{s}\, d\mathbf{r}$ is the amplitude filtering term.

Focusing on the kinematic aspect of equation (2.10), the amplitude term $L(\mathbf{x})$ can be ignored. Therefore, for a given $\mathbf{p}_s$ and $\mathbf{p}_r$ combination, we have

$$I(\mathbf{x},\mathbf{p}_s,\mathbf{p}_r)=P(\mathbf{p}_s,\mathbf{p}_r,\tau(\mathbf{x},\mathbf{p}_s)+\tau(\mathbf{x},\mathbf{p}_r)-(\mathbf{p}_s+\mathbf{p}_r)\cdot(\mathbf{x}_h-\mathbf{x}_{ref})), \tag{2.11}$$

which is the basic imaging building block for the Kirchhoff-based DPW depth migration. Equation (2.11) suggests that for a given $\mathbf{p}_s$ and $\mathbf{p}_r$ combination, the image at $\mathbf{x}$ can be obtained by finding the DPW data whose total vertical delay time is $\tau(\mathbf{x},\mathbf{p}_s)+\tau(\mathbf{x},\mathbf{p}_r)-(\mathbf{p}_s+\mathbf{p}_r)\bullet(\mathbf{x}_h-\mathbf{x}_{ref})$, and then positioning the corresponding DPW data at the image point $\mathbf{x}$.

In equations (2.10) and (2.11), the term, $\tau(\mathbf{x},\mathbf{p}_s)+\tau(\mathbf{x},\mathbf{p}_r)-(\mathbf{p}_s+\mathbf{p}_r)\cdot(\mathbf{x}_h-\mathbf{x}_{ref})$, indicates that the total vertical delay time for any $\mathbf{x}$ with given ray-parameters $\mathbf{p}_s$ and $\mathbf{p}_r$ is the sum of $\mathbf{p}_s$ and $\mathbf{p}_r$ vertical delay times to the point $\mathbf{x}$ with the time correction, $-(\mathbf{p}_s+\mathbf{p}_r)\cdot(\mathbf{x}_h-\mathbf{x}_{ref})$. As previously discussed, the traveltime term in shot profile Kirchhoff depth migration can be interpreted as the kinematic part of the imaging condition for shot profile RTM. Similarly, the traveltime term in the Kirchhoff-based DPW depth migration can be interpreted as the kinematic part of a RTM imaging condition used to migrate the DPW data. Therefore, based on the Kirchhoff-based DPW depth migration imaging condition equation (2.11), I propose the DPW-based RTM imaging condition for the Ps-Pr DPW data as following:

$$I(\mathbf{x},\mathbf{p}_s,\mathbf{p}_r)=\sum_{\tau}\frac{\partial^2 U_{\mathbf{p}_s}(\mathbf{p}_s,\mathbf{x},\tau)}{\partial\tau^2}U_{\mathbf{p}_r}(\mathbf{p}_s,\mathbf{p}_r,\mathbf{x},\tau-(\mathbf{p}_s+\mathbf{p}_r)\cdot(\mathbf{x}_h-\mathbf{x}_{ref})), \tag{2.12}$$

where $I(\mathbf{x},\mathbf{p}_s,\mathbf{p}_r)$ is the image obtained by migrating a single Ps-Pr trace from a DPW dataset, $U_{\mathbf{p}_s}$ and $U_{\mathbf{p}_r}$ represent the forward propagated synthetic source plane

wavefield for $\mathbf{p}_s$ and the backward propagated DPW plane wavefield for $\mathbf{p}_r$ in terms of vertical delay time τ, respectively. τ in equation (2.12) is the vertical delay time with respect to $\mathbf{x}_h$. $U_{\mathbf{p}_s}$ and $U_{\mathbf{p}_r}$ can be obtained by performing time marching for the two-way wave equation with a plane wave source or the DPW data.

In equation (2.12), $U_{\mathbf{p}_s}$ and $U_{\mathbf{p}_r}$ propagate plane waves in terms of τ with respect to $\mathbf{x}_h$. At each $\mathbf{x}_h$ position, the DPW data in vertical delay times with respect to $\mathbf{x}_h$ are required to implement the imaging condition. However, the DPW data transformed from shot gathers are in vertical delay times with respect to $\mathbf{x}_{ref}$. Therefore, during plane wavefield propagation processes, a time correction term $-(\mathbf{p}_s + \mathbf{p}_r)\cdot(\mathbf{x}_h - \mathbf{x}_{ref})$ needs to be applied to the plane wavefields at each $\mathbf{x}_h$, so that the original vertical delay time of the DPW data, which is with respect to $\mathbf{x}_{ref}$, is corrected to the vertical delay time with respect to $\mathbf{x}_h$. The time correction can be performed for either forward or backward propagated wavefields, although I chose performing the time correction for the backward propagated wavefields. Plane wavefields $U_{\mathbf{p}_s}$ and $U_{\mathbf{p}_r}$ will be shown in the numerical tests section.

The Kirchhoff-based DPW depth migration provides a solution to the wave equation in an integral form and performs downward continuation with the DPW data. To perform the proposed DPW-based RTM in the time domain, the same wave equation needs to be solved via the explicit time marching where a plane wave source or the DPW data are used as the initial condition. Then, the cross-correlation imaging condition is applied for forward and backward propagated wavefields to obtain image at each time step. This procedure is similar to that of the pre-stack shot profile RTM. However, plane wave source or the DPW data should be used as the initial condition to solve the wave equation.

Since each Ps-Pr trace in the DPW dataset is indexed by both $\mathbf{p}_s$ and $\mathbf{p}_r$, $U_{\mathbf{p}_r}$ is indexed by $\mathbf{p}_s$, as well as by $\mathbf{p}_r$. Equation (2.12) is the basic imaging building block for the DPW-based RTM. It indicates that for a single Ps-Pr trace, we need to backward propagate this plane wave trace using ray-parameter $\mathbf{p}_r$ and forward propagate a synthetic source plane wave with ray-parameter $\mathbf{p}_s$. To obtain images, the cross-correlation imaging condition is applied at each time step. Alternatively, the reciprocity principle can be utilized to perform the proposed DPW-based RTM. For the same Ps-Pr trace, backward propagation can be performed using this Ps-Pr trace with ray-parameter $\mathbf{p}_s$, and forward propagation can be performed using a synthetic source plane wave with ray-parameter $\mathbf{p}_r$. The cross-correlation imaging condition is then applied to those plane wavefields. The image obtained by migrating the Ps-Pr trace in this way should be the same as the image obtained previously. For an entire DPW dataset, the image generated by a half of the DPW dataset is the same as that generated by migrating the other half of the DPW dataset. Therefore, only a half of a DPW dataset needs to be migrated explicitly, and efficiency of the proposed method can be improved by utilizing the reciprocity principle. More discussions on utilizing the reciprocity principle for the DPW data and the DPW migration will be demonstrated in Chapter 4.

According to equation (2.12), different plane wave components can be migrated independently, and therefore, interfaces with different dips can be imaged separately, leading to a target-oriented imaging algorithm. Equation (2.12) also suggests that since individually migrated images are indexed by ray-parameter $\mathbf{p}_r$, the ray-parameter common image gathers (CIGs) can be obtained easily by lining up images indexed by $\mathbf{p}_r$. In CIGs, the flatness of horizons verifies the accuracy of velocity models, and we can adjust velocity models accordingly.

Images containing information from all selected DPW traces can be obtained by stacking all independently migrated sections:

$$I(\mathbf{x}) = \sum_{\mathbf{p}_s} \sum_{\mathbf{p}_r} \sum_{\tau} \frac{\partial^2 U_{\mathbf{p}_s}(\mathbf{p}_s, \mathbf{x}, \tau)}{\partial \tau^2} U_{\mathbf{p}_r}(\mathbf{p}_s, \mathbf{p}_r, \mathbf{x}, \tau - (\mathbf{p}_s + \mathbf{p}_r) \cdot (\mathbf{x}_h - \mathbf{x}_{ref})). \qquad (2.13)$$

Substituting relationships between the Ps-Pr and the Ps-Po DPW data (i.e., equations (1.17) and (1.18)) with the prime dropped for $\mathbf{p}_{s'}$, the DPW-based RTM imaging condition for the Ps-Po DPW data can be written as

$$I(\mathbf{x}, \mathbf{p}_s, \mathbf{p}_o) = \sum_{\tau} \frac{\partial^2 U_{\mathbf{p}_s}(\mathbf{p}_s - \mathbf{p}_o, \mathbf{x}, \tau)}{\partial \tau^2} U_{\mathbf{p}_o}(\mathbf{p}_s, \mathbf{p}_o, \mathbf{x}, \tau - \mathbf{p}_s \cdot (\mathbf{x}_h - \mathbf{x}_{ref})), \qquad (2.14)$$

and

$$I(\mathbf{x}) = \sum_{\mathbf{p}_s} \sum_{\mathbf{p}_o} \sum_{\tau} \frac{\partial^2 U_{\mathbf{p}_s}(\mathbf{p}_s - \mathbf{p}_o, \mathbf{x}, \tau)}{\partial \tau^2} U_{\mathbf{p}_o}(\mathbf{p}_s, \mathbf{p}_o, \mathbf{x}, \tau - \mathbf{p}_s \cdot (\mathbf{x}_h - \mathbf{x}_{ref})), \qquad (2.15)$$

where $U_{\mathbf{p}_o}$ is the backward propagated DPW offset plane wavefield. (Note: in equations (2.12) to (2.15), plane waves are propagated in terms of τ not *t*).

In the imaging condition equation (2.13), the forward propagated plane wave $U_{\mathbf{p}_s}(\mathbf{p}_s, \mathbf{x}, \tau)$ is indexed by $\mathbf{p}_s$, this means that $U_{\mathbf{p}_s}$ for a given ray-parameter $\mathbf{p}_s$ can be used for imaging all DPW traces that share the same $\mathbf{p}_s$ value. As a result, the forward propagated plane wavefield $U_{\mathbf{p}_s}$ does not need to be calculated for every DPW trace. Each $U_{\mathbf{p}_s}$ can be reused throughout the migration, which improves the migration efficiency. The same analysis applies to equation (2.15).

Typically, thousands of DPW traces need to be migrated to obtain an image with reasonable resolution. However, this number remains relatively constant even if the number of shots increases dramatically. Therefore, the proposed method is suitable for seismic datasets with a large number of shots, and the efficiency improves as the number of shots increases.

2.6. PLANE WAVEFIELD

All of the derived imaging conditions for the DPW-based RTM requires plane wavefields propagated in terms of τ not t. In this section, I present detailed the procedure to obtain plane wavefields propagated in terms of τ.

For a given ray-parameter, a plane wave propagating in terms of traveltime t can be obtained by injecting source functions or plane wave data at the model surface with a time delay at each surface location. This procedure is illustrated in Figure 2.1.

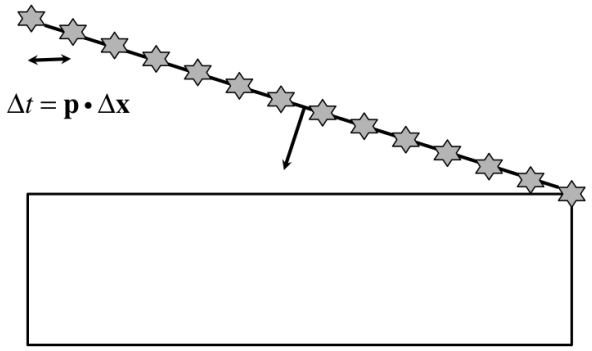

Figure 2.1. A 2D illustration of initiating a plane wave at the surface. Δt is the time delay calculated according to the plane wave ray-parameter $\mathbf{p}$ and $\Delta \mathbf{x}$, where $\Delta \mathbf{x}$ is the grid spacing in the horizontal direction.

Injecting a plane wave source with ray-parameter $\mathbf{p}_s$ at the surface and using the injected plane wave source as the boundary condition to solve the two-way wave equation forward in time, we can obtain $U_{\mathbf{p}_s}(\mathbf{p}_s,\mathbf{x},t)$, which is the synthetic plane wavefields propagated in terms of *t*. Similarly, given a Ps-Pr trace, the trace needs to be injected at each surface location with a time delay $\mathbf{p}_r \cdot \Delta\mathbf{x}$ to achieve a boundary condition that contains the DPW data. Then, solving the two-way wave equation backward in time with the boundary condition, we can obtaine $U_{\mathbf{p}_r}(\mathbf{p}_s,\mathbf{p}_r,\mathbf{x},t)$, which is the backward propagated plane wavefields propagating in terms of *t*.

The simple relationship between τ and t (Diebold and Stoffa 1981) can be written as

$$\tau = t - \mathbf{p}\cdot\mathbf{x}_h. \tag{2.16}$$

Therefore, I propose two equations to obtain plane wavefields propagated in terms of τ:

$$U_{\mathbf{p}_s}(\mathbf{p}_s,\mathbf{x},\tau) = U_{\mathbf{p}_s}(\mathbf{p}_s,\mathbf{x},t-\mathbf{p}_s\cdot\mathbf{x}_h), \tag{2.17}$$

and

$$U_{\mathbf{p}_r}(\mathbf{p}_s,\mathbf{p}_r,\mathbf{x},\tau) = U_{\mathbf{p}_r}(\mathbf{p}_s,\mathbf{p}_r,\mathbf{x},t-\mathbf{p}_r\cdot\mathbf{x}_h). \tag{2.18}$$

A time correction term $-(\mathbf{p}_s+\mathbf{p}_r)\cdot(\mathbf{x}_h-\mathbf{x}_{ref})$ needs to be applied for the backward propagated plane wavefields $U_{\mathbf{p}_r}(\mathbf{p}_s,\mathbf{p}_r,\mathbf{x},\tau)$ at each $\mathbf{x}_h$, to obtain $U_{\mathbf{p}_r}(\mathbf{p}_s,\mathbf{p}_r,\mathbf{x},\tau-(\mathbf{p}_s+\mathbf{p}_r)\cdot(\mathbf{x}_h-\mathbf{x}_{ref}))$.

The same procedures can be used to obtain $U_{\mathbf{p}_s}(\mathbf{p}_s - \mathbf{p}_o, \mathbf{x}, \tau)$ and $U_{\mathbf{p}_o}(\mathbf{p}_s, \mathbf{p}_o, \mathbf{x}, \tau - \mathbf{p}_o \cdot (\mathbf{x}_h - \mathbf{x}_{ref}))$.

2.7. COMPENSATION FOR ILLUMINATION

The normalized imaging condition for the pre-stack shot profile RTM (Chattopadhyay and McMechan 2008) was introduced to obtain images with balanced amplitude and reflection coefficients. It usually helps to increase the migration energy for the deeper parts of images. Thus, the normalized imaging condition is often considered as the illumination compensation. Here, I propose normalized imaging conditions for the DPW-based RTM that can achieve illumination compensation and lead to images with better quality at depth.

The compensation can be achieved through normalizing either source plane wavefields or receiver/offset plane wavefields. By normalizing source plane wavefields, the compensated imaging conditions for the Ps-Pr and the Ps-Po DPW data can be written as

$$I_{N\mathbf{P}_s}(\mathbf{x}) = \frac{\sum_{\mathbf{p}_s}\sum_{\mathbf{p}_r}\sum_{\tau} \frac{\partial^2 U_{\mathbf{p}_s}(\mathbf{p}_s, \mathbf{x}, \tau)}{\partial \tau^2} U_{\mathbf{p}_r}(\mathbf{p}_s, \mathbf{p}_r, \mathbf{x}, \tau - (\mathbf{p}_s + \mathbf{p}_r) \cdot (\mathbf{x}_h - \mathbf{x}_{ref}))}{\sum_{\mathbf{p}_s}\sum_{\tau} \left\| U_{\mathbf{p}_s}(\mathbf{p}_s, \mathbf{x}, \tau) \right\|^2}, \tag{2.19}$$

and

$$I_{N\mathbf{P}_s}(\mathbf{x}) = \frac{\sum_{\mathbf{p}_s}\sum_{\mathbf{p}_o}\sum_{\tau} \frac{\partial^2 U_{\mathbf{p}_s}(\mathbf{p}_s - \mathbf{p}_o, \mathbf{x}, \tau)}{\partial \tau^2} U_{\mathbf{p}_o}(\mathbf{p}_s, \mathbf{p}_o, \mathbf{x}, \tau - \mathbf{p}_s \cdot (\mathbf{x}_h - \mathbf{x}_{ref}))}{\sum_{\mathbf{p}_s}\sum_{\tau} \left\| U_{\mathbf{p}_s}(\mathbf{p}_s - \mathbf{p}_o, \mathbf{x}, \tau) \right\|^2}, \tag{2.20}$$

respectively, where $I_{N\mathbf{P}_s}(\mathbf{x})$ is the source plane wave normalized image.

Normalizing images by receiver or offset plane wavefields, we can arrive at the compensated imaging conditions for the Ps-Pr and the Ps-Po DPW data as follows,

$$I_{N\mathbf{P}_r}(\mathbf{x}) = \frac{\sum_{\mathbf{p}_s}\sum_{\mathbf{p}_r}\sum_{\tau}\frac{\partial^2 U_{\mathbf{p}_s}(\mathbf{p}_s,\mathbf{x},\tau)}{\partial\tau^2}U_{\mathbf{p}_r}(\mathbf{p}_s,\mathbf{p}_r,\mathbf{x},\tau-(\mathbf{p}_s+\mathbf{p}_r)\cdot(\mathbf{x}_h-\mathbf{x}_{ref}))}{\sum_{\mathbf{p}_r}\sum_{\tau}\left\|U_{\mathbf{p}_r}(\mathbf{p}_s,\mathbf{p}_r,\mathbf{x},\tau-(\mathbf{p}_s+\mathbf{p}_r)\cdot(\mathbf{x}_h-\mathbf{x}_{ref}))\right\|^2}, \tag{2.21}$$

and

$$I_{N\mathbf{P}_o}(\mathbf{x}) = \frac{\sum_{\mathbf{p}_s}\sum_{\mathbf{p}_o}\sum_{\tau}\frac{\partial^2 U_{\mathbf{p}_s}(\mathbf{p}_s-\mathbf{p}_o,\mathbf{x},\tau)}{\partial\tau^2}U_{\mathbf{p}_o}(\mathbf{p}_s,\mathbf{p}_o,\mathbf{x},\tau-\mathbf{p}_s\cdot(\mathbf{x}_h-\mathbf{x}_{ref}))}{\sum_{\mathbf{p}_o}\sum_{\tau}\left\|U_{\mathbf{p}_o}(\mathbf{p}_s,\mathbf{p}_o,\mathbf{x},\tau-\mathbf{p}_s\cdot(\mathbf{x}_h-\mathbf{x}_{ref}))\right\|^2}, \tag{2.22}$$

respectively. $I_{N\mathbf{P}_r}(\mathbf{x})$ and $I_{N\mathbf{P}_o}(\mathbf{x})$ are receiver and offset plane wavefield normalized imaging conditions, respectively. Migration results using the normalized imaging condition will be shown in the following section.

2.8. NUMERICAL RESULTS

Alhough all the derivations in previous sections are in 3D, only 2D numerical examples will be demonstrated. In all examples, the rapid expansion method (REM) (Tal-Ezer et al., 1987; Pestana and Stoffa 2010) was used to propagate wavefields and to generate synthetic shot gathers. I first test the impulse responses of the proposed method

for a homogenous model to demonstrate that the DPW-based RTM is able to achieve images that are equivalent to those of the shot profile RTM. Then, a simple three-layer model and the SEG/EAGE salt model (Aminzadeh et al., 1997) are used to show the flexibility of the proposed method. The proposed illumination imaging condition, equation (2.20), is also applied to the salt model.

2.8.1. Impulse response

A simple homogenous velocity model with $v = 2$ km/s was selected for testing impulse responses. There were 200 horizontal points and 100 vertical points with an interval of 0.02 km in both directions. The upper left corner is set to be the origin as shown in Figure 2.2. Only one shot located at $\mathbf{s}(s_x = 2 \text{ km}, s_z = 0 \text{ km})$ with one band-limited impulse at zero offset was migrated by the shot profile RTM. The result is shown in Figure 2.2, which is overlaid by a dashed half-circle.

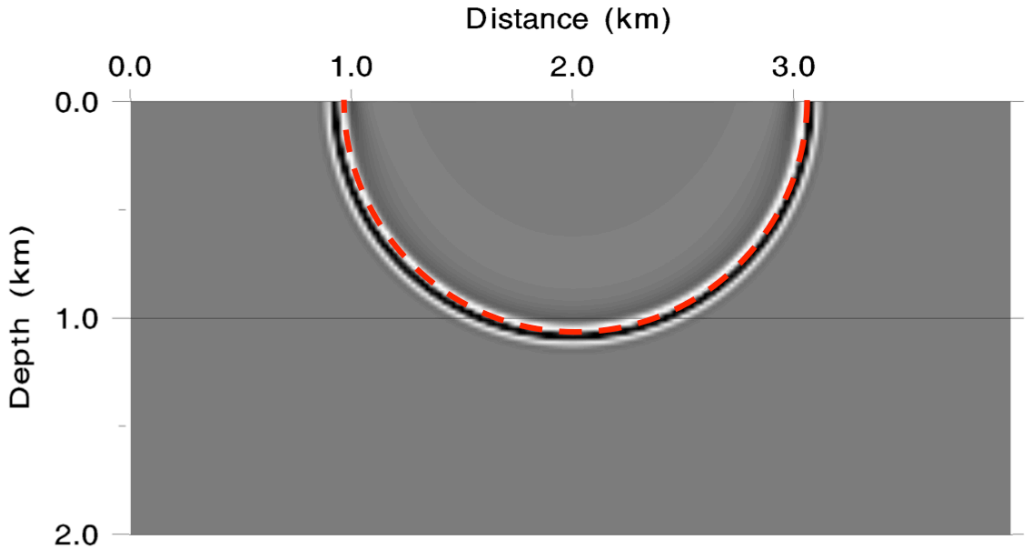

Figure 2.2. The impulse response of the shot profile RTM. The image is overlaid by a dashed half-circle.

The shot gather that had only one zero offset trace was then decomposed into a DPW dataset with 101 $\mathbf{p}_s$ and 101 $\mathbf{p}_r$ plane waves. Both $\mathbf{p}_s$ and $\mathbf{p}_r$ plane wave components were equally spaced between -0.5 to 0.5 s/km. For the DPW transform, the maximum $\mathbf{p}$ value should be chosen according to the time dips in shot gathers and the minimum velocity of the model, such that most of the plane wave components arriving at the surface can be captured. In this case, the slowness of the velocity was chosen to be the maximum ray-parameter value.

Figure 2.3 shows several selected DPW profiles. Panels shown in Figure 2.3a) and in Figure 2.3b) are constant $\mathbf{p}_s$ panels and constant $\mathbf{p}_r$ panels, respectively. The impulse signal can be regarded as a received signal composed by plane waves coming from all directions. Therefore, decomposed plane wave energy for all $\mathbf{p}_s$ and $\mathbf{p}_r$ plane

waves can be expected in both constant $\mathbf{p}_s$ and $\mathbf{p}_r$ profiles. Horizontal events for all plane waves at the same vertical delay time are observed in Figure 2.3.

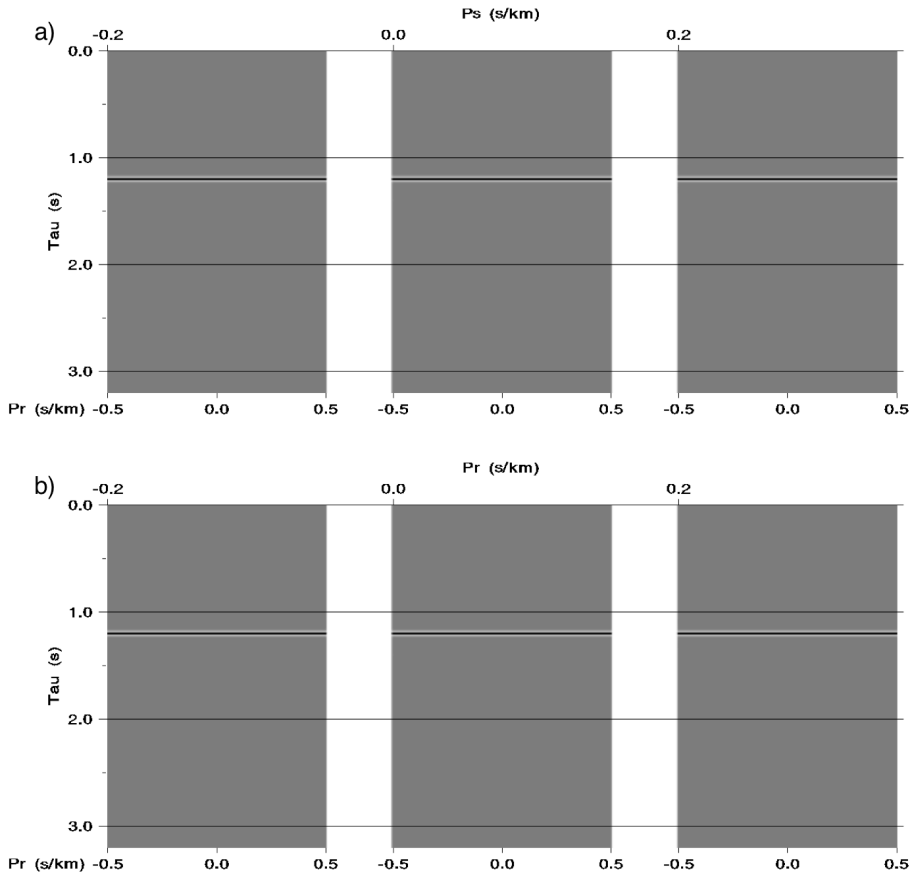

Figure 2.3. a) Three constant $\mathbf{p}_s$ profiles. $\mathbf{p}_s$ = -0.2, 0.0 and 0.2 s/km for each panel from left to right. In each panel, $\mathbf{p}_r$ = -0.5 ~ 0.5 s/km. b) Three constant $\mathbf{p}_r$ profiles where $\mathbf{p}_r$ = -0.2, 0.0 and 0.2 s/km for each panel from left to right, respectively. $\mathbf{p}_s$ = -0.5 ~ 0.5 s/km in each panel.

Figure 2.4 demonstrates how to inject a plane wave source and a DPW trace at the surface. In Figure 2.4a), Ricker wavelets are injected at the surface at each grid point with a time delay $\Delta t = \mathbf{p}_s \cdot \Delta \mathbf{x}$ to achieve a synthetic plane wave source with ray-parameter

$\mathbf{p}_s$ < 0.0 s/km. Similarly, to calculate backward propagated plane wavefields, a Ps-Pr or Ps-Po trace from a DPW dataset needs to be reversed in time and injected at each grid point with a time delay $\Delta t = \mathbf{p}_r \cdot \Delta \mathbf{x}$ with $\mathbf{p}_r$ < 0.0 s/km, as shown in Figure 2.4b). Injecting a plane wave source and a DPW trace with $\mathbf{p}_s$ > 0.0 s/km and $\mathbf{p}_r$ > 0.0 s/km are demonstrated in Figure 2.4c) and 2.4d), respectively.

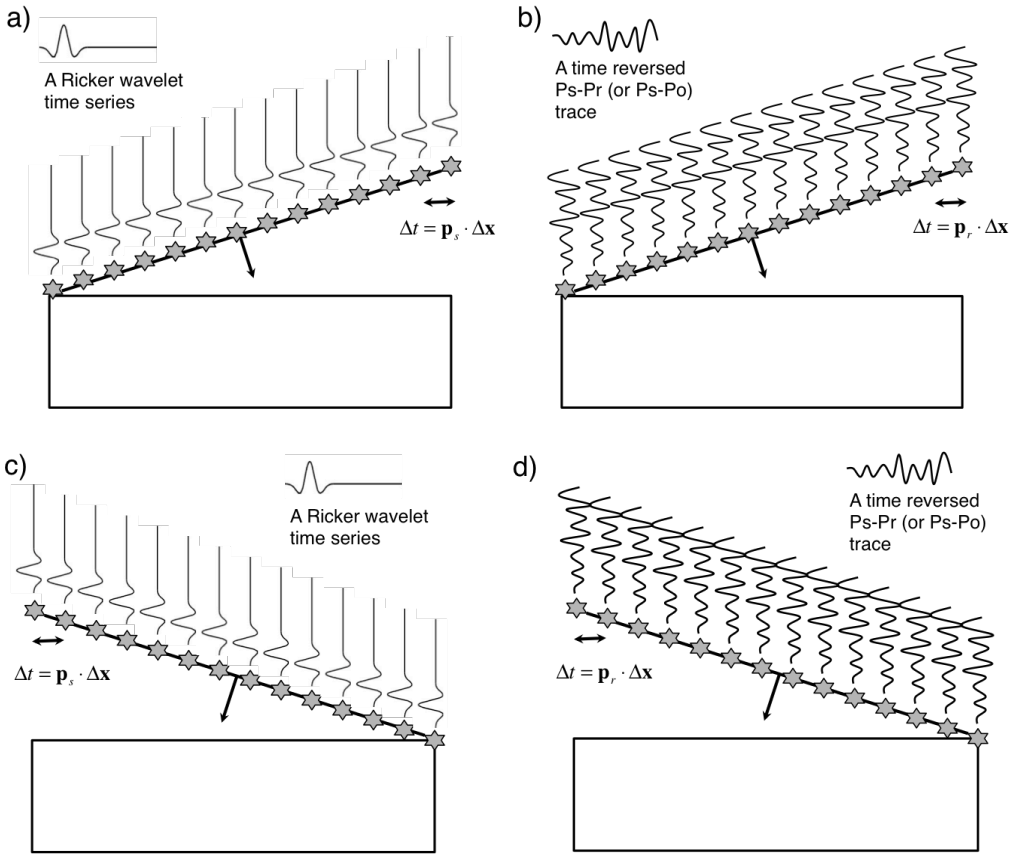

Figure 2.4. a) An illustration of injecting a synthetic plane wave source with ray-parameter $\mathbf{p}_s$ < 0.0 s/km. b) An illustration of injecting a Ps-Pr or Ps-Po trace from a DPW dataset with ray-parameter $\mathbf{p}_r$ < 0.0 s/km. c) and d) are similar to a) and b), but with the opposite sign for $\mathbf{p}_s$ and $\mathbf{p}_r$, respectively.

Forward and backward propagated plane wavefields can be obtained by solving the two-way wave equation with the synthetic plane wave source or the injected Ps-Pr traces serving as the initial conditions. To demonstrate forward and backward propagated plane wavefields in τ, a trace from the DPW dataset where $\mathbf{p}_s$ and $\mathbf{p}_r$ were both equal to -0.3 s/km was migrated. $U_{\mathbf{p}_s}(\mathbf{p}_s,\mathbf{x},\tau)$ and $U_{\mathbf{p}_r}(\mathbf{p}_s,\mathbf{p}_r,\mathbf{x},\tau-(\mathbf{p}_s+\mathbf{p}_r)\cdot(\mathbf{x}_h-\mathbf{x}_{ref}))$ plane wavefields at different τ steps are shown in Figure 2.5a) to Figure 2.5d) and in Figure 2.5e) to Figure 2.5h), respectively. Plane wavefields shown in row 1, 2, 3 and 4 correspond to different wavefields at time steps τ = 0.2 s, τ = 0.4 s, τ = 0.6 s and τ = 0.8 s. The corresponding multiplication (i.e., cross-correlation) between the forward and backward propagated plane wavefields at those time steps are shown in Figure 2.5i) to Figure 2.5l). The accumulated images over time are shown in Figure 2.5m) to Figure 2.5p).

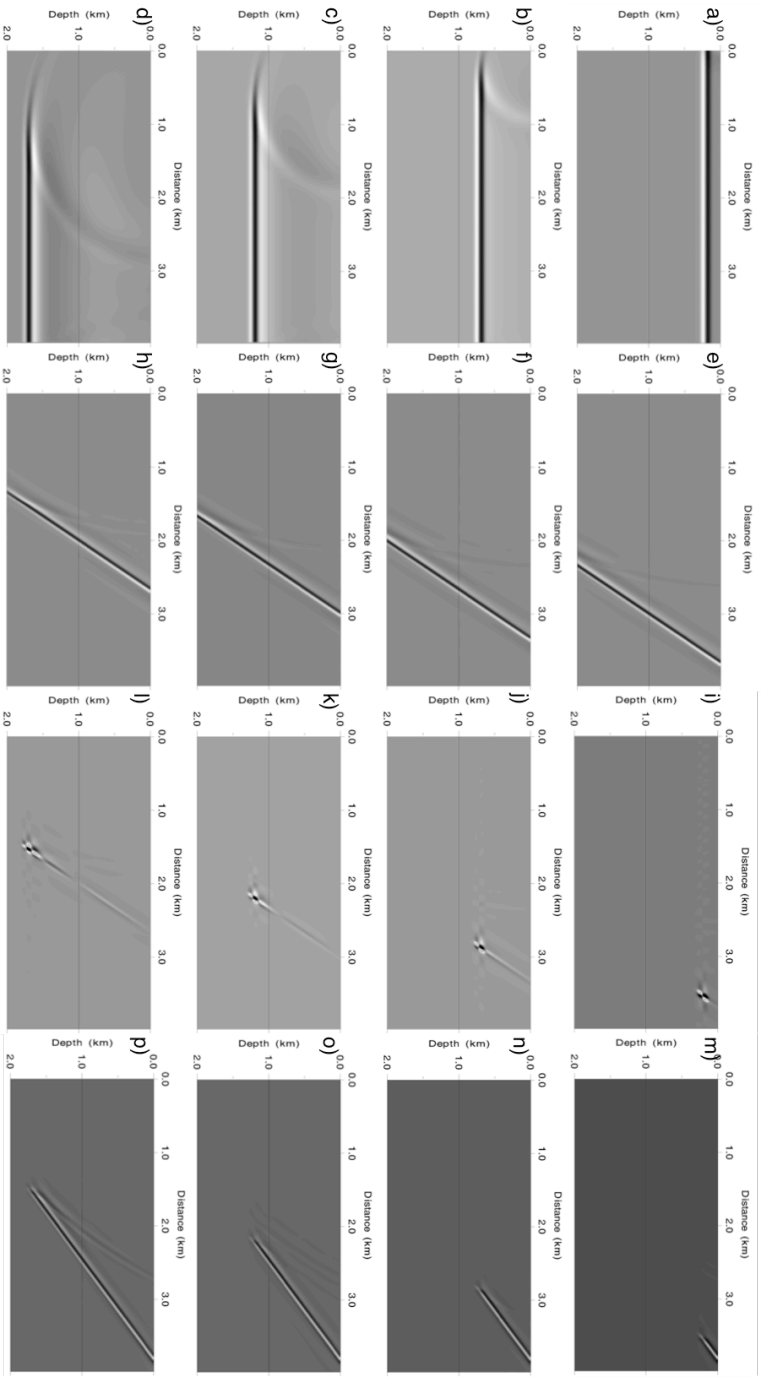

Figure 2.5. An illustration of the DPW-based RTM imaging processes. Columns 1, 2, 3 and 4 correspond to forward propagated plane wavefields, backward propagated plane wavefields, multiplication results between the forward and the backward plane wavefields, and the accumulated images over τ, respectively.

Figure 2.6 through 2.10 show the impulse responses after performing the DPW-based RTM using different parts of the DPW dataset. Equation (2.13) was utilized for migration. Each result was overlaid by a half-circle identical to the one shown in Figure 2.2. The subsets of the DPW dataset used to generate images shown in Figure 2.6 through 2.10 are listed in Table 2.1.

	Figure 2.6	Figure 2.7	Figure 2.8	Figure 2.9	Figure 2.10
$\mathbf{p}_s$ range (s/km)	0.0	0.0	0.0 ~ 0.4	0.0 ~ 0.5	-0.5 ~ 0.5
$\mathbf{p}_r$ range (s/km)	0.0	-0.5 ~ 0.5	-0.5 ~ 0.5	-0.5 ~ 0.5	-0.5 ~ 0.5

Table 2.1. Subsets of the DPW dataset used for testing the impulse response of the DPW-based RTM.

The image shown in Figure 2.6 was generated by migrating only one DPW trace where $\mathbf{p}_s$ and $\mathbf{p}_r$ are both equal to 0.0 s/km. A horizontal event was imaged and it was tangent to the overlaid half-circle, meaning that the image coincided with the horizontal portion of the impulse response of the shot profile RTM. Because only one trace was migrated, the obtained impulse response partially corresponded to the impulse response of the shot profile RTM. The other parts of the impulse response are regarded as migration artifacts pointed out by the arrows. The impulse response shown in Figure 2.7 was generated by migrating a constant $\mathbf{p}_s$ profile where $\mathbf{p}_s$ = 0.0 s/km and $\mathbf{p}_r$ = -0.5 ~ 0.5 s/km. The image is a hyperbola that does not have the horizontal artifacts. The horizontal artifacts shown in Figure 2.6 were canceled by including more $\mathbf{p}_r$ plane waves into the migration. However, the hyperbola is not kinematically equal to the

impulse response of the shot profile RTM. The wings of the hyperbola, indicated by arrows in Figure 2.7, are also artifacts generated due to insufficient $\mathbf{p}_s$ sampling.

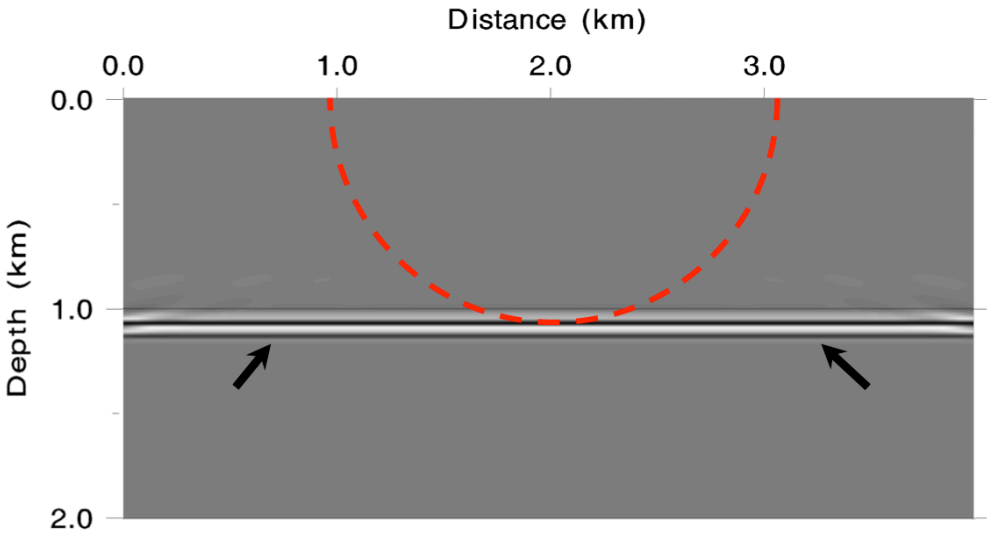

Figure 2.6. The impulse response obtained by migrating one trace from the DPW dataset where both $\mathbf{p}_s$ and $\mathbf{p}_r$ are equal to 0.0 s/km.

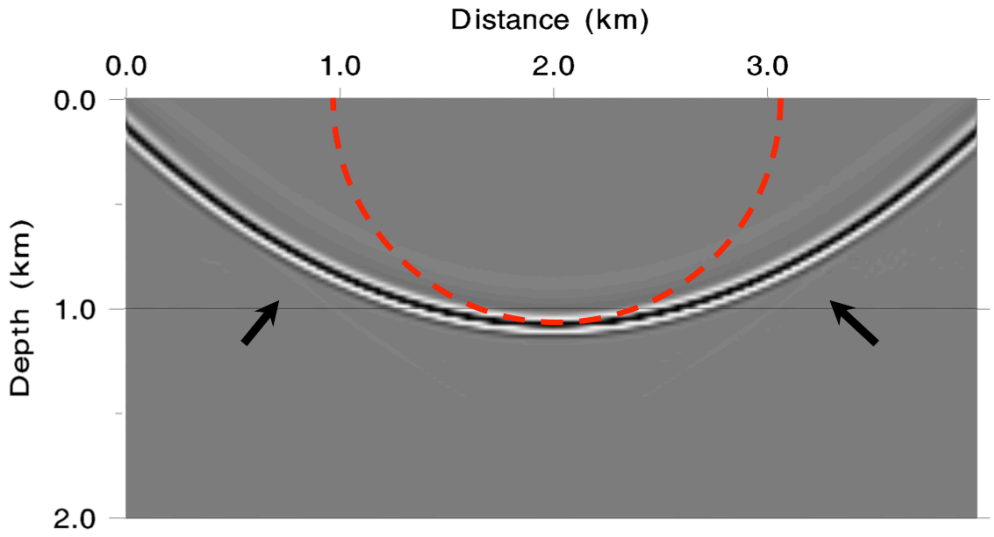

Figure 2.7. The impulse response obtained by migrating a constant $\mathbf{p}_s$ profile where $\mathbf{p}_s = 0.0$ s/km and 101 $\mathbf{p}_r$ = -0.5 ~ 0.5 s/km.

I increased the $\mathbf{p}_s$ aperture and obtained impulse responses shown in Figure 2.8 and 2.9 where again $\mathbf{p}_r$ = -0.5 ~ 0.5 s/km were used for migration. 41 $\mathbf{p}_s$ plane waves ranging from 0.0 to 0.4 s/km and 51 $\mathbf{p}_s$ plane waves ranging from 0.0 to 0.5 s/km were used to generate the results shown in Figure 2.8 and 2.9, respectively. Because more $\mathbf{p}_s$ plane waves were used for migration, the impulse response shown in Figure 2.8 formed a part of a circle. Similarly, the impulse response became a quarter circle, as shown in Figure 2.9 as 51 $\mathbf{p}_s$ plane waves were include into the migration. There are a small amount of artifacts indicated by arrows in Figure 2.8 and 2.9.

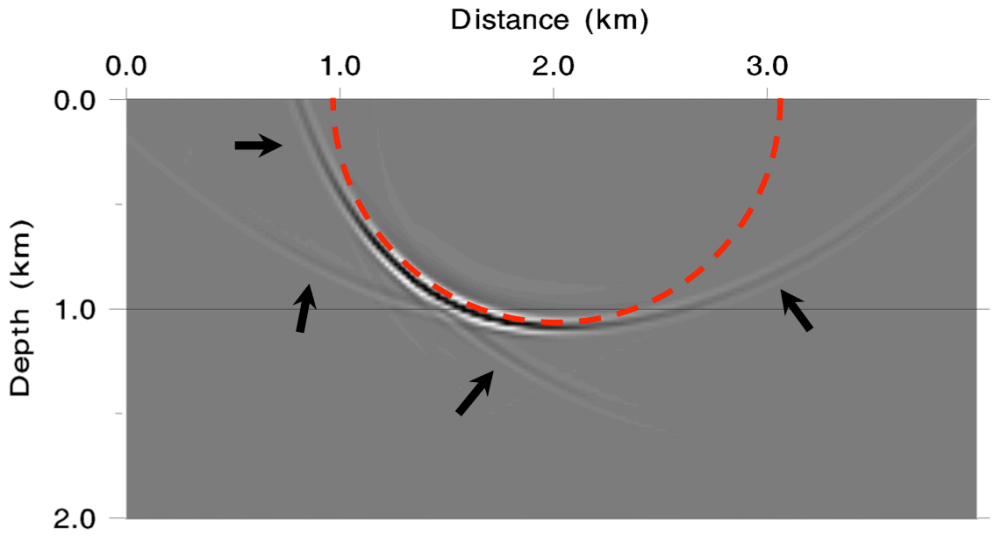

Figure 2.8. The impulse response obtained by migrating 41 $\mathbf{p}_s$ plane waves ranging from 0.0 to 0.4 s/km and 101 $\mathbf{p}_r$ plane waves ranging from -0.5 to 0.5 s/km.

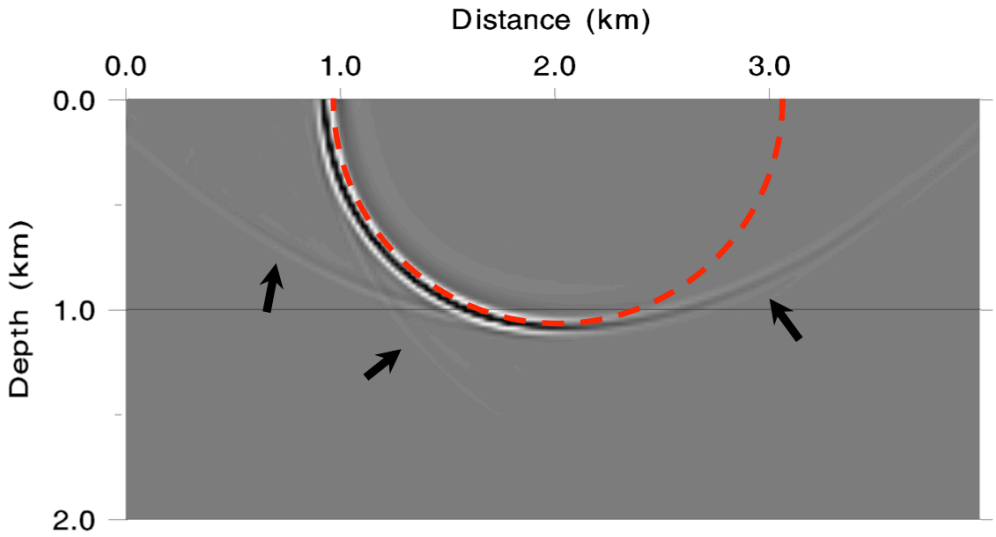

Figure 2.9. The impulse response obtained by migrating 51 $\mathbf{p}_s$ plane waves ranging from 0.0 to 0.5 s/km and 101 $\mathbf{p}_r$ plane waves ranging from -0.5 to 0.5 s/km.

Figure 2.10 shows the impulse response where all traces from the DPW dataset were migrated. Even though there were still some artifacts indicated by arrows, the impulse response has the same shape as that of the shot profile RTM, suggesting that the proposed DPW-based RTM is kinematically identical to the shot profile RTM if all plane waves are migrated.

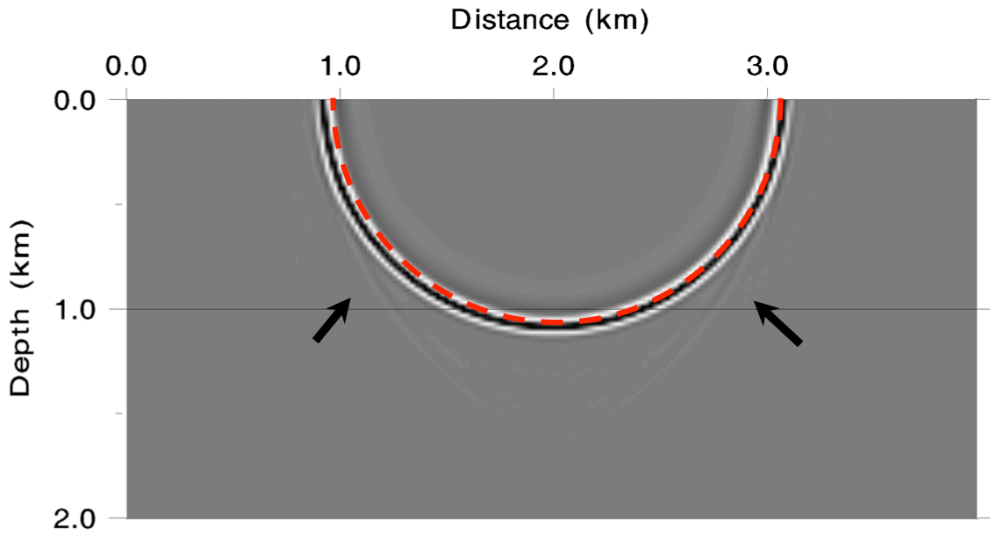

Figure 2.10. The impulse response obtained by migration all traces from the DPW dataset. Except for some small amount of artifacts indicated by black arrows, the image has the same shape with impulse response of the shot profile RTM.

The evolution from Figure 2.6 to 2.10 shows that increasing the $\mathbf{p}_s$ aperture is able to reduce the migration artifacts and to build the half-circle impulse response. This phenomenon can also be explained by the Huygens principle. It is also shown that specific ranges of $\mathbf{p}_s$ and $\mathbf{p}_r$ plane waves can be migrated independently to form a

part of the half-circle impulse response. As a result, we can employ this property to image subsurface interfaces with given dips.

2.8.2. Three-layer model

The proposed method can selectively image subsurface structures by dips, and it is demonstrated with a simple three-layer model. The model size and grid intervals were the same as those used in the previous homogenous model. The velocity model is shown in Figure 2.11, where there are one horizontal interface, one dipping interface and one diffractor. The REM was used to generate 200 shots. Each shot gather had 200 receivers.

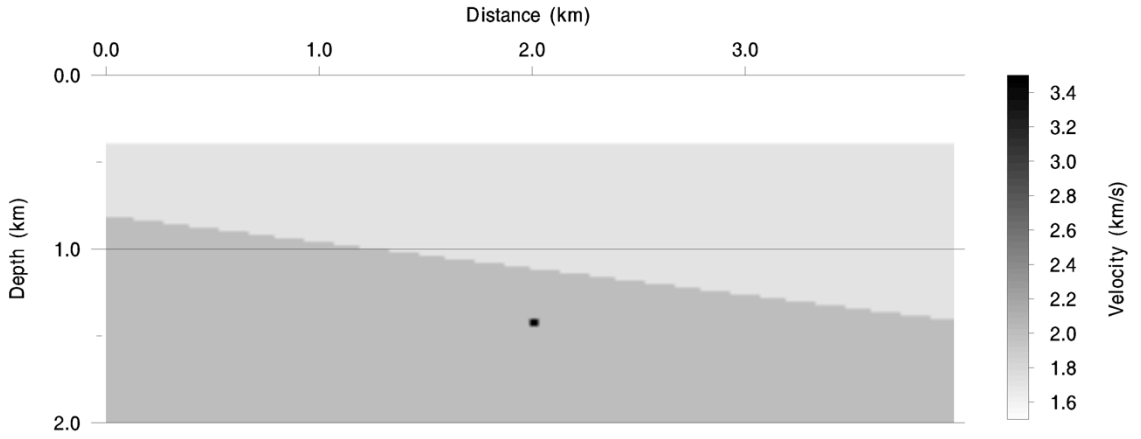

Figure 2.11. The three-layer model. There are one horizontal interface, one dipping interface and one diffractor.

The shot gather were transformed to a Ps-Po DPW dataset with 121 $\mathbf{p}_s$ and 121 $\mathbf{p}_o$ plane waves, resulting in 14641 traces in the Ps-Po DPW dataset. Both $\mathbf{p}_s$ and $\mathbf{p}_o$ plane waves were equally spaced from -0.6 to 0.6 s/km. Selected constant $\mathbf{p}_s$ and $\mathbf{p}_o$

profiles are shown in Figure 2.12. Constant $\mathbf{p}_o$ profiles shown in Figure 2.12a) contain elliptical events that are similar to moveout curves in traditional $\tau - \mathbf{p}$ profiles. Figure 2.12b) shows constant $\mathbf{p}_s$ profiles where two localized events were circled, which are around $\mathbf{p}_s = 0.0$ s/km and $\mathbf{p}_s = 0.16$ s/km, respectively. This indicates that there are two interfaces with different dips in the model. The recorded diffractions were transformed into hyperbolic events, which are indicated by black arrows.

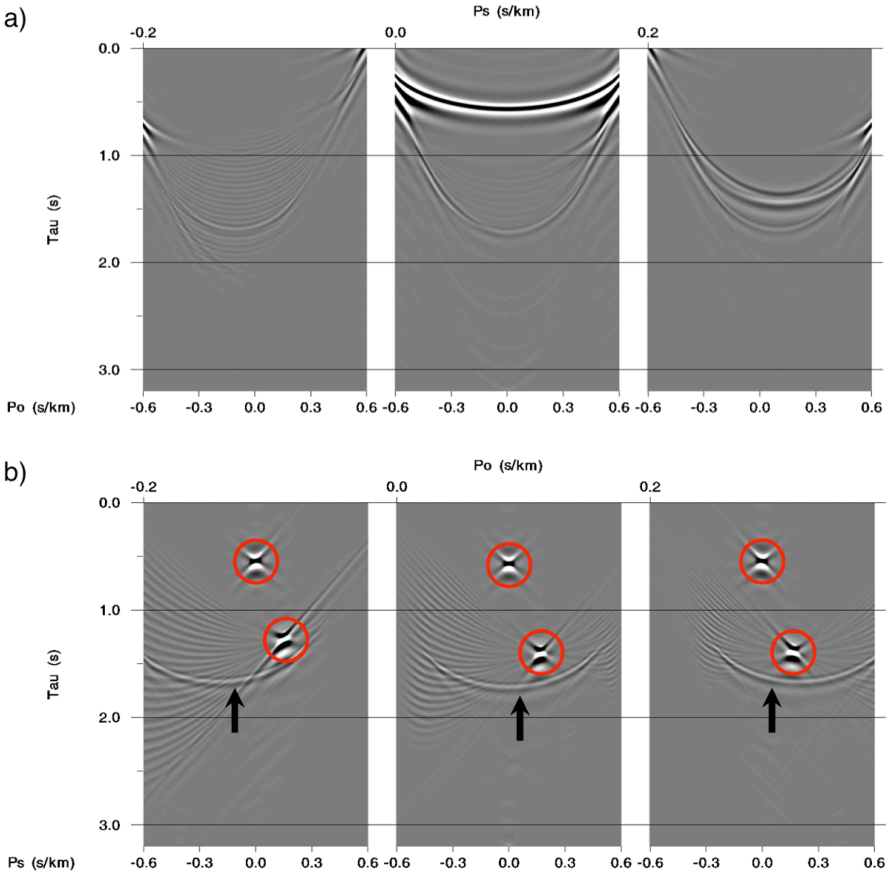

Figure 2.12. a) Three constant $\mathbf{p}_s$ profiles. From left to right, $\mathbf{p}_s$ = -0.2, 0.0 and 0.2 s/km, respectively. In each panel, $\mathbf{p}_o$ = -0.6 ~ 0.6 s/km. b) Contains three constant $\mathbf{p}_o$ profiles. From left to right, $\mathbf{p}_o$ = -0.2, 0.0 and 0.2 s/km for each panel, respectively. $\mathbf{p}_s$ = -0.6 ~ 0.6 s/km in each panel.

Equation (2.15) was employed to generate the image shown in Figure 2.13 where 31 $\mathbf{p}_o$ plane waves ranging from 0.0 to 0.3 s/km and 5 $\mathbf{p}_s$ plane waves ranging from -0.02 to 0.02 s/km were migrated. The $\mathbf{p}_s$ plane waves used for migration included most of the energy from the localized event around $\mathbf{p}_s = 0$ s/km. The horizontal interface was successfully imaged. Some diffraction energy was migrated to build the diffractor, which is indicated by the black arrow. However, the diffractor was not fully reconstructed.

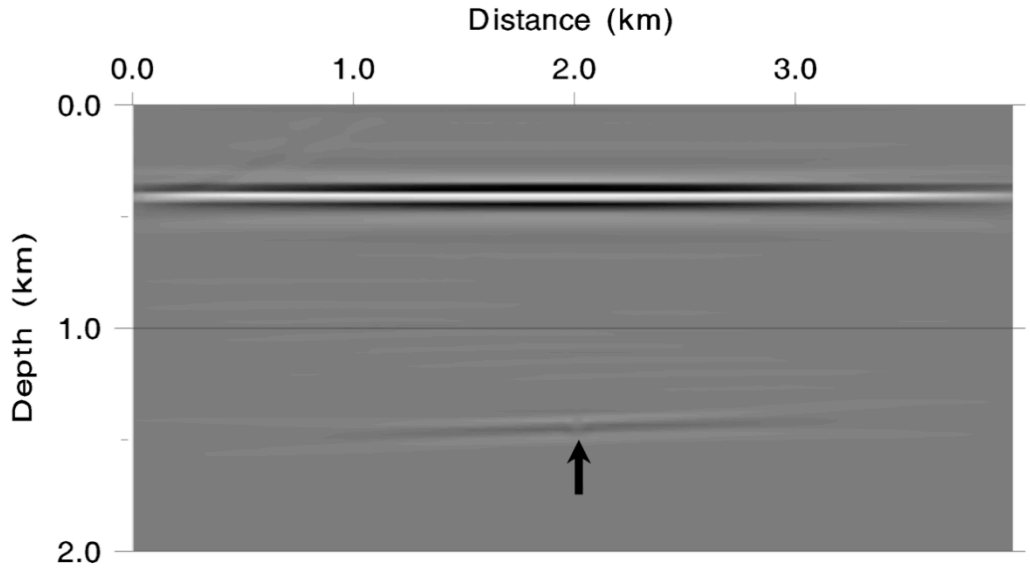

Figure 2.13. The image obtained by migrating 5 $\mathbf{p}_s$ and 31 $\mathbf{p}_o$ plane waves. The plane wave ranges are -0.02 ~ 0.02 s/km and 0.0 ~ 0.3 s/km for $\mathbf{p}_s$ and $\mathbf{p}_o$ plane waves, respectively.

By keeping the $\mathbf{p}_o$ range the same as the previous case and migrating $\mathbf{p}_s$ from 0.15 to 0.19 s/km, I obtained the image shown in Figure 2.14. The dipping interface is

now well imaged. The diffractor was also partly imaged with poor resolution, see the black arrow.

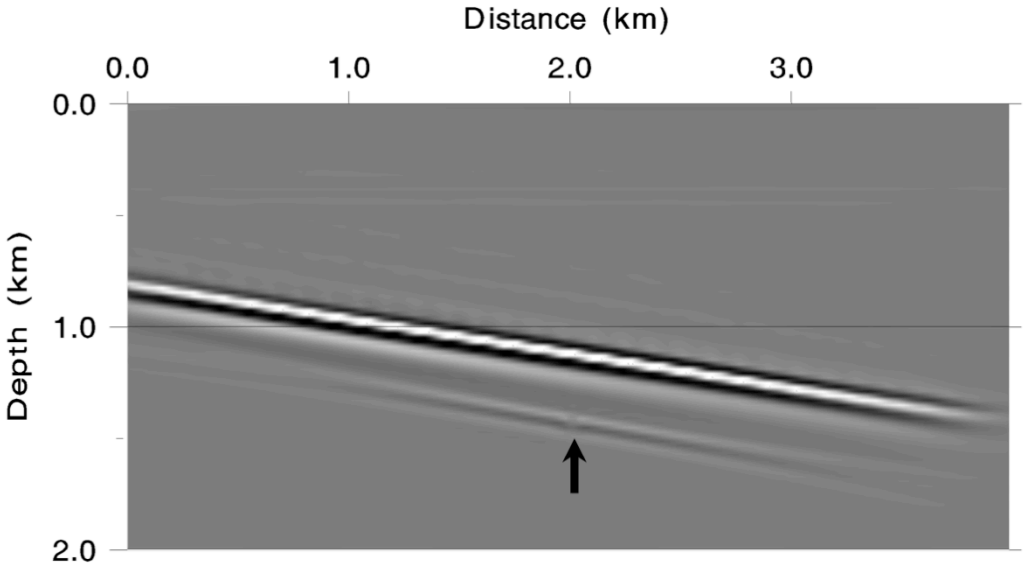

Figure 2.14. The image obtained by migrating 5 $\mathbf{p}_s$ and 31 $\mathbf{p}_o$ plane waves. The plane wave ranges are 0.15 ~ 0.19 s/km and 0.0 ~ 0.3 s/km for $\mathbf{p}_s$ and $\mathbf{p}_o$ plane wave, respectively.

In the previous cases, I only migrated a small portion of the $\mathbf{p}_s$ plane waves, which resulted in images with low resolution for the diffractor. More diffraction energy needs to be included into the migration to fully recover the diffractor. Therefore, I migrated all of the $\mathbf{p}_s$ plane waves and 31 $\mathbf{p}_o$ plane waves and obtained the image shown in Figure 2.15a). Because all of the decomposed $\mathbf{p}_s$ plane waves coming from the two interfaces and the diffractor were migrated, both interfaces were successfully recovered, as well as the diffractor. The corresponding CIGs are shown in Figure 2.15b).

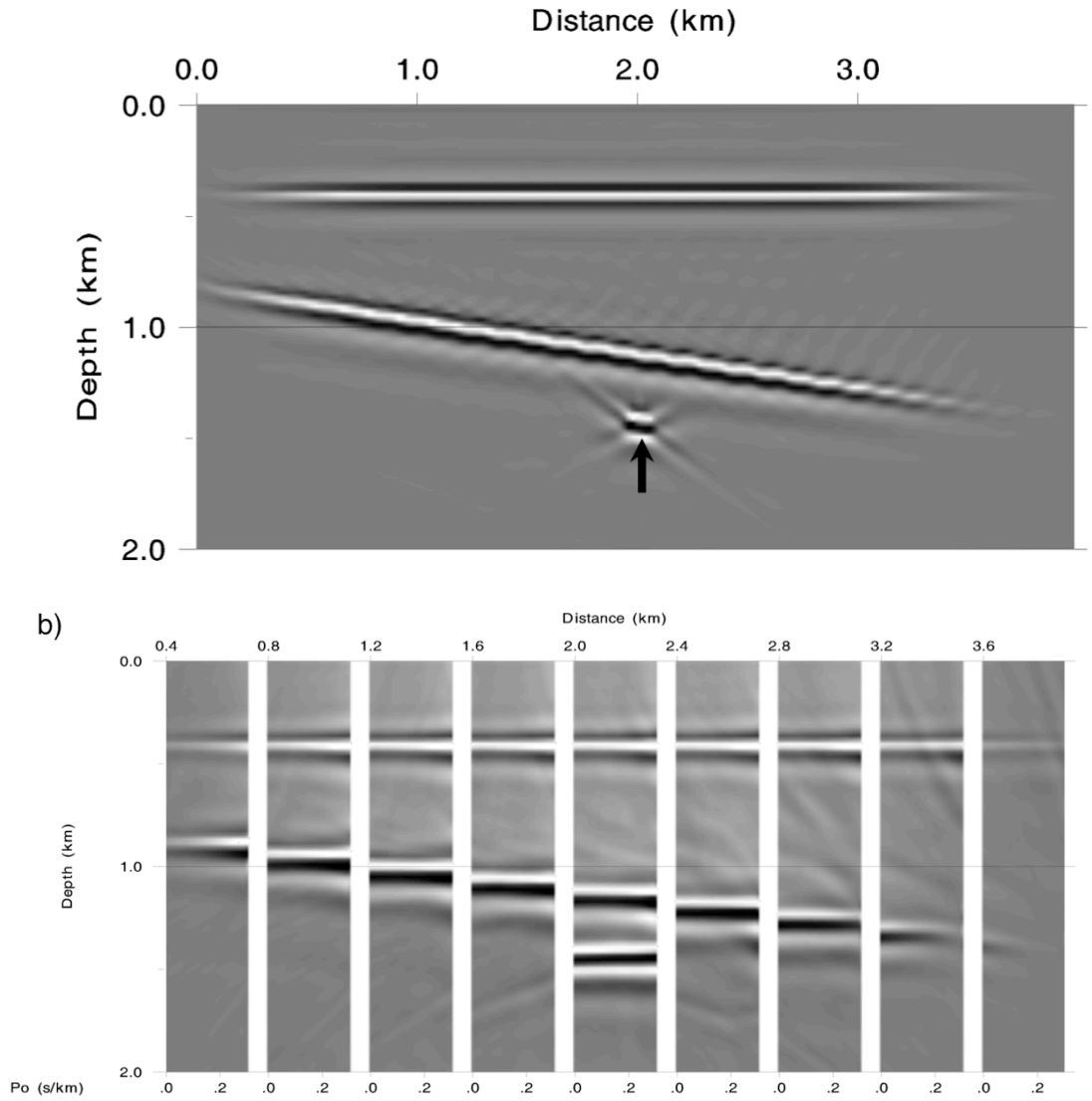

Figure 2.15. a) The image obtained by migrating 121 $\mathbf{p}_s$ and 31 $\mathbf{p}_o$ plane waves. The plane wave ranges are -0.6 ~ 0.6 s/km and 0.0 ~ 0.3 s/km for $\mathbf{p}_s$ and $\mathbf{p}_o$ plane wave, respectively. b) The corresponding CIGs. All events are horizontal indicating that the correct velocity model was used for migration.

2.8.3. SEG/EAGE salt model

A 2D line from the 3D SEG/EAGE salt model (Figure 2.16) was selected to test the proposed method on a complex velocity model. 675 shot gathers were generated using the REM. Each shot gather had 675 receivers. Both source and receiver spacing were 0.02 km.

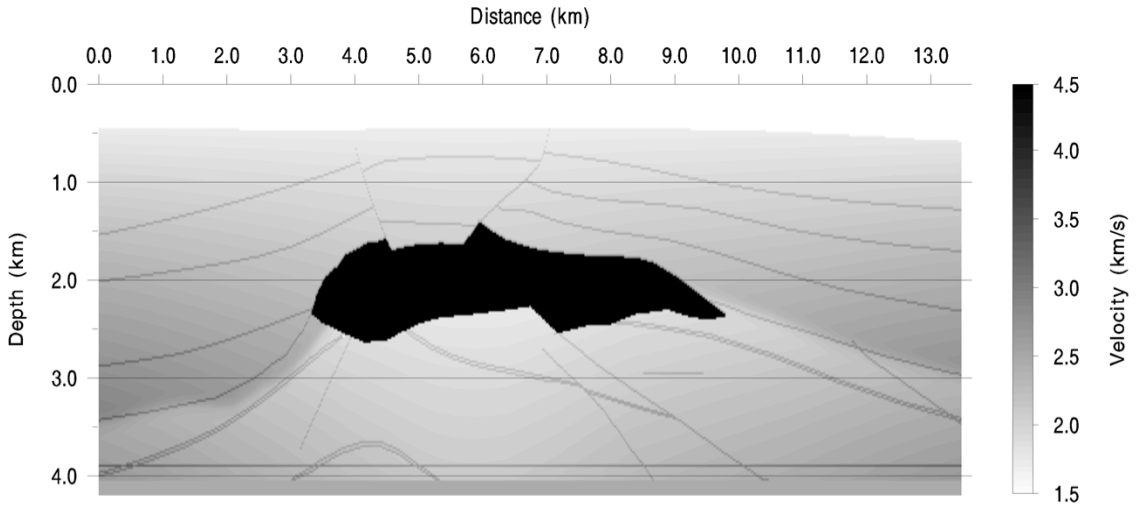

Figure 2.16. The 2D line of the 3D SEG/EAGE salt model.

Shot gathers were decomposed into 241 $\mathbf{p}_s$ and 241 $\mathbf{p}_o$ plane waves. Therefore, there were 58081 traces in the Ps-Po DPW dataset. Both $\mathbf{p}_s$ and $\mathbf{p}_o$ were equally sampled between -0.6 s/km and 0.6 s/km. The migration result for a targeted imaging is shown in Figure 2.17, where I included 31 $\mathbf{p}_o$ plane waves and limited the $\mathbf{p}_s$ plane waves from -0.1 to 0.1 s/km with a 0.05 s/km interval. Small dips and horizontal reflectors were recovered by limiting the $\mathbf{p}_s$ aperture around 0.0 s/km. Migrating a limited $\mathbf{p}_s$ aperture is very efficient and can be used as a part of a velocity model building strategy. In this case, only 71 forward propagations were performed. As a

result, trial images, as well as CIGs, can be obtained promptly, and they can be used to verify velocity models. As more $\mathbf{p}_s$ plane waves are migrated, more detailed structures can be recovered, resulting in the increased spatial resolution. I suggest that staging over $\mathbf{p}_s$ plane waves and structures can be a useful tool for migration velocity analysis.

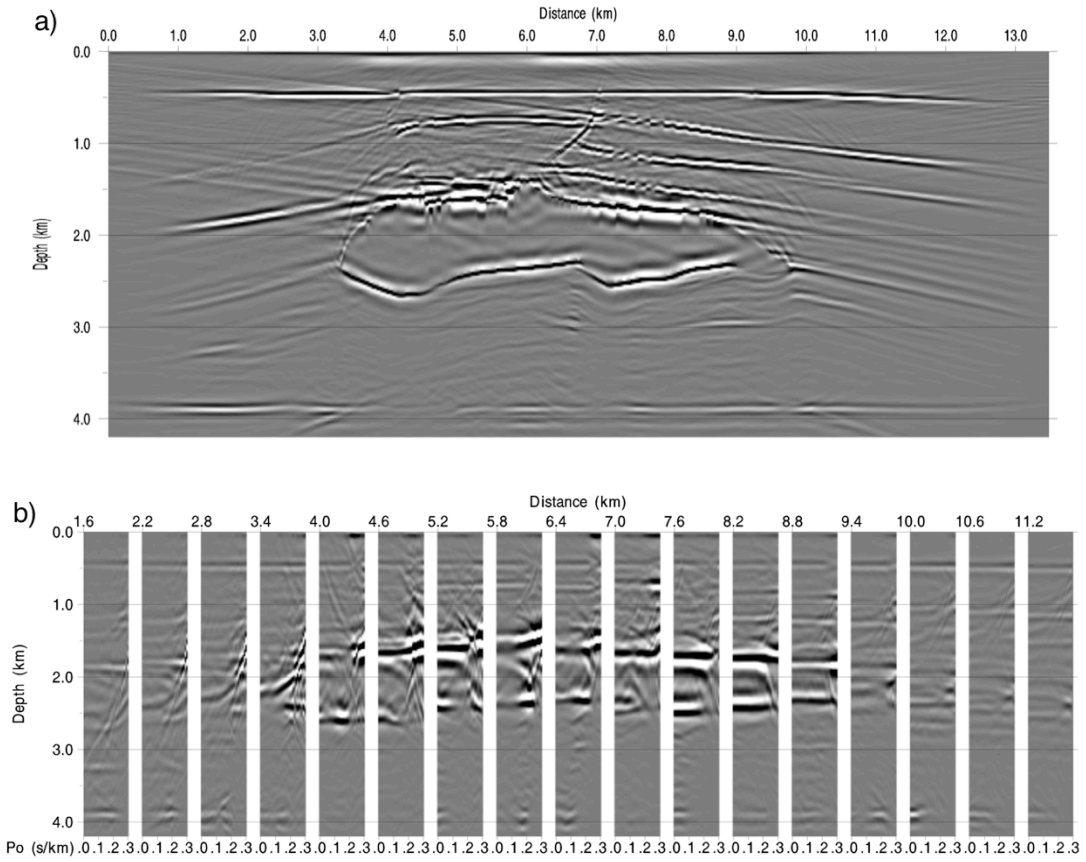

Figure 2.17. a) The image obtained by migrating 41 $\mathbf{p}_s$ plane waves and 31 $\mathbf{p}_o$ plane waves. The $\mathbf{p}_s$ range and $\mathbf{p}_o$ range are -0.1 ~ 0.1 s/km and 0.0 ~ 0.3 s/km, respectively. There were 1271 traces used for migration. b) The corresponding CIGs for the migration. Each shown horizontal position contains 31 $\mathbf{p}_o$ plane waves.

I increased the $\mathbf{p}_s$ aperture to include all $\mathbf{p}_s$ plane waves ranging from -0.6 to 0.6 s/km for migration, and obtained the image shown in Figure 2.18a). The image has improved resolution for most of reflectors compared to that shown in Figure 2.17a). The corresponding CIGs are shown in Figure 2.18b). As previously mentioned, only a limited number of forward propagations are needed. In this case, I computed 271 forward propagations to migrate all selected traces.

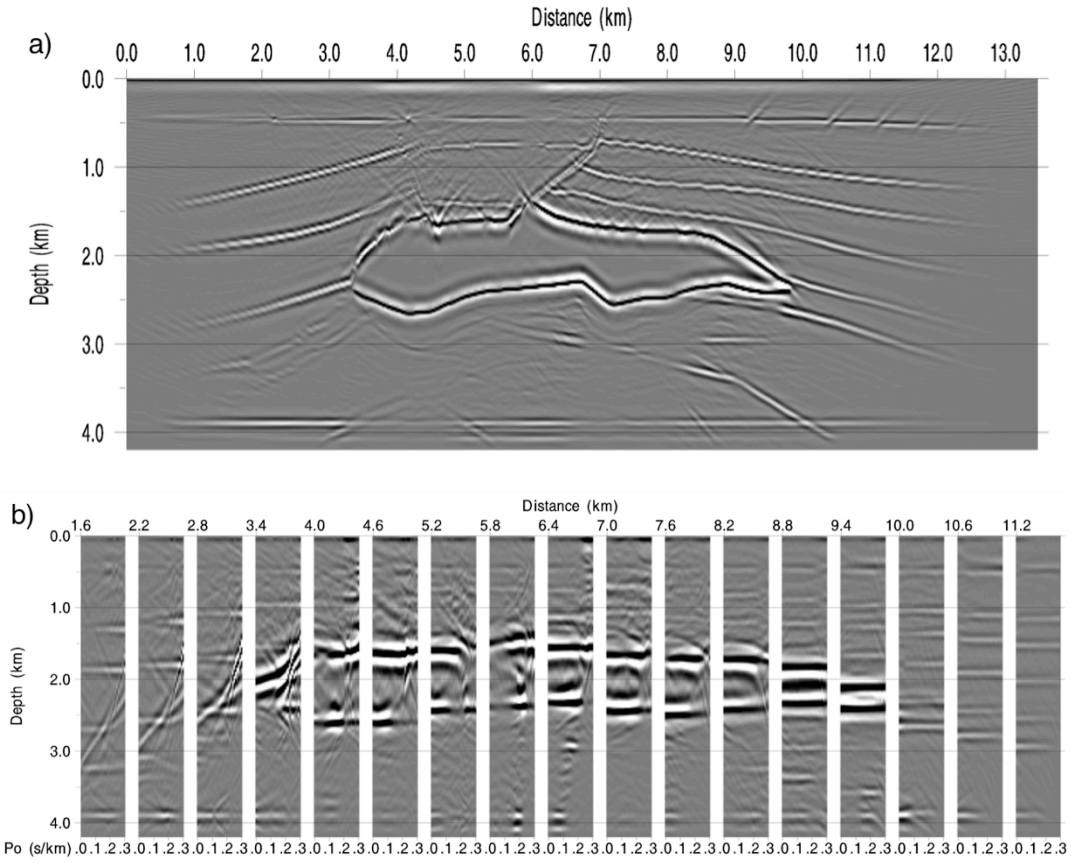

Figure 2.18. a) The image obtained by migrating all 241 $\mathbf{p}_s$ plane waves and 31 $\mathbf{p}_o$ plane waves. There were 7471 traces used for migration. b) The corresponding CIGs for the migration. Each shown horizontal position contains 31 $\mathbf{p}_o$ plane waves.

Figure 2.19 to 2.22 show results of migrating all $\mathbf{p}_s$ plane waves, while the $\mathbf{p}_o$ aperture was varied. This is equivalent to staging over offsets or subsurface angles. The $\mathbf{p}_o$ apertures used for migration in Figure 2.19 to 2.22 were 0.0 s/km (vertical incidence for offset plane waves), 0.0 to 0.1 s/km (small offset or incident angles), 0.0 to 0.2 s/km (moderate offsets or incident angles) and 0.0 to 0.4 s/km (larger offsets or incident angles), respectively. The ranges of the DPW subsets are listed in Table 2.2.

	Figure 2.18	Figure 2.19	Figure 2.20	Figure 2.21	Figure 2.22
$\mathbf{p}_s$ range (s/km)	-0.6 ~ 0.6	-0.6 ~ 0.6	-0.6 ~ 0.6	-0.6 ~ 0.6	-0.6 ~ 0.6
$\mathbf{p}_o$ range (s/km)	0.0 ~ 0.3	0.0	0.0 ~ 0.1	0.0 ~ 0.2	0.0 ~ 0.4

Table 2.2. The subsets of the DPW dataset used for generating the images shown in Figure 2.18 to 2.22.

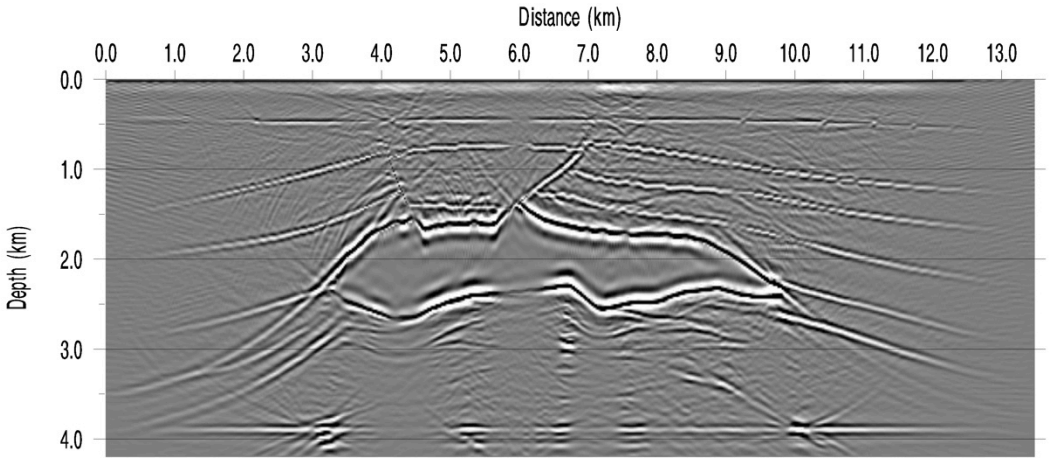

Figure 2.19. The image obtained by migrating all $\mathbf{p}_s$ plane waves and 1 $\mathbf{p}_o$ plane wave. Only 241 traces from the DPW dataset were used for migration.

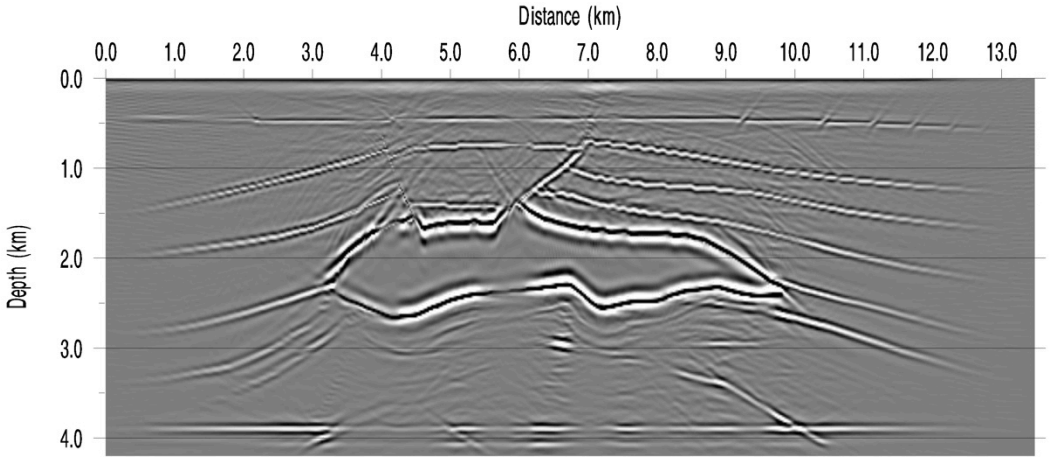

Figure 2.20. The image obtained by migrating all $\mathbf{p}_s$ plane waves and 11 $\mathbf{p}_o$ plane waves. 2651 traces were migrated.

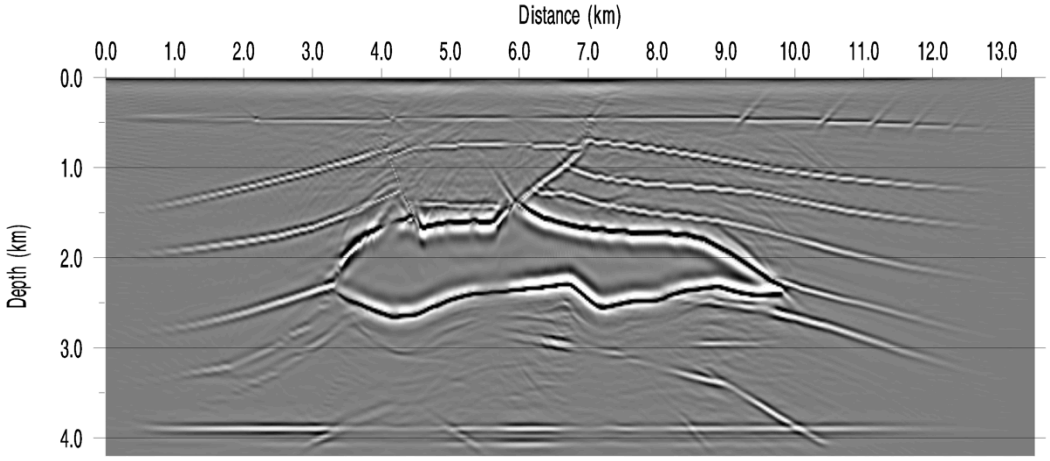

Figure 2.21. The image obtained by migrating all $\mathbf{p}_s$ plane waves and 21 $\mathbf{p}_o$ plane waves. 5061 traces were migrated.

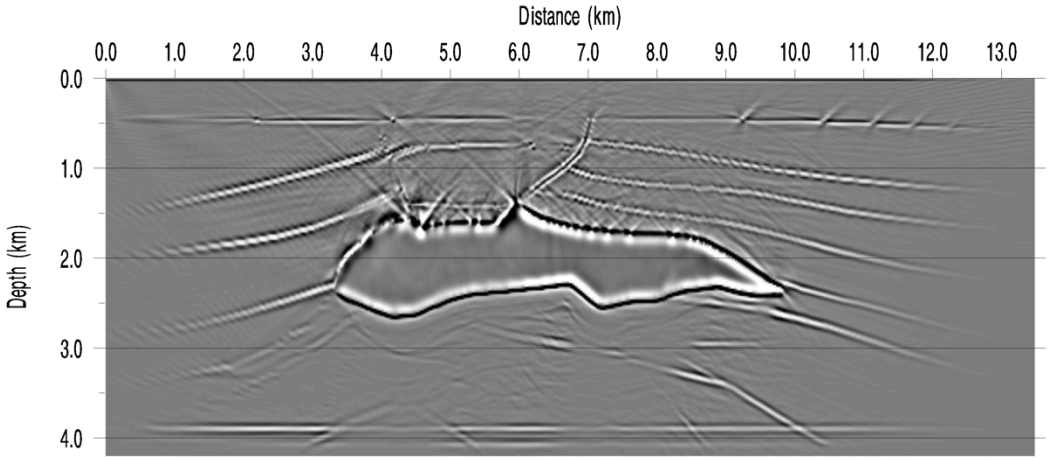

Figure 2.22. The image obtained by migrating all $\mathbf{p}_s$ plane waves and 41 $\mathbf{p}_o$ plane waves. 9881 traces from the DPW dataset were used for migration.

Comparing images shown in Figure 2.18a), 2.19, 2.20, 2.21 and 2.22 where all $\mathbf{p}_s$ were used for migration, we can notice that the image, as shown in Figure 2.18a), obtained with 31 $\mathbf{p}_o$ from 0.0 to 0.3 s/km has the highest resolution and highest signal to noise (S/N) ratio among the five images expect for the artifacts above the salt. The S/N ratio of images became visibly worse when $\mathbf{p}_o$ aperture dropped to 11.

The images shown in Figure 2.18a), 2.21 and 2.22 are of similar quality, especially in the subsalt region. That is because $\mathbf{p}_o$ plane waves with larger take-off angles at the surface had shallower penetration depths, and $\mathbf{p}_o$ plane waves with large ray-parameter values did not contribute to the image in the deepest part. Three sets of CIGs from the images shown in Figure 2.21, 2.18a) and 2.22 are shown in Figure 2.23. The $\mathbf{p}_o$ ranges of the three sets of CIGs are 0.0 ~ 0.2 s/km, 0.0 ~ 0.3 s/km and 0.0 ~ 0.4 s/km, respectively. In Figure 2.23c), vertical dashed lines delineate $\mathbf{p}_o = 0.3$ s/km. In Figure 2.23a) and b), flat horizons are up to the maximum $\mathbf{p}_o$ value. As shown in Figure

2.23c), however, plane waves $\mathbf{p}_o > 0.3$ s/km contain little energy and contribute little to the deeper part of the model, which are target subsalt areas.

Although the images shown in Figure 2.21, 2.18a) and 2.22 have similar quality, Figure 2.21 requires the least computational cost. The computational cost of obtaining Figure 2.21 is approximately 6/10 of that of Figure 2.18a), and it is approximately 4/10 of that of Figure 2.22.

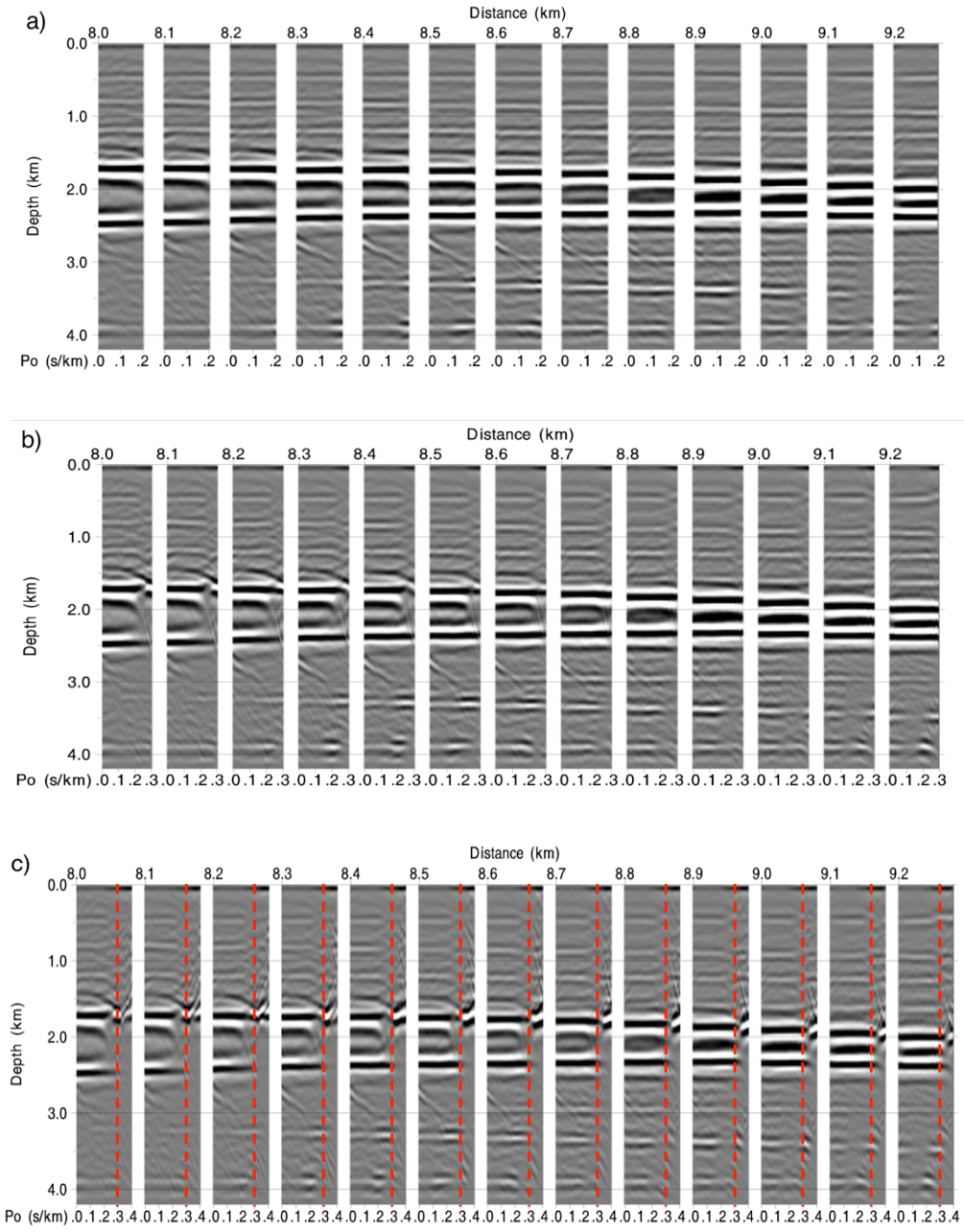

Figure 2.23. a) The CIGs from the image shown in Figure 2.21. Each shown location has 21 $\mathbf{p}_o$ plane waves. b) The CIGs from the image shown in Figure 2.18a). Each shown location contains 31 $\mathbf{p}_o$ plane waves. c) The CIGs from the image shown in Figure 2.22. Each shown location has 41 $\mathbf{p}_o$ plane waves. a), b) and c) have similar horizons in the deeper part.

According to the previous analysis, migrating all traces in DPW data volume is not necessary, especially when the target lies in the deep part of the model and velocities increase dramatically with depth. Migrating less DPW traces improves the migration efficiency. However, appropriately selecting $\mathbf{p}_o$ apertures for migration requires previous geological information.

The image shown in Figure 2.24 was obtained by migrating all 241 $\mathbf{p}_s$ and 31 $\mathbf{p}_o$ plane waves, where the illumination compensation imaging condition described by equation (2.15) was implemented. Although, Figure 2.24 and 2.18a) were obtained by migrating the same DPW traces, the image shown in Figure 2.24, which was obtained with illumination compensation, has more balanced amplitudes and higher resolution in the subsalt region.

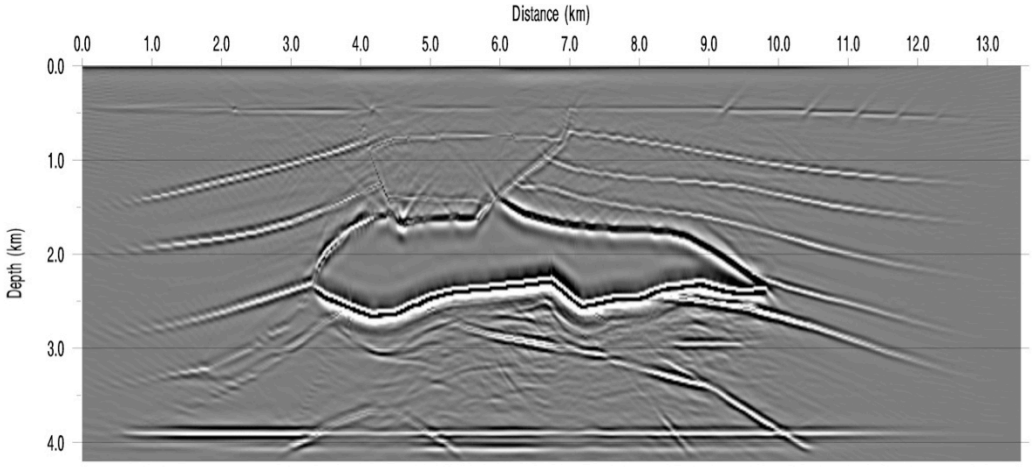

Figure 2.24. The image obtained by migrating all 241 $\mathbf{p}_s$ plane waves and 31 $\mathbf{p}_o$ plane waves using illumination compensation imaging condition.

2.9. DISCUSSIONS

1. For the DPW transform, we need to transform shot gathers into different plane waves for different models depending on the maximum dip angle of reflectors and the minimum velocity of the model.

2. In order to generate an image with reasonable resolution, we only need to migrate a small number of $\mathbf{p}_o$ plane waves. I found that using $\mathbf{p}_r$ or $\mathbf{p}_o$ plane waves up to an absolute value of 0.3 s/km would be sufficient for most cases. Adding $\mathbf{p}_r$ or $\mathbf{p}_o$ plane waves with large ray-parameter values for migration would not improve image quality for the deeper parts significantly, as a result of shallow penetration for rays with large take off-angles. However, traces for migration should be chosen with caution based on previous geological information.

3. Obtaining CIGs easily and rapidly, together with staging over $\mathbf{p}_s$ apertures, gives the proposed method the potential to become a useful tool for migration velocity analysis.

4. The DPW-based RTM is kinematically equivalent to the shot profile RTM, if appropriate plane waves are migrated.

2.10. CONCLUSIONS

Analyzing the relationship between the pre-stack shot profile Kirchhoff depth migration and the shot profile RTM, I proposed a plane wave RTM strategy based on the Kirchhoff-based DPW depth migration. The proposed DPW-based RTM method offers several advantages over the traditional pre-stack shot profile RTM. First, seismic data are regularized during the DPW transform, and the DPW data are not dependent on source and receiver locations, which makes it easier to inject the synthetic source and seismic data for irregular source and receiver positioning than the shot profile RTM. Secondly,

the number of forward propagations required for the DPW-based RTM is limited. Besides that, the number of forward and backward propagations remains relatively constant, even when the number of shots increases dramatically. Therefore, the DPW-based RTM can be more efficient than the shot profile RTM. Thirdly, subsets of DPW datasets can be migrated independently. As a result, subsurface interfaces can be imaged according to their dips. This makes the proposed method a candidate for target-oriented imaging. Finally, gradually enlarging the apertures for plane waves (both source and receiver or offset plane waves) used for migration is demonstrated to be a potential tool for velocity analysis. Trial and intermediate images and CIGs can be obtained efficiently by migrating a small portion of the DPW dataset, and the velocity model can be updated rapidly according to the CIGs. The illumination compensation imaging condition for the DPW-based RTM was introduced to enhance the resolution for deep structures.

Chapter 3: Double Plane Wave Migration in the Frequency Domain

3.1. INTRODUCTION

As introduced in the Chapter 2, reverse time migration (RTM) (Baysal et al., 1983; McMechan 1983) solves the two-way wave equation during wave field propagation processes. Although powerful computers have made traditional pre-stack shot gather RTM a practical migration procedure, pre-stack shot gather RTM is still computationally intensive. The traditional pre-stack shot gather RTM in the time domain needs to compute wave field time marching explicitly, which is time consuming. Also, considerable memory or disk space is required to store those wavefields for large models. Therefore, extensive efforts have been made to increase the efficiency of the pre-stack RTM and to reduce the storage demands. Delayed shot and harmonic source migration strategies (Whitmore 1995; Zhang et al., 2005; Liu et al., 2006) were applied by several authors to improve the performance of RTM (Zhang et al., 2007; Zhang and Sun 2008).

Recently, RTM in the frequency domain has been investigated as an alternative to the time domain RTM. In the frequency domain, the acoustic wave equation becomes the Helmholtz equation (Marfurt 1984). Several authors (Shin et al., 2001; Xu et al., 2010; Kim et al., 2011) successfully demonstrated the effectiveness of the frequency domain RTM via solving the linear system of the Helmholtz equation.

In this chapter, performing RTM in the frequency domain using DPW data is investigated. I first briefly review the DPW-based RTM in the time domain introduced in the Chapter 2. Then, I propose two methods that can migrate DPW data in the frequency domain. The first method is analogous to the DPW-based RTM in the time domain. So, it is named the "DPW-based RTM in the frequency domain". Based on the inverse

scattering theory (Bleistein et al., 2001; Stolt and Weglein 2012), I derive imaging conditions for migrating DPW data using frequency plane wave Green's function. And I designate the second method the frequency domain DPW RTM (or DPW RTM in the frequency domain). The two methods are shown to be kinematically equivalent. However, the frequency domain DPW RTM is much faster than the DPW-based RTM in that the number of wavefield computations required by the frequency domain DPW RTM is considerably smaller than that required by the DPW-based RTM. So, I focus on analyzing the frequency domain DPW RTM.

The frequency domain DPW RTM is fast, accurate and flexible. The method can also be used as a target-oriented imaging method that benefits the migration velocity analysis. Again, the method is equivalent to the shot profile RTM if appropriate plane wave components are migrated. The method achieves a speedup more than an order of magnitude comparing to the shot profile RTM.

Migrating DPW data can include anisotropy, and the frequency domain DPW RTM method is tested on two synthetic vertical transversely isotropic (VTI) models.

3.2. DPW-BASED RTM IN THE TIME AND THE FREQUENCY DOMAINS

3.2.1. DPW-based RTM in the time domain

As shown in Chapter 2, the imaging condition for the DPW-based RTM in the time domain can be written as

$$I(\mathbf{x}) = \sum_{\mathbf{p}_s} \sum_{\mathbf{p}_r} \sum_{\tau} \frac{\partial^2 U_{\mathbf{p}_s}(\mathbf{p}_s, \mathbf{x}, \tau)}{\partial \tau^2} U_{\mathbf{p}_r}(\mathbf{p}_s, \mathbf{p}_r, \mathbf{x}, \tau - (\mathbf{p}_s + \mathbf{p}_r) \cdot (\mathbf{x}_h - \mathbf{x}_{ref})). \qquad (3.1)$$

where $\mathbf{p}_s$ and $\mathbf{p}_r$ are ray-parameters of source and receiver plane waves, respectively, τ is the vertical delay time, and $\mathbf{x}_h = (x_h, y_h, z_h = 0)$ is the horizontal position of the subsurface image point $\mathbf{x} = (x, y, z)$. U_{p_s} and U_{p_r} are the forward propagated source plane wave field and the backward propagated receiver plane wave field, respectively. Using the relationships between the Ps-Pr and the Ps-Po DPW data, the imaging condition for the Ps-Po DPW data can be written as

$$I(\mathbf{x}) = \sum_{\mathbf{p}_s} \sum_{\mathbf{p}_o} \sum_{\tau} \frac{\partial^2 U_{\mathbf{p}_s}(\mathbf{p}_s - \mathbf{p}_o, \mathbf{x}, \tau)}{\partial \tau^2} U_{\mathbf{p}_o}(\mathbf{p}_s, \mathbf{p}_o, \mathbf{x}, \tau - \mathbf{p}_s \cdot (\mathbf{x}_h - \mathbf{x}_{ref})), \tag{3.2}$$

where $\mathbf{p}_o$ is the ray-parameter of an offset plane wave, and $U_{\mathbf{p}_o}$ represents the backward propagated offset plane wave field. The imaging conditions described by equations (3.1) and (3.2) are very similar to the adjoint state method used for calculating the gradient of the misfit function in shot profile full waveform inversion (FWI) in the time domain (Plessix 2006), where forward propagated source wavefields are cross-correlated with backward propagated shot gathers.

3.2.2. DPW-based RTM in the frequency domain

Here, to derive the DPW-based RTM in the frequency domain, I start with the adjoint state method in the frequency domain. In the frequency domain, the wave equation becomes the Helmholtz equation and can be written in a complex linear system (Marfurt 1984) as

$$\tilde{\mathbf{S}}\tilde{\mathbf{u}} = \tilde{\mathbf{f}}, \tag{3.3}$$

where $\tilde{\mathbf{S}}$ is the impedance matrix, $\tilde{\mathbf{u}}$ is the pressure field due to the source $\tilde{\mathbf{f}}$ located at source locations, and the symbol ~ represents the frequency domain wavefield and data. The pressure field can be obtained by

$$\tilde{\mathbf{u}} = \tilde{\mathbf{S}}^{-1}\tilde{\mathbf{f}}, \tag{3.4}$$

where the superscript -1 denotes the inverse of a matrix.

In the frequency domain, the adjoint state method is employed to calculate the gradient in FWI, and it can be formulated as (Pratt 1999; Plessix 2006)

$$\nabla_m F = \mathrm{Re}((\frac{\partial \tilde{\mathbf{S}}}{\partial m}\tilde{\mathbf{u}})^T \tilde{\mathbf{v}}), \tag{3.5}$$

where $\nabla_m F$ is the gradient of the misfit function in FWI, $\frac{\partial \tilde{\mathbf{S}}}{\partial m}$ is the partial derivative of impedance matrix with respect to an earth parameter m, and the superscript T denotes the transpose of a matrix or a vector. $\tilde{\mathbf{v}}$ in equation (3.5) is calculated by

$$\tilde{\mathbf{v}} = (\tilde{\mathbf{S}}^{-1})^T \delta\tilde{\mathbf{d}}^*, \tag{3.6}$$

which is the backward propagated wavefield.

Assuming $(\tilde{\mathbf{S}}^{-1}) = (\tilde{\mathbf{S}}^{-1})^T$ (Pratt 1999), $\tilde{\mathbf{v}} = \tilde{\mathbf{S}}^{-1}\delta\tilde{\mathbf{d}}^*$, where $\delta\tilde{\mathbf{d}}$ is the difference between the observed data and the predicted data, and the superscript * represents the

conjugate of a complex number. The gradient can be obtained by taking the real part of the right hand side of equation (3.5).

An RTM image can be obtained as $\delta\tilde{\mathbf{d}}$ in equation (3.6) is replaced with $\tilde{\mathbf{d}}$, which is the observed data. This results in:

$$I = \mathrm{Re}((\frac{\partial\tilde{\mathbf{S}}}{\partial m}\tilde{\mathbf{u}})^T\tilde{\mathbf{v}}), \tag{3.7}$$

where I is the RTM image. The backward propagated wavefield $\tilde{\mathbf{v}}$ can be obtained by

$$\tilde{\mathbf{v}} = \tilde{\mathbf{S}}^{-1}\tilde{\mathbf{d}}^*, \tag{3.8}$$

which performs backward propagation for seismic records. Equation (3.7) indicates that an RTM image can be obtained by performing cross-correlation between the forward propagated wavefield $\tilde{\mathbf{u}}$ and the backward propagated wavefield $\tilde{\mathbf{v}}$ in the frequency domain.

Although equation (3.7) is a general imaging condition that can be used to migrate any seismic data, it is often implemented to migrate shot gathers. In such cases, $\tilde{\mathbf{u}}$ and $\tilde{\mathbf{v}}$ represent forward propagated point source wavefields and backward propagated shot gathers wavefields, respectively. In our case, I propose employing equation (3.7) to migrate the DPW data with forward and backward propagated frequency domain plane wavefields.

If $\tilde{\mathbf{f}}$ represents a synthetic plane wave source at the surface, and $\tilde{\mathbf{d}}^*$ represents the complex conjugate of DPW traces at each surface location, forward propagated plane

wavefield $\tilde{\mathbf{u}}$ and backward propagated plane wavefield $\tilde{\mathbf{v}}$ can be obtained by solving equations (3.4) and (3.8), respectively. Because $\tilde{\mathbf{S}}$ in equation (3.3) is the impedance matrix of the two-way wave equation, frequency domain plane wavefields obtained by solving equations (3.4) and (3.8), such as $\tilde{\mathbf{u}}$ and $\tilde{\mathbf{v}}$, are equivalent to time domain plane wavefields propagated in terms of traveltime *t*. However, to migrate the DPW data, the required frequency domain plane wavefields should be equivalent to the time domain plane wavefields propagated in terms of τ with respect to $\mathbf{x}_h$.

Obtaining plane wavefields propagated in terms of τ in the time domain was introduced in Chapter 2, where I used the relationship between τ and *t*:

$$\tau = t - \mathbf{p}\cdot\mathbf{x}_h, \tag{3.9}$$

and computed the time domain plane wavefields propagated in terms of τ by

$$U_{\mathbf{p}_s}(\mathbf{p}_s,\mathbf{x},\tau) = U_{\mathbf{p}_s}(\mathbf{p}_s,\mathbf{x},t-\mathbf{p}_s\cdot\mathbf{x}_h), \tag{3.10}$$

and

$$U_{\mathbf{p}_r}(\mathbf{p}_s,\mathbf{p}_r,\mathbf{x},\tau) = U_{\mathbf{p}_r}(\mathbf{p}_s,\mathbf{p}_r,\mathbf{x},t-\mathbf{p}_r\cdot\mathbf{x}_h). \tag{3.11}$$

The counter parts of equations (3.9) and (3.10) in the frequency domain can be written as

$$\hat{\tilde{u}}_{\mathbf{p}_s}(\mathbf{p}_s,\mathbf{x},\omega) = \tilde{u}_{\mathbf{p}_s}(\mathbf{p}_s,\mathbf{x},\omega)\exp(+i\omega\mathbf{p}_s\cdot\mathbf{x}_h), \tag{3.12}$$

and

$$\hat{\tilde{v}}_{\mathbf{p}_r}(\mathbf{p}_s,\mathbf{p}_r,\mathbf{x},\omega)=\tilde{v}_{\mathbf{p}_r}(\mathbf{p}_s,\mathbf{p}_r,\mathbf{x},\omega)\exp(+i\omega\mathbf{p}_r\cdot\mathbf{x}_h), \tag{3.13}$$

where $\exp(+i\omega\mathbf{p}_s\cdot\mathbf{x}_h)$ and $\exp(+i\omega\mathbf{p}_r\cdot\mathbf{x}_h)$ are the phase shift terms that perform the computation indicated by equation (3.9) in the frequency domain. $\hat{\tilde{u}}_{\mathbf{p}_s}(\mathbf{p}_s,\mathbf{x},\omega)$ and $\hat{\tilde{v}}_{\mathbf{p}_r}(\mathbf{p}_s,\mathbf{p}_r,\mathbf{x},\omega)$ are frequency domain plane wavefields that are equivalent to time domain plane wavefields propagated in terms of τ.

As discussed in the previous two chapters, a time correction term $-(\mathbf{p}_s+\mathbf{p}_r)\cdot(\mathbf{x}_h-\mathbf{x}_{ref})$ needs to be applied to the plane wavefields at each $\mathbf{x}_h$, so that the original vertical delay time of the DPW data, which is with respect to $\mathbf{x}_{ref}$, is corrected to the vertical delay time with respect to $\mathbf{x}_h$. In the frequency domain, the time correction term becomes a phase shift term $\exp(+i\omega(\mathbf{p}_s+\mathbf{p}_r)\cdot(\mathbf{x}_h-\mathbf{x}_{ref}))$. Substituting $\hat{\tilde{u}}_{\mathbf{p}_s}(\mathbf{p}_s,\mathbf{x},\omega)$ and $\hat{\tilde{v}}_{\mathbf{p}_r}(\mathbf{p}_s,\mathbf{p}_r,\mathbf{x},\omega)$ into equation (3.7) with the phase shift term $\exp(+i\omega(\mathbf{p}_s+\mathbf{p}_r)\cdot(\mathbf{x}_h-\mathbf{x}_{ref}))$ applied to $\hat{\tilde{v}}_{\mathbf{p}_r}(\mathbf{p}_s,\mathbf{p}_r,\mathbf{x},\omega)$ and summing over contributions from all traces in a Ps-Pr DPW dataset, I arrive at the imaging condition for the DPW-based RTM in the frequency domain as

$$\begin{aligned} I(\mathbf{x})=\sum_{\omega}\sum_{\mathbf{p}_s}\sum_{\mathbf{p}_r}&\mathrm{Re}(\omega^2\hat{\tilde{u}}_{\mathbf{p}_s}(\mathbf{p}_s,\mathbf{x},\omega)\hat{\tilde{v}}_{p_r}{}^{*}(\mathbf{p}_s,\mathbf{p}_r,\mathbf{x},\omega)\\ &\times\exp(-i\omega(\mathbf{p}_s+\mathbf{p}_r)\cdot(\mathbf{x}_h-\mathbf{x}_{ref}))), \end{aligned} \tag{3.14}$$

Employing the relationships between the Ps-Pr and the Ps-Po DPW data (i.e., equations 1.17 and 1.18), I propose the following imaging condition for the Ps-Po DPW data

$$I(\mathbf{x}) = \sum_{\omega}\sum_{\mathbf{p}_s}\sum_{\mathbf{p}_o} \mathrm{Re}(\omega^2 \hat{\tilde{u}}_{\mathbf{p}_s}(\mathbf{p}_s - \mathbf{p}_o, \mathbf{x}, \omega)\hat{\tilde{v}}_{p_o}(\mathbf{p}_s, \mathbf{p}_o, \mathbf{x}, \omega) \times \exp(-i\omega \mathbf{p}_s \cdot (\mathbf{x}_h - \mathbf{x}_{ref}))), \tag{3.15}$$

where $\hat{\tilde{v}}_{p_o}$ is the backward propagated offset plane wavefield.

Equations (3.14) and (3.15) are imaging conditions for the DPW-based RTM in the frequency domain derived with the adjoint state method. According the analyses in the previous section, images obtained by the DPW-based RTM in the frequency domain are kinematically equivalent to those obtained by the DPW-based RTM in the time domain.

The DPW-based RTMs in the time and the frequency domains are accurate and flexible. They solve the two-way wave equation, either by explicitly propagating time domain wavefields or by solving the linear system of the Helmholtz equation. Typically, thousands of traces from a DPW dataset need to be migrated. Because the adjoint state method is employed, each trace needs to be propagated explicitly by solving the two-way wave equation, if using those two methods. Therefore, directly implementing the methods is not suitable for small seismic datasets that only have hundreds of shot gathers.

3.3. BORN MODELING AND ITS ADJOINT

To address the computation issue of the DPW-based RTM (both in the time and in the frequency domains), I start with the forward and the inverse scattering theories in the frequency domain. For simplicity, the symbol ~, which represents frequency domain data and wavefields, is dropped. The forward scattering potential (Bleistein et al., 2001; Stolt

and Weglein 2012) under the Born approximation in the frequency domain can be written as

$$\delta P(\mathbf{s},\mathbf{r},\omega) = -\omega^2 f_s(\omega) \int \frac{m(\mathbf{x})}{c^2(\mathbf{x})} G(\mathbf{s},\mathbf{x},\omega) G(\mathbf{x},\mathbf{r},\omega) d\mathbf{x}, \tag{3.16}$$

where $c(\mathbf{x})$ is the velocity, $G(\mathbf{x},\mathbf{r},\omega)$ is the Green's function from the source to the subsurface point $\mathbf{x}$, $G(\mathbf{x},\mathbf{r},\omega)$ is the Green's function from the subsurface point to the receiver, $\delta P(\mathbf{s},\mathbf{r},\omega)$ is the scattered field associate with the source and the receiver, $m(\mathbf{x})$ represents the perturbation of model parameter, and $\delta P(\mathbf{s},\mathbf{r},\omega)$ is the frequency seismic source. Equation (3.16) is often referred to as the Born modeling.

Taking the adjoint of equation (3.16) (Bleistein et al., 2001), the model perturbation can be calculated by

$$m(\mathbf{x}) = -\mathrm{Re}\left(\iiint \frac{\omega^2}{c^2(\mathbf{x})} f_s^*(\omega) G^*(\mathbf{s},\mathbf{x},\omega) G^*(\mathbf{x},\mathbf{r},\omega) \delta P(\mathbf{s},\mathbf{r},\omega) d\mathbf{s}\, d\mathbf{r}\, d\omega\right), \tag{3.17}$$

where the superscript * again denotes the complex conjugate of a complex number, and the model perturbation is obtained by taking the real part of the right hand side of equation (3.17). Equation (3.17) is often referred to as the first order inverse scattering potential integral. Based on equation (3.17), adjoint-state method was applied to FWI to calculate the velocity perturbation (Sirgue and Pratt 2004; Tao and Sen 2013b; Tromp et al., 2005). To perform the migration, the data perturbation $\delta P(\mathbf{s},\mathbf{r},\omega)$ in equation (3.17) should be substituted with the recorded data. Therefore, we have

$$I(\mathbf{x}) = \mathrm{Re}\left(\iiint \frac{\omega^2}{c^2(\mathbf{x})} f_s^*(\omega) G^*(\mathbf{s},\mathbf{x},\omega) G^*(\mathbf{x},\mathbf{r},\omega) P(\mathbf{s},\mathbf{r},\omega)\, d\mathbf{s}\, d\mathbf{r}\, d\omega\right), \tag{3.18}$$

where $P(\mathbf{s},\mathbf{r},\omega)$ is the recorded seismic data, and $I(\mathbf{x})$ is the image obtained by taking the real part of the right hand side of equation (3.18). Equation (3.18) can serve as the RTM imaging condition for shot gathers in the frequency domain, and it is the counterpart of imaging condition for the time domain RTM (Chattopadhyay and McMechan 2008).

3.4. FREQUENCY DOMAIN DPW RTM USING PLANE WAVE GREEN'S FUNCTIONS

Starting from equation (3.18), a new frequency domain DPW RTM imaging condition is derived. The proposed imaging condition not only increases the computational efficiency of the migration substantially, but also retains the accuracy and flexibility of the previously introduced DPW-based RTM methods.

Let's rewrite the inverse DPW transform for the Ps-Pr DPW data:

$$P(\mathbf{s},\mathbf{r},\omega) = \omega^4 \iint P(\mathbf{p}_s,\mathbf{p}_r,\omega) \exp(+i\omega[\mathbf{p}_s \cdot (\mathbf{s}-\mathbf{x}_{ref}) + \mathbf{p}_r \cdot (\mathbf{r}-\mathbf{x}_{ref})])\, d\mathbf{p}_s\, d\mathbf{p}_r. \tag{3.19}$$

Substituting equation (3.19) into equation (3.18), we obtain

$$\begin{aligned} I(\mathbf{x}) = \mathrm{Re}\Bigg(\int \frac{\omega^6}{c^2(\mathbf{x})} \iint\iint f_s^*(\omega) G^*(\mathbf{s},\mathbf{x},\omega) G^*(\mathbf{x},\mathbf{r},\omega) P(\mathbf{p}_s,\mathbf{p}_r,\omega) \\ \times \exp(+i\omega[\mathbf{p}_s \cdot (\mathbf{s}-\mathbf{x}_{ref}) + \mathbf{p}_r \cdot (\mathbf{r}-\mathbf{x}_{ref})]) \\ \times d\mathbf{p}_s d\mathbf{p}_r d\mathbf{s} d\mathbf{r} d\omega\Bigg). \end{aligned} \tag{3.20}$$

Adding terms $\mathbf{p}_s \cdot (\mathbf{x}_h - \mathbf{x}_h) = 0$ and $\mathbf{p}_r \cdot (\mathbf{x}_h - \mathbf{x}_h) = 0$ into equation (3.20), we get

$$\begin{aligned} I(\mathbf{x}) = \mathrm{Re}(\int \frac{\omega^6}{c^2(\mathbf{x})} \iint \iint \iint f_s^*(\omega) G^*(\mathbf{s},\mathbf{x},\omega) G^*(\mathbf{x},\mathbf{r},\omega) P(\mathbf{p}_s,\mathbf{p}_r,\omega) \\ \times \exp(+i\omega[\mathbf{p}_s \cdot (\mathbf{s} - \mathbf{x}_{ref}) + \mathbf{p}_s \cdot (\mathbf{x}_h - \mathbf{x}_h) + \mathbf{p}_r \cdot (\mathbf{r} - \mathbf{x}_{ref}) + \mathbf{p}_r \cdot (\mathbf{x}_h - \mathbf{x}_h)]) \\ \times d\mathbf{p}_s d\mathbf{p}_r d\mathbf{s} d\mathbf{r} d\omega), \end{aligned} \tag{3.21}$$

where $\mathbf{x}_h$ is again the horizontal position of the subsurface imaging point $\mathbf{x}$. The reason for adding terms $\mathbf{p}_s \cdot (\mathbf{x}_h - \mathbf{x}_h)$ and $\mathbf{p}_r \cdot (\mathbf{x}_h - \mathbf{x}_h)$ will be explained in detail in the next section. Reorganizing terms in equation (3.21) leads to

$$\begin{aligned} I(\mathbf{x}) = \mathrm{Re}(\int \frac{\omega^6}{c^2(\mathbf{x})} \iint \iint \iint f_s^*(\omega) G^*(\mathbf{s},\mathbf{x},\omega) \exp(+i\omega \mathbf{p}_s \cdot (\mathbf{s} - \mathbf{x}_h)) \\ \times G^*(\mathbf{x},\mathbf{r},\omega) \exp(+i\omega \mathbf{p}_r \cdot (\mathbf{r} - \mathbf{x}_h)) P(\mathbf{p}_s,\mathbf{p}_r,\omega) \\ \times \exp(+i\omega(\mathbf{p}_s + \mathbf{p}_r) \cdot (\mathbf{x}_h - \mathbf{x}_{ref})) d\mathbf{p}_s d\mathbf{p}_r d\mathbf{s} d\mathbf{r} d\omega). \end{aligned} \tag{3.22}$$

Using the reciprocity property of Green's function, $G(\mathbf{r},\mathbf{x},\omega)$ is equal to $G(\mathbf{x},\mathbf{r},\omega)$. The Green's functions for both sources and receivers are slant stacked to obtain source and receiver plane wave Green's functions:

$$G^*(\mathbf{p}_s,\mathbf{x},\omega) = \int G^*(\mathbf{s},\mathbf{x},\omega) \exp(+i\omega \mathbf{p}_s \cdot (\mathbf{s} - \mathbf{x}_h)) d\mathbf{s}, \tag{3.23}$$

$$G^*(\mathbf{p}_r,\mathbf{x},\omega) = \int G^*(\mathbf{r},\mathbf{x},\omega) \exp(+i\omega \mathbf{p}_r \cdot (\mathbf{r} - \mathbf{x}_h)) d\mathbf{r}, \tag{3.24}$$

where $G(\mathbf{p}_s,\mathbf{x},\omega)$ and $G(\mathbf{p}_r,\mathbf{x},\omega)$ are source and receiver plane wave Green's functions, respectively. Substituting equations (3.23) and (3.24) into equation (3.22), we obtain the frequency domain DPW RTM imaging condition for the Ps-Pr DPW data as

$$I(\mathbf{x}) = \mathrm{Re}(\int \frac{\omega^6}{c^2(\mathbf{x})} \iint f_s^*(\omega) G^*(\mathbf{p}_s,\mathbf{x},\omega) G^*(\mathbf{p}_r,\mathbf{x},\omega) \times P(\mathbf{p}_s,\mathbf{p}_r,\omega) \exp(+i\omega(\mathbf{p}_s+\mathbf{p}_r)\cdot(\mathbf{x}_h-\mathbf{x}_{ref}))d\mathbf{p}_s d\mathbf{p}_r d\omega). \tag{3.25}$$

Subsisting the relationships between the Ps-Pr DPW data and the Ps-Po DPW data into equation (3.25), the imaging condition for the Ps-Po DPW data becomes

$$I(\mathbf{x}) = \mathrm{Re}(\int \frac{\omega^6}{c^2(\mathbf{x})} \iint f_s^*(\omega) G^*(\mathbf{p}_s-\mathbf{p}_o,\mathbf{x},\omega) G^*(\mathbf{p}_o,\mathbf{x},\omega) \times P(\mathbf{p}_s,\mathbf{p}_o,\omega) \exp(+i\omega\mathbf{p}_s\cdot(\mathbf{x}_h-\mathbf{x}_{ref}))d\mathbf{p}_s d\mathbf{p}_o d\omega). \tag{3.26}$$

where $G(\mathbf{p}_o,\mathbf{x},\omega)$ is the offset plane wave Green's function. Equations (3.25) and (3.26) are frequency domain DPW RTM imaging conditions for the Ps-Pr DPW data and the Ps-Po DPW data, respectively. They are analogous to equations 35 and 39 in Stoffa et al. (2006), while here, plane wave Green's functions replace their approximations that only included plane wave times.

Equations (3.14) and (3.25) are equivalent except for the amplitude filtering term. The source plane wave field in equation (3.14) can be viewed as the multiplication of source signature and a plane wave Green's function in equation (3.25). The receiver plane wave field in equation (3.14) can be viewed as the multiplication of a plane Green's

function and the complex conjugate of the DPW data in equation (3.24). The same analysis can be conducted for equations (3.15) and (3.26). Ignoring the amplitude filtering terms, equations (3.14) and (3.25) are equivalent, and so as equations (3.15) and (3.26). The proof of the equivalence is shown in Appendix A.

The proposed imaging condition for the DPW data is in a similar form to that for shot gathers. To implement the imaging condition for shot gathers, equation (3.17), one need to calculate Green's function for each source to imaging points, as well as Green's function from imaging points to each receiver. In the proposed imaging condition, plane wave Green's functions for $\mathbf{p}_s$ and $\mathbf{p}_r$ or $\mathbf{p}_o$ for each imaging point need to be computed. The plane wave Green's functions do not depend on source and receiver locations. Once a plane wave Green's function has been calculated, it can be reused for plane wave components with the same ray-parameter. Therefore, only a limited number of plane wave Green's functions need to be computed for migrating an entire DPW dataset. Reducing the computation for Green's function greatly increases the migration efficiency.

Removing the filter $\frac{\omega^6}{c^2(\mathbf{x})}$ and the integrals in equations (3.25) and (3.26), we have

$$\begin{aligned} I(\mathbf{x},\mathbf{p}_s,\mathbf{p}_r,\omega) = \mathrm{Re}(&f_s^*(\omega)G^*(\mathbf{p}_s,\mathbf{x},\omega)G^*(\mathbf{p}_r,\mathbf{x},\omega) \\ &\times P(\mathbf{p}_s,\mathbf{p}_r,\omega)\exp(+i\omega(\mathbf{p}_s+\mathbf{p}_r)\cdot(\mathbf{x}_h-\mathbf{x}_{ref}))), \end{aligned} \tag{3.27}$$

and

$$\begin{aligned} I(\mathbf{x},\mathbf{p}_s,\mathbf{p}_o,\omega) = \mathrm{Re}(&f_s^*(\omega)G^*(\mathbf{p}_s-\mathbf{p}_o,\mathbf{x},\omega)G^*(\mathbf{p}_o,\mathbf{x},\omega) \\ &\times P(\mathbf{p}_s,\mathbf{p}_o,\omega)\exp(+i\omega\mathbf{p}_s\cdot(\mathbf{x}_h-\mathbf{x}_{ref}))), \end{aligned} \tag{3.28}$$

Equation (3.27) or (3.28) defines the basic building block for the frequency domain DPW RTM. Each plane wave component and frequency can be migrated separately and parallelly. Images can be obtained using different combination of plane wave components and frequencies. Images $I(\mathbf{x},\mathbf{p}_s,\mathbf{p}_r,\omega)$ and $I(\mathbf{x},\mathbf{p}_s,\mathbf{p}_o,\omega)$ are indexed by $\mathbf{p}_r$ an $\mathbf{p}_o$ respectively. Once all desired plane wave components are migrated, the ray-parameter common imaging gathers (CIGs) can be easily obtained by lining images indexed by $\mathbf{p}_r$ or $\mathbf{p}_o$. The desired images can be achieved by stacking CIGs for each image point. I will demonstrate the method using two synthetic examples.

3.5. COMPUTING FREQUENCY DOMAIN PLANE WAVE GREEN'S FUNCTIONS

Frequency domain plane wave Green's functions need to be constructed to implement the proposed imaging condition. In this study, I first perform time domain wave field extrapolation to calculate time domain plane wave fields. A discrete Fourier transform (DFT) is performed to obtain the plane wave frequency responses:

$$u(\mathbf{p},\mathbf{x},\omega) = \Delta\tau \sum_{\tau=0}^{\tau_{\max}} U(\mathbf{p},\mathbf{x},\tau) e^{-i\omega\tau}, \tag{3.29}$$

where $\Delta\tau$ is the vertical delay time sampling rate, and $u(\mathbf{p},\mathbf{x},\omega)$ is the frequency response given a plane wave with ray-parameter $\mathbf{p}$. Similar procedures were introduced to obtain wave field frequency responses for point sources (Furse, 2000; Nihei and Li, 2007). Frequency domain plane wave Green's function can be extracted by performing a simple division to $u(\mathbf{p},\mathbf{x},\omega)$ with source frequency signature $f_s(\omega)$. The following expression is used to ensure the stability of the process:

$$G(\mathbf{p},\mathbf{x},\omega) \approx u(\mathbf{p},\mathbf{x},\omega) f_s^*(\omega) / (f_s(\omega) f_s^*(\omega) + \varepsilon), \tag{3.30}$$

where $f_s^*(\omega)$ is the complex conjugate of the source, and ε is the small value to ensure the stability of the division. An example of a plane wave Green's function will be shown in the numerical tests.

Other options to construct frequency domain Green's functions is solving the linear system of the Helmholtz equation (Marfurt 1984; Operto et al., 2002; Hustedt et al., 2004) or using the rapid expansion method (REM) frequency response modeling method (Chu and Stoffa 2012).

3.6. FREQUENCY DOMAIN DPW RTM IN VTI MEDIA

The proposed method can be implemented in the region that includes anisotropy. The REM in VTI media proposed by Pestana et al. (2012) and the frequency domain finite difference method in tilted transversely isotropic (TTI) media (Operto et al., 2009) can be used to compute plane wave Green's function in VTI or TTI media, respectively.

In this chapter, I implement the frequency domain DPW RTM in VTI media. As in the previous case, I perform the time marching to compute the plane wavefields in anisotropic media. After obtaining the time domain plane wavefields, plane wave Green's functions are extracted. This procedure is described by equations (3.29) and (3.30). The time marching of plane wavefield in the VTI medium is implemented via the REM proposed by Pestana at el. (2012). The impulse responses in a homogenous VTI medium and migration results of Hess synthetic VTI model will be shown in the numerical tests section.

3.7. RELATIONSHIP BETWEEN VERTICAL DELAY TIMES

Figure 3.1 explains the reason for adding terms $\mathbf{p}_s \cdot (\mathbf{x}_h - \mathbf{x}_h) = 0$ and $\mathbf{p}_r \cdot (\mathbf{x}_h - \mathbf{x}_h) = 0$ into equation (3.20). As shown in Figure 3.1, we have a homogenous velocity model with *v*=1, such that the raypath length can represent the traveltime for a ray.

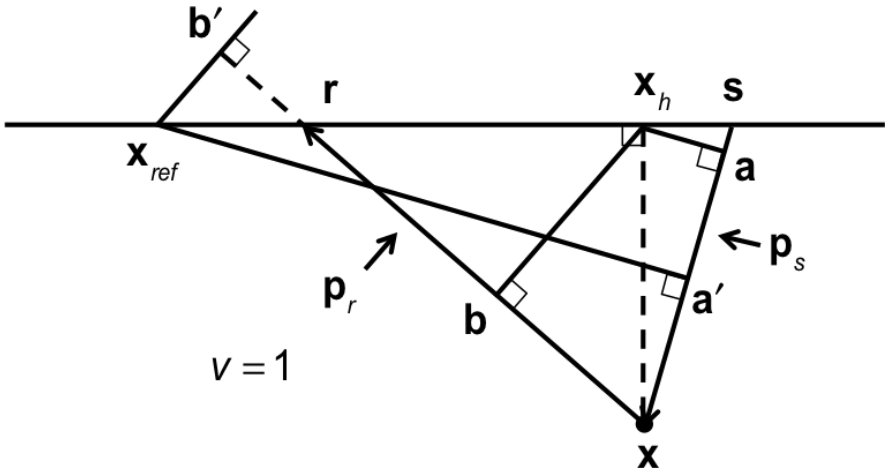

Figure 3.1. An illustration of a homogenous velocity model with raypath drawn. $\mathbf{s} = (s_x, s_y = 0, s_z = 0)$ is the source location, $\mathbf{r} = (r_x, r_y = 0, r_z = 0)$ is the receiver location, $\mathbf{x} = (x, y = 0, z)$ is the diffractor, $\mathbf{x}_h = (x_h, y_h = 0, z_h = 0)$ is the horizontal position of the diffractor, and $\mathbf{x}_{ref} = (x_{ref}, y_{ref} = 0, z_{ref} = 0)$ is the reference point for the DPW transform. $\mathbf{p}_s = (p_{sx}, 0)$ and $\mathbf{p}_r = (p_{rx}, 0)$ are ray- parameters for incident ray and received ray, respectively. $\mathbf{a}$, $\mathbf{a}'$, $\mathbf{b}$ and $\mathbf{b}'$ have geometrical meanings as shown in the figure.

As shown in Figure 3.1, a ray initiated from **s** with ray-parameter $\mathbf{p}_s$ hits the diffractor **x**. A scattered ray with ray-parameter $\mathbf{p}_r$ and received by **r** is selected to form

a full raypath from the source to the receiver. Because the ray traveltime can be represented by the raypath, for the ray initiated from the source, vertical delay time $\tau_{\mathbf{x}_h}(\mathbf{p}_s,\mathbf{x})$ and $\tau_{\mathbf{x}_{ref}}(\mathbf{p}_s,\mathbf{x})$ can be written as

$$\tau_{\mathbf{x}_h}(\mathbf{p}_s,\mathbf{x}) = t_{\mathbf{sx}}(\mathbf{s},\mathbf{x}) - \mathbf{p}_s \cdot (\mathbf{s} - \mathbf{x}_h) = \mathbf{sx} - \mathbf{sa} = \mathbf{ax}, \tag{3.31}$$

$$\tau_{\mathbf{x}_{ref}}(\mathbf{p}_s,\mathbf{x}) = t_{\mathbf{sx}}(\mathbf{s},\mathbf{x}) - \mathbf{p}_s \cdot (\mathbf{s} - \mathbf{x}_{ref}) = \mathbf{sx} - \mathbf{sa}' = \mathbf{a}'\mathbf{x}, \tag{3.32}$$

where $t_{\mathbf{sx}}(\mathbf{s},\mathbf{x})$ is the traveltime from $\mathbf{s}$ to $\mathbf{x}$, $\mathbf{x}_h$ is the horizontal position of $\mathbf{x}$, $\tau_{\mathbf{x}_h}(\mathbf{p}_s,\mathbf{x})$ is the plane wave vertical delay time with $\mathbf{x}_h$ as the reference point, and $\tau_{\mathbf{x}_{ref}}(\mathbf{p}_s,\mathbf{x})$ is the plane wave vertical delay time with $\mathbf{x}_{ref}$ as the reference point. According to Figure 3.1, $\tau_{\mathbf{x}_{ref}}(\mathbf{p}_s,\mathbf{x})$ can also be represented by

$$\begin{aligned} \tau_{\mathbf{x}_{ref}}(\mathbf{p}_s,\mathbf{x}) &= \mathbf{a}'\mathbf{x} \\ &= \mathbf{sx} - \mathbf{sa}' \\ &= \mathbf{sx} - \mathbf{sa} - \mathbf{aa}'. \end{aligned} \tag{3.33}$$

Substituting $\mathbf{sx} = t_{\mathbf{sx}}(\mathbf{s},\mathbf{x})$, $\mathbf{sa} = \mathbf{p}_s \cdot (\mathbf{s} - \mathbf{x}_h)$ and $\mathbf{aa}' = \mathbf{p}_s \cdot (\mathbf{x}_h - \mathbf{x}_{ref})$ into equation (3.33), we have

$$\tau_{\mathbf{x}_{ref}}(\mathbf{p}_s,\mathbf{x}) = t_{\mathbf{sx}}(\mathbf{s},\mathbf{x}) - \mathbf{p}_s \cdot (\mathbf{s} - \mathbf{x}_h) - \mathbf{p}_s \cdot (\mathbf{x}_h - \mathbf{x}_{ref}). \tag{3.34}$$

Rearranging terms in equation (3.34), we obtain

$$\tau_{\mathbf{x}_{ref}}(\mathbf{p}_s,\mathbf{x}) = t_{\mathbf{sx}}(\mathbf{s},\mathbf{x}) - \mathbf{p}_s \cdot (\mathbf{s} - \mathbf{x}_{ref}) + \mathbf{p}_s \cdot (\mathbf{x}_h - \mathbf{x}_h), \tag{3.35}$$

where $\mathbf{p}_s \cdot (\mathbf{x}_h - \mathbf{x}_h) = 0$ is the term added into equation (3.20). This zero term is an important factor for getting vertical delay time of plane wave with respect to the horizontal position of the imaging point.

Substituting $t_{\mathbf{sx}}(\mathbf{s},\mathbf{x}) - \mathbf{p}_s \cdot (\mathbf{s} - \mathbf{x}_h) = \tau_{\mathbf{x}_h}(\mathbf{p}_s,\mathbf{x})$ into equation (3.34), equation (3.34) becomes

$$\tau_{\mathbf{x}_{ref}}(\mathbf{p}_s,\mathbf{x}) = \tau_{\mathbf{x}_h}(\mathbf{p}_s,\mathbf{x}) - \mathbf{p}_s \cdot (\mathbf{x}_h - \mathbf{x}_{ref}). \tag{3.36}$$

Equation (3.36) suggests that the vertical delay time with respect to $\mathbf{x}_{ref}$ is the summation of vertical delay time with respect to $\mathbf{x}_h$ and a time correction term $-\mathbf{p}_s \cdot (\mathbf{x}_h - \mathbf{x}_{ref})$.

Following the above developments, for the ray received by receiver with ray-parameter $\mathbf{p}_r$, we obtain

$$\tau_{\mathbf{x}_{ref}}(\mathbf{p}_r,\mathbf{x}) = t_{\mathbf{rx}}(\mathbf{r},\mathbf{x}) - \mathbf{p}_r \cdot (\mathbf{r} - \mathbf{x}_{ref}) + \mathbf{p}_r \cdot (\mathbf{x}_h - \mathbf{x}_h), \tag{3.37}$$

where $\mathbf{p}_r \cdot (\mathbf{x}_h - \mathbf{x}_h) = 0$ is the extra term.

The above analysis also applies to 3D complex velocity models. This analysis is performed in the time domain. In the frequency domain, terms $\mathbf{p}_s \cdot (\mathbf{x}_h - \mathbf{x}_h) = 0$ and $\mathbf{p}_r \cdot (\mathbf{x}_h - \mathbf{x}_h) = 0$ are added into the phase shift term in equation (3.20).

The above derivations are in 3D, while 2D examples will be shown in the next section.

3.8. NUMERICAL TESTS

3.8.1. Frequency domain DPW RTM example in isotropic media

3.8.1.1. Three-layer model

The simple three-layer velocity model shown in Figure 3.2 was used to demonstrate the DPW transform and the proposed DPW imaging condition. The model contained 200 horizontal grid points and 100 vertical grid points with a grid spacing of 0.02 km in both x and z directions. The seismic dataset contained 200 shot gathers, each of which had 200 receivers. The DPW transform was performed using equation (3.26) with the slant stacking reference point at the middle of the model (i.e., $\mathbf{x}_{ref}$ = 2 km). There were 241 $\mathbf{p}_s$ and 241 $\mathbf{p}_o$ plane waves recovered from the original shot gathers, both plane waves ranged from -0.6 to +0.6 s/km. The corresponding DPW dataset contained $241 \times 241 = 58081$ traces.

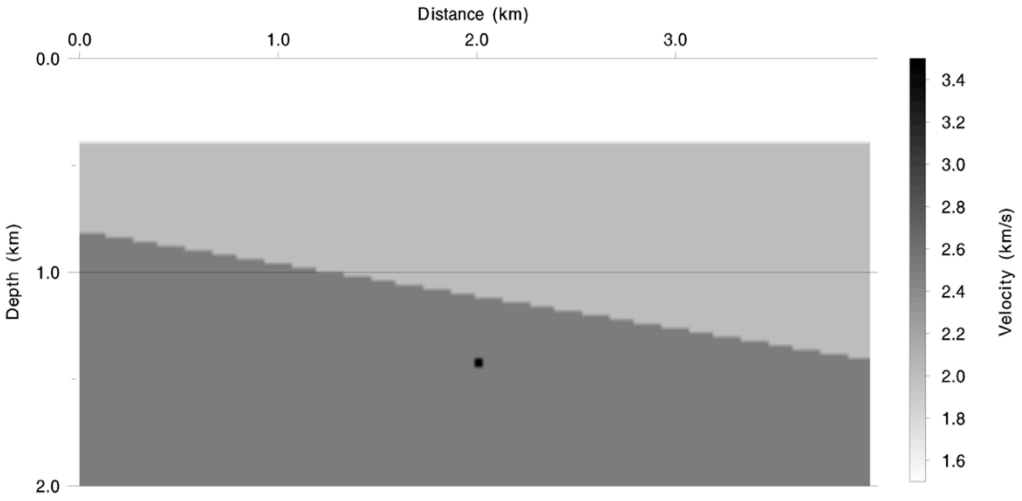

Figure 3.2. A simple velocity model used to demonstrate the DPW transform and the DPW imaging. The model was designed to have one flat interface, one dipping interface and a diffractor.

Figure 3.3 shows three constant $\mathbf{p}_o$ sections. In each of the three panels, there are two localized events recovered from the reflections from two different interfaces. There is also a hyperbolic event recovered from the diffraction energy. After performing DPW transform, plane waves with different incident angles at the surface were separated. Migration can be performed for selected $\mathbf{p}_s$ in a constant $\mathbf{p}_o$ section to imaging interfaces with given dips.

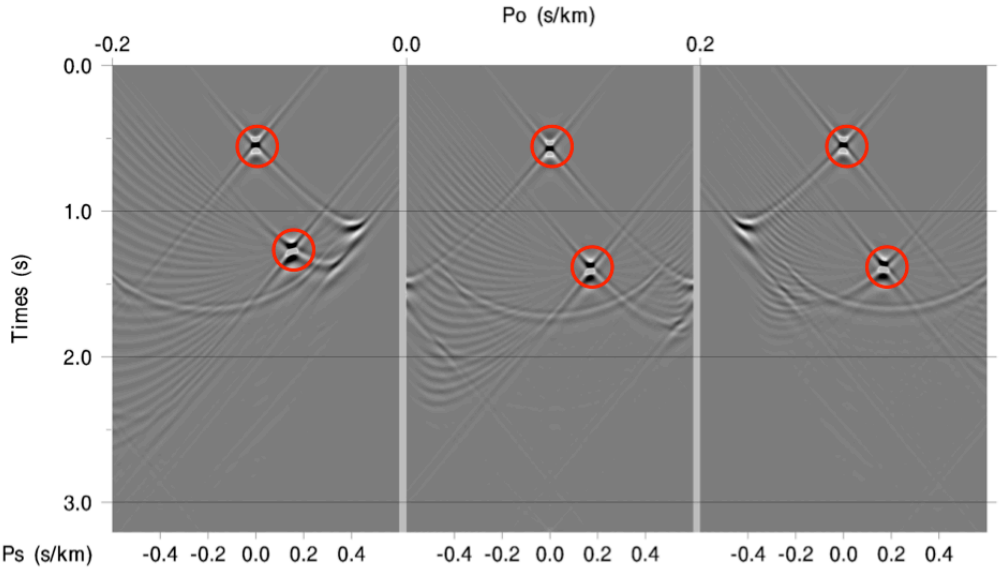

Figure 3.3. The constant $\mathbf{p}_o$ sections from the Ps-Po DPW dataset for the simple velocity model. Circles mark the two localized events. For all sections, $\mathbf{p}_s$ is from -0.6 to + 0.6 s/km. $\mathbf{p}_o$ = -0.2, 0.0 and + 0.2 s/km for each panel from left to right, respectively.

Figure 3.4 shows the opposite case of Figure 3.3, where $\mathbf{p}_s$ is constant for each panel with $\mathbf{p}_o$ varying. Each panel is similar to the conventional $\tau - \mathbf{p}$ transform. Performing migration for selected range of $\mathbf{p}_o$ in a constant $\mathbf{p}_s$ section can migrate the energy slant stacked into a $\mathbf{p}_s$ plane wave and achieve ray-parameter CIGs.

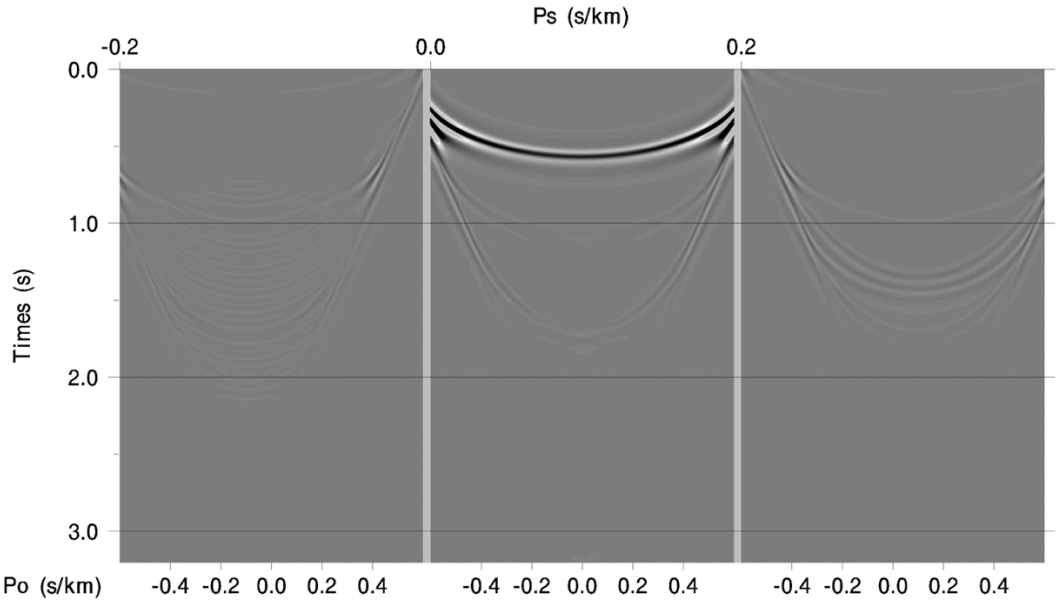

Figure 3.4. The constant $\mathbf{p}_s$ sections from the Ps-Po for the simple velocity model. For each panel from left to right, $\mathbf{p}_s$ = -0.2, 0.0 and + 0.2 s/km with all $\mathbf{p}_o$ plane waves ranging from -0.6 to + 0.6 s/km.

Frequency domain plane wave Green's functions are required to migrate the DPW dataset. Figure 3.5 shows a frequency domain plane wave Green's function at 11.25 Hz. The ray-parameter of the plane wave Green's function is $\mathbf{p}$ = -0.3 s/km.

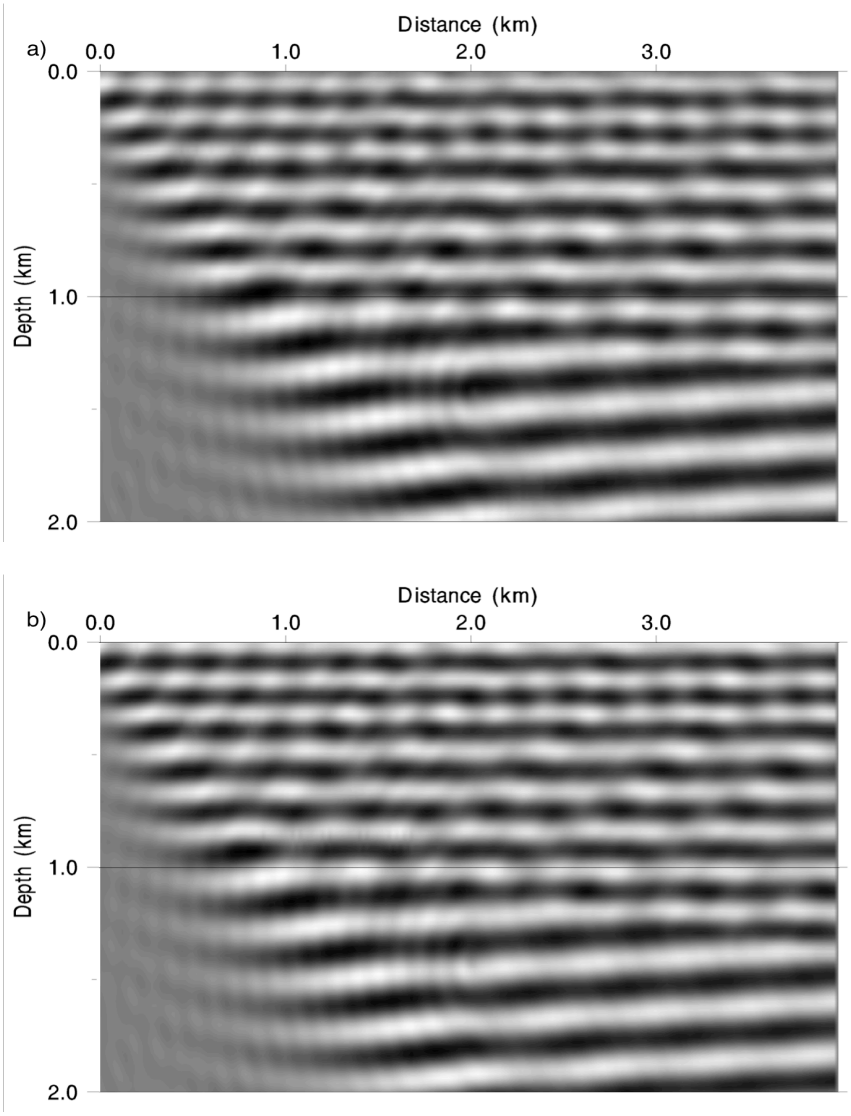

Figure 3.5. a) The real part of a frequency domain plane wave Green's function at 11. 25 Hz with **p** = -0.3 s/km. b) The imaginary part of the same frequency domain plane wave Green's function.

The time domain DPW dataset was transformed into frequency domain to perform the migration using equation (3.26). For the DPW dataset, 65 frequencies ranging from 5 to 25 Hz were used for migration. To obtain a desired subsurface image,

different combinations of the plane waves were migrated. Interfaces with different dips can be imaged independently for the entire velocity model by migrating a given range of plane wave components.

Migration results using selected ranges of the DPW dataset are shown in Figure 3.6, 3.7, 3.8 and 3.9. The Laplacian filter was applied to the images to suppress back-scattering artifacts. Figure 3.6 shows the image obtained by migrating 5 $\mathbf{p}_s$ plane waves ranging from -0.01 to +0.01 s/km and 31 $\mathbf{p}_o$ plane waves ranging from 0.0 to +0.3 s/km. The horizontal interface was well imaged, and some diffraction energy was migrated to build the image of the diffractor. The diffractor, which is marked by a black arrow, was poorly imaged due to the limited aperture of $\mathbf{p}_s$ plane waves used for migration. Figure 3.7 shows the migration result where $\mathbf{p}_o$ used for migration had same ranges as in Figure 3.6, but $\mathbf{p}_s$ ranged from +0.17 to +0.19 s/km. The dipping interface was recovered. However, the diffractor was again imaged with low resolution. The aperture for $\mathbf{p}_s$ was increased to include all of the 241 $\mathbf{p}_s$ plane waves for migration, so that the resolution of the diffractor can be enhanced. The corresponding image and ray-parameter CIGs are shown in Figure 3.8 and 3.9, respectively. The diffractor and the interfaces were well recovered. Most of the horizons in Figure 3.9 are flat suggesting that the correct velocity was used for migration.

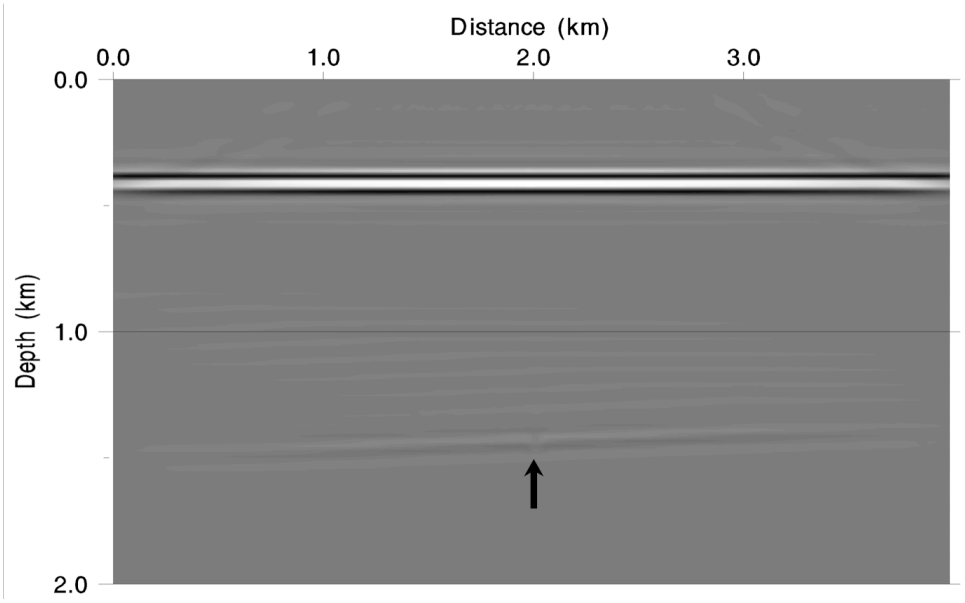

Figure 3.6. The image obtained by migrating 31 $\mathbf{p}_o$ plane waves ranging from 0.0 to +0.3 s/km with a 0.01 s/km interval and 5 $\mathbf{p}_s$ plane waves ranging from -0.01 to +0.01 s/km with a 0.005 s/km interval.

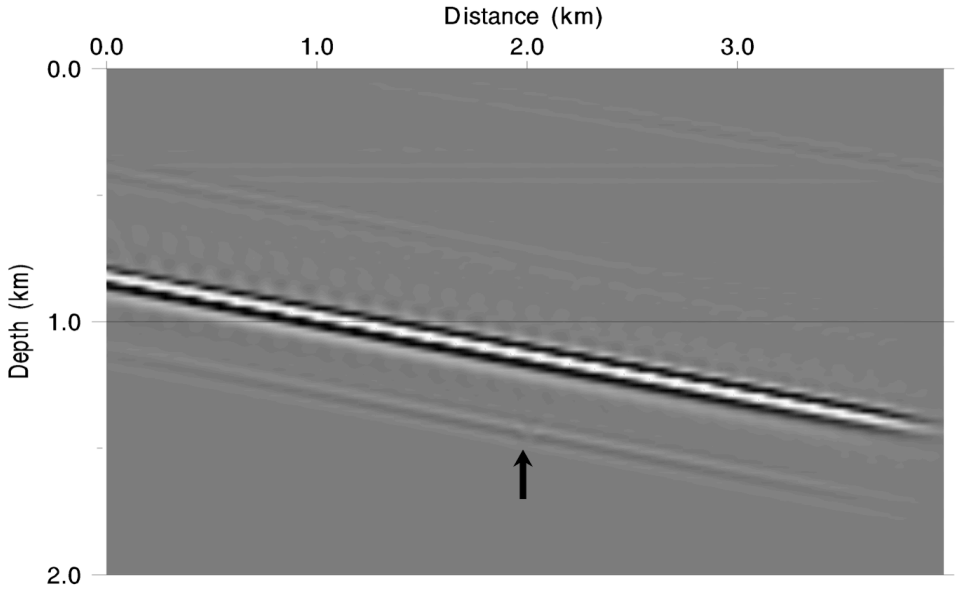

Figure 3.7. The image obtained by migrating 31 $\mathbf{p}_o$ plane waves ranging from 0.0 to +0.3 s/km and 5 $\mathbf{p}_s$ plane waves ranging from +0.17 to +0.19 s/km. The diffractor is marked by the black arrow.

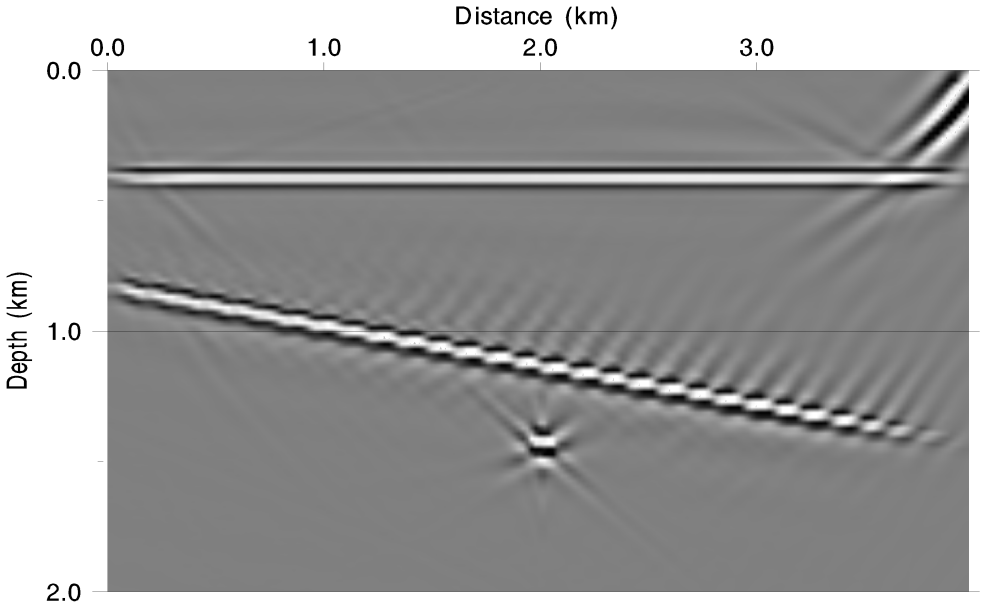

Figure 3.8. The final image obtained by migrating 31 $\mathbf{p}_o$ plane waves ranging from 0.0 to +0.3 s/km and all 241 $\mathbf{p}_s$ plane waves. The diffractor point was imaged, as well as the two interfaces.

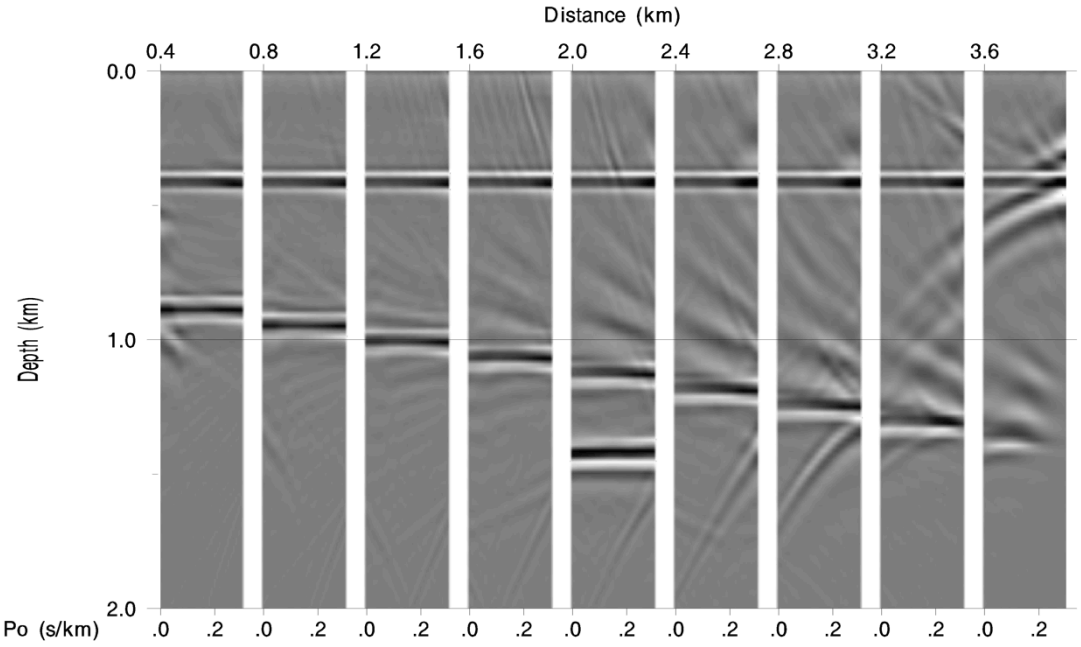

Figure 3.9. The ray-parameter CIGs for the simple velocity model with 20 horizontal points increment. Each shown horizontal position contains 31 $\mathbf{p}_o$ plane waves ranging from 0.0 to +0.3 s/km.

3.8.1.2. SEG/EAGE salt model

To demonstrate the effectiveness of the proposed method for a complex velocity model, I generated shot gathers for a 2D line (cf. Figure 3.10) extracted from the SEG/EAGE 3D salt model (Aminzadeh et al., 1997). The model had 675 horizontal grid points and 210 vertical grid points with a grid spacing of 0.02 km in both x and z directions. The seismic acquisition proceeded from left (x = 0.0 km) to right (x = 13.48 km) simulating a land survey with receivers located on both sides of the source except for the first and last shot. The number of recording traces per shot was 675, and 675 shots were recorded with a 0.02 km shot spacing.

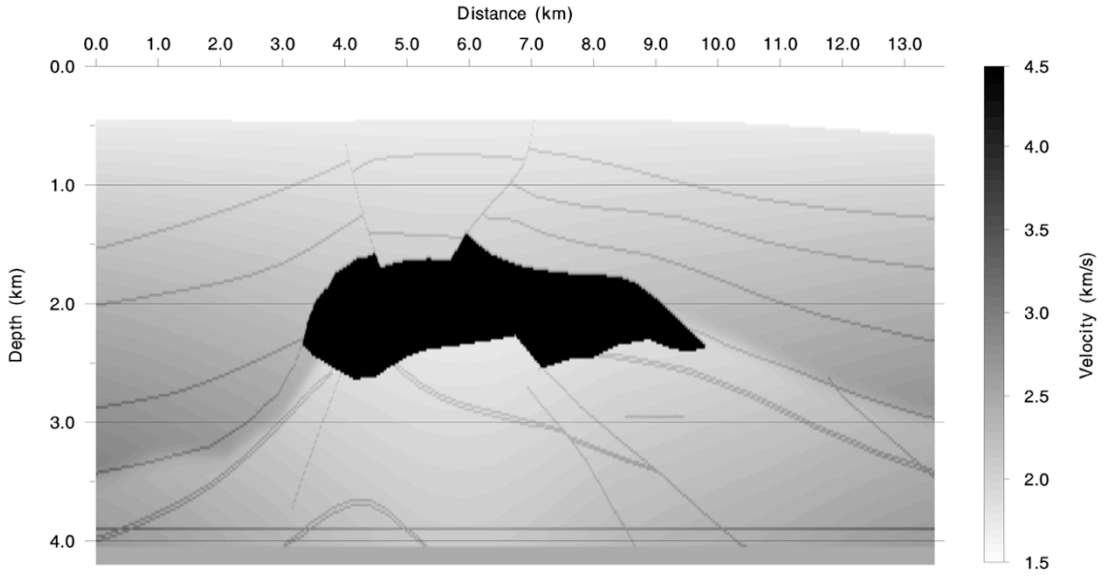

Figure 3.10. The 2D line of SEG/EAGE salt model used for DPW migration.

The DPW transform was carried out in the shot-offset coordinates with $\mathbf{x}_{ref}$ = 6.74 km. The shot records were transformed into 241 plane wave components for each set of plane waves ($\mathbf{p}_s$ and $\mathbf{p}_o$ plane waves). Both $\mathbf{p}_s$ and $\mathbf{p}_o$ were equally spaced from -0.6 to +0.6 s/km. The corresponding DPW domain contained $241 \times 241 = 58081$ traces.

The frequency domain DPW dataset was migrated using equation (3.26) with 101 frequencies, which were equally spaced from 5 to 25 Hz. Two selected subsets of DPW dataset were migrated to image specific subsurface structures. The Laplacian filter was applied to the images to suppress the back-scattering artifacts. Figure 3.11 shows two subsets of the Ps-Po DPW dataset used for migration. In Figure 3.11a), there are 41 $\mathbf{p}_s$ plane waves ranging from -0.1 to +0.1 s/km; in Figure 3.11b), there are 201 $\mathbf{p}_s$ plane waves ranging from -0.5 to +0.5 s/km. Both subsets have 31 $\mathbf{p}_o$ plane waves ranging from 0.0 to +0.3 s/km. The image, shown in Figure 3.12, was obtained by migrating the

DPW subset shown in Figure 3.11a). Parts of the corresponding CIGs are shown in Figure 3.13. Because a small part of the $\mathbf{p}_s$ plane waves around 0.0 s/km was used for migration, only nearly horizontal reflectors can be recovered. Images of salt flanks and other steep interfaces were missing. Nevertheless, migrating a small range of $\mathbf{p}_s$ plane waves is very efficient and CIGs can be generated. Those CIGs can be used as guidance for determining velocity. Therefore, images and CIGs can be obtained rapidly as updated velocity model is available. When more accurate velocity model becomes determined, more $\mathbf{p}_s$ plane wave can be migrated to enhance image resolution. The procedure is beneficial for migration velocity analysis.

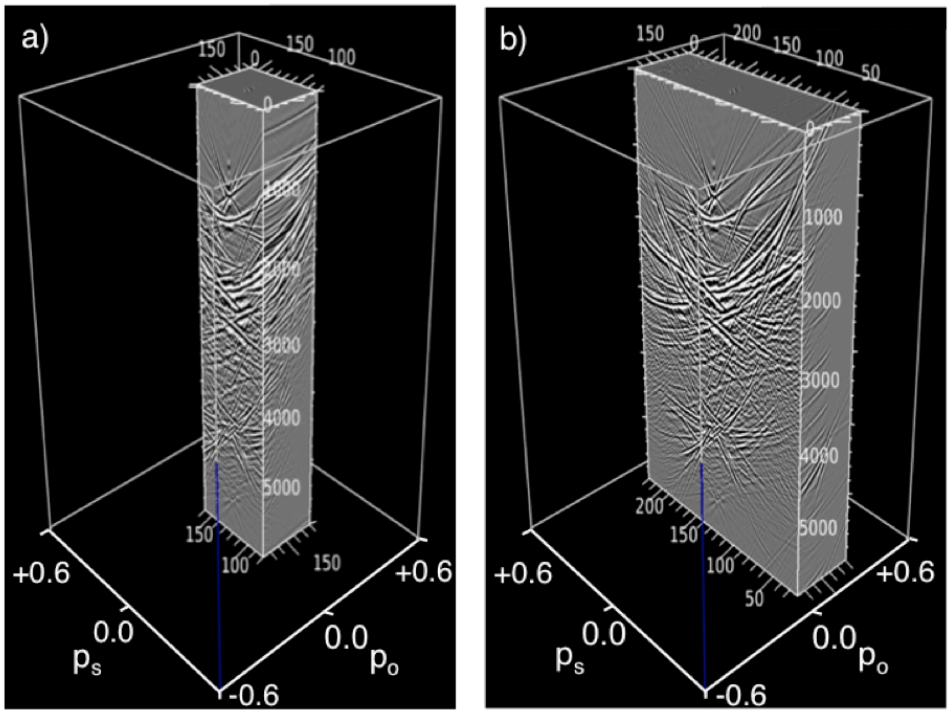

Figure 3.11. The selected DPW subsets for migration. a) 41 $\mathbf{p}_s$ plane wave components ranged -0.01 ~ +0.01 s/km were. b) 201 $\mathbf{p}_s$ plane wave components ranged -0.5 ~ +0.5 s/km. There are 31 $\mathbf{p}_o$ plane wave ranges from 0.0 to +0.3 s/km for the both subsets.

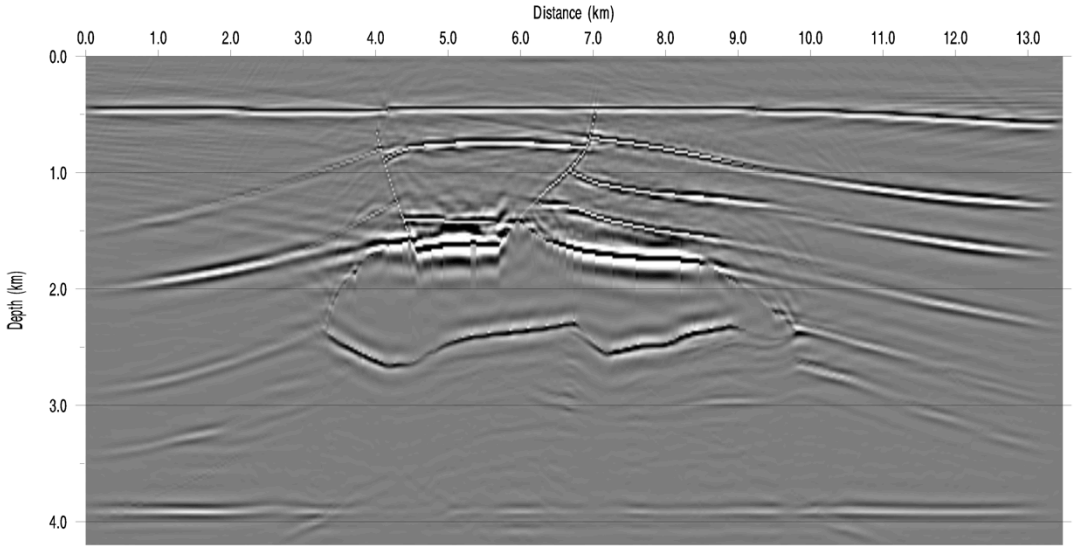

Figure 3.12. The image obtained by migrating 31 $\mathbf{p}_o$ plane waves equally spaced from 0.0 to +0.3 s/km and 41 $\mathbf{p}_s$ plane waves equally spaced from -0.1 to +0.1 s/km.

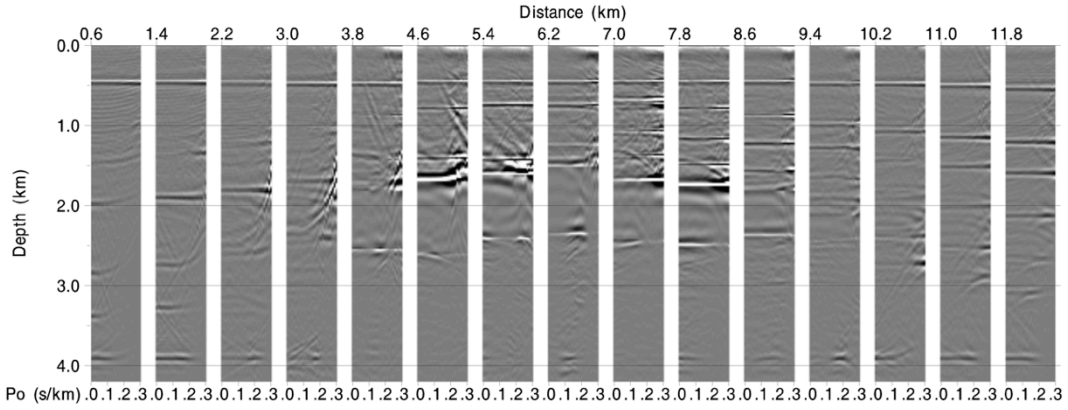

Figure 3.13. The CIGs for salt model with 40 horizontal points increment. Each shown horizontal position contains 31 $\mathbf{p}_o$ plane wave components ranging from 0.0 to +0.3 s/km. $\mathbf{p}_s$ aperture used for migration is from -0.1 to +0.1 s/km.

The image shown in Figure 3.14 is the obtained by migrating the DPW subset shown in Figure 3.11b). Because more $\mathbf{p}_s$ plane wave components were included into the migration, almost all the reflectors can be imaged resulting in the increased spatial-frequency resolution. Parts of its corresponding CIGs are shown in Figure 3.15. In Figure 3.14 and 3.15, $201 \times 31 = 6231$ traces were used for migration. However, only 261 plane wave Green's functions were constructed and used for migrating both $\mathbf{p}_s$ and $\mathbf{p}_o$ plane waves. It requires much less computation for Green's functions than that for conventional shot gathers RTM, which speeds up the migration process.

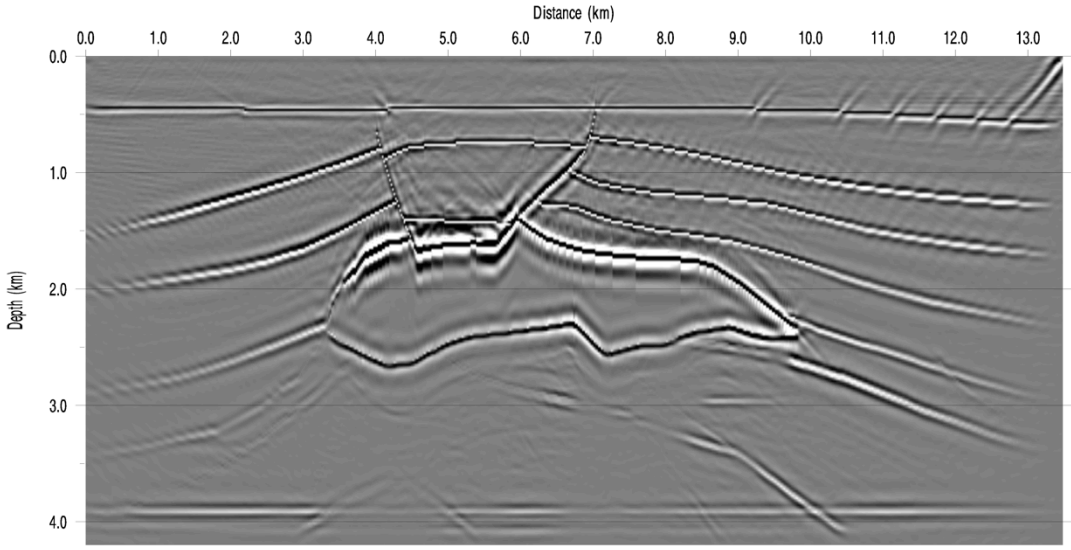

Figure 3.14. The image obtained by migrating 31 $\mathbf{p}_o$ plane waves and 201 $\mathbf{p}_s$ plane waves.

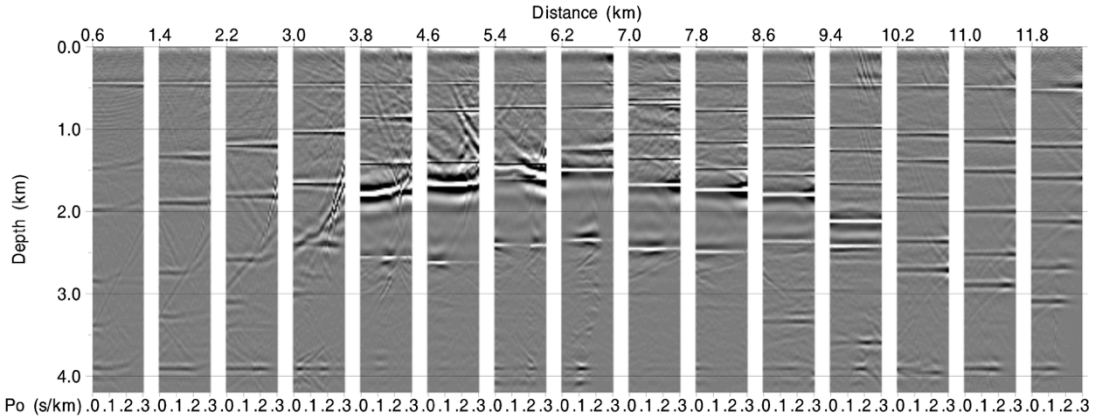

Figure 3.15. The CIGs for salt model with 40 horizontal points increment. Each shown horizontal position contains 31 $\mathbf{p}_o$ plane wave components ranging from 0.0 to +0.3 s/km. 201 $\mathbf{p}_s$ plane waves were used for migration. Most of the events in CIGs are flat suggesting that correct velocity was used for migration.

3.8.2. Frequency domain DPW RTM example in VTI media

3.8.2.1. Impulse response in a homogenous VTI medium

A simple homogenous VTI model with $v = 2$ km/s , $\varepsilon = 0.24$ and $\delta = 0.1$ was selected to test the impulse response of the frequency domain DPW RTM in a VTI media. There were 200 horizontal points and 100 vertical points with an interval of 0.02 km in both directions. The upper left corner is set to be the origin as shown in Figure 3.16. There was only one shot located at $\mathbf{s}(s_x = 3 \text{ km}, s_z = 0 \text{ km})$ with one band-limited impulse at the zero offset. The gather was then decomposed into a Ps-Pr DPW dataset with 101 $\mathbf{p}_s$ and 101 $\mathbf{p}_r$ plane waves. Each set of plane wave was equally spaced between -0.5 to 0.5 s/km. The shot gather was first migrated using the shot profile RTM in VTI media. The corresponding image is shown in Figure 3.16.

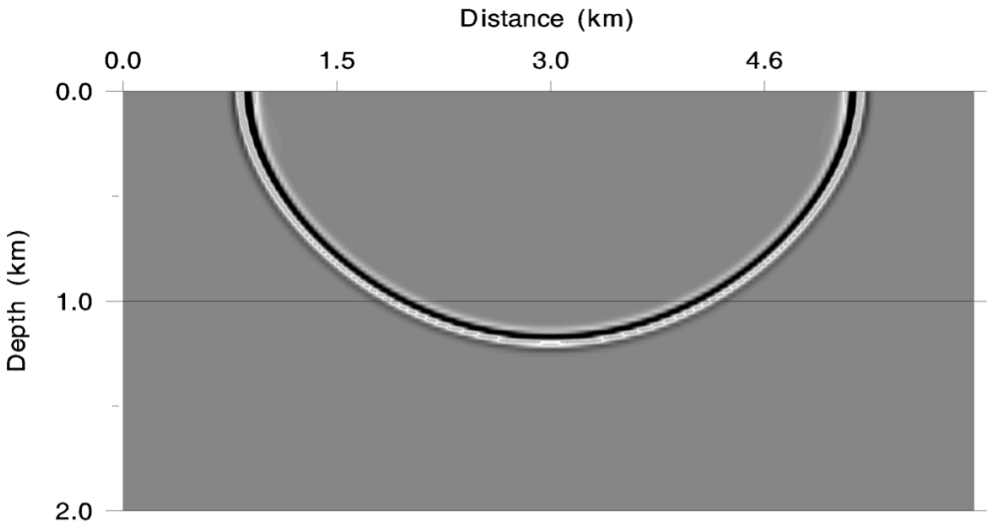

Figure 3.16. The impulse response of the shot profile RTM.

Then DPW RTM was performed with different parts of the DPW dataset using equation (3.25) to generate migration results shown in Figure 3.17 to 3.21. The subsets of the original DPW dataset used to generate those images are listed in Table 3.1.

	Figure 3.17	Figure 3.18	Figure 3.19	Figure 3.20	Figure 3.21
$\mathbf{p}_s$ range (s/km)	0.0	0.0	-0.4 ~ 0.0	-0.5 ~ 0.0	-0.5 ~ 0.5
$\mathbf{p}_r$ range (s/km)	0.0	-0.5 ~ 0.5	-0.5 ~ 0.5	-0.5 ~ 0.5	-0.5 ~ 0.5

Table 3.1. The subsets of the DPW dataset used to test the impulse response of the frequency domain DPW RTM.

The image shown in Figure 3.17 was generated by migrating only one DPW trace where $\mathbf{p}_s$ and $\mathbf{p}_r$ were both equal 0.0 s/km. A horizontal event was imaged, and it coincide with the horizontal portion of the image shown in Figure 3.16. Because only one trace was migrated, the obtained image only partially corresponded to the impulse

response of the shot profile RTM. The other parts of the image are regarded as migration artifacts pointed out by the arrows. The image shown in Figure 3.18 was generated by migrating a constant $\mathbf{p}_s$ profile where $\mathbf{p}_s$ = 0.0 s/km and $\mathbf{p}_r$ = -0.5 ~ 0.5 s/km. The image is a hyperbola that does not have the horizontal artifacts. The wings of the horizontal event shown in Figure 3.17 were canceled by including more $\mathbf{p}_r$ plane waves into the migration. However, the hyperbola is not kinematically equal to the impulse response of the shot profile RTM. The wings of the hyperbola, indicated by arrows in Figure 3.18, are considered as artifacts due to insufficient $\mathbf{p}_s$ sampling.

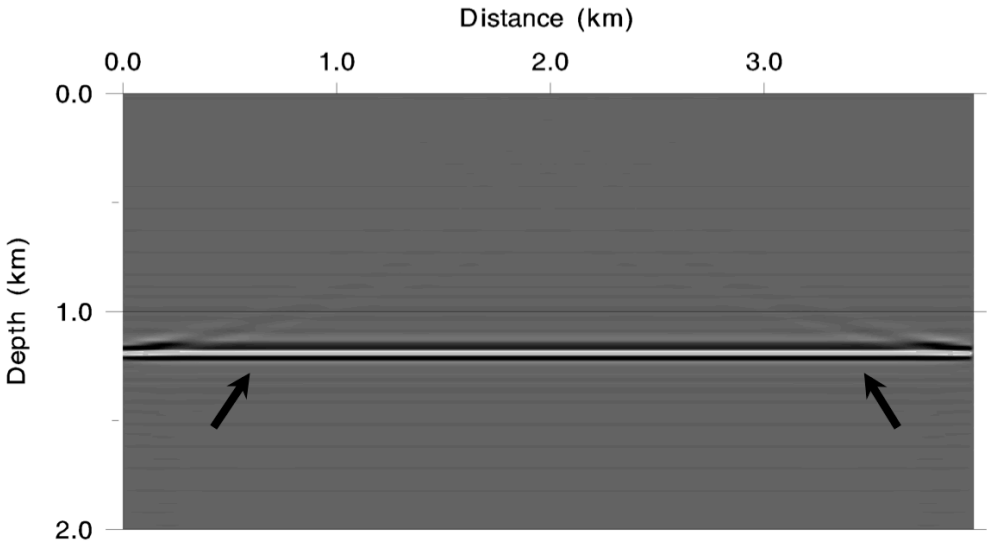

Figure 3.17. The impulse response obtained by migrating one trace from the DPW dataset where both $\mathbf{p}_s$ and $\mathbf{p}_r$ were equal to 0.0 s/km.

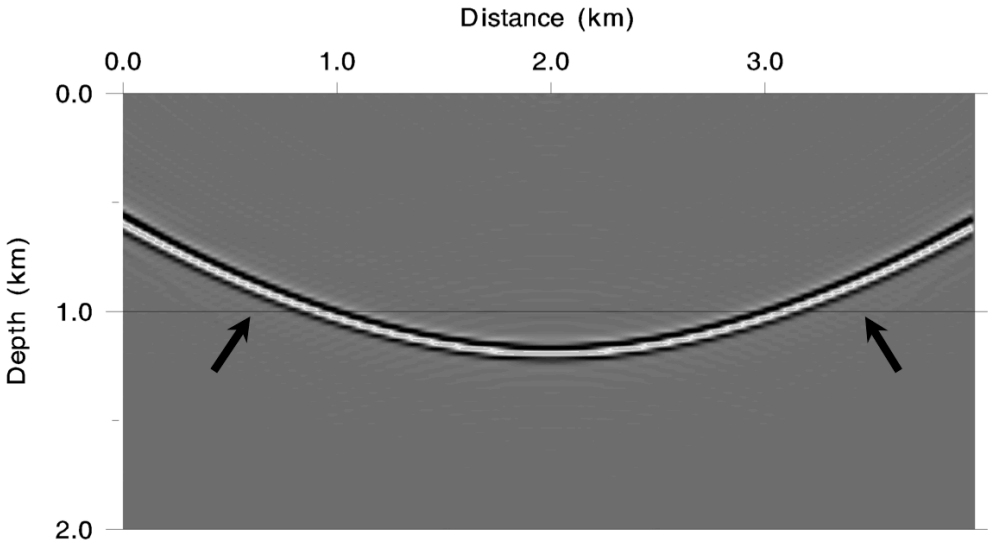

Figure 3.18. The impulse response obtained by migrating a constant $\mathbf{p}_s$ profile where $\mathbf{p}_s = 0.0$ s/km and 101 $\mathbf{p}_r$ = -0.5 ~ 0.5 s/km.

Including more $\mathbf{p}_s$ plane wave into the migration, I obtained images shown in Figure 3.19 and 3.20. 41 $\mathbf{p}_s$ plane waves ranging from 0.0 to 0.4 s/km and 51 $\mathbf{p}_s$ plane waves ranging from 0.0 to 0.5 s/km were used to generate the results shown in Figure 3.19 and 3.20, respectively. In both cases, $\mathbf{p}_r$ = -0.5 ~ 0.5 s/km were used for migration. Because more $\mathbf{p}_s$ plane waves were used for migration, the images were getting close to the impulse response shown in Figure 3.16. However, there are small amount of migration energy indicated by arrows cannot be cancelled during the migration. Figure 3.21 shows the migration result where all traces from the DPW dataset were migrated. The image has the same shape as the impulse response of shot profile RTM shown in Figure 3.16, suggesting that the proposed frequency domain DPW RTM is kinematically identical to the shot profile RTM in VTI media if all plane waves are migrated.

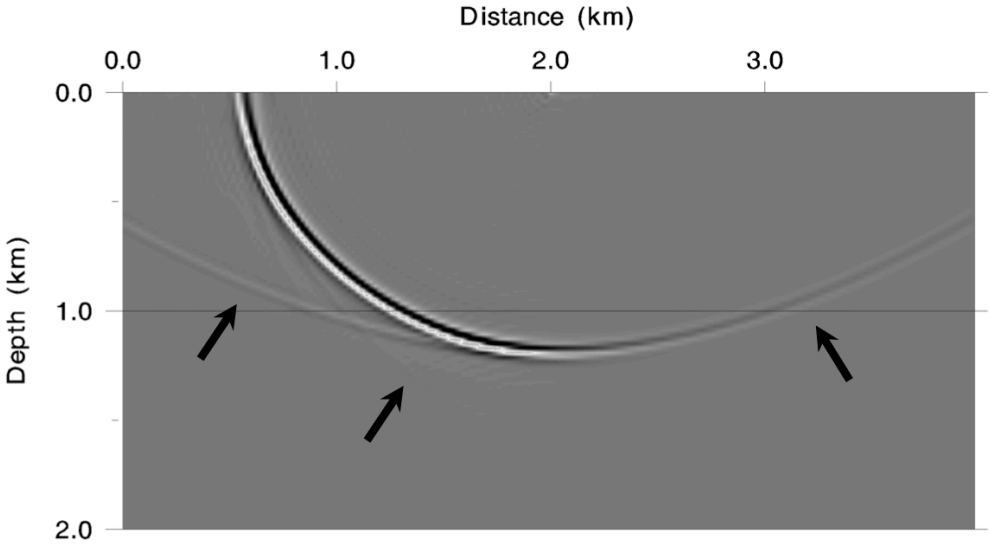

Figure 3.19. The impulse response obtained by migrating 41 $\mathbf{p}_s$ plane waves ranging from -0.4 to 0.0 s/km and 101 $\mathbf{p}_r$ plane waves ranging from -0.5 to 0.5 s/km.

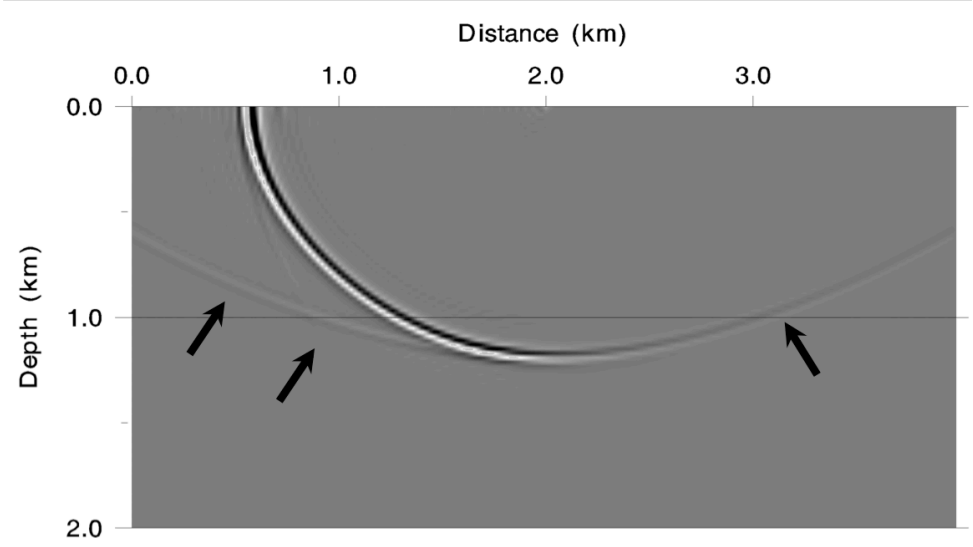

Figure 3.20. The impulse response obtained by migrating 51 $\mathbf{p}_s$ plane waves ranging from -0.5 to 0.0 s/km and 101 $\mathbf{p}_r$ plane waves ranging from -0.5 to 0.5 s/km.

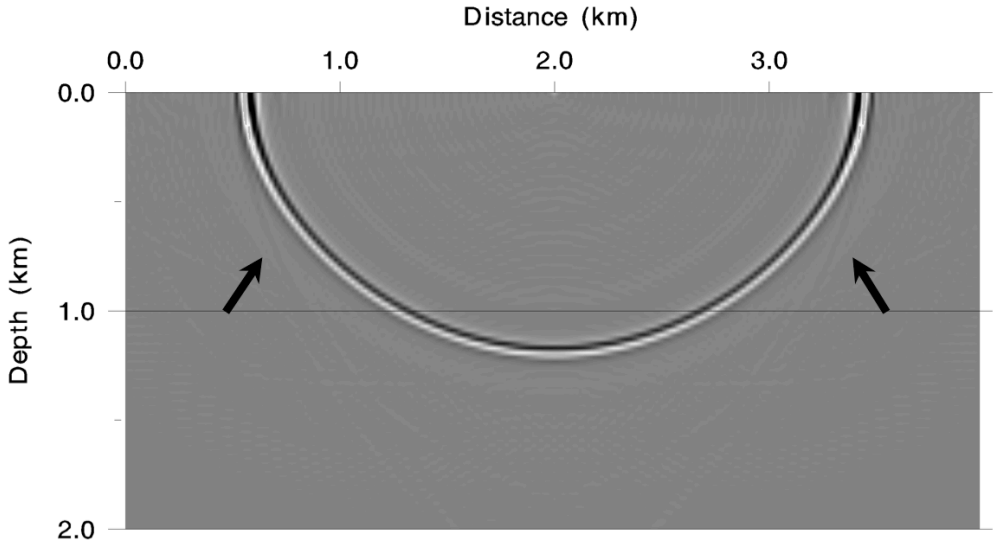

Figure 3.21. The impulse response obtained by migration all traces from the DPW dataset. Except for some small amount of artifacts indicated by black arrows, the image has the same shape with the impulse response of the shot profile RTM.

3.8.2.2. Hess VTI model

The Hess VTI model was chosen to demonstrate the proposed method in a complex VTI medium. The model and the shot gathers were from the Hess VTI synthetic datasets (Liu and Morton 2006). The models are shown in Figure 3.22, 3.23 and 3.24. The original Hess VTI model was subsampled into 730 horizontal grid points and 250 vertical grid points. Grid spacing for Δx and Δz were both 0.03048 km. The seismic acquisition proceeded from right to left, simulating a marine survey with receivers located on the right sides of each source. The DPW transform was carried out in the shot-receiver coordinates with the slant stacking reference point at the middle of the model ($\mathbf{x}_{ref}$ = 11.125 km). The original shot gathers were decomposed into 241 $\mathbf{p}_s$ plane

waves and 241 $\mathbf{p}_r$ plane waves with both ray-parameters ranging from -0.6 s/km to 0.6 s/km; the corresponding DPW dataset contains $241 \times 241 = 58081$ traces.

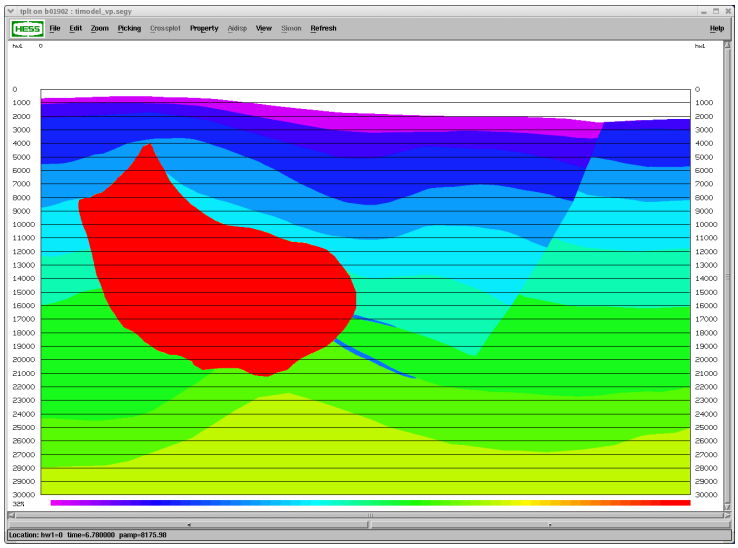

Figure 3.22. The velocity model (Provided courtesy of the HESS Corporation, Liu and Morton 2006).

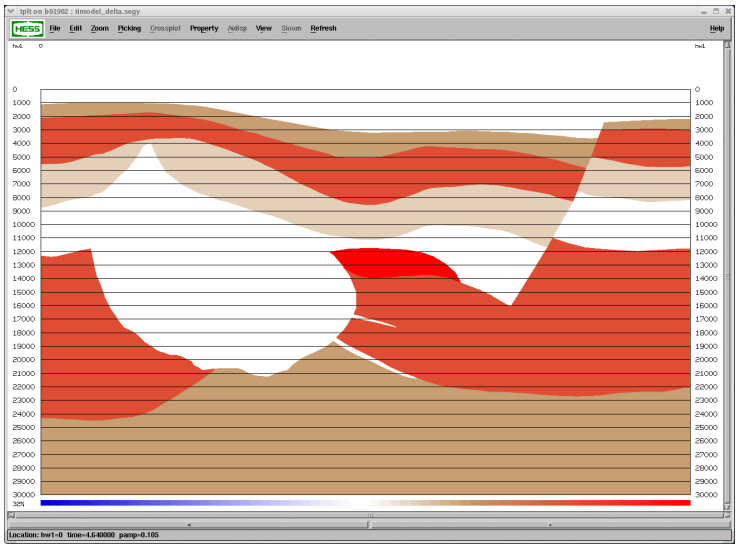

Figure 3.23. The δ model (Provided courtesy of the HESS Corporation, Liu and Morton 2006).

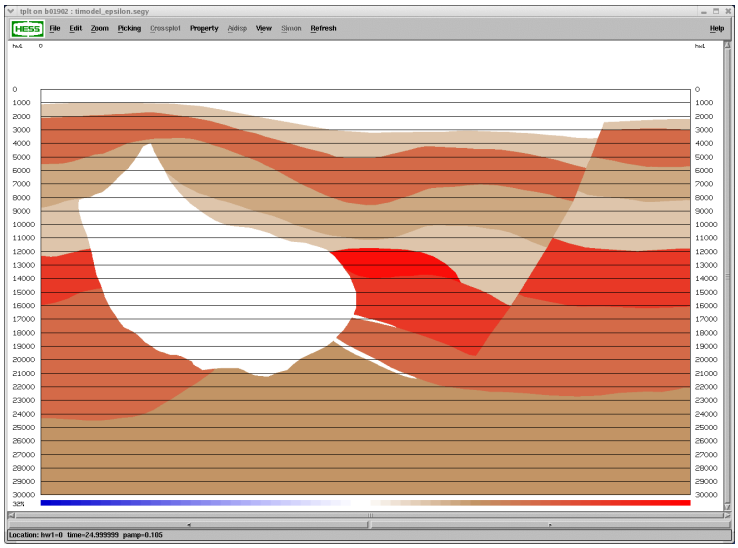

Figure 3.24. The ε model (Provided courtesy of the HESS Corporation, Liu and Morton 2006).

Three DPW subsets from the original DPW dataset were chosen to generate images shown in Figure 3.25, 3.26 and 3.27. The ranges of the three DPW subsets are shown in Table 3.2. In all three cases, the sampling intervals for $\mathbf{p}_s$ and $\mathbf{p}_r$ were 0.005 and 0.01 s/km, respectively. Equation (3.25) was used to perform the frequency domain DPW RTM.

	Figure 3.25	Figure 3.26	Figure 3.27
$\mathbf{p}_s$ range (s/km)	-0.2 ~ 0.2 s/km	-0.3 ~ 0.3 s/km	-0.6 ~ 0.6 s/km
$\mathbf{p}_r$ range (s/km)	-0.2 ~ 0.2 s/km	-0.3 ~ 0.3 s/km	-0.6 ~ 0.6 s/km

Table 3.2. The subsets from the original DPW dataset used to image the Hess VTI model.

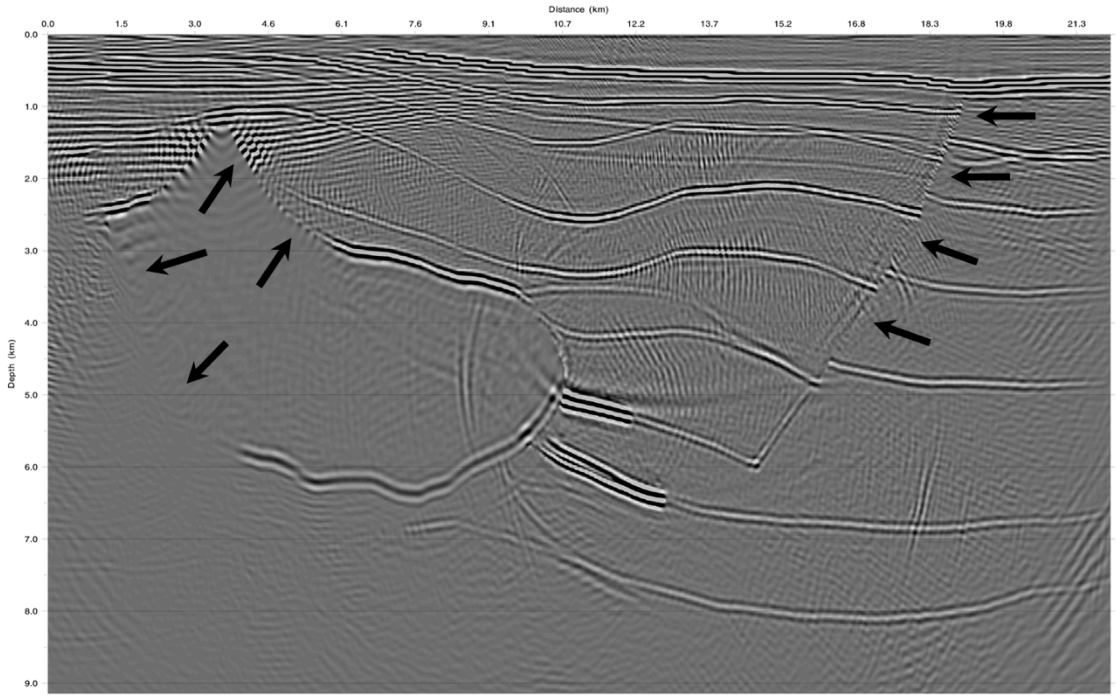

Figure 3.25. The image obtained by migrating 81 $\mathbf{p}_s$ plane waves and 41 $\mathbf{p}_r$ plane waves. $\mathbf{p}_s$ and $\mathbf{p}_r$ both ranged -0.2 ~ 0.2 s/km.

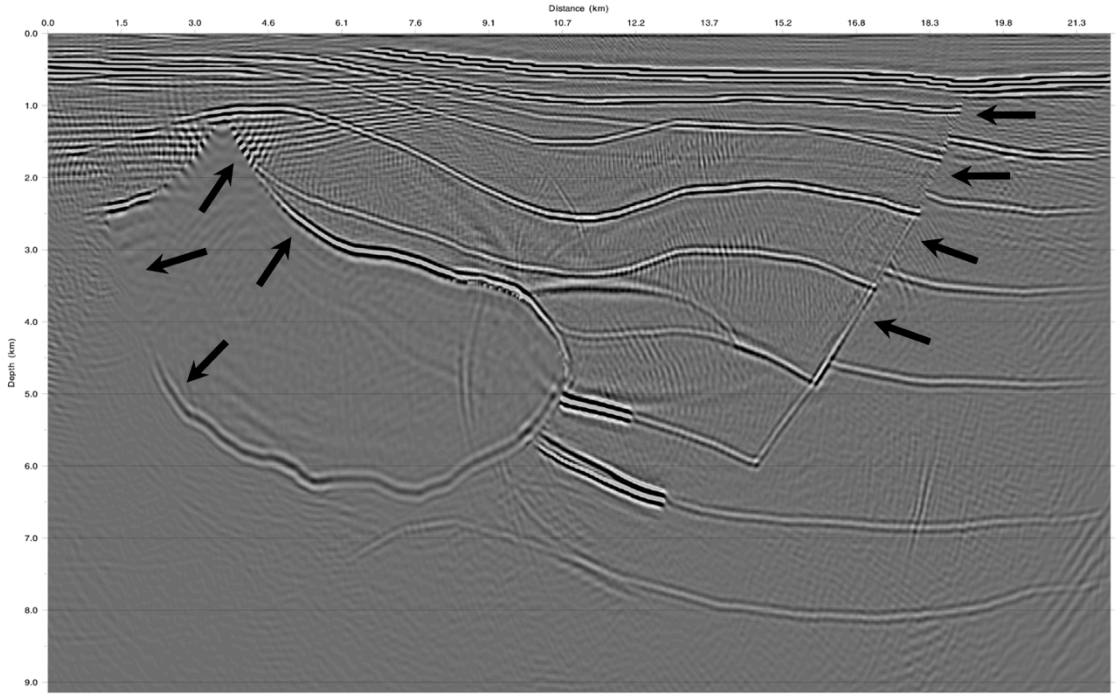

Figure 3.26. The image obtained by migrating 121 $\mathbf{p}_s$ plane waves and 61 $\mathbf{p}_r$ plane waves. $\mathbf{p}_s$ and $\mathbf{p}_r$ both ranged -0.3 ~ 0.3 s/km.

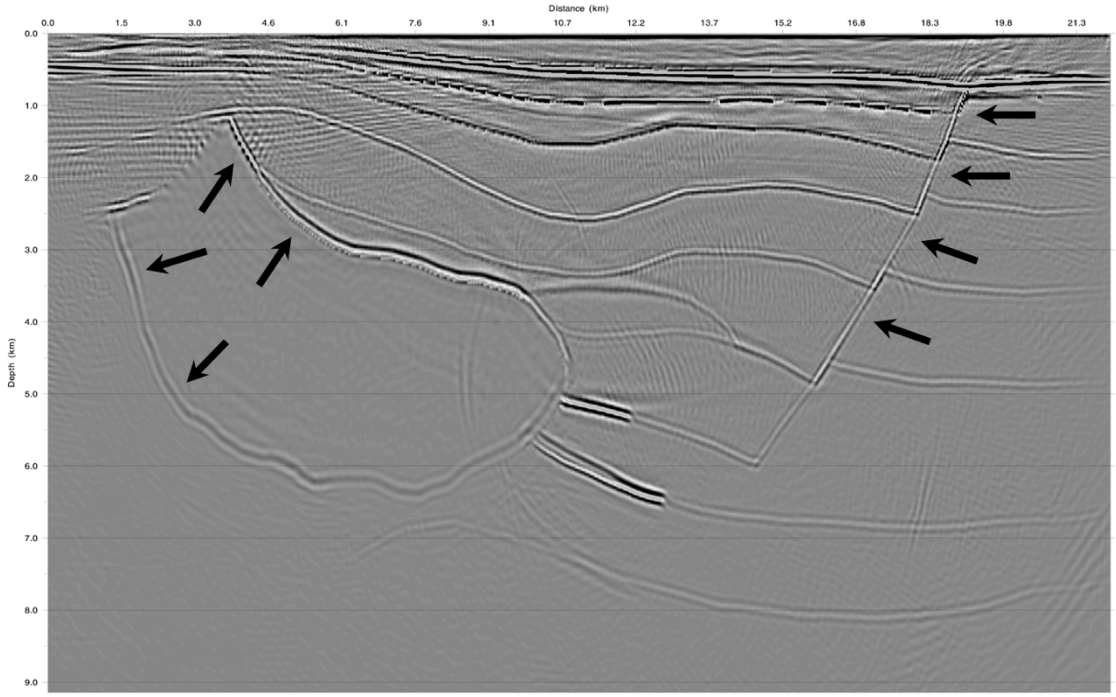

Figure 3.27. The image obtained by migrating 241 $\mathbf{p}_s$ plane waves and 121 $\mathbf{p}_r$ plane waves. $\mathbf{p}_s$ and $\mathbf{p}_r$ both ranged -0.6 ~ 0.6 s/km.

The salt body and the faults on the right part of the model, indicated by arrows in Figure 3.25, 3.26 and 3.27, became better defined as increasing the aperture for $\mathbf{p}_s$ and $\mathbf{p}_r$. Migrating a subset of the original DPW dataset is very efficient. Only 61, 121 and 241 plane wave Green's functions were constructed to generate images shown in Figure 3.25, 3.26 and 3.27, respectively.

The ray-parameter CIGs shown in Figure 3.28 were generated by migrating 241 $\mathbf{p}_s$ and 121 $\mathbf{p}_r$ plane waves. As discussed in the Chapter 2, staging over $\mathbf{p}_s$ and $\mathbf{p}_r$ aperture might be a useful tool for the migration velocity and the anisotropic parameter analyses.

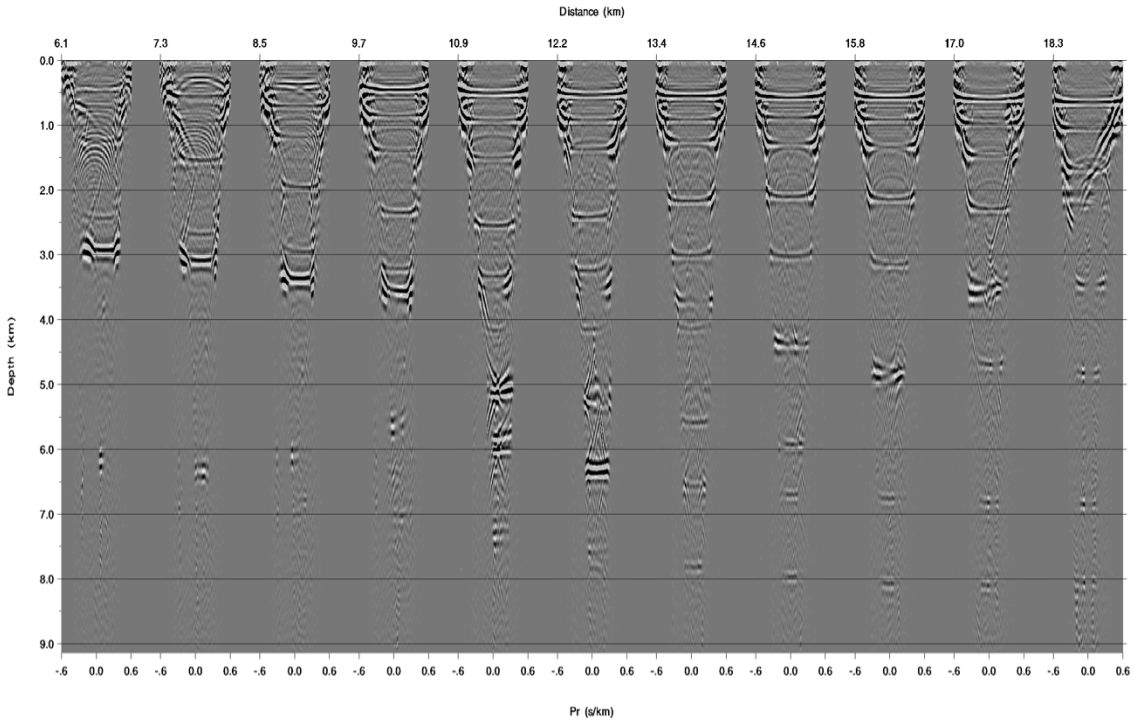

Figure 3.28. The ray-parameter CIGs for the Hess model. Each shown horizontal position contains 121 $\mathbf{p}_r$ plane waves ranging from -0.6 to 0.6 s/km. 241 $\mathbf{p}_s$ plane waves were used for migration. Most of the events in CIGs are flat suggesting that correct models were used for migration.

For the DPW data in the frequency domain, shot gathers are completely decomposed from **s, r** and time into $\mathbf{p}_s$, $\mathbf{p}_r$ or $\mathbf{p}_o$ plane waves and frequencies. Any part of the fully decomposed DPW data can be selected for migration, which makes the algorithm highly flexible. Images with good resolution can be obtained by migrating a selected DPW volume that satisfies the sampling requirements for each set of components.

3.9. CONCLUSIONS

In this chapter, I briefly reviewed the DPW-based RTMs in the time and frequency domains. Based on the Born approximation, I derived the imaging conditions for the frequency domain DPW RTM. There are several advantages of the frequency domain DPW RTM. First, only a limited number of plane wave Green's functions needs to be construct to obtain images with reasonable resolutions, which considerably increases the migration efficiency. Secondly, the method is highly flexible. Frequencies and plane wave components can be migrated independently. Migrating all the frequencies and plane wave components is not necessary if one only wants to image subsurface structures with specific dipping angles. Thirdly, ray-parameter CIGs can be easily obtained after the migration. Additionally, gradually increasing the aperture for plane waves can be used to obtain trial images and CIGs promptly. It can speed up the velocity updating process substantially, which makes the DPW imaging a powerful tool for the velocity analysis. Finally, the frequency domain DPW RTM can easily be extended to include anisotropy by constructing the frequency domain plane wave Green's functions in anisotropic media.

Chapter 4: Reciprocity and Double Plane Wave Migration

4.1. INTRODUCTION

Migration efficiency can be improved by implementing plane wave migration techniques (Whitmore 1995; Liu et al., 2002; Zhang et al., 2005; Liu et al., 2006; Stoffa et al., 2006; Zhao, Sen, et al., 2014; Zhao, Stoffa, et al., 2014). High quality slant stacked plane wave data are required to perform optimal plane wave migration method. Modern marine seismic acquisition is predominantly one-sided but with appropriate source and receiver spatial resolution so that plane wave data can be constructed with minimal transform artifacts.

Marine seismic data acquired with common source (shot) geometry are usually reorganized into common receiver gathers and then slant stacked to produce plane wave datasets in order to perform traditional plane wave migration methods (Whitmore 1995; Liu et al., 2002; Zhang et al., 2005; Liu et al., 2006). When one-sided gathers are transformed into the plane wave domain, most plane wave energy appears in the positive ray-parameter sections (Liu et al., 2004). Useful signal might also appear in negative the ray-parameter sections because of complex subsurface structures. Unfortunately, artifacts generated during slant stacking procedures often dominate negative ray-parameter sections due to the original one-sided gathers and limited acquisition aperture. Migrating such negative ray-parameter sections produces noisy images with low resolution (Liu et al., 2004). Consequentially, the reciprocity principle was invoked to collect split-spread gathers, so that high quality plane wave sections can be produced by slant stacking these split-spread gathers collected from one-sided gathers (Liu et al., 2004). Images with improved resolution can be generated using these more complete plane wave sections

since more viewing angles of the subsurface are sampled. Obtaining such plane wave datasets is crucial to successfully implementing traditional plane wave migration methods.

The aforementioned problems for traditional plane wave migration exist in double plane wave (DPW) migration methods: one-sided gathers cannot recover plane wave energy in both positive and negative ray-parameter sections, and artifacts can be generated as a result of missing reflections in the original one-sided gathers. Therefore, one-sided gathers do not honor the optimal implementation of the DPW migration. Seifoullaev et al. (2005) employed the reciprocity principle for one-sided gathers to generate an optimal DPW dataset, known as the reciprocal DPW dataset, where seismic energy is recovered in both positive and negative ray-parameter sections. The method is straightforward and it avoids assumptions about source and receiver locations to form split-spread gathers.

In this chapter, I investigate a new application for the reciprocity principle that can obtain optimal DPW datasets from one-sided gathers. The proposed method merges two DPW datasets so that both positive and negative ray-parameter plane waves are recovered from one-sided gathers. It is faster than the method proposed by Seifoullaev et al. (2005). I show that a merged DPW dataset is also a reciprocal DPW dataset, and it is a very good approximation to a DPW dataset transformed from split-spread gathers with the same acquisition aperture. I also demonstrate that the number of DPW traces needed for the DPW RTM can be reduced by half using the reciprocity principle. Therefore, DPW RTM efficiency can be increased while all possible viewing angles in the acquired data can still be imaged.

4.2. RECIPROCITY PRINCIPLE

Under the acoustic assumption, the reciprocity principle can be intuitively stated as the same seismic response should be obtained if source and receiver locations are interchanged. From the plane wave perspective, when source and receiver locations are interchanged, the source and receiver ray-parameters are interchanged as well. Figure 4.1 illustrates the reciprocity principle. In Figure 4.1a), a ray initiated at the source location $\mathbf{s}_0$ with a ray-parameter $\mathbf{p}_{s0}$ hits the diffractor $\mathbf{x}$ and bounces to the receiver at location $\mathbf{r}_0$ with a ray-parameter $\mathbf{p}_{r0}$. Because of the reciprocity principle, the same raypath can be achieved when source and receiver locations are interchanged, as illustrated in Figure 4.1b). A ray initiated at the source location $\mathbf{s}_0'$ with a ray-parameter $\mathbf{p}_{s0}'$ hits the diffractor at $\mathbf{x}$ and bounces to the surface at the receiver location $\mathbf{r}_0'$ with a ray-parameter $\mathbf{p}_{r0}'$. If $\mathbf{s}_0' = \mathbf{r}_0$ and $\mathbf{r}_0' = \mathbf{s}_0$, we have $\mathbf{p}_{s0}' = \mathbf{p}_{r0}$ and $\mathbf{p}_{r0}' = \mathbf{p}_{s0}$.

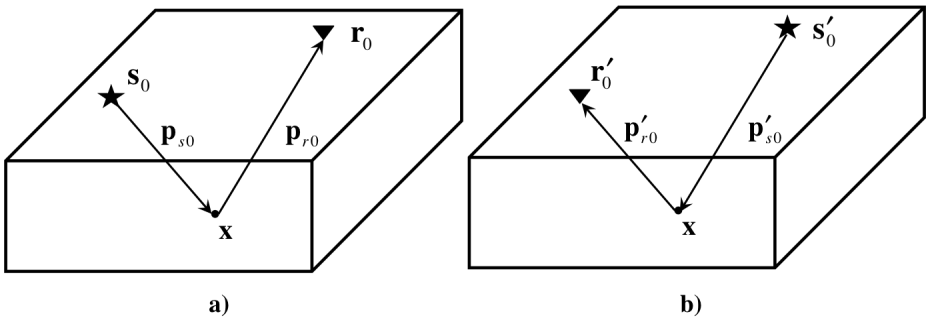

Figure 4.1. a) Simple geometry showing a ray that initiates at a source location $\mathbf{s}_0$ and arrives at a receiver location $\mathbf{r}_0$. b) Considering the reciprocity principle, when the original receiver location $\mathbf{r}_0$ becomes the new source location $\mathbf{s}_0'$, and the original source location $\mathbf{s}_0$ becomes the new receiver location $\mathbf{r}_0'$ (i.e., $\mathbf{s}_0' = \mathbf{r}_0$ and $\mathbf{r}_0' = \mathbf{s}_0$), $\mathbf{p}_{s0}'$ is the same as $\mathbf{p}_{r0}$, and $\mathbf{p}_{r0}'$ is the same as $\mathbf{p}_{s0}$ (i.e., $\mathbf{p}_{s0}' = \mathbf{p}_{r0}$ and $\mathbf{p}_{r0}' = \mathbf{p}_{s0}$).

Under the ideal acquisition conditions and acoustic assumption, theoretical point sources are excited and point receivers are used to record seismic data without converted waves. Therefore utilizing the reciprocity principle will be straightforward. In practices, however, such theoretical point sources and receivers might not be available, and converted waves might be recorded. Therefore, appropriate pre-processing jobs are necessary to reduce those problems. The arguments below are based on the theoretical point source and point receiver that are not available in real seismic acquisitions. But if the pre-processing jobs are implemented correctly, we can obtain seismic data that are close enough to the teoratical wave behavior.

4.3. UTILIZING THE RECIPROCITY PRINCIPLE FOR THE DPW TRANSFORM

As introduced in the Chapter 1, simultaneously slant stacking over $\mathbf{s}$ and $\mathbf{r}$ transforms seismic data into a coupled ray-parameter domain, known as the DPW domain. The corresponding double slant stacking process is called the DPW transform (Tatalovic et al., 1991b; Fokkema and van den Berg 1992; Stoffa et al., 2006), which can be written as

$$P(\mathbf{p}_s,\mathbf{p}_r,\omega)=\iint P(\mathbf{s},\mathbf{r},\omega)\exp(-i\omega[\mathbf{p}_s\cdot(\mathbf{s}-\mathbf{x}_{ref})+\mathbf{p}_r\cdot(\mathbf{r}-\mathbf{x}_{ref})])\,d\mathbf{s}\,d\mathbf{r}, \qquad (4.1)$$

where $P(\mathbf{p}_s,\mathbf{p}_r,\omega)$ is a DPW dataset. The DPW domain is a pure plane wave domain. By performing the DPW transform, seismic data are fully decomposed into $\mathbf{p}_s$ and $\mathbf{p}_r$ plane waves. The trace in the DPW domain is indexed by $\mathbf{p}_s$ and $\mathbf{p}_r$, suggesting that a receiver plane wave arriving at the surface with a ray-parameter $\mathbf{p}_r$ is introduced by a source plane wave initiated at the surface with a ray-parameter $\mathbf{p}_s$.

In 2D cases, a DPW dataset is a 3D volume. In 3D cases, a DPW dataset becomes a 5D volume. Although all derivations are in 3D, 2D examples will be demonstrated. 2D shot gathers arranged in the source-receiver coordinates are shown in Figure 4.2. Illustrations of the corresponding transformed DPW dataset and its horizontal plane obtained from the 2D gathers are shown in Figure 4.3. For brevity, I use Ps-Pr to represent the DPW transformed $P(\mathbf{p}_s,\mathbf{p}_r,\omega)$ dataset.

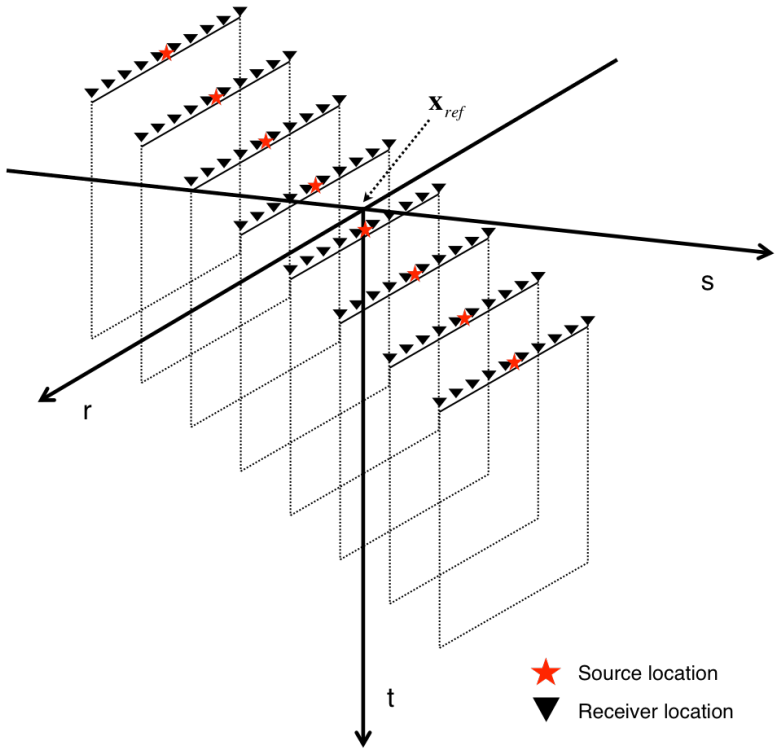

Figure 4.2. An illustration of shot gathers arranged in the source-receiver coordinates. According to the illustration, we have both positive and negative values for $\mathbf{s}$, $\mathbf{r}$, $\mathbf{p}_s$ and $\mathbf{p}_r$.

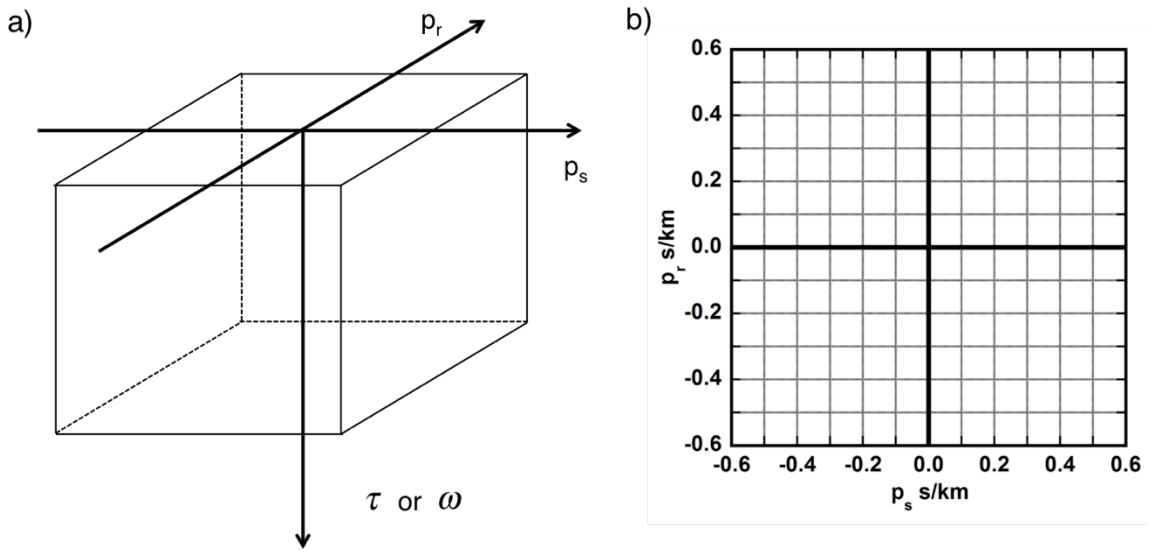

Figure 4.3. a) An illustration of a Ps-Pr dataset volume transformed from the 2D gathers shown in Figure 4.2. Vertical axis can be ω or τ depending upon the domain of the dataset. Two horizontal axes are $\mathbf{p}_s$ and $\mathbf{p}_r$, respectively. b) An illustration of the horizontal plane of the Ps-Pr dataset.

A DPW dataset is optimal when plane wave energy appears in both the positive and negative ray-parameter sections for $\mathbf{p}_s$ and $\mathbf{p}_r$ plane waves so that plane waves arriving at the surface from all angles are captured. However, current marine seismic acquisition systems using towed streamers produce one-sided seismic gathers that cannot be used directly to generate such an optimal DPW dataset. Performing the DPW transform for one-sided gathers generates plane wave energy mostly in positive $\mathbf{p}_s$ and negative $\mathbf{p}_r$ sections. The corresponding DPW dataset is called the non-reciprocal DPW dataset. Because subsurface structures can be complex, some plane wave energy might be mapped into negative $\mathbf{p}_s$ and positive $\mathbf{p}_r$ sections. Often, those useful information is masked by strong stacking artifacts, which are generated by slant stacking of missing reflections in the original one-sided gathers. Migrating traces in those sections are

expected to be noisy. However, it is not appropriate to exclude those sections from migration if we want to migrate all seismic energy and generate properly represented ray-parameter common image gathers (CIGs) where horizons appear in both negative and positive $\mathbf{p}_r$. Studies (Seifoullaev et al., 2005) were carried out to produce optimal DPW dataset by utilizing the reciprocity principle.

4.4. RECIPROCAL DPW TRANSFORM METHOD

As previously discussed, given the reciprocity principle, $\mathbf{s}$ and $\mathbf{r}$ are interchangeable, so are $\mathbf{p}_s$ and $\mathbf{p}_r$. As a result, if seismic data is acquired under ideal acquisition conditions or appropriate preprocessing is performed, the shot gather DPW transform is equivalent to the receiver gather DPW transform with $\mathbf{p}_s$ and $\mathbf{p}_r$ interchanged. Seifoullaev et al. (2005) defined the receiver gather DPW transform as

$$P_R(\mathbf{p}_r,\mathbf{p}_s,\omega)=\iint P_R(\mathbf{r},\mathbf{s},\omega)\exp(-i\omega[\mathbf{p}_r\cdot(\mathbf{r}-\mathbf{x}_{ref})+\mathbf{p}_s\cdot(\mathbf{s}-\mathbf{x}_{ref})])\,d\mathbf{r}\,d\mathbf{s}, \qquad (4.2)$$

where $P_R(\mathbf{r},\mathbf{s},\omega)$ is the receiver gather and $P_R(\mathbf{p}_r,\mathbf{p}_s,\omega)$ is the receiver gather DPW transformed DPW dataset. Employing the reciprocity principle (Seifoullaev et al., 2005), $\mathbf{p}_s$ and $\mathbf{p}_r$ can be interchanged, and equation (4.2) becomes

$$P_R(\mathbf{p}_s,\mathbf{p}_r,\omega)=\iint P_R(\mathbf{r},\mathbf{s},\omega)\exp(-i\omega[\mathbf{p}_s\cdot(\mathbf{r}-\mathbf{x}_{ref})+\mathbf{p}_r\cdot(\mathbf{s}-\mathbf{x}_{ref})])\,d\mathbf{r}\,d\mathbf{s}. \qquad (4.3)$$

Because seismic data is invariant, $P(\mathbf{s},\mathbf{r},\omega)$ is identical to $P_R(\mathbf{r},\mathbf{s},\omega)$. Equations (4.1) and (4.3) can be combined to achieve (Seifoullaev et al., 2005)

$$P(\mathbf{p}_s,\mathbf{p}_r,\omega)=\iint P(\mathbf{s},\mathbf{r},\omega)\{\exp(-i\omega[\mathbf{p}_s\cdot(\mathbf{s}-\mathbf{x}_{ref})+\mathbf{p}_r\cdot(\mathbf{r}-\mathbf{x}_{ref})])$$
$$+\exp(-i\omega[\mathbf{p}_s\cdot(\mathbf{r}-\mathbf{x}_{ref})+\mathbf{p}_r\cdot(\mathbf{s}-\mathbf{x}_{ref})])\}d\mathbf{s}d\mathbf{r}. \quad (4.4)$$

Equation (4.4) indicates that an $\mathbf{s}$ can be treated as an $\mathbf{r}$ during the slant stacking procedure, and vice versa. And an additional phase shift term, (i.e., second exponential term), is introduced to utilize the reciprocity principle. Implementing equation (4.4) can generate an optimal DPW dataset with plane wave energy in both positive and negative $\mathbf{p}_s$ and $\mathbf{p}_r$ sections. With the reciprocity principle, split-spread seismic gathers do not need to be physically collected. That avoids the difficulty associated with locating $\mathbf{s}$ and $\mathbf{r}$ being at irregular or even random intervals (Seifoullaev et al., 2005). We call equation (4.4) the reciprocal DPW transform and the corresponding optimal DPW dataset the reciprocal DPW dataset.

4.5. MERGING METHOD – AN ALTERNATIVE

Taking reciprocity into account in the DPW transform is shown to be straightforward, easy and effective with equation (4.4). However, directly implementing this approach requires doubling the computational cost compared to implementing equation (4.1). I propose a new strategy based on the reciprocity principle to generate a reciprocal DPW dataset with little extra cost.

Because of the reciprocity principle, $\mathbf{p}_s$ and $\mathbf{p}_r$ are interchangeable, as illustrated in Figure 4.1. Therefore, a $\mathbf{p}_s$ section in the DPW dataset can be viewed as a $\mathbf{p}_r$ section, and vice versa. Figure 4.4 illustrates the horizontal plane of a DPW dataset with a constant $\mathbf{p}_s$ and a constant $\mathbf{p}_r$ profile. In Figure 4.4, the horizontal dashed line

indicates a constant $\mathbf{p}_r$ profile, and the vertical dashed line indicates a constant $\mathbf{p}_s$ profile. Applying the reciprocity principle, the vertical dashed line can be regarded as a constant $\mathbf{p}_r$ profile instead. As a result, the two profiles indicated by the vertical and the horizontal dash line share the same $\mathbf{p}_r$ value and the same $\mathbf{p}_s$ range. The two profiles can be added together to generate a merged $\mathbf{p}_r$ profile. As previously discussed, the DPW dataset obtained from one-sided gathers has most energy in positive $\mathbf{p}_s$ and negative $\mathbf{p}_r$ sections. Using the reciprocity principle, the same DPW dataset can be viewed as a DPW dataset that has the energy dominant in negative $\mathbf{p}_s$ and positive $\mathbf{p}_r$ sections. Therefore, the merged $\mathbf{p}_r$ profile contains plane wave energy appears in both negative and positive $\mathbf{p}_r$ sections. A reciprocal DPW dataset can be obtained by repeating the merging procedure for all $\mathbf{p}_r$ profiles in the non-reciprocal DPW dataset. The merged reciprocal DPW dataset is an optimal DPW dataset with plane wave energy in both positive and negative sections of both $\mathbf{p}_r$ and $\mathbf{p}_r$ plane waves. This procedure is called the merging method. The merging method is simple, and only little extra work is needed compare to implementing equation (4.4). Examples of a non-reciprocal DPW dataset and a merged reciprocal DPW dataset are shown in the numerical tests section. Ray-parameter CIGs obtained by using different DPW dataset are also compared.

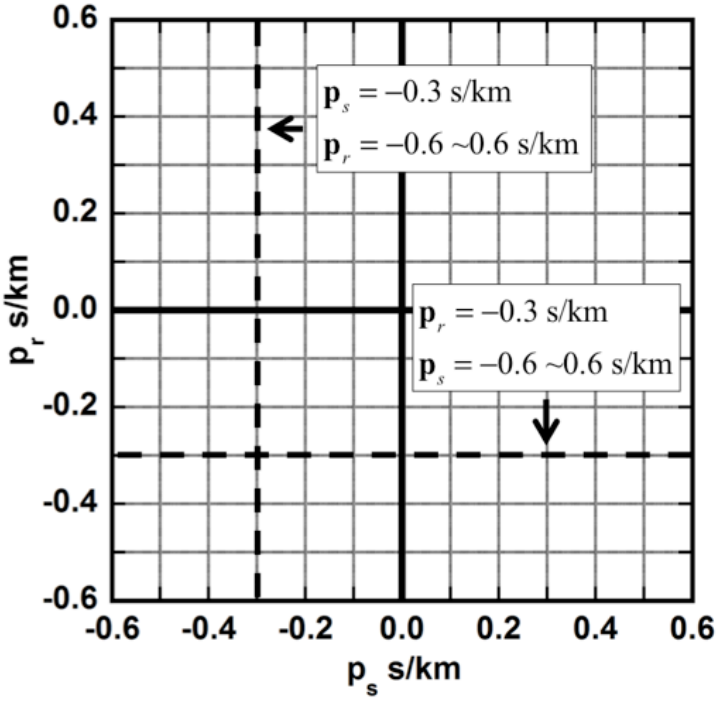

Figure 4.4. An illustration of a horizontal plane of the DPW dataset. The $\mathbf{p}_s$ and $\mathbf{p}_r$ sections are interchangeable given the reciprocity principle.

4.6. UTILIZING THE RECIPROCITY PRINCIPLE FOR THE DPW RTM

Using the two previous discussed methods, a reciprocal DPW dataset with plane wave energy in both positive and negative both $\mathbf{p}_r$ and $\mathbf{p}_r$ sections can be easiliy obtained. The reciprocal DPW dataset can be used in the DPW RTM to generate properly represented ray-parameter CIGs with seismic horizons in both negative and positive $\mathbf{p}_r$ sections. The migration efficiency of the DPW RTM can be increased by employing the reciprocity principle.

As introduced in the previous chapter, the imaging condition for DPW RTM in the frequency domain can be written as

$$I(\mathbf{x}) = \mathrm{Re}\Big(\int \frac{\omega^6}{c^2(\mathbf{x})} \iint f_s^*(\omega) G^*(\mathbf{p}_s, \mathbf{x}, \omega) G^*(\mathbf{p}_r, \mathbf{x}, \omega) \times P(\mathbf{p}_s, \mathbf{p}_r, \omega) \exp(+i\omega(\mathbf{p}_s + \mathbf{p}_r) \cdot (\mathbf{x}_h - \mathbf{x}_{ref})) d\mathbf{p}_s d\mathbf{p}_r d\omega \Big). \tag{4.5}$$

where the superscript represent the complex conjugate of a complex number, $c(\mathbf{x})$ is the velocity, $f_s(\omega)$ is the frequency source, $G(\mathbf{p}_s, \mathbf{x}, \omega)$ and $G(\mathbf{p}_r, \mathbf{x}, \omega)$ are source and receiver plane wave Green's functions, respectively, $P(\mathbf{p}_s, \mathbf{p}_r, \omega)$ is the DPW dataset, and $\mathbf{x}_h$ is the horizontal location of the subsurface imaging point $\mathbf{x}$. An image can be obtained by taking the real part of the right-hand side of equation (4.5). Equation (4.5) is used to migrate selected DPW traces, while each Ps-Pr trace can be migrated independently by

$$I(\mathbf{x}, \mathbf{p}_s, \mathbf{p}_r) = \mathrm{Re}\Big(\int \frac{\omega^6}{c^2(\mathbf{x})} f_s^*(\omega) G^*(\mathbf{p}_s, \mathbf{x}, \omega) G^*(\mathbf{p}_r, \mathbf{x}, \omega) \times P(\mathbf{p}_s, \mathbf{p}_r, \omega) \exp(+i\omega(\mathbf{p}_s + \mathbf{p}_r) \cdot (\mathbf{x}_h - \mathbf{x}_{ref})) d\omega \Big). \tag{4.6}$$

where $I(\mathbf{x}, \mathbf{p}_s, \mathbf{p}_r)$ is the image obtained from one Ps-Pr trace.

According to Figure 4.1, the same raypath can be achieved by interchanging $\mathbf{p}_s$ and $\mathbf{p}_r$. Therefore, the image $I(\mathbf{x}, \mathbf{p}_s, \mathbf{p}_r)$ obtained by migrating a Ps-Pr trace $P(\mathbf{p}_s, \mathbf{p}_r, \omega)$ is expected to be the same as the image $I(\mathbf{x}, \mathbf{p}_r, \mathbf{p}_s)$ obtained by migrating a Ps-Pr trace $P(\mathbf{p}_r, \mathbf{p}_s, \omega)$. The two traces are called reciprocal traces. For example, the trace with $\mathbf{p}_s$ ($p_{xs} = 0.2$ s/km, $p_{ys} = 0.0$ s/km), $\mathbf{p}_r$ ($p_{rx} = 0.4$ s/km, $p_{ry} = 0.0$ s/km) and the trace with $\mathbf{p}_s$ ($p_{xs} = 0.4$ s/km, $p_{ys} = 0.0$ s/km), $\mathbf{p}_r$ ($p_{rx} = 0.2$ s/km, $p_{ry} = 0.0$ s/km) are reciprocal traces, and the images obtained from those two traces are expected to be identical. Typically, a great number of DPW traces need to be migrated to generate high-

resolution images. So for one-sided seismic data, we first construct a reciprocal DPW dataset using either of the above methods. Then using the reciprocity principle for this DPW dataset, only half of these traces need to be migrated explicitly. Therefore, the computational cost is reduced, and images and CIGs of the same quality can be obtained. Migrations results with and without utilizing the reciprocity principle will be demonstrated in the numerical tests section.

4.7. NUMERICAL TESTS

A 2D line, as shown in Figure 4.5, from the 3D SEG/EAGE salt model (Aminzadeh et al., 1997) was used to demonstrate the proposed methods. There were 675 horizontal and 210 vertical grid points with 0.02 km intervals in both directions. Source and receiver intervals were both 0.02 km. Two methods were implemented to obtain the reciprocal DPW dataset from the one-sided acquisition geometry. The reciprocity principle was applied to the DPW RTM to generate images. It can be shown that the reciprocity principle helps to reduce computational cost of the DPW RTM.

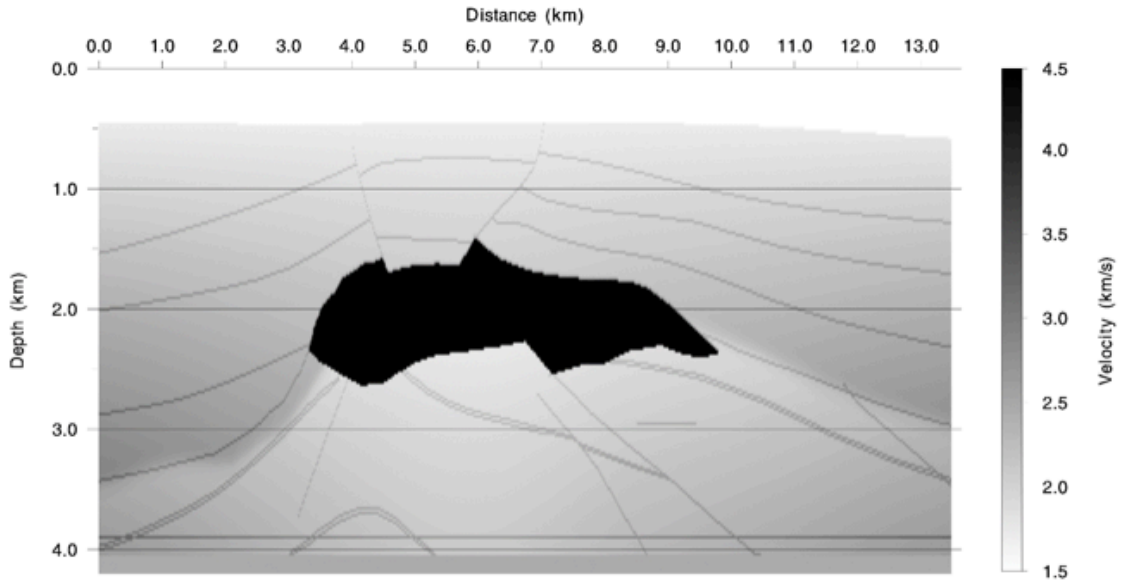

Figure 4.5. The 2D line from the SEG/EAGE salt model.

4.7.1. The one-sided transformed DPW dataset vs. the reciprocal DPW dataset

A marine towed streamer acquisition experiment was conducted to produce one-sided shot gathers. The acquisition proceeded from left to right with a maximum of 50 receivers towed on the left of each source location. The maximum offset was 1 km, given a 0.02 km receiver interval. The DPW transform using equation (4.1) was performed to generate a non-reciprocal DPW dataset without using the reciprocity principle. All shot gathers were decomposed into 241 $\mathbf{p}_s$ and 241 $\mathbf{p}_r$ plane waves. Each set of plane waves were equally spaced between -0.6 and 0.6 s/km. Several constant $\mathbf{p}_s$ and $\mathbf{p}_r$ profiles from the DPW dataset are shown in Figure 4.6. As expected, most of plane wave energy was in the positive $\mathbf{p}_s$ and negative $\mathbf{p}_r$ plane wave sections due to the one-sided acquisition geometry.

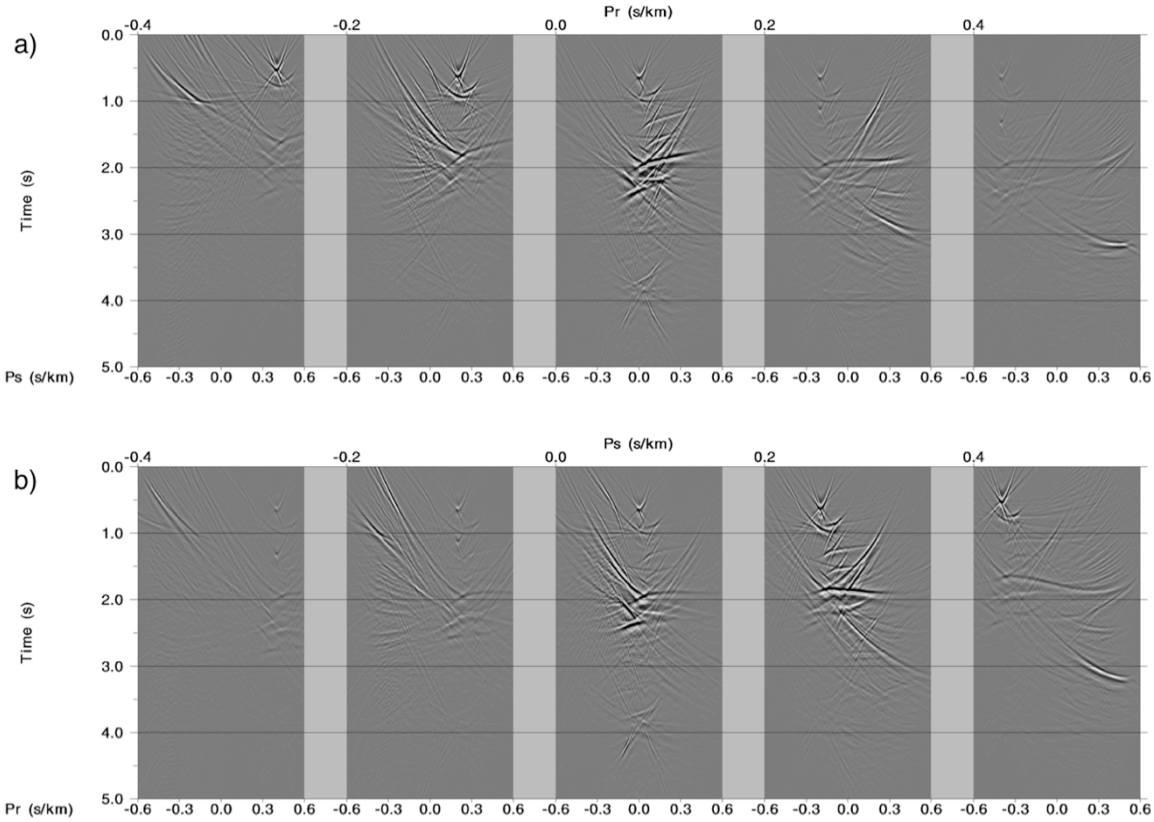

Figure 4.6. a) Five constant $\mathbf{p}_r$ profiles, where $\mathbf{p}_r$ = -0.4, -0.2, 0.0, 0.2 and 0.4 s/km $\mathbf{p}_s$ = -0.6 ~ 0.6 s/km in each profile. b) Five constant $\mathbf{p}_s$ profiles, where $\mathbf{p}_s$ = -0.4, -0.2, 0.0, 0.2 and 0.4 s/km. $\mathbf{p}_r$ = -0.6 ~ 0.6 s/km in each profile. The maximum offset of the one-sided gathers was 1 km.

The reciprocal DPW transform and the merging method were then implemented to obtain two reciprocal DPW datasets, where the same $\mathbf{p}_s$ and $\mathbf{p}_r$ settings were maintained. Constant $\mathbf{p}_s$ and $\mathbf{p}_r$ profiles from the two reciprocal DPW datasets obtained by the reciprocal DPW transform and by the merging method are shown in Figure 4.7 and 4.8, respectively. In both datasets, plane wave energy was recovered for both positive and negative $\mathbf{p}_s$ and $\mathbf{p}_r$ sections. The overall difference of the two

reciprocal DPW datasets generated by the two methods was less than 1e-7, as expected, indicating the two methods were equivalent.

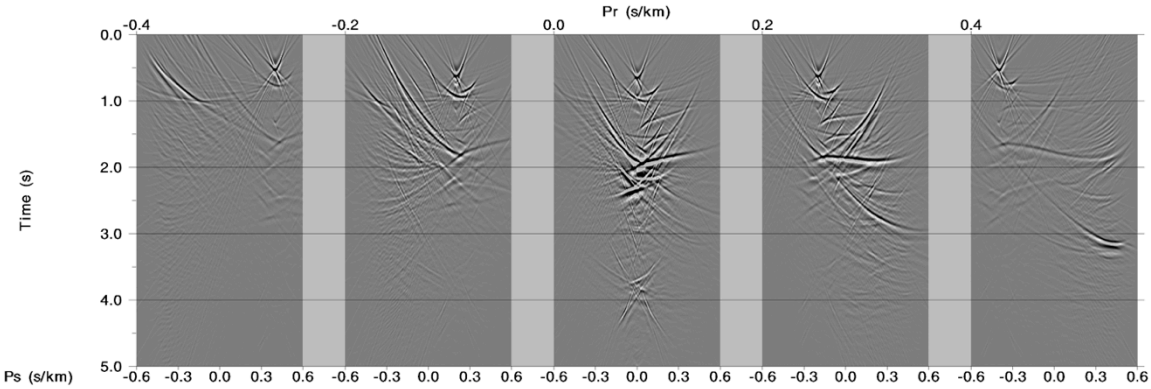

Figure 4.7. Five constant $\mathbf{p}_r$ profiles transformed from the one-sided gathers by the reciprocal DPW transform where $\mathbf{p}_r$ = -0.4, -0.2, 0.0, 0.2 and 0.4 s/km. $\mathbf{p}_s$ = -0.6 ~ 0.6 s/km in each profile. The maximum offset of the one-sided gathers was 1 km.

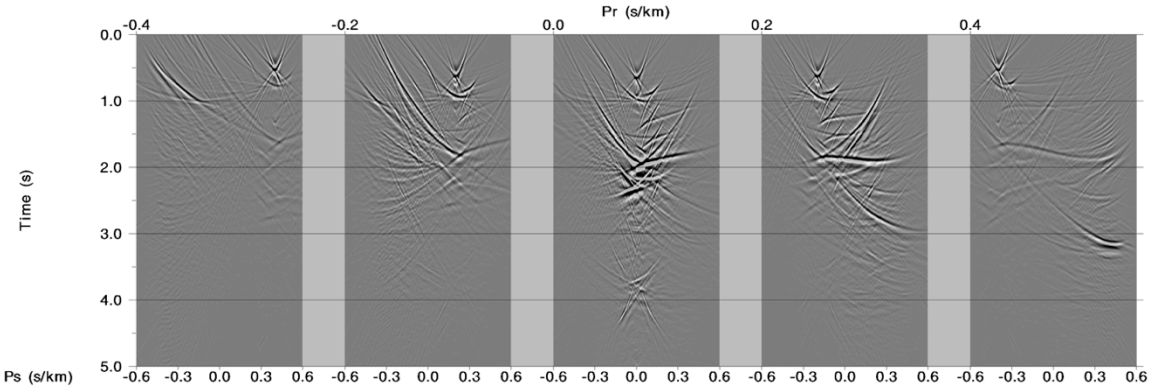

Figure 4.8. Five constant $\mathbf{p}_r$ profiles transformed by the one-sided gathers by the merging method where $\mathbf{p}_r$ = -0.4, -0.2, 0.0, 0.2 and 0.4 s/km. $\mathbf{p}_s$ = -0.6 ~ 0.6 s/km in each profile. The maximum offset of the one-sided gathers was 1 km.

For comparison, a split-spread acquisition experiment was conducted, which was acquired as split-spread shot gathers where the shot number and the interval were same as the previous one-sided acquisition experiment. A maximum of 100 receivers were deployed, and the maximum offset of the split-spread geometry was 1 km. The DPW transform was performed using equation (4.1) with the same $\mathbf{p}_s$ and $\mathbf{p}_r$ settings as in previous cases. Selected constant $\mathbf{p}_r$ profiles from the corresponding DPW dataset are shown in Figure 4.9. Profiles shown in Figure 4.7, 4.8 and 4.9 are visually the same, indicating that the two reciprocal DPW datasets transformed from the one-sided acquisition geometry were very good approximations to that transformed from the split-spread acquisition geometry.

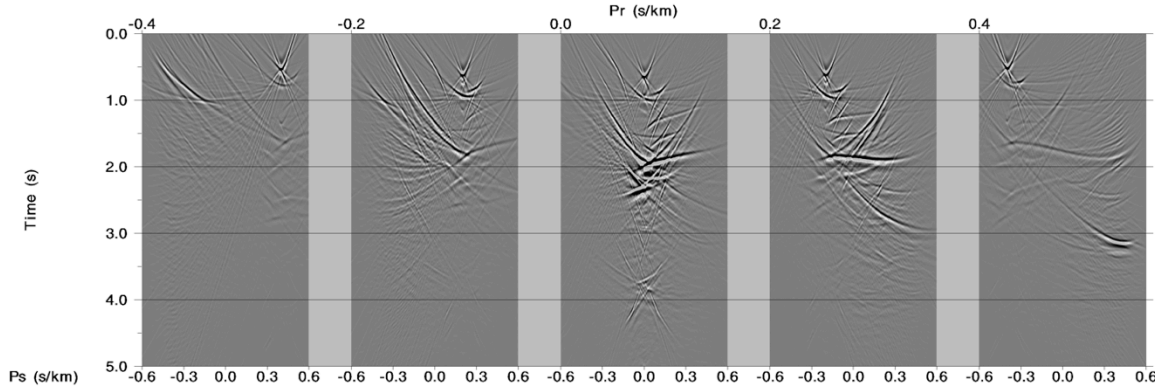

Figure 4.9. Five constant $\mathbf{p}_r$ profiles, transformed from the split-spread gathers using equation (4.1), where $\mathbf{p}_r$ = -0.4, -0.2, 0.0, 0.2 and 0.4 s/km. $\mathbf{p}_s$ = -0.6 ~ 0.6 s/km in each profile. The maximum offset of the one-sided gathers was 1 km.

Because reciprocal DPW datasets have recovered plane wave energy for all $\mathbf{p}_s$ and $\mathbf{p}_r$ plane waves, migrating the reciprocal DPW datasets helps to generate ray-

parameter CIGs with seismic horizons in both positive and negative $\mathbf{p}_r$ sections. 201 $\mathbf{p}_s$ and 201 $\mathbf{p}_r$ plane waves from the non-reciprocal DPW dataset and the reciprocal DPW dataset obtained by the merging method were selected to perform the DPW RTM. CIGs shown in Figure 4.10a) were obtained by migrating the non-reciprocal DPW dataset. Since the true velocity model was used for migration, horizontal events in CIGs across $\mathbf{p}_r$ were expected. However, due to the missing positive $\mathbf{p}_r$ energy in the non-reciprocal DPW dataset, events in Figure 4.10a) were not flat across the $\mathbf{p}_r$. Horizontal events were truncated and titled downward when $\mathbf{p}_r$ was slightly greater than 0.0 s/km. On the contrary, CIGs shown in Figure 4.10b), which were obtained by migrating the reciprocal DPW dataset, had horizontal events across all $\mathbf{p}_r$ ranges. Stacking CIGs with horizontal events on both positive and negative $\mathbf{p}_r$ sections produced images with higher resolution. In both cases, 40401 DPW traces were used for migration. However, the reciprocal DPW dataset helped to generate CIGs with higher quality events, which helps improve image resolution.

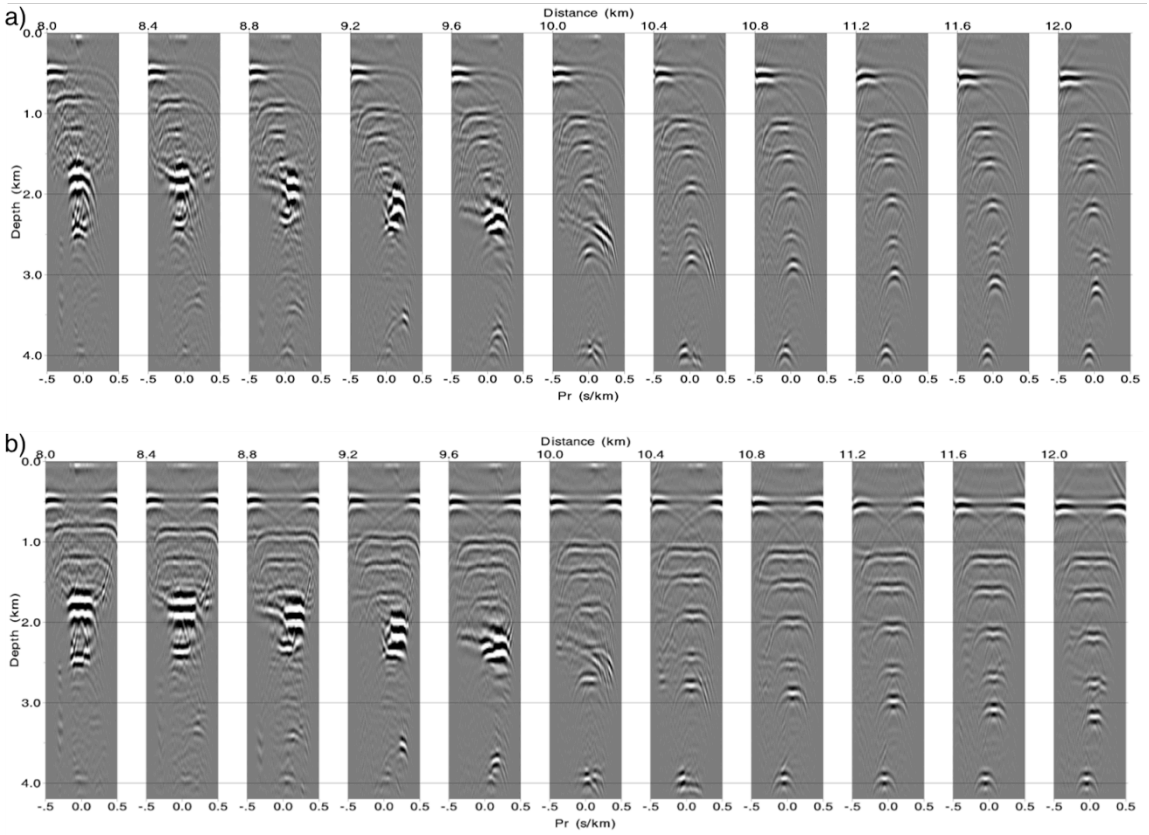

Figure 4.10. CIGs obtained by migrating a) non-reciprocal DPW dataset and b) merged reciprocal DPW dataset. Energy appears on both positive and negative ray-parameter sections in b).

Using the reciprocity principle, one-sided shot gathers can be transformed into an optimal reciprocal DPW dataset, so that plane wave energy is obtained in both positive and negative $\mathbf{p}_s$ and $\mathbf{p}_r$ sections. The reciprocal DPW dataset transformed from one-sided shot gathers approximates the DPW dataset transformed from split-spread shot gathers well, both of which have the same maximum offset. Notably, a one-sided acquisition geometry only requires half of the acquisition receivers comparing with a split-spread acquisition geometry. Therefore, given a fixed receiver array length, a one-

sided acquisition geometry can encompass larger maximum offsets (positive and negative offsets included), and acquire more seismic information because of those larger offsets compared to a split-spread acquisition geometry. Then the reciprocity principle can be utilized to form a reciprocal DPW dataset transformed from these one-sided gathers, with even more viewing angles of the subsurface. This approach may benefit the design of acquisition surveys: given a fixed and limited receiver array, we can obtain more seismic information and increase the acquisition efficiency by using a one-sided acquisition geometry and we do not require the limiting assumptions of common midpoint processing.

To illustrate this observation, another one-sided marine seismic acquisition experiment was conducted where the acquisition also proceeded from left to right, but with a maximum of 100 receivers towed on the left of each source location. Therefore, the maximum offset was 2 km, given the 0.02 km receiver interval. Then, shot gathers were transformed to a reciprocal DPW dataset with the merging method. The new reciprocal DPW dataset had the same $\mathbf{p}_s$ and $\mathbf{p}_r$ settings as previous cases. Selected constant $\mathbf{p}_r$ profiles from the new reciprocal DPW dataset are shown in Figure 4.11. Comparing with constant $\mathbf{p}_r$ profile shown in Figure 4.9 where the DPW dataset was transformed from the split-spread gathers with 1 km maximum offset, constant $\mathbf{p}_r$ profiles shown in Figure 4.11 contained more energy for large $\mathbf{p}_s$ values at large $\mathbf{p}_r$ sections. To illustrate this point, the DPW dataset transformed was subtracted from the split-spread gathers from the new reciprocal DPW dataset and obtained a difference-DPW dataset. Selected constant $\mathbf{p}_r$ profiles from the difference-DPW dataset are shown in Figure 4.12, which have the same ray-parameter settings as in Figure 4.8 and 4.9. The differences between the two DPW dataset clearly suggest that, more subsurface information was obtained with a larger aperture, yet with the same number of receivers.

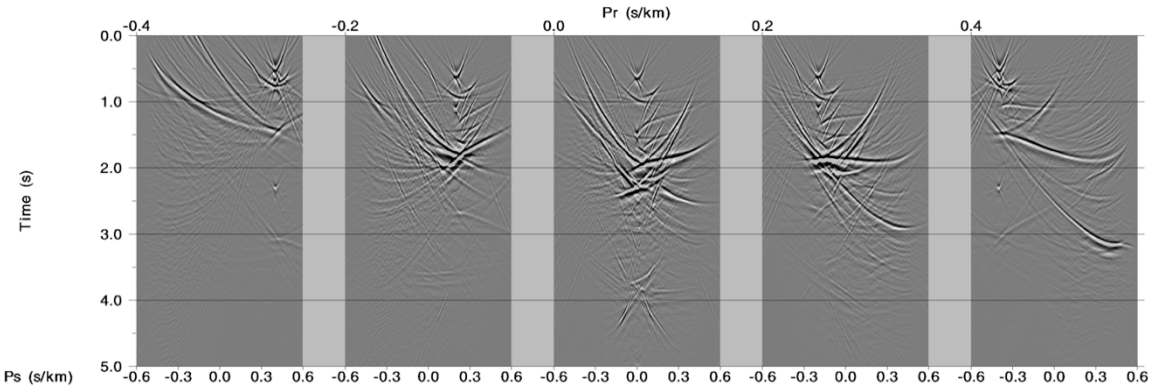

Figure 4.11. Five constant $\mathbf{p}_r$ profiles transformed by the one-sided gathers by the merging method where $\mathbf{p}_r$ = -0.4, -0.2, 0.0, 0.2 and 0.4 s/km $\mathbf{p}_s$ =-0.6 ~ 0.6 s/km in each profile. The maximum offset of the one-sided gathers was 2 km.

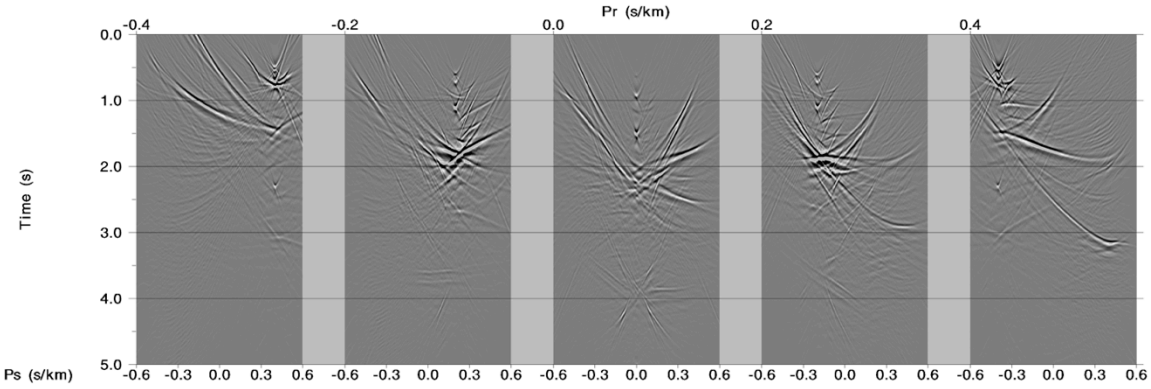

Figure 4.12. The differences between constant $\mathbf{p}_s$ profiles shown in Figure 4.9 and those shown in Figure 4.11.

As shown in Figure 4.12, using larger acquisition aperture with the same number of receivers, we obtained more energy for both small and large $\mathbf{p}_s$ and $\mathbf{p}_r$ values.

Because plane waves with larger ray-parameter have a shallower penetration depth, deep events are illuminated mainly by plane wave with small ray-parameters. Therefore, obtaining more energy for small $\mathbf{p}_s$ and $\mathbf{p}_r$ plane waves is beneficial to image deep structures

Images shown in Figure 4.13a) and 4.13b) were generated using the DPW datasets generated from split-spread gathers and the new reciprocal DPW dataset, respectively. $\mathbf{p}_s$ = -0.5 ~ 0.5 s/km and $\mathbf{p}_r$ = -0.5 ~ 0.5 s/km were used to obtain both images. Because we acquired more seismic energy for small $\mathbf{p}_s$ and $\mathbf{p}_r$ values at larger offsets, horizontal interfaces and a fault, indicated by arrows, beneath the salt became clear in Figure 4.13b) compared to that shown in Figure 4.13a).

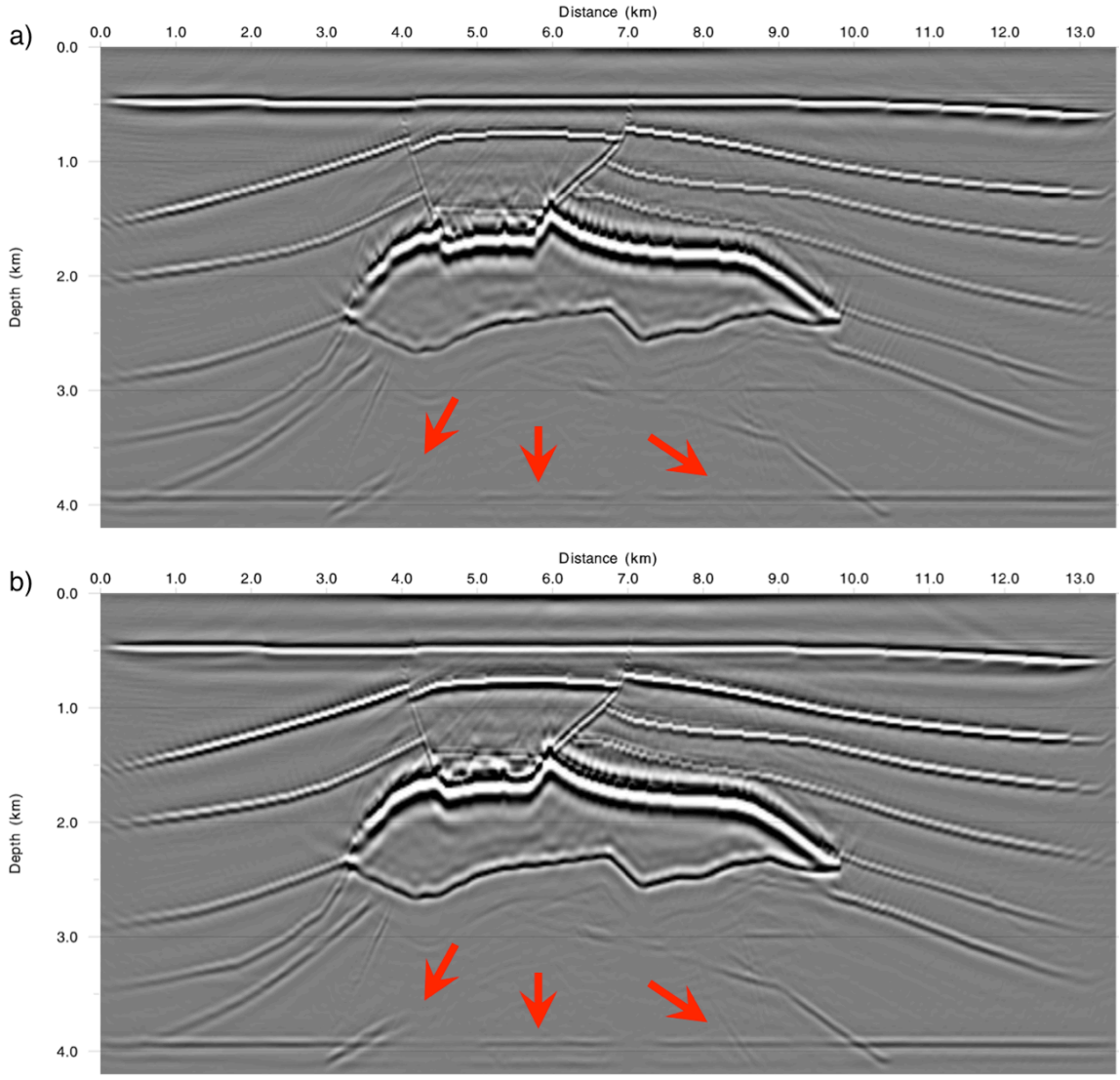

Figure 4.13. a) An image obtained by migrating the DPW dataset transformed from the split-spread gathers where the maximum offset was 1 km. b) An image obtained by migrating the DPW dataset transformed from the one-sided gathers where the maximum offset was 2 km. The same range of plane waves were used for migration in both cases.

4.7.2. Utilizing the reciprocity principle for the DPW RTM

As a result of the reciprocity principle, given a pair of $\mathbf{p}_s$ and $\mathbf{p}_r$, the image obtained by migrating the DPW trace $P(\mathbf{p}_s,\mathbf{p}_r,\omega)$ is equivalent to the image obtained by migrating the DPW trace $P(\mathbf{p}_r,\mathbf{p}_s,\omega)$. Two traces from the reciprocal DPW dataset were selected to perform DPW RTM. The first trace was $\mathbf{p}_s =$ 0.1 s/km and $\mathbf{p}_r =$ -0.1 s/km, and the second one was $\mathbf{p}_s =$ -0.1 s/km and $\mathbf{p}_r =$ 0.1 s/km. The two traces are reciprocal. Images shown in Figure 4.14 are migration results for the trace $\mathbf{p}_s$ = 0.1 s/km, $\mathbf{p}_r$ = -0.1 s/km and the trace $\mathbf{p}_s$ = -0.1 s/km, $\mathbf{p}_r$ = 0.1 s/km, respectively. The two images are almost identical due to the reciprocity principle.

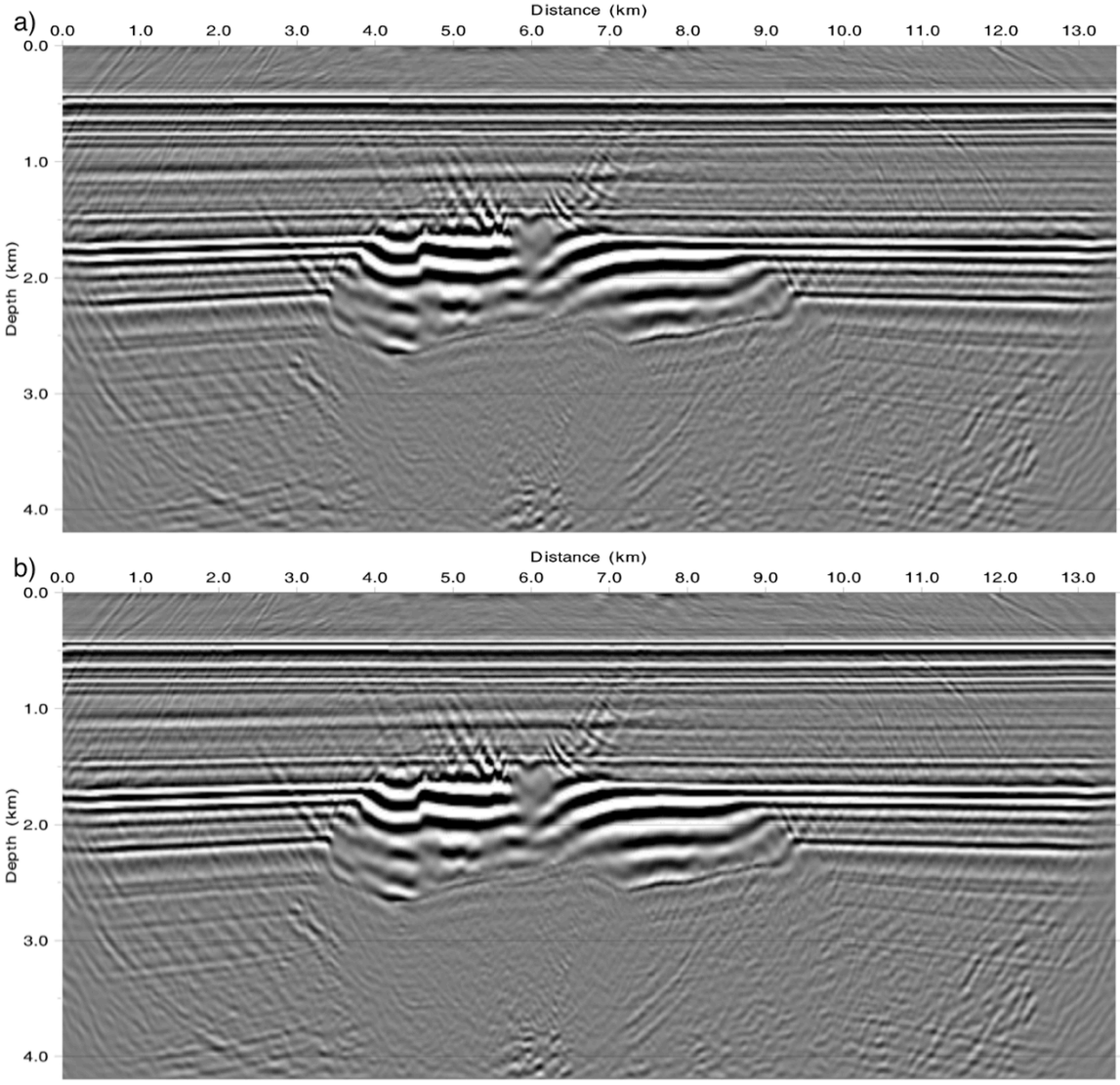

Figure 4.14. a) An image obtained by migrating the trace that $\mathbf{p}_s$ = 0.1 s/km, $\mathbf{p}_r$ = -0.1 s/km. b) An image obtained by migrating the trace that $\mathbf{p}_s$ = -0.1 s/km, $\mathbf{p}_r$ = 0.1 s/km.

Combinations of $\mathbf{p}_s$ and $\mathbf{p}_r$ were migrated to show the impact of the reciprocity on the DPW RTM. Figure 4.15 shows the horizontal plane of a DPW dataset where different combination of $\mathbf{p}_s$ and $\mathbf{p}_r$ were labeled. The letter A and B represent

the DPW traces within the shadowed lower triangular area, and the red squared area, respectively. Traces inside area B were $\mathbf{p}_s$ = -0.5 ~ 0.5 s/km and $\mathbf{p}_r$ = -0.5 ~ 0.5 s/km . The number of traces inside area A was half of those inside area B. Images generated by migrating DPW traces inside areas A and B are shown in Figure 4.16a) and 4.16b), respectively. A reciprocal DPW dataset was used for migration. The two images are visually identical. However, since half of the plane wave energy was omitted for migration to generate the image shown in Figure 4.16a), we were not able to build ray-parameter CIGs with horizons for all ray-parameters. This is demonstrated by selected CIGs shown in Figure 4.17 where only DPW traces within area A were used for migration. Horizons in only negative $\mathbf{p}_r$ were built due to omitting plane wave energy where $\mathbf{p}_s < \mathbf{p}_r$ for migration.

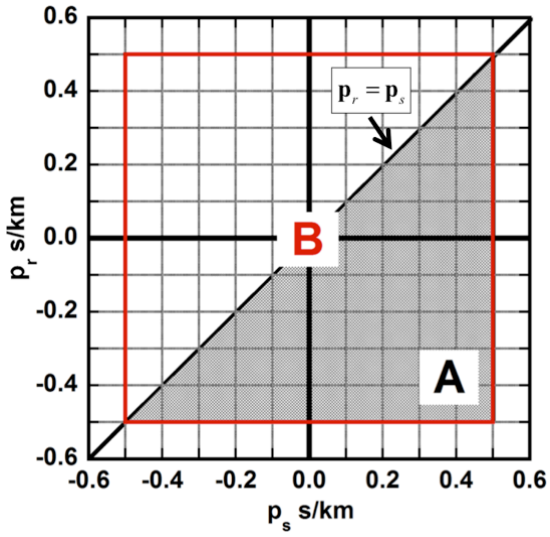

Figure 4.15. The horizontal plane of the DPW dataset. The red squared area is labeled by letter B where $\mathbf{p}_s$ = -0.5 ~ 0.5 s/km and $\mathbf{p}_r$ = -0.5 ~ 0.5 s/km. The shadowed triangular is labeled by letter A where $\mathbf{p}_s > \mathbf{p}_r$. The diagonal line indicates the line that $\mathbf{p}_s = \mathbf{p}_r$.

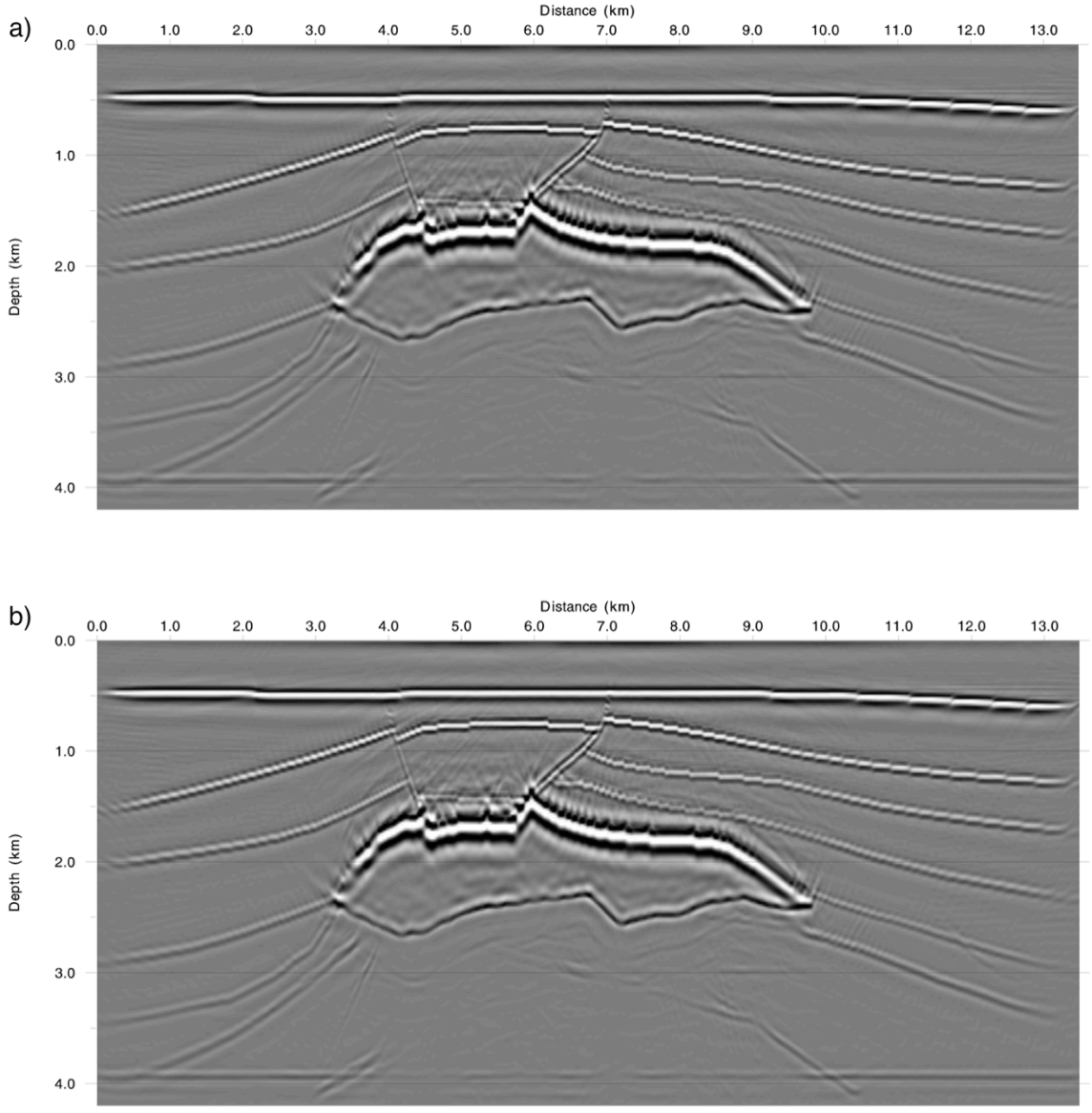

Figure 4.16. a) An image obtained by migrating DPW traces inside area A in Figure 4.15.
b) An image obtained by migrating DPW traces inside area B Figure 4.15.

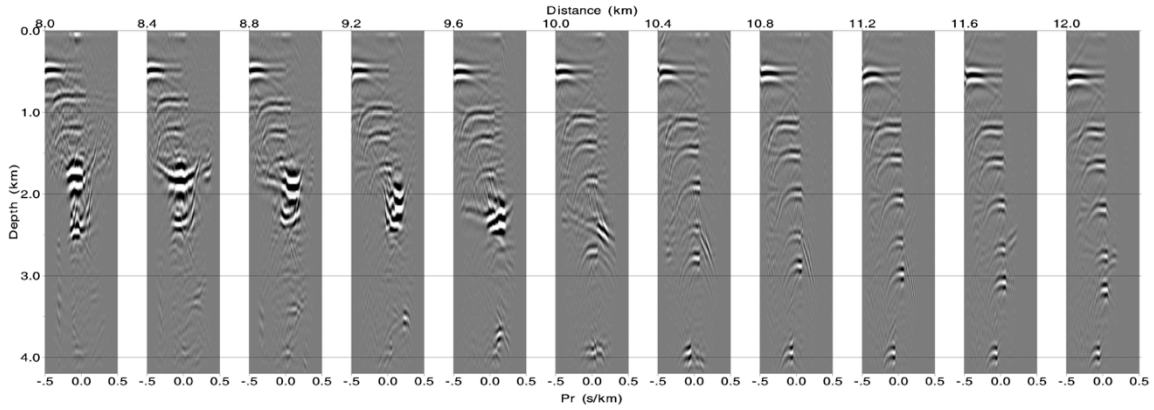

Figure 4.17. Selected CIGs for migrating DPW traces in the shadowed triangular area A.

Migrating DPW traces within area A with the reciprocity applied generated the image shown in Figure 4.18. The image is visually identical to the image shown in Figure 4.16b) where all traces within area B were used migrated. However, utilizing the reciprocity principle, the number of DPW traces used for migration was reduced by half, hence, the increase in migration efficiency. Selected CIGs shown in Figure 4.19a) and 4.18b) were obtained by migrating DPW traces labeled by A and B, respectively. The reciprocity principle was used to generate Figure 4.19a). The two selected CIGs show very similar pattern. Comparing with the CIGs shown in Figure 4.17, the CIGs shown in Figure 4.19a) had continuous horizons across all $\mathbf{p}_r$ as if all the DPW traces in the squared area B were migrated.

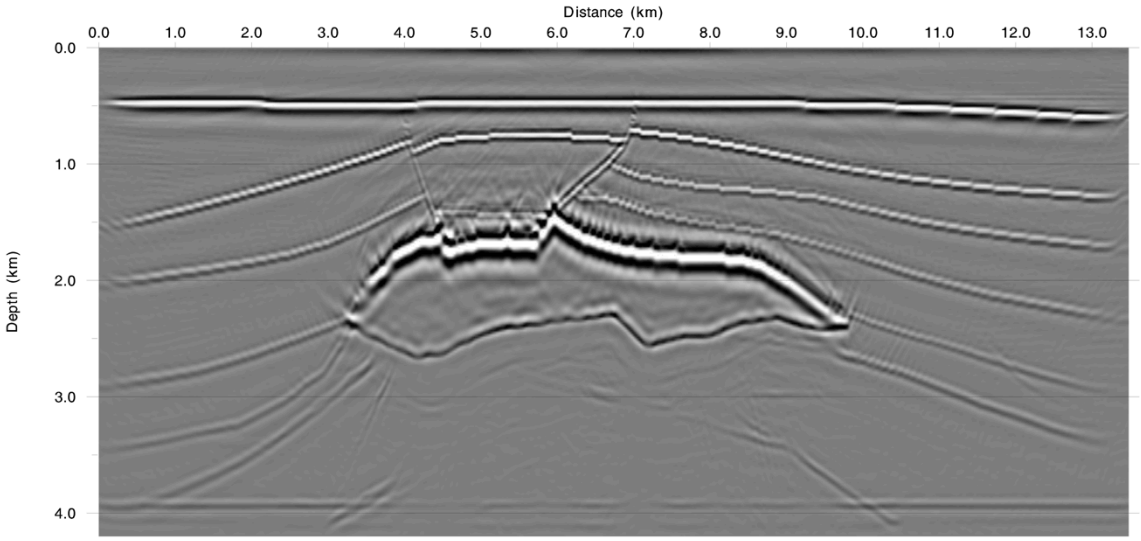

Figure 4.18. An image obtained by migrating DPW traces within area B in Figure 4.15. The reciprocity principle was applied to reduce the number of input traces.

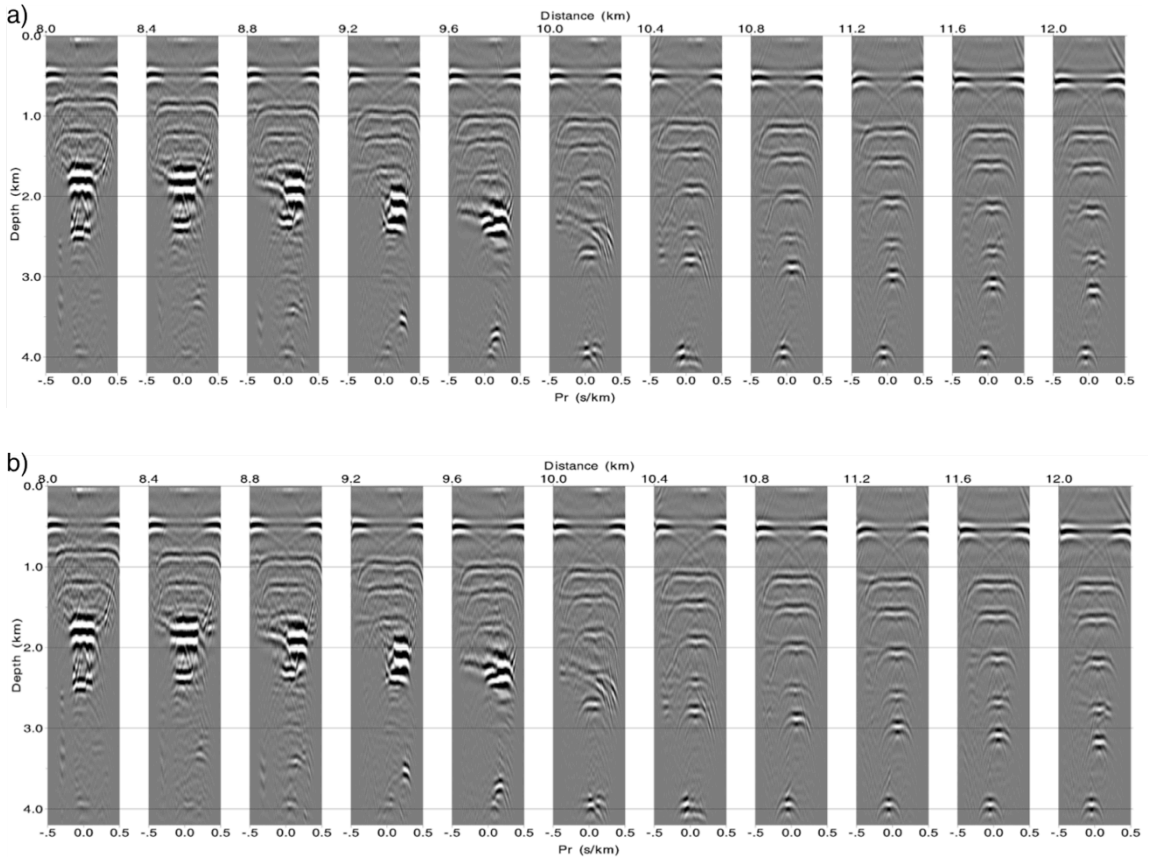

Figure 4.19. Selected CIGs obtained by migrating the merged reciprocal DPW dataset. a) DPW traces within area A in Figure 4.15 were used for migration. The reciprocity principle was applied for the DPW RTM. b) DPW traces within area B in Figure 4.15 were used for migration.

4.8. CONCLUSIONS

In this chapter, the use of the reciprocity principle in obtaining an optimal DPW dataset was investigated, so that plane energy in both positive and negative $\mathbf{p}_s$ and $\mathbf{p}_r$ sections can be recovered. An easy and efficient way to generate optimal reciprocal DPW datasets from one-sided gathers was proposed. I demonstrated that the reciprocal DPW dataset transformed from one-sided gathers was in good agreement with the DPW dataset

transformed from split-spread gathers given the same maximum acquisition aperture. I showed that for a fixed number of receivers, a one-sided acquisition geometry is preferred over a split-spread geometry, because longer acquisition aperture can be achieved to acquire more seismic information. The split-spread information can be obtained using the reciprocity principle for the DPW dataset. Utilizing the reciprocity principle, the efficiency of the DPW RTM can be improved by reducing the number of traces needed for migration.

Chapter 5: Double Plane Wave Least Squares Reverse Time Migration

5.1. INTRODUCTION

Seismic migration technique is critical in recovering subsurface structures. Given a seismic dataset and subsurface models, performing migration can produce subsurface images with location and amplitude information. The obtained images can be used to predict seismic data by the seismic modeling technique. Comparing the predicted data with the observed data, we can verify our original models. The migration and the modeling techniques are essentially multidimensional filtering processes, which were recognized to have errors due to inadequacies in the data (Nemeth et al., 1999) or the digital implementation (e.g. finite filter lengths or bandwidth limitations in space or time for the filter and the data). The errors that generated by the filtering processes can be reduced if we minimize the misfit between the predicted data and the observed data. The most commonly used measure to minimize the misfit is the least error energy filter, which is known as the least squares migration (Schuster 1993).

The least squares migration (Schuster 1993; Nemeth et al., 1999) has been successfully implemented to obtain images with high resolution, accurate reflectivity and reduced migration noises. Those images are more readily interpreted and closer to the desired result in the least squared error energy sense. The least squares migration is often performed in the data space that requires a great number of iterations to update reflectivity models. For large seismic datasets, a large amount of forward modeling and migration operations are needed in each iteration, which makes the least square migration a time consuming procedure.

Traditional shot profile least squares RTM (Dong et al., 2012) in the time domain needs three explicit wavefield propagation processes per iteration: one forward Born modeling, one forward wavefield simulation for synthetic sources, and one backward wavefield simulation for shot gathers. The number of wavefield propagation processes increases dramatically with increasing number of shots and iterations. Phase encoded or multi-source least squares RTM (Dai et al., 2011; Dai and Schuster 2013) has been proposed to reduce the number of wavefield propagations, so that the migration efficiency of the least squares RTM can be improved.

The shot profile least squares RTM in the frequency domain (Ren et al., 2013) has the potential to be more efficient than the time domain least squares RTM in that it might not require wavefield computations during the iterative model updating processes. In the frequency domain, the Born modeling and migration operators can be explicitly represented with source and receiver Green's functions. Once the source and receiver Green's functions are pre-computed, they can be utilized for both the Born modeling and the migration operations throughout iterations. As a result, the efficiency of the shot profile least squares RTM can be improved. However, if source and receiver locations do not coincide, and the number of receivers is large, computing and storing Green's functions for all shot and receiver locations becomes infeasible. Consequently, frequency domain shot profile least squares RTM is rarely implemented using both source and receiver Green's functions.

In this chapter, I describe the least squares RTM with double plane wave (DPW) data in the DPW-frequency domain, which is a fully decomposed plane wave domain (Zhao, Sen, et al., 2014). Here, I derive a Born modeling operator that predicts the DPW data at the surface with reflectivity models. The proposed modeling operator is named as DPW Born modeling operator. The adjoint of the DPW Born modeling operator is

recognized as the frequency domain DPW RTM operator (Zhao et al., 2015). The DPW Born modeling operator together with it adjoint leads to an efficient DPW least squares RTM. To improve the convergence rate and obtain images with better balanced amplitude, I derive an approximate Hessian matrix for the misfit function of the DPW data. The diagonal matrix of the approximate Hessian is used as the pre-conditioner for the gradient of the misfit function. I show that the wavefield propagations are not required for the DPW least squares RTM during model updating processes, which significantly improves the efficiency of the least squares RTM.

I first discuss shot profile least squares RTM in the frequency and the time domains. Then, starting with a new misfit function for the DPW data, I introduce the DPW Born modeling operator in the frequency domain. Two synthetic examples are used to demonstrate that the proposed DPW least squares RTM can generate migration images with improved spatial resolution and more balanced amplitude than the traditional RTM. Also, migration artifacts can be reduced during the model updating process.

5.2. SHOT PROFILE LEAST SQUARES RTM

5.2.1. Misfit function

Migration can be formulated as an inverse problem by minimizing differences between observed data and predicted data (Tarantola 1984). The differences are usually defined by a misfit function, which can be written as

$$F(\mathbf{m}) = \frac{1}{2}\delta\mathbf{d}^{\dagger}\delta\mathbf{d}, \tag{5.1}$$

where $F(\mathbf{m})$ is the misfit function (also known as the objective function), $\mathbf{m}$ is the model parameter, $\delta\mathbf{d} = \mathbf{d}_{obs} - \mathbf{d}_{pre}$ is the difference between the observed data $\mathbf{d}_{obs}$ and the predicted data $\mathbf{d}_{pre}$, and the superscript † represents the adjoint operator (conjugate transpose). $\mathbf{d}_{pre}$ is a function of the model parameter, (i.e., $\mathbf{d}_{pre} = \mathbf{d}_{pre}(\mathbf{m})$). The best model parameter is found as the misfit function reaches its minimum.

Expanding the misfit function in the vicinity of the best solution of the least squares problem (i.e., equation (5.1)) and retaining terms up to the quadratic order (Pratt et al., 1998; Virieux and Operto 2009), the misfit function becomes

$$F(\mathbf{m}_0 + \delta\mathbf{m}) = F(\mathbf{m}_0) + \delta\mathbf{m}^T \nabla_{\mathbf{m}} F(\mathbf{m}_0) + \frac{1}{2}\delta\mathbf{m}^T \mathbf{H} \delta\mathbf{m} + O(|\delta\mathbf{m}|^3), \tag{5.2}$$

where $\mathbf{m}_0$ is the starting model in the vicinity of the best model, $\delta\mathbf{m}$ is the model perturbation, the superscript T represents the transpose of a matrix, $\nabla_{\mathbf{m}} F(\mathbf{m}_0)$ is the gradient of the misfit function with respect to the model parameter at $\mathbf{m}_0$, and $\mathbf{H}$ is the Hessian second derivative matrix of the misfit function. In this case, the gradient and the Hessian matrix are defined as

$$\nabla_{\mathbf{m}} F(\mathbf{m}_0) = \frac{\partial F(\mathbf{m}_0)}{\partial \mathbf{m}}, \tag{5.3}$$

and

$$\mathbf{H} = \frac{\partial^2 F(\mathbf{m}_0)}{\partial \mathbf{m}^2}, \tag{5.4}$$

respectively.

The misfit function reaches its minimum when the gradient of the misfit function vanishes (Tarantola 1984; Pratt et al., 1998). So, taking the gradient of right hand side of equation (5.2), and setting it equals to zero, we obtain

$$\delta \mathbf{m} = -\mathbf{H}^{-1} \nabla_{\mathbf{m}} F(\mathbf{m}_0), \tag{5.5}$$

where $\mathbf{H}^{-1}$ is the inverse of the Hessian matrix. In linear cases, equation (5.5) can be used to minimize a misfit function and achieve the best model parameter in one iteration. Therefore, the gradient and the Hessian of the misfit function are required to implement equation (5.5). The model update is calculated by scaling the gradient in the opposite direction with the inverse of the Hessian matrix at $\mathbf{m}_0$.

Taking the first and the second derivative for $F(\mathbf{m})$ with respect to the model parameter $\mathbf{m}$ at $\mathbf{m}_0$ and retaining the real part of the derivatives, we can obtain

$$\nabla_{\mathbf{m}} F(\mathbf{m}_0) = \mathrm{Re}(\mathbf{J}_0^{\dagger} \delta \mathbf{d}_0) \tag{5.6}$$

and

$$\mathbf{H} = \mathrm{Re}[\mathbf{J}_0^{\dagger} \mathbf{J}_0 + \frac{\partial}{\partial \mathbf{m}^T} \mathbf{J}_0^{\dagger} (\delta \mathbf{d}_0 .. \delta \mathbf{d}_0)], \tag{5.7}$$

for $\nabla_{\mathbf{m}} F(\mathbf{m})$ and $\mathbf{H}$, at $\mathbf{m}_0$, respectively. $\delta \mathbf{d}_0$ is the initial data misfit. $\mathbf{J}_0 = \frac{\partial \mathbf{d}_{pre}(\mathbf{m}_0)}{\partial \mathbf{m}}$ is the sensitive matrix or the Fréchet derivative matrix. Detailed derivations for equations (5.6) and (5.7) are reported elsewhere (Plessix and Mulder 2004). The second term of the Hessian matrix is relatively small, so it can be neglected in

most cases. Therefore, substituting the gradient (i.e., $\mathrm{Re}(\mathbf{J}_0^\dagger \delta\mathbf{d}_0)$) and the approximate Hessian $\mathbf{H}_a = \mathrm{Re}(\mathbf{J}_0^\dagger \mathbf{J}_0)$ into equation (5.5), the model perturbation or the model update $\delta\mathbf{m}$ can be written as

$$\delta\mathbf{m} \approx -\mathrm{Re}(\mathbf{J}_0^\dagger \mathbf{J}_0)^{-1}\,\mathrm{Re}(\mathbf{J}_0^\dagger \delta\mathbf{d}_0). \tag{5.8}$$

In linear cases, $\mathbf{d}(\mathbf{m}) = \mathbf{L}\mathbf{m}$, where $\mathbf{L}$ is the forward modeling operator, so $\mathbf{J} = \mathbf{L}$. Therefore, we have

$$\nabla_{\mathbf{m}} F(\mathbf{m}_0) = \mathrm{Re}(\mathbf{L}^\dagger \delta\mathbf{d}_0), \tag{5.9}$$

and

$$\mathbf{H}_a = \mathrm{Re}[\mathbf{L}^\dagger \mathbf{L}], \tag{5.10}$$

where $\mathbf{L}^\dagger$ is the adjoint of the forward operator $\mathbf{L}$. And model update can be computed by

$$\delta\mathbf{m} \approx -\mathrm{Re}(\mathbf{L}^\dagger \mathbf{L})^{-1}\,\mathrm{Re}(\mathbf{L}^\dagger \delta\mathbf{d}_0). \tag{5.11}$$

To implement equation (5.11), $\mathbf{L}$ can be chosen from the Kirchhoff modeling operator, in the Gaussian beam modeling operator or the wave equation modeling operator. Similarly the $\mathbf{L}^\dagger$ can be chosen from the Kirchhoff migration operator, the Gaussian beam migration operator or the wave equation migration operator. In the following sections, we will focus on minimizing the misfit function with least squares RTM

methods. Therefore, the operators $\mathbf{L}$ and $\mathbf{L}^{\dagger}$ are based on solving the two-way wave equation.

5.2.2. Shot profile least squares RTM in the frequency domain

In the frequency domain, the constant density acoustic two-way wave equation can been written as (Marfurt 1984; Pratt et al., 1998)

$$(-\nabla^2 - \sigma_0^2(\mathbf{x})\omega^2)u_0(\mathbf{s},\mathbf{x},\omega) = f(\omega), \tag{5.12}$$

where ∇^2 is the Laplacian operator, $\sigma_0(\mathbf{x})$ is the subsurface background slowness at subsurface point $\mathbf{x}$, $\mathbf{s}$ is the source location, ω is the angular frequency, $u_0(\mathbf{s},\mathbf{x},\omega)$ is the wavefield created by $\mathbf{s}$, and $f(\omega)$ is the frequency source term at the source location. $u_0(\mathbf{s},\mathbf{x},\omega)$ is often called the incident wavefield or the background wavefield.

The square of the slowness model can be expressed as a sum of the square of the background slowness and a perturbation:

$$\sigma^2(\mathbf{x}) = \sigma_0{}^2(\mathbf{x}) + m(\mathbf{x}), \tag{5.13}$$

where $m(\mathbf{x})$ is the slowness perturbation. Similarly, we can write the corresponding wavefield as follows

$$u(\mathbf{s},\mathbf{x},\omega) = u_0(\mathbf{s},\mathbf{x},\omega) + \delta u(\mathbf{s},\mathbf{x},\omega), \tag{5.14}$$

where $u(\mathbf{s},\mathbf{x},\omega)$ is the total wavefield, and $\delta u(\mathbf{s},\mathbf{x},\omega)$ is the scattered wavefield (or wavefield perturbation) introduced by the slowness perturbation. The total wavefield $u(\mathbf{s},\mathbf{x},\omega)$ satisfies the wave equation

$$(-\nabla^2 - \sigma^2(\mathbf{x})\omega^2)u(\mathbf{s},\mathbf{x},\omega) = f(\omega). \tag{5.15}$$

Substituting equations (5.13) and (5.14) into equation (5.15) we can obtain

$$(-\nabla^2 - \sigma_0^2(\mathbf{x})\omega^2)\delta u(\mathbf{s},\mathbf{x},\omega) = \omega^2 m(\mathbf{x})[u_0(\mathbf{s},\mathbf{x},\omega) + \delta u(\mathbf{s},\mathbf{x},\omega)]. \tag{5.16}$$

The higher order term $\omega^2 m(\mathbf{x})\delta u(\mathbf{s},\mathbf{x},\omega)$ is ignored according to the Born approximation (Plessix and Mulder 2004; Virieux and Operto 2009). Therefore, equation (5.16) becomes

$$(-\nabla^2 - \sigma_0^2(\mathbf{x})\omega^2)\delta u(\mathbf{s},\mathbf{x},\omega) = \omega^2 m(\mathbf{x})u_0(\mathbf{s},\mathbf{x},\omega). \tag{5.17}$$

The scattered wavefield $\delta u(\mathbf{s},\mathbf{x},\omega)$ can be calculated using equation (5.17) with $\omega^2 m(\mathbf{x})$ serving as the source wavefield.

Because a Green's function satisfies

$$(-\nabla^2 - \sigma_0^2(\mathbf{x})\omega^2)G(\mathbf{s},\mathbf{x},\omega) = \delta(\mathbf{s}-\mathbf{x}), \tag{5.18}$$

where the Green's function $G(\mathbf{s},\mathbf{x},\omega)$ represents the computed wavefield with the impulse source $\delta(\mathbf{s}-\mathbf{x})$ located at $\mathbf{s}$. Therefore, the scattered wavefield $\delta u(\mathbf{s},\mathbf{y},\omega)$ measured at the subsurface point $\mathbf{y}$, can be computed with a Green's function and the source wavefield $m(\mathbf{x})u_0(\mathbf{s},\mathbf{x},\omega)$ as

$$\delta u(\mathbf{s},\mathbf{y},\omega) = \omega^2 \sum_{\mathbf{x}} m(\mathbf{x}) u_0(\mathbf{s},\mathbf{x},\omega) G(\mathbf{x},\mathbf{y},\omega). \tag{5.19}$$

According to equations (5.12) and (5.18), the incident wavefield $u_0(\mathbf{s},\mathbf{x},\omega)$ can be represented as

$$u_0(\mathbf{s},\mathbf{x},\omega) = f(\omega) G(\mathbf{s},\mathbf{x},\omega). \tag{5.20}$$

Substituting equation (5.20) into equation (5.19) and projecting the scattered wavefield to receiver locations, the predicted wavefield measured at the receiver location $\mathbf{r}$ can be written as

$$d_{pre}(\mathbf{s},\mathbf{r},\omega,m(\mathbf{x})) = \omega^2 \sum_{\mathbf{x}} m(\mathbf{x}) f(\omega) G(\mathbf{s},\mathbf{x},\omega) G(\mathbf{x},\mathbf{r},\omega). \tag{5.21}$$

where $G(\mathbf{x},\mathbf{r},\omega) = G(\mathbf{r},\mathbf{x},\omega)$ due to their reciprocity. Equation (5.21) can be written in a matrix form as

$$\mathbf{d}_{pre}(\mathbf{m}) = \mathbf{L}\mathbf{m}, \tag{5.22}$$

where $\mathbf{L}$ depends on $f(\omega)$, ω, and Green's functions $G(\mathbf{s},\mathbf{x},\omega)$ and $G(\mathbf{x},\mathbf{r},\omega)$. Equation (5.22) is often called the Born modeling, and $\mathbf{L}$ is known as the Born modeling operator.

Taking the adjoint of $\mathbf{L}$ and substituting it into equation (5.9), the gradient can be expressed in an entry wise multiplication form as (Plessix and Mulder 2004; Virieux and Operto 2009; Ren et al., 2013; Tao and Sen 2013)

$$g(\mathbf{x}) = \mathrm{Re}(\sum_{\omega}\sum_{\mathbf{s}}\sum_{\mathbf{r}} \omega^2 f^*(\omega) G^*(\mathbf{s},\mathbf{x},\omega) G^*(\mathbf{r},\mathbf{x},\omega) \times (d_{pre}(\mathbf{s},\mathbf{r},\omega,m(\mathbf{x})) - d_{obs}(\mathbf{s},\mathbf{r},\omega))). \tag{5.23}$$

where the superscript * represents the complex conjugate of a complex number. Equation (5.23) is also recognized as the imaging condition of the shot profile RTM in the frequency domain. Equation (5.23) can be written in a matrix form as

$$\nabla_{\mathbf{m}} F(\mathbf{m}) = \mathrm{Re}(\mathbf{L}^{\dagger}\delta\mathbf{d}), \tag{5.24}$$

where $\mathbf{L}^{\dagger}$ is the RTM operator in the frequency domain. Because a great number of receivers are often deployed in a seismic survey, computing and storing the Green's function for each receiver location is computationally expensive. Therefore, the adjoint state method (Pratt 1999; Plessix 2006), which requires forward and backward wavefield computations, is typically implemented to evaluate the gradient, and $G(\mathbf{x},\mathbf{r},\omega)$ is rarely computed.

Substituting $\mathbf{L}$ and $\mathbf{L}^{\dagger}$ into equation (5.10), we can obtain the approximate Hessian matrix in an entry wise multiplication form as (Plessix and Mulder 2004)

$$H_a(\mathbf{x},\mathbf{y}) = \mathrm{Re}(\sum_{\omega} \omega^4 ||f(\omega)||^2 \sum_{\mathbf{s}} G(\mathbf{s},\mathbf{x},\omega) G^*(\mathbf{s},\mathbf{y},\omega) \sum_{\mathbf{r}} G(\mathbf{r},\mathbf{x},\omega) G^*(\mathbf{r},\mathbf{y},\omega)). \quad (5.25)$$

According to equation (5.11), the frequency domain least squares RTM requires the approximate Hessian matrix and the gradient to achieve the best model in one iteration. However, the size of an approximate Hessian matrix can be enormous, explicitly constructing and inverting such large matrices are computationally expensive. Therefore, iterative methods are often used to minimize the misfit function.

Iteratively solving equation (5.11) can be expressed as (Tarantola 1984; Claerbout 1985)

$$\mathbf{m}^{k+1} = \mathbf{m}^k + \alpha \mathbf{K}[\mathbf{L}^{\dagger}(\mathbf{L}\mathbf{m}^k - \mathbf{d}_{obs})] \quad (5.26)$$

where $\mathbf{m}^{k+1}$ is the current updated reflectivity at step k+1, $\mathbf{m}^k$ is the previous reflectivity, α is the step length along the gradient direction. $\mathbf{K}$ is the pre-conditioning matrix, which can speed up the convergence of the iterative process. In the frequency domain, the inverse of the diagonal matrix of the approximate Hessian matrix, $\mathbf{H}_{diag}$, is often chosen to be $\mathbf{K}$. Therefore, the diagonal element of $\mathbf{K}$ can be computed by

$$K(\mathbf{x},\mathbf{x}) = H_a(\mathbf{x},\mathbf{x}) = \mathrm{Re}(\sum_{\omega} \omega^4 ||f(\omega)||^2 \sum_{\mathbf{s}} ||G(\mathbf{s},\mathbf{x},\omega)||^2 \sum_{\mathbf{r}} ||G(\mathbf{r},\mathbf{x},\omega)||^2)^{-1}. \quad (5.27)$$

According to equation (5.27), both $G(\mathbf{s},\mathbf{x},\omega)$ and $G(\mathbf{r},\mathbf{x},\omega)$ need to be explicitly computed for each source and receiver location to construct the pre-conditioning matrix. $G(\mathbf{s},\mathbf{x},\omega)$ can be easily obtained, as it has been computed during the gradient computation. However, as previously stated, computing $G(\mathbf{r},\mathbf{x},\omega)$ for each receiver location is not trivial, and equation (5.27) is rarely implemented.

Assuming the receiver coverage is infinite for each shot, the term $\sum_{\mathbf{r}} ||G(\mathbf{r},\mathbf{x},\omega)||^2$ becomes nearly a constant (Plessix and Mulder 2004). Therefore, the term $\sum_{\mathbf{r}} ||G(\mathbf{r},\mathbf{x},\omega)||^2$ can be dropped and the diagonal element of $\mathbf{K}$ can be approximated by

$$K(\mathbf{x},\mathbf{x}) \approx \mathrm{Re}\Big(\sum_{\omega} \omega^4 ||f(\omega)||^2 \sum_{\mathbf{s}} ||G(\mathbf{s},\mathbf{x},\omega)||^2\Big)^{-1}. \tag{5.28}$$

Equation (5.28) can be easily implemented, and $\mathbf{K}$ is often referred to as the illumination compensation pre-conditioner (Plessix and Mulder 2004; Zhang et al., 2005). Once $\mathbf{K}$ is computed, it can be used throughout the iterative updating process. Other approximations to equation (5.27) were proposed, and details about those approximations can be found in Plessix and Mulder 2004.

If the number of $G(\mathbf{s},\mathbf{x},\omega)$ and $G(\mathbf{r},\mathbf{x},\omega)$ are relative small, the Green's functions can be pre-computed and stored in the computer's memories or disks. Then, the Born modeling and the frequency domain RTM processes can be directly implemented according to equations (5.21) and (5.23). Therefore, only cross-correlation operations are performed during iterations to obtain the gradient and the predicted data, and wavefield computation processes are no longer required, which reduces the computational cost. However, if the number of sources and receivers is large, computing and storing a large

number of Green's functions become infeasible. In those cases, the adjoint state method is implemented to compute the gradient. The Born modeling process is computed using equation (5.17). Therefore, two forward and one backward wavefield computations are required for each shot location per iteration. The computational cost increases dramatically with increasing shots and iterations.

5.2.3. Shot profile least squares RTM in the time domain

In the time domain, the constant density two-way wave equation becomes

$$(\sigma_0^2(\mathbf{x})\frac{\partial^2}{\partial t^2}-\nabla^2)u_0(\mathbf{s},\mathbf{x},t)=f(t), \tag{5.29}$$

where $\frac{\partial^2}{\partial t^2}$ is the second derivative of wavefield $u_0(\mathbf{s},\mathbf{x},t)$ with respect to time, and $f(t)$ is the source time series. Equation (5.17) can be written in the time domain as

$$(\sigma_0^2(\mathbf{x})\frac{\partial^2}{\partial t^2}-\nabla^2)\delta u(\mathbf{s},\mathbf{x},t)=m(\mathbf{x})\frac{\partial^2 u_0(\mathbf{s},\mathbf{x},t)}{\partial t^2}, \tag{5.30}$$

where $\delta u(\mathbf{s},\mathbf{x},t)$ is the scattered wavefield in the time domain. Equation (5.30) indicates that the scattered wavefield can be computed by solving the wave equation by injecting the source, which is the product of the reflectivity and the background wavefield, at each location **x**. Equation (5.30) can be written in a symbolic matrix form as in equation (5.22), so the predicted wavefield is in a linear relationship with the reflectivity. And

equation (5.30) is used to perform the Born modeling in the time domain, which has a symbolic matrix form of $\mathbf{L}$.

As previously stated, in the frequency domain, the gradient can be computed by the adjoint state method. In the time domain, the adjoint state method is also implemented to evaluate the gradient. The gradient can be written as

$$g(\mathbf{x}) = \sum_{\mathbf{s}} \sum_{t} \frac{\partial^2 u_0(\mathbf{s},\mathbf{x},t)}{\partial t^2} q(\mathbf{s},\mathbf{x},t), \tag{5.31}$$

where the $u_0(\mathbf{s},\mathbf{x},t)$ is the background wavefield obtained via solving equation (5.29), and the $q(\mathbf{s},\mathbf{x},t)$ is the backward propagated wavefield obtained by solving

$$(\sigma_0^2(\mathbf{x})\frac{\partial^2}{\partial t^2} - \nabla^2) q(\mathbf{s},\mathbf{x},t) = d_{obs}(\mathbf{s},\mathbf{r},t), \tag{5.32}$$

where $d_{obs}(\mathbf{s},\mathbf{r},t)$ is the shot gather for a given $\mathbf{s}$. Equation (5.31) is also known as the imaging condition for the shot profile RTM in the time domain (Zhang et al., 2007; Chattopadhyay and McMechan 2008; Zhang and Sun 2008). The time domain RTM is symbolically expressed as $\mathbf{L}^{\dagger}$.

To implement the shot profile least squares RTM in the time domain, the reflectivity model is iteratively updated using equation (5.26). The pre-conditioner in the time domain is often chosen as

$$K(\mathbf{x},\mathbf{x}) \approx (\sum_{\mathbf{s}} \sum_{t} \left\| \frac{\partial^2 u_0(\mathbf{s},\mathbf{x},t)}{\partial t^2} \right\|^2)^{-1}, \tag{5.33}$$

which is the time domain equivalent of equation (5.28).

In the time domain, implementing equation (5.26) requires performing the shot profile Born modeling and the RTM for each shot per iteration. The Born modeling process requires performing forward propagation. The RTM requires forward propagation for sources and backward propagation for shot gathers. Therefore, at least three wavefield propagations are needed for each shot per iteration.

In both the time and the frequency domains, the number of wavefield calculations required by the least squares RTM is much larger than that required by the traditional RTM. So, least squares RTM is considered to be computationally expensive. Phase encoding (Dai et al., 2011), and plane wave least squares RTM (Dai and Schuster 2013) methods were introduced to reduce the number of wavefield propagations. By using the composite shot gathers or plane wave data in the $\tau - \mathbf{p}$ domain, those methods greatly reduce the number of wavefield propagations in each iteration, leading to increase in migration efficiency. However, almost all of those methods were implemented in the time domain, and they all require wavefield propagations during the iterative updating process. To further reduce computational cost of the least square RTM, I consider performing least square RTM in the frequency domain using DPW data. In the following section, I will introduce the DPW least squares RTM in the frequency domain, where wavefield propagation is not required during the model updating process. As a result, the efficiency of the least squares RTM can be significantly improved.

5.3. DPW LEAST SQUARES RTM

5.3.1. Misfit function

In the DPW domain, the objective is again to minimize the differences between predicted data and observed data, while DPW data transformed from shot gathers become our observed data. Therefore, we define the misfit function as

$$\hat{F}(\mathbf{m}) = \frac{1}{2}\delta\hat{\mathbf{d}}^{\dagger}\delta\hat{\mathbf{d}}, \tag{5.34}$$

where $\hat{F}(\mathbf{m})$ is the misfit function for the DPW data, $\delta\hat{\mathbf{d}} = \hat{\mathbf{d}}_{pre} - \hat{\mathbf{d}}_{obs}$, $\hat{\mathbf{d}}_{pre}$ is the predicted DPW data, and $\hat{\mathbf{d}}_{obs}$ is the observed DPW data.

Following the same derivation as equations (5.1) to (5.11), we can arrive at an expression for the best-fitted reflectivity model:

$$\delta\mathbf{m} \approx -\hat{\mathbf{H}}_a^{-1}\nabla_{\mathbf{m}}\hat{F}(\mathbf{m}_0). \tag{5.35}$$

$\nabla_{\mathbf{m}}\hat{F}(\mathbf{m}_0)$ and $\hat{\mathbf{H}}_a$ are defined as follows:

$$\nabla_{\mathbf{m}}\hat{F}(\mathbf{m}_0) = \mathrm{Re}(\hat{\mathbf{L}}^{\dagger}\delta\mathbf{d}_0), \tag{5.36}$$

and

$$\hat{\mathbf{H}}_a = \mathrm{Re}[\hat{\mathbf{L}}^{\dagger}\hat{\mathbf{L}}], \tag{5.37}$$

where $\hat{\mathbf{L}}$ is the forward modeling operator for the DPW data, and $\hat{\mathbf{L}}^{\dagger}$ is the adjoint of the forward operator $\hat{\mathbf{L}}$. If both $\nabla_{\mathbf{m}}\hat{F}(\mathbf{m}_0)$ and $\hat{\mathbf{H}}_a^{-1}$ are available, the best-fitted model can be obtained in one iteration.

5.3.2. DPW Born modeling and DPW RTM operators

In this section, I start with the frequency domain shot profile Born modeling operator and derive the DPW Born modeling operator. I also show that the adjoint operator of the DPW Born modeling operator has a similar form to that of the frequency domain DPW RTM imaging condition introduced in Chapter 3.

The shot profile Born modeling operator in the frequency domain (i.e., equation (5.21)) can be rewritten in the continuous form as

$$d_{pre}(\mathbf{s},\mathbf{r},\omega,m(\mathbf{x})) = \omega^2 \int m(\mathbf{x}) f(\omega) G(\mathbf{s},\mathbf{x},\omega) G(\mathbf{r},\mathbf{x},\omega) d\mathbf{x}. \tag{5.38}$$

Performing the double slant stacking (i.e., equation (1.9)) for equation (5.38) (Zhao, Sen, Stoffa, et al., 2015), we can obtain

$$\begin{aligned} &\iint d_{pre}(\mathbf{s},\mathbf{r},\omega,m(\mathbf{x}))\exp(-i\omega(\mathbf{p}_s(\mathbf{s}-\mathbf{x}_{ref})+\mathbf{p}_r(\mathbf{r}-\mathbf{x}_{ref})))d\mathbf{s}d\mathbf{r} \\ &= \omega^2 \iiint m(\mathbf{x}) f(\omega) G(\mathbf{s},\mathbf{x},\omega) G(\mathbf{r},\mathbf{x},\omega) \\ &\times \exp(-i\omega(\mathbf{p}_s(\mathbf{s}-\mathbf{x}_{ref})+\mathbf{p}_r(\mathbf{r}-\mathbf{x}_{ref})))d\mathbf{x}d\mathbf{s}d\mathbf{s}d\mathbf{r}. \end{aligned} \tag{5.39}$$

Rearranging terms in equation (5.39), we get

$$d_{pre}(\mathbf{p}_s,\mathbf{p}_r,\omega,m(\mathbf{x})) = \omega^2 f(\omega)\int m(\mathbf{x}) \times\int G(\mathbf{s},\mathbf{x},\omega)\exp(-i\omega\mathbf{p}_s\cdot[(\mathbf{s}-\mathbf{x}_h)+(\mathbf{x}_h-\mathbf{x}_{ref})])d\mathbf{s} \times\int G(\mathbf{r},\mathbf{x},\omega)\exp(-i\omega\mathbf{p}_r\cdot[(\mathbf{r}-\mathbf{x}_h)+(\mathbf{x}_h-\mathbf{x}_{ref})])d\mathbf{r}d\mathbf{x}, \quad (5.40)$$

where $\mathbf{x}_h$ is the horizontal location of the subsurface point $\mathbf{x}$. Performing slant stacking for Green's functions, we can achieve

$$d_{pre}(\mathbf{p}_s,\mathbf{p}_r,\omega,m(\mathbf{x})) = \omega^2 f(\omega)\int m(\mathbf{x})G(\mathbf{p}_s,\mathbf{x},\omega)G(\mathbf{p}_r,\mathbf{x},\omega) \times\exp[-i\omega(\mathbf{p}_s+\mathbf{p}_r)\cdot(\mathbf{x}_h-\mathbf{x}_{ref})]d\mathbf{x}, \quad (5.41)$$

where

$$G(\mathbf{p}_s,\mathbf{x},\omega) = \int G(\mathbf{s},\mathbf{x},\omega)\exp[-i\omega\mathbf{p}_s\cdot(\mathbf{s}-\mathbf{x}_h)]d\mathbf{s}, \quad (5.42)$$

and

$$G(\mathbf{p}_r,\mathbf{x},\omega) = \int G(\mathbf{r},\mathbf{x},\omega)\exp[-i\omega\mathbf{p}_r\cdot(\mathbf{r}-\mathbf{x}_h)]d\mathbf{r}. \quad (5.43)$$

$G(\mathbf{p}_s,\mathbf{x},\omega)$ and $G(\mathbf{p}_r,\mathbf{x},\omega)$ are the source and receiver plane wave Green's functions, respectively. The predicted DPW data can be computed via equation (5.41) with a given reflectivity model and plane wave Green's functions. Discretizing equation (5.41), we obtain

$$d_{pre}(\mathbf{p}_s,\mathbf{p}_r,\omega,m(\mathbf{x})) = \omega^2 f(\omega)\sum_{\mathbf{x}} m(\mathbf{x})G(\mathbf{p}_s,\mathbf{x},\omega)G(\mathbf{p}_r,\mathbf{x},\omega) \times \exp[-i\omega(\mathbf{p}_s+\mathbf{p}_r)\cdot(\mathbf{x}_h-\mathbf{x}_{ref})]. \tag{5.44}$$

Equation (5.44) can be written in a matrix form as follows

$$\hat{\mathbf{d}}_{pre}(\mathbf{m}) = \hat{\mathbf{L}}\mathbf{m}, \tag{5.45}$$

where $\hat{\mathbf{L}}$ is the DPW Born modeling operator.

Taking the adjoint of the DPW Born modeling operator and substituting the adjoint into equation (5.36), the discretized gradient for the DPW misfit function can be written as

$$g(\mathbf{x}) = \mathrm{Re}(\sum_{\omega}\omega^2\sum_{\mathbf{p}_s}\sum_{\mathbf{p}_r} f^*(\omega)G^*(\mathbf{p}_s,\mathbf{x},\omega)G^*(\mathbf{p}_r,\mathbf{x},\omega) \times \exp[+i\omega(\mathbf{p}_s+\mathbf{p}_r)\cdot(\mathbf{x}_h-\mathbf{x}_{ref})]\delta\hat{d}(\mathbf{p}_s,\mathbf{p}_r,\omega,m(\mathbf{x}))), \tag{5.46}$$

where

$$\delta\hat{d}(\mathbf{p}_s,\mathbf{p}_r,\omega,m(\mathbf{x})) = \hat{d}_{pre}(\mathbf{p}_s,\mathbf{p}_r,\omega,m(\mathbf{x})) - \hat{d}_{obs}(\mathbf{p}_s,\mathbf{p}_r,\omega). \tag{5.47}$$

Equation (5.46) can be written in a matrix form as

$$\nabla_{\mathbf{m}}\hat{F}(\mathbf{m}) = \mathrm{Re}(\hat{\mathbf{L}}^{\dagger}\delta\mathbf{d}), \tag{5.48}$$

where $\hat{\mathbf{L}}^{\dagger}$ is adjoint operator of $\hat{\mathbf{L}}$. Equation (5.46) is in a form very similar to the frequency domain DPW RTM imaging condition (cf. equation (3.25)) descripted in Chapter 3:

$$I(\mathbf{x}) = \mathrm{Re}(\int \frac{\omega^6}{c^2(\mathbf{x})} \iint f_s^*(\omega) G^*(\mathbf{p}_s, \mathbf{x}, \omega) G^*(\mathbf{p}_r, \mathbf{x}, \omega) \times P(\mathbf{p}_s, \mathbf{p}_r, \omega) \exp(+i\omega(\mathbf{p}_s + \mathbf{p}_r) \cdot (\mathbf{x}_h - \mathbf{x}_{ref})) d\mathbf{p}_s d\mathbf{p}_r d\omega). \tag{5.49}$$

Ignoring the amplitude filtering term, equations (5.46) and (3.25) are the same. Therefore, computing the gradient according to equation (5.46) is the same as performing the frequency domain DPW RTM.

Substituting $\hat{\mathbf{L}}$ and $\hat{\mathbf{L}}^{\dagger}$ into equation (5.37), we obtain expression for the approximate Hessian matrix as

$$\hat{H}_a(\mathbf{x}, \mathbf{y}) = \mathrm{Re}(\sum_{\omega} \omega^4 \sum_{\mathbf{p}_s} \sum_{\mathbf{p}_r} G(\mathbf{p}_s, \mathbf{x}, \omega) G^*(\mathbf{p}_s, \mathbf{y}, \omega) G(\mathbf{p}_r, \mathbf{x}, \omega) G^*(\mathbf{p}_r, \mathbf{y}, \omega) \times |f(\omega)|^2 \exp[+i\omega(\mathbf{p}_s + \mathbf{p}_r) \cdot (\mathbf{x}_h - \mathbf{x}_{ref})] \exp[+i\omega(\mathbf{p}_s + \mathbf{p}_r) \cdot (\mathbf{y}_h - \mathbf{x}_{ref})]). \tag{5.50}$$

Constructing and inverting the above approximate Hessian matrix is still computationally expensive, and the perturbation model is rarely computed by directly implementing equation (5.35). In the following section, two methods by which the misfit function can be iteratively minimized are introduced.

5.3.3. DPW least squares RTM workflow

Similar to the previous introduced shot profile least squares RTM, minimizing the misfit function (5.34) is formulated as an iterative process due to the difficulty of inverting the approximated Hessian matrix. The steepest decent method (Claerbout 1985) can be implemented to the minimization process. The steepest decent method can be written as

$$\mathbf{m}^{k+1} = \mathbf{m}^{k} + \alpha[\hat{\mathbf{L}}^{\dagger}(\hat{\mathbf{L}}\mathbf{m}^{k} - \hat{\mathbf{d}}_{obs})], \tag{5.51}$$

where α is again the step length, $\hat{\mathbf{L}}$ is the DPW Born modeling operator, and $\hat{\mathbf{L}}^{\dagger}$ is the migration operator.

The pre-conditioned steepest decent method, as shown in equation (5.26), can also be implemented to minimize the misfit function for the DPW data. Again, the pre-conditioner is chosen to be the diagonal matrix of the approximate Hessian matrix, $\hat{\mathbf{H}}_{diag}$. And this pre-conditioned steepest method is in a form similar to that of the shot profile least squares RTM:

$$\mathbf{m}^{k+1} = \mathbf{m}^{k} + \alpha\hat{\mathbf{K}}[\hat{\mathbf{L}}^{\dagger}(\hat{\mathbf{L}}\mathbf{m}^{k} - \hat{\mathbf{d}}_{obs})], \tag{5.52}$$

where $\hat{\mathbf{K}}$ is the pre-conditioning matrix (i.e., the inverse of the diagonal matrix of the approximate Hessian matrix $\hat{\mathbf{H}}_{a}$), and α is again the step length (Claerbout 1985). The diagonal element of the proposed pre-conditioning matrix can be calculated by

$$\hat{K}(\mathbf{x},\mathbf{x}) = \mathrm{Re}(\sum_{\omega} \omega^4 \sum_{\mathbf{p}_s} \sum_{\mathbf{p}_r} \left|\left| f(\omega) \right|\right|^2 \left|\left| G(\mathbf{p}_s,\mathbf{x},\omega) \right|\right|^2 \left|\left| G(\mathbf{p}_r,\mathbf{x},\omega) \right|\right|^2 \times \left|\left| \exp[+i\omega(\mathbf{p}_s + \mathbf{p}_r)\cdot(\mathbf{x}_h - \mathbf{x}_{ref})] \right|\right|^2 d\mathbf{p}_s d\mathbf{p}_r d\omega)^{-1}, \tag{5.53}$$

where $\hat{K}(\mathbf{x},\mathbf{x})$ is the diagonal element of the proposed pre-conditioner.

In the updating process, plane wave Green's functions are needed for computing the gradient, the predicted DPW data and the pre-conditioner. Plane wave Green's functions depend on $\mathbf{p}_s$ and $\mathbf{p}_r$ ray-parameters. Hence, a plane wave Green's function can be used for both source and receiver plane waves, if they have the same ray-parameter. Only a limited number of plane wave Green's functions are required to compute all the DPW data and the gradient. In most cases, that number is on an order of hundreds even for datasets that have thousands of shots. Based on tests with synthetic and real datasets, I found that the number of plane wave Green's functions required for the modeling and the migration is about 100 ~ 400. Therefore, all plane wave Green's functions can be pre-computed and stored in disks or memories, and the reflectivity updating process only requires performing cross-correlations. Because wavefield propagations are not necessary in the model updating processes, the efficiency of the least squares RTM is improved significantly. Figure 5.1 demonstrates the workflow of the proposed DPW least squares RTM.

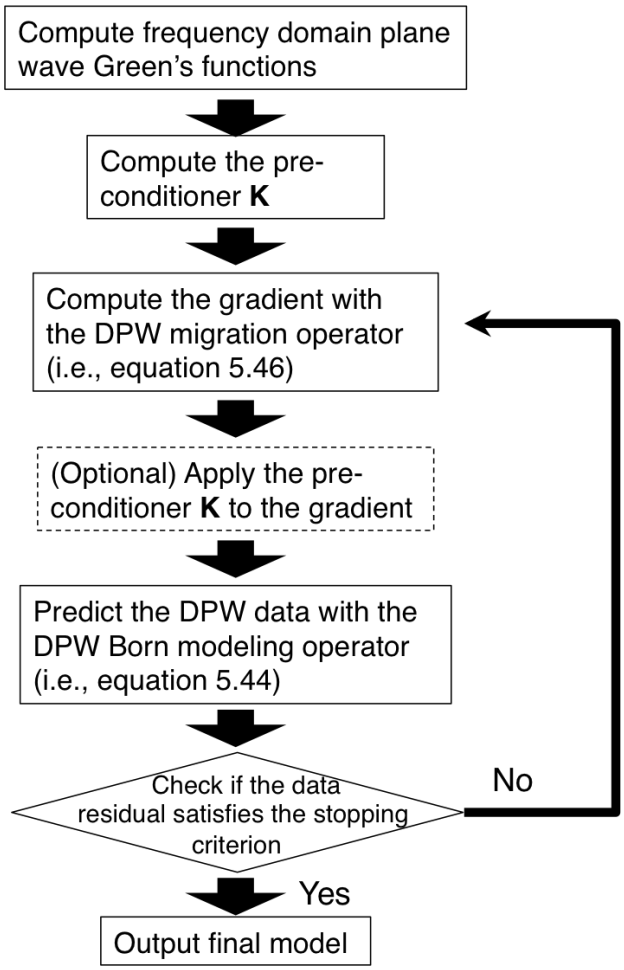

Figure 5.1. An illustration of the workflow of the DPW least squares RTM.

5.3.4. Illumination compensation imaging condition for the frequency domain DPW RTM

According to equations (5.46), (5.52) and (5.53), the pre-conditioned gradient can be written as

$$
\begin{aligned}
n(\mathbf{x}) = \mathrm{Re}(&\sum_{\omega}\omega^2\sum_{\mathbf{p}_s}\sum_{\mathbf{p}_r} f^*(\omega)G^*(\mathbf{p}_s,\mathbf{x},\omega)G^*(\mathbf{p}_r,\mathbf{x},\omega) \\
&\times\exp[+i\omega(\mathbf{p}_s+\mathbf{p}_r)\cdot(\mathbf{x}_h-\mathbf{x}_{ref})]\delta\hat{d}(\mathbf{p}_s,\mathbf{p}_r,\omega,m(\mathbf{x}))) \\
&/(\mathrm{Re}(\sum_{\omega}\omega^4\sum_{\mathbf{p}_s}\sum_{\mathbf{p}_r}\left|\left|f(\omega)\right|\right|^2\left|\left|G(\mathbf{p}_s,\mathbf{x},\omega)\right|\right|^2\left|\left|G(\mathbf{p}_r,\mathbf{x},\omega)\right|\right|^2 \\
&\times\left|\left|\exp[+i\omega(\mathbf{p}_s+\mathbf{p}_r)\cdot(\mathbf{x}_h-\mathbf{x}_{ref})]\right|\right|^2 d\mathbf{p}_s d\mathbf{p}_r d\omega)^{-1}),
\end{aligned}
\tag{5.54}
$$

where $n(\mathbf{x})$ represents the pre-conditioned gradient.

Equation (5.54) is similar to the illumination compensation imaging condition for the time domain DPW-based RTM (cf. equation (2.19)) proposed in Chapter 2:

$$
I_{N\mathbf{P}_s}(\mathbf{x}) = \frac{\sum_{\mathbf{p}_s}\sum_{\mathbf{p}_r}\sum_{\tau}\frac{\partial^2 U_{\mathbf{p}_s}(\mathbf{p}_s,\mathbf{x},\tau)}{\partial\tau^2}U_{\mathbf{p}_r}(\mathbf{p}_s,\mathbf{p}_r,\mathbf{x},\tau-(\mathbf{p}_s+\mathbf{p}_r)\cdot(\mathbf{x}_h-\mathbf{x}_{ref}))}{\sum_{\mathbf{p}_s}\sum_{\tau}\left|\left|U_{\mathbf{p}_s}(\mathbf{p}_s,\mathbf{x},\tau)\right|\right|^2}. \tag{5.55}
$$

Equation (5.54) can be regarded as the illumination compensation imaging condition for the frequency domain DPW RTM. And $n(\mathbf{x})$ also represents the illumination compensated image, where the migration energy in the deeper parts of the images can be improved. The amplitude in the compensated image is more balanced than that in the images obtained by the frequency domain DPW RTM without compensating the illumination.

Migration results of the frequency domain DPW RTM with and without compensating the illumination and of the proposed DPW least squares RTM will be shown in the following section.

5.4. NUMERICAL TESTS

While all of the above derivations are in 3D, only 2D examples will be demonstrated. Two synthetic models were selected to test the proposed method. I compared the images generated by the frequency domain DPW RTM and those generated by the proposed DPW least squares RTM.

5.4.1. Three-layer model

The simple three-layer model, shown in Figure 5.2, had 200 horizontal and 100 vertical grid points. Grid spacing was 0.02 km for both directions. In this test, I generated a DPW dataset using equation (5.44) with the reflectivity model shown in Figure 5.3. The DPW dataset contained 121 $\mathbf{p}_s$ and 121 $\mathbf{p}_r$ plane waves. Each plane wave set ranged from -0.6 to 0.6 s/km with an interval of 0.01 s/km. In total, there were 121X121=14641 traces in the DPW dataset.

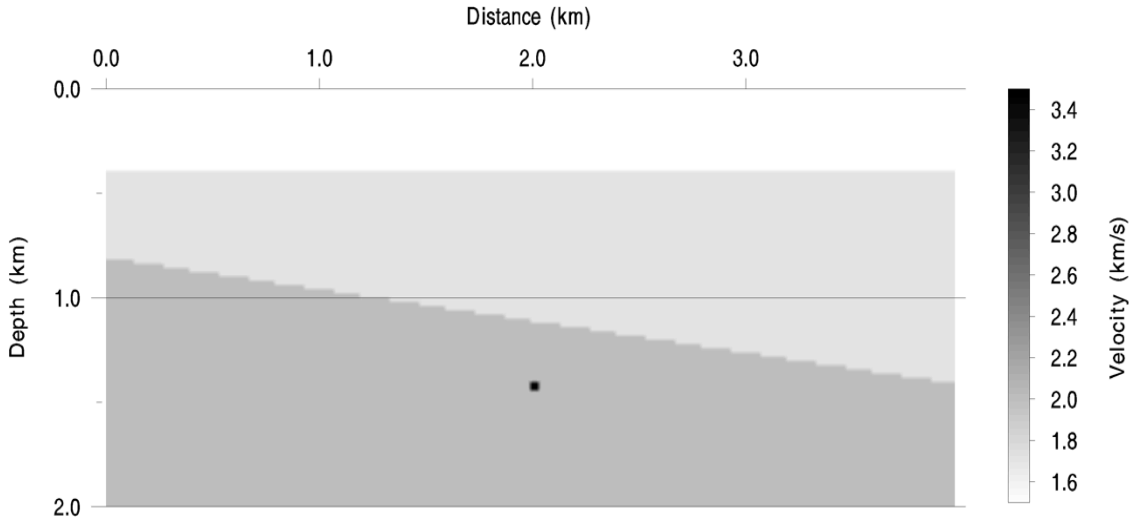

Figure 5.2. The three-layer model. There are one horizontal interface, one dipping interface and one point diffractor.

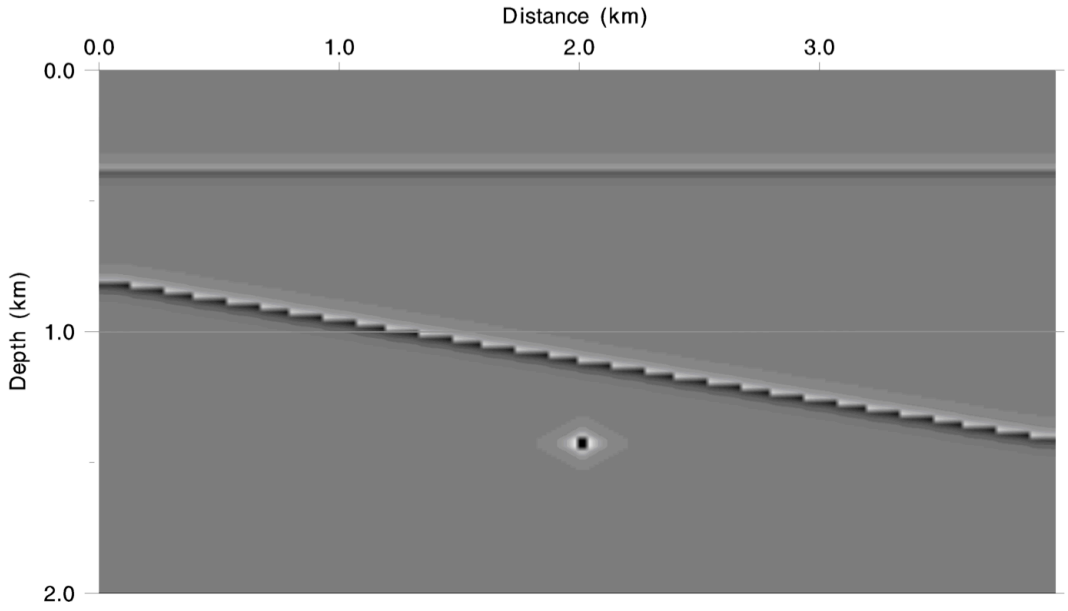

Figure 5.3. The reflectivity model used for generating the DPW dataset.

A subset of the DPW dataset, where 81 $\mathbf{p}_s$ and 41 $\mathbf{p}_r$ plane waves both ranged -0.4 ~ 0.4 s/km and 81 frequencies ranged 5 ~ 30 Hz, were used for migration. Only 81 plane wave Green's functions were constructed to migrate 1681 traces. The Green's functions were used for both the DPW Born modeling and the DPW RTM through iterations.

The images obtained by the frequency domain DPW RTM with and without compensating the illumination are shown in Figure 5.4 and 5.5, respectively. The diffractor and the two interfaces were successfully recovered. However, the images of the diffractor were not completely focused due to limited plane wave apertures used for migration, and the side lobes of the two interfaces are strong.

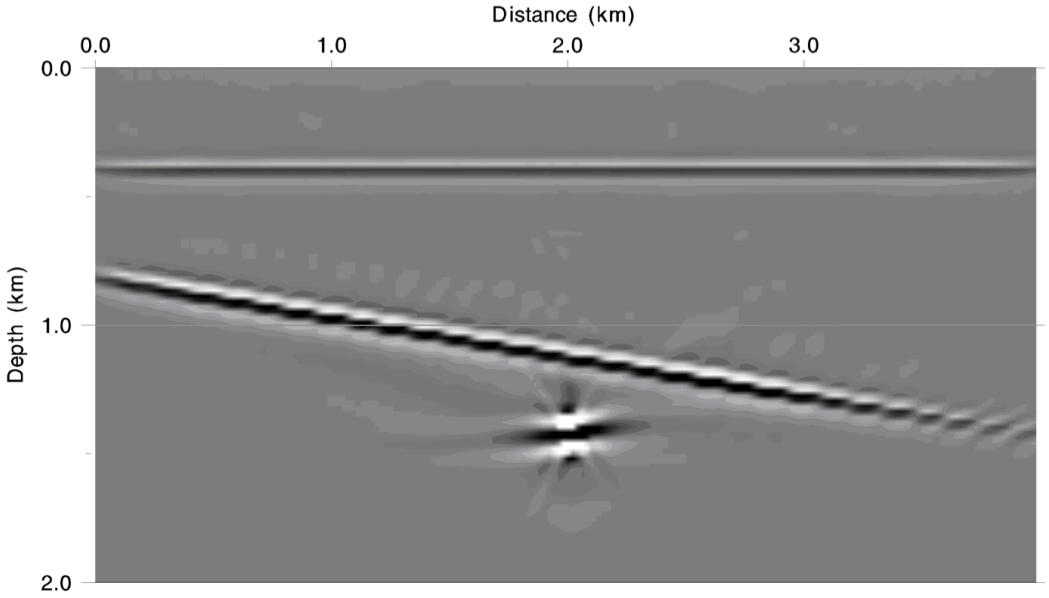

Figure 5.4. The migration result of the frequency domain DPW RTM without applying the illumination compensation. Equation (5.46) was implemented.

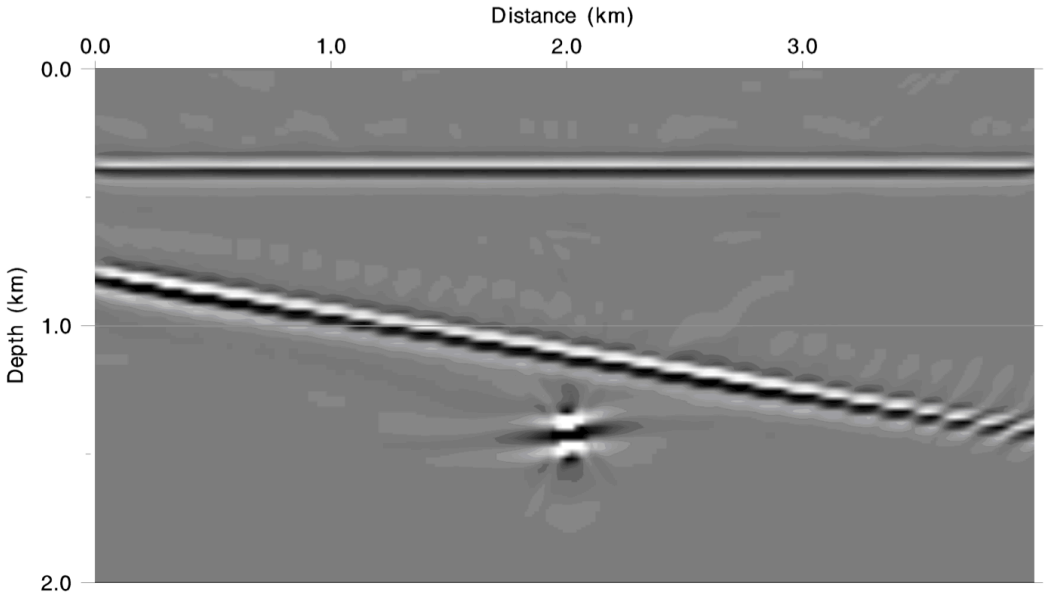

Figure 5.5. The migration result of the frequency domain DPW RTM with applying the illumination compensation imaging condition equation (5.54).

The same DPW subset was then used to perform the proposed DPW least squares RTM. The image shown in Figure 5.6 is the migration result after performing the DPW least squares RTM using equation (5.51) for 30 iterations. The image shown in Figure 5.7 is the migration result after performing the DPW least squares RTM using equation (5.52) for 30 iterations. Compared to the images shown in Figure 5.4 and 5.5, the images shown in Figure 5.6 and 5.7 have higher resolution for the two interfaces, and the diffractor is much better focused. The images shown in Figure 5.6 and 5.7 are visually identical.

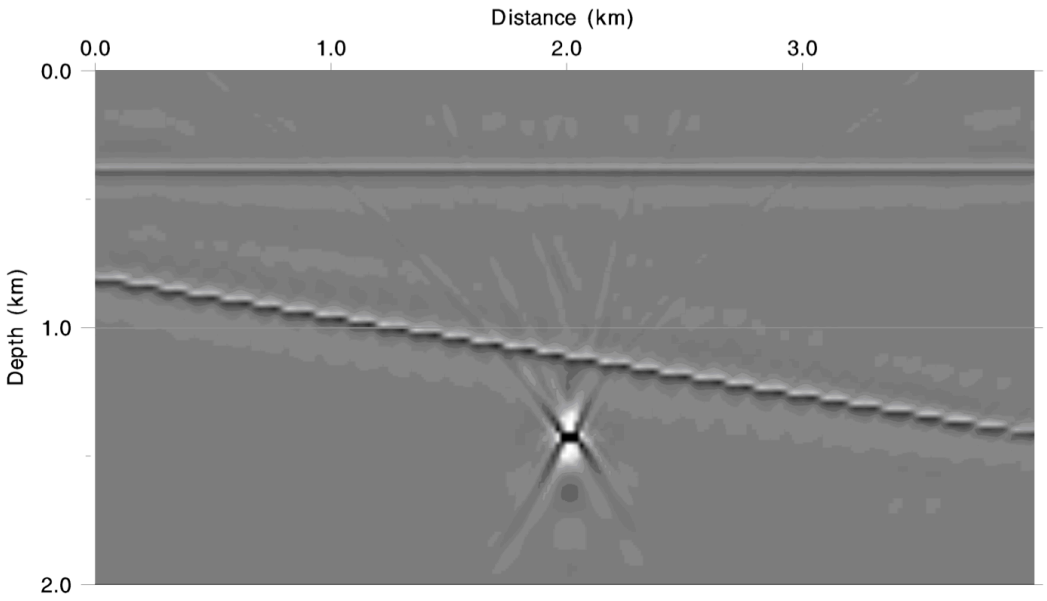

Figure 5.6. The migration result of the DPW least squares RTM without applying the pre-conditioner after 30 iterations.

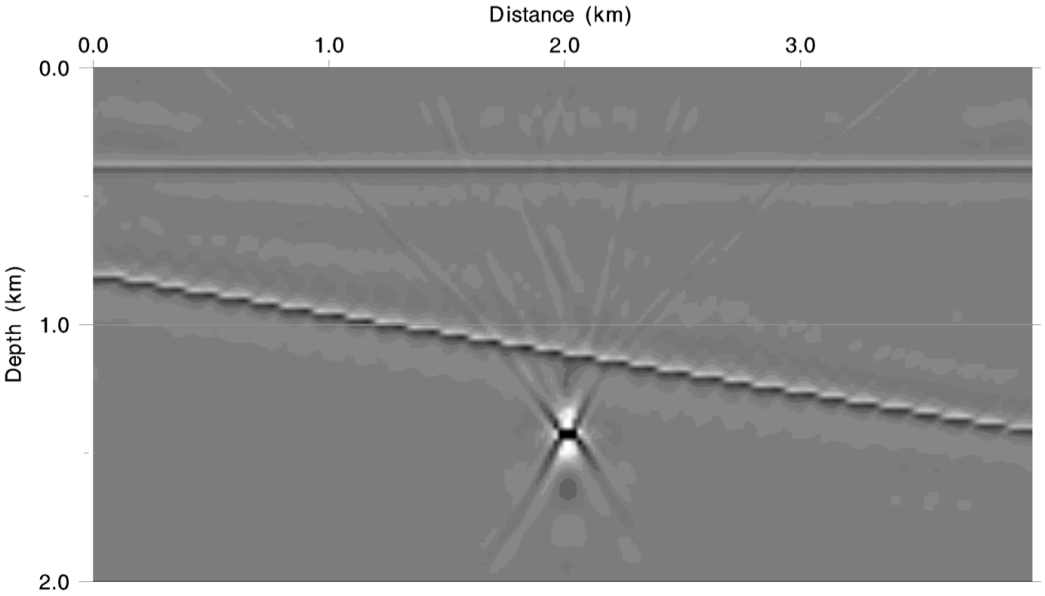

Figure 5.7. The migration result of the DPW least squares RTM with applying the pre-conditioner after 30 iterations.

The inverse of the diagonal matrix of the approximate Hessian matrix was obtained by equation (5.53). The diagonal element of the approximate Hessian matrix is shown in Figure 5.8, suggesting the illumination compensation. The hot and cold colors represent less and more amplitude compensation, respectively.

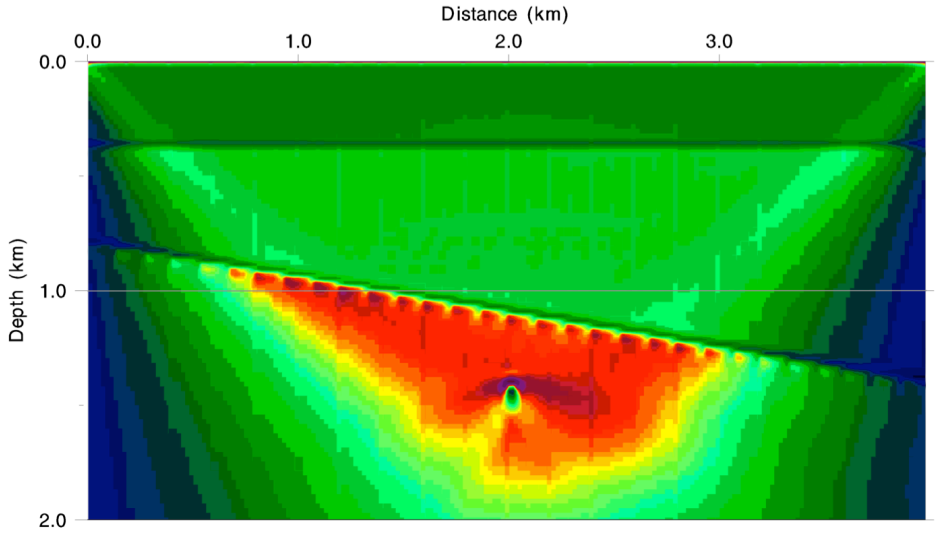

Figure 5.8. The diagonal element of the approximate Hessian matrix.

Wiggle traces extracted from Figure 5.3, 5.4, 5.5 and 5.6 at location x = 2 and 3 km were plotted in Figure 5.9 and 5.11, respectively. A zoomed part of Figure 5.9 is shown in Figure 5.10. The solid black line corresponds to the true reflectivity. The red dashed line corresponds to the trace extracted from the image obtained by the DPW least squares RTM with the pre-conditioner. The blue dashed line corresponds to the trace extracted from the image obtained by the frequency domain DPW RTM without applying the illumination compensation. The black dot line corresponds to the image obtained by the frequency domain DPW RTM with the illumination compensation. Because the image obtained by the DPW least squares RTM without the pre-conditioner is very similar to that obtained by the DPW least squares RTM with the pre-conditioner, the wiggle trace was not plotted for this case. The trace from the result of the frequency domain DPW RTM without applying the illumination compensation was multiply by a factor of 1e-18, so that it is on the same magnitude as the other three traces. The trace

from the image of the frequency domain DPW RTM with applying the illumination compensation over estimates the reflectivity. It is clear that, the images obtained by the DPW least squares RTM better represent the true reflectivity.

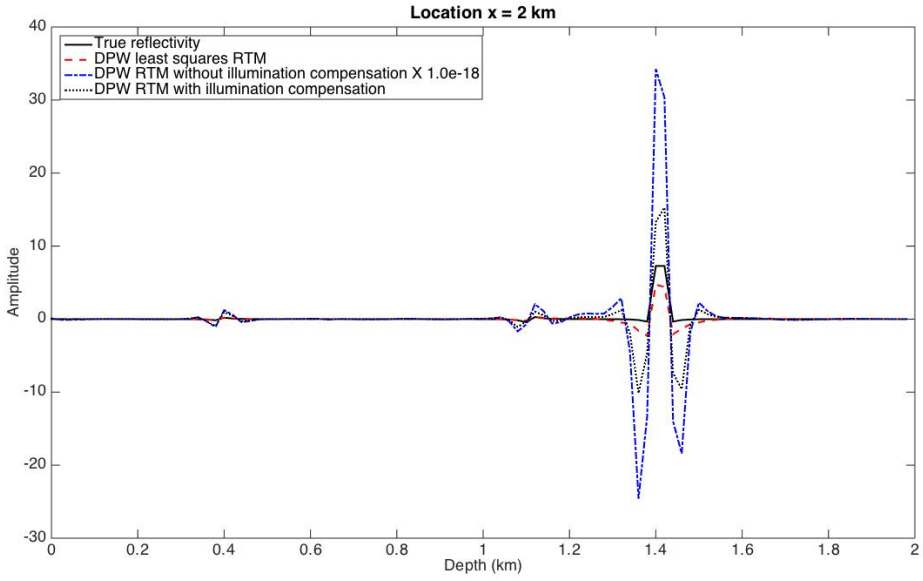

Figure 5.9. The comparison between wiggle traces extracted from the true reflectivity, the image obtained by the DPW least squares RTM, frequency domain DPW RTM with and without illumination compensation, respectively.

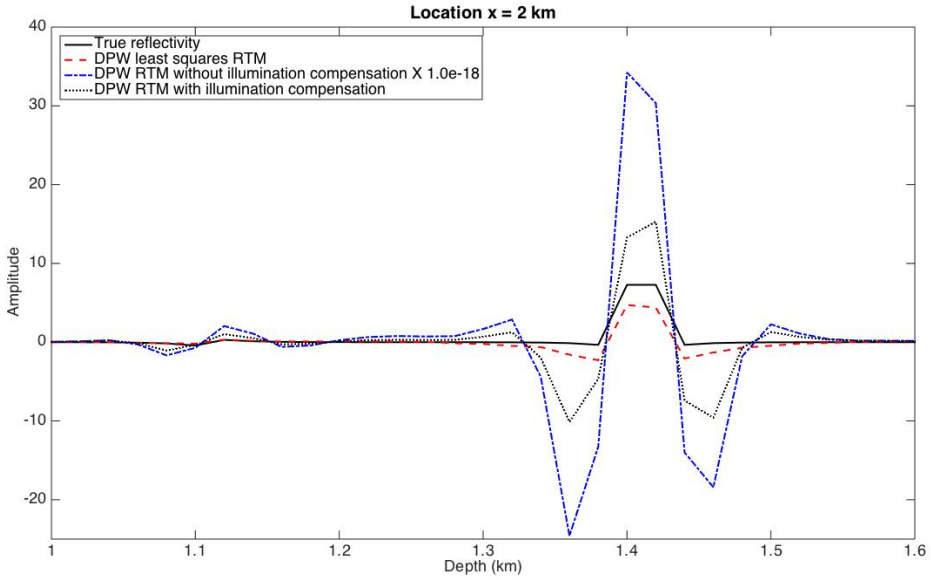

Figure 5.10. The zoomed region of Figure 5.9, starting from the depth at 1 km.

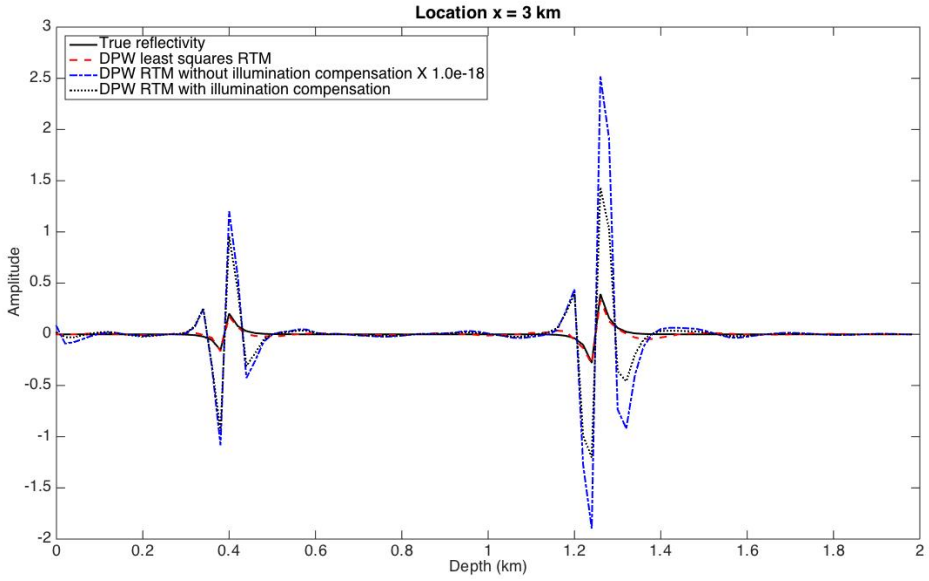

Figure 5.11. The comparison between wiggle traces extracted from the true reflectivity, the image obtained by the DPW least squares RTM, frequency domain DPW RTM with and without illumination compensation, respectively.

5.4.2. Marmousi model

The second test was performed on the 2D Marmousi model. The model, as shown in Figure 5.12, comprised 1150 horizontal and 375 vertical grid points, with a grid spacing of 0.008 km for both x and z directions. 1150 shot gathers were generated using the REM in the time domain. Each shot gather was acquired with 1150 receivers. Shot and receiver intervals were both 0.008 km. Then, the original shot gathers were transformed into a DPW dataset with 241 $\mathbf{p}_s$ and 241 $\mathbf{p}_r$ plane waves, both of which were equally spaced between -0.6 to 0.6 s/km. 241 $\mathbf{p}_s$ and 61 $\mathbf{p}_r$ plane waves ranging from -0.6 to 0.6 s/km were selected to perform migrations. Sampling intervals for $\mathbf{p}_s$ and $\mathbf{p}_r$ were 0.005 and 0.02 s/km, respectively. 81 frequencies ranging from 5 to 25 Hz were migrated. In total, only 241 plane waves Green's functions were calculated.

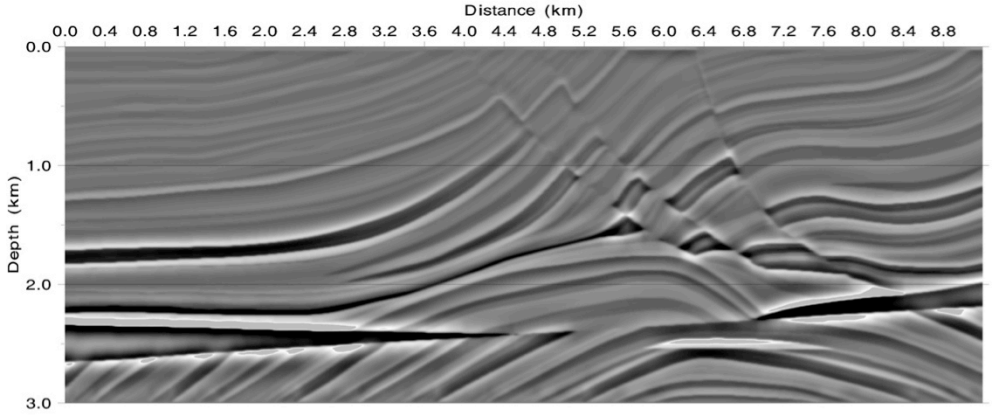

Figure 5.12. The Marmousi velocity model.

Figure 5.13 and 5.14 show the images obtained by performing the frequency domain DPW RTM without and with the illumination compensation, respectively. The top parts of the model were well imaged. However, the anticline at the bottom of the model, especially the flank of the anticline, was not clearly recovered in Figure 5.13 where the illumination compensation imaging condition was not applied. The image obtained with the illumination compensation has better definition for the deeper parts of the model, as shown in Figure 5.14.

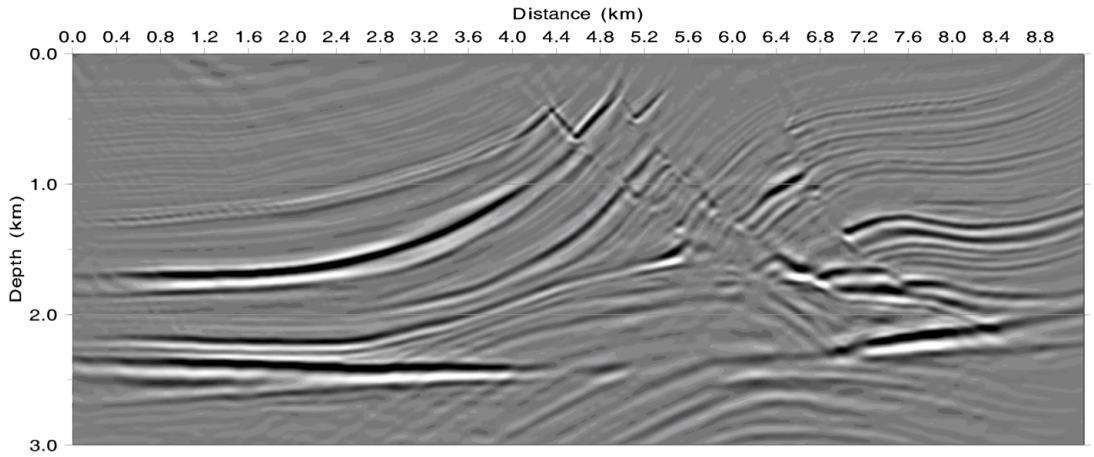

Figure 5.13. The migration result of the frequency domain DPW RTM without the illumination compensation. Equation (5.46) was implemented.

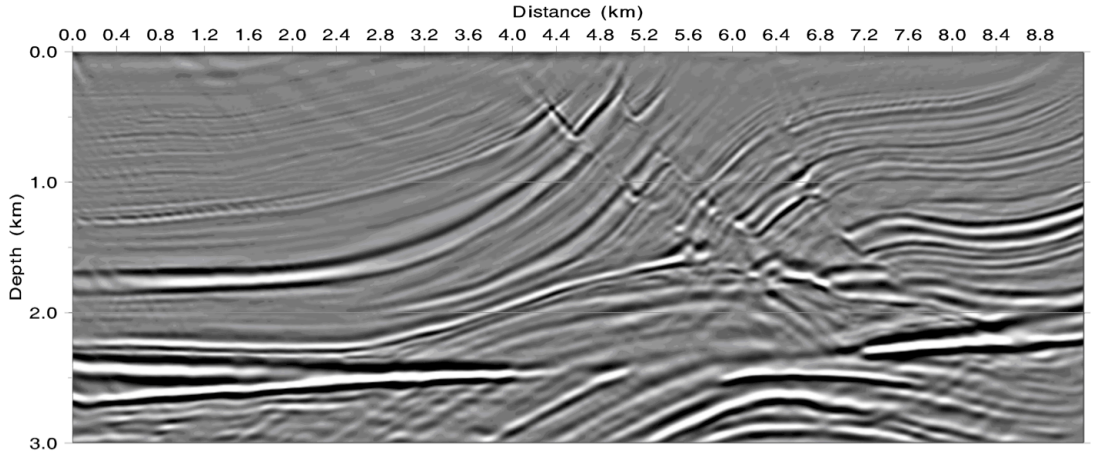

Figure 5.14. The migration result of the frequency domain DPW RTM with applying the illumination compensation imaging condition equation (5.54).

The image shown in Figure 5.15 was obtained by performing the DPW least squares RTM for 30 iterations without using the pre-conditioner. The image has a higher resolution comparing to the previous two images. Both the shallow and the deep parts of the model were well imaged. The image shown in Figure 5.16 was obtained by performing the DPW least squares RTM for 30 iterations with the pre-conditioner. With the help of the pre-conditioner, which compensated the illumination during the iterative updating process, the corresponding image has better resolution and more balanced amplitude comparing to the previous three images. And the misfit function converged faster than the case where the pre-conditioner was not applied to the gradient. The diagonal element of the approximate Hessian is shown in Figure 5.17. Again, the hot and cold colors represent less and more amplitude compensation, respectively.

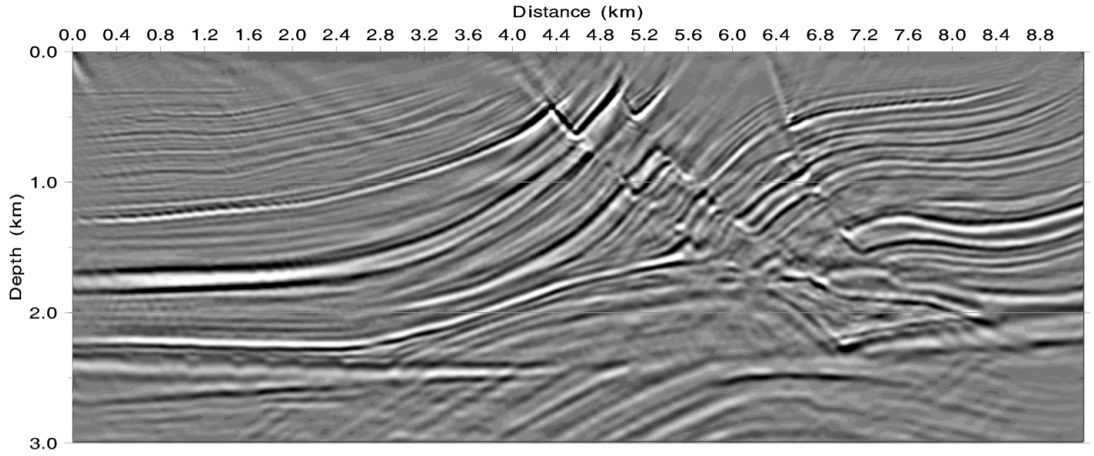

Figure 5.15. The migration result of the DPW least squares RTM without the pre-conditioner after 30 iterations.

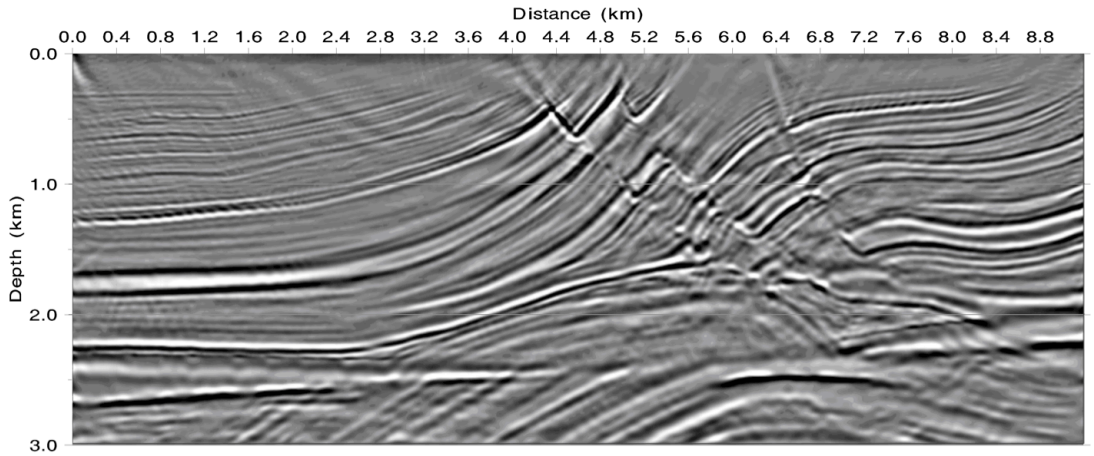

Figure 5.16. The migration result of the DPW least squares RTM with the pre-conditioner after 30 iterations.

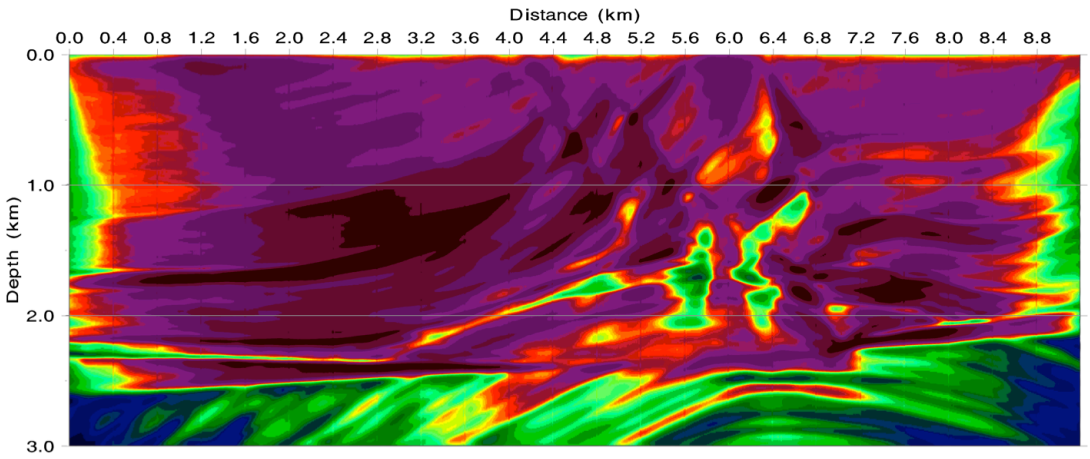

Figure 5.17. The diagonal element of the approximate Hessian matrix.

Wiggle traces extracted from Figure 5.14, 5.15 and 5.16 were compared to the true reflectivity at location x = 1.76 km in Figure 5.18. Because, only relative reflectively can be obtained by the migrations, the amplitude of the traces was calibrated to the depth at 0.384 km. In Figure 5.18, the solid black line corresponds to the true reflectivity. The red dashed line corresponds to the trace extracted from the image obtained by the DPW least squares RTM without the pre-conditioner. The blue dashed line corresponds to the trace extracted from the image obtained by the DPW least squares RTM with the pre-conditioner. The black dot line corresponds to the image obtained by the frequency domain DPW RTM with the illumination compensation. It is clear that, the image obtained by the DPW least squares RTM with the pre-conditioner better represent the true reflectivity for the entire model. The RTM result with the illumination compensation overestimated the reflectively for the deep parts of the model. However, the true reflectivity can be recovered for the shallow parts of the model by simply implementing the illumination compensation. The trace from Figure 5.13 was not compared, because it is far less than the true reflectivity.

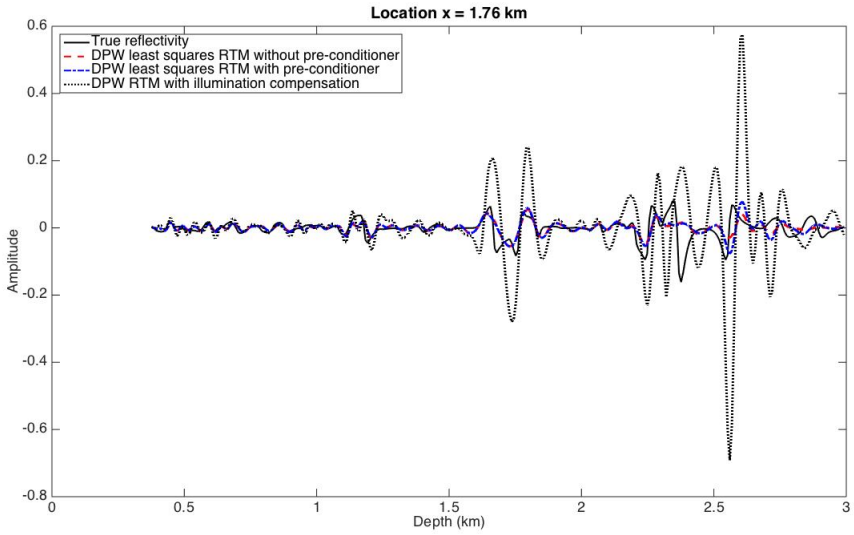

Figure 5.18. The comparison between wiggle traces extracted from the true reflectivity, the images obtained by the DPW least squares RTM with and without the pre-conditioner, and the image obtained by the frequency domain DPW RTM with the illumination compensation, respectively.

5.5. DISCUSSIONS

The proposed method is considerably faster than the traditional shot profile least squares RTM in that it does not require computing wavefield propagation for each iteration. Once plane wave Green's functions have been calculated, they can be reused for modeling and migration throughout iterations. For the three-layer case, the cumulative time for performing the frequency domain DPW RTM is about 750 s, where 620 s and 130 s were on computing plane wave Green's functions and imaging, respectively. The cumulative time for performing the proposed DPW least squares RTM for 30 iterations is about 4850 s, which is only about 7 times larger than the time spent on the frequency

domain DPW RTM. If the shot profile least squares RTM was performed, it could be as much as 30 times slower than the shot profile RTM.

As shown in the numerical results, applying the illumination compensation imaging condition for the frequency domain DPW RTM successfully enhanced the image at the deep parts of the model. Besides that, the illumination compensated migration results also have good correlations with the true reflectivity models. However, the images obtained by applying the illumination compensation tend to overestimate the reflectivity. By iteratively fitting the observed data, the least squares migration process can generate images whose amplitude is closer to the true reflectivity. Also, the migrated energy in images generated by the least squares migration is more focused, and the resolution of the images can be improved.

Worth mentioning, there are assumptions for implementing the least squares migration: the observed data should be well processed and contain little noises, the background velocity model should be close enough to the true velocity. Otherwise, performing the least squares migration, which requires extra work compared to the traditional migration methods, with noisy data on inaccurate velocity model would not be able to generate images that are superior to images generated by the traditional migration methods.

5.6. CONCLUSIONS

In this chapter, I proposed the DPW least squares RTM using the iterative updating method. The DPW Born modeling operator by which DPW data can be predicted using plane wave Green's functions was derived. The adjoint operator of the DPW Born modeling operator is similar to the frequency domain DPW RTM operator.

The adjoint operator can be used to obtain the gradient of the misfit function. The approximate Hessian matrix calculated with plane wave Green's functions was also derived. The inverse of the diagonal matrix of the approximate Hessian matrix was employed as the pre-conditioner to achieve the illumination compensation for the gradient. Compared to the shot profile least squares RTM, the DPW least squares RTM requires far less wavefield propagations. Only a limited number of plane wave Green's functions are needed to predict DPW data and to perform the migration during iterations. Besides that, the same set of plane wave Green's functions can be used for the DPW Born modeling and the DPW migration. Therefore, wavefields calculations are not necessary during the model updating process, and the computational cost can be reduced significantly. By minimizing the differences between the predicted DPW data and the observed DPW data, the migrated images have higher resolution and more balanced amplitude, which is comparable with the true reflectivity.

Chapter 6: Conclusions and Recommendations

6.1. SUMMARY

RTM solves the two-way wave equation during wave field propagation process. Although powerful computers have made traditional pre-stack shot gather RTM a practical migration procedure, pre-stack shot gather RTM is still computationally intensive. In my research, I focused on improving the migration efficiency of the RTM using the DPW data, which is the fully decomposed plane wave data. The DPW-based RTM in the time and the frequency domains were derived using the adjoint state methods. They have the potential to improve efficiency for large seismic datasets. The frequency domain DPW RTM method was derived under the Born approximation. This method can increase the RTM efficiency by an order of magnitude. A least squares RTM method using the DPW was also proposed.

In chapter 2, I introduced the DPW-based RTM in the time domain. Unlike the pre-stack shot profile RTM where the number of forward propagations is proportional to the number of shots, the number of forward propagations needed for the DPW-based RTM remains constant and is relatively small even for large seismic datasets. Therefore, the DPW-based RTM can improve RTM efficiency and be suitable for migrating large datasets. Selected plane wave components can be migrated to obtain subsurface interfaces with different dips. This feature makes the method target-oriented. Illumination compensation imaging conditions for the DPW-based RTM were also proposed to improve images in the deeper part of the section.

In chapter 3, migration methods using the DPW data were investigated in the frequency domain. The adjoint state method was employed to derive the DPW-based

RTM in the frequency domain. Then, a new DPW migration algorithm, which was named frequency domain DPW RTM, was derived under the Born approximation. Frequency plane wave Green's functions were utilized to migrate the DPW data. The number of frequency plane wave Green's functions required for migration was limited. As a result, the migration efficiency can be substantially improved. The proposed frequency domain DPW RTM can also include anisotropy by constructing plane wave Green's functions in anisotropic media.

Chapter 4 investigated the applicability of the reciprocity principle in the DPW domain. The reciprocity principle can be applied to the seismic data that are processed with proper seismic processing flows. Utilizing the reciprocity principle, a DPW dataset transformed from one-sided gathers can approximate a DPW dataset generated from split-spread shot gathers. Two methods were demonstrated to obtain optimal reciprocal DPW datasets. Under the ideal acquisition conditions, I suggested that one-sided acquisition geometries should be extended to the largest possible offsets, and reciprocity should be invoked to improve subsurface illumination. Migration efficiency was improved for the DPW migrations with the help of the reciprocity principle.

In chapter 5, a least squares migration method using plane wave data in a fully decomposed DPW-frequency domain was proposed. A Born modeling operator that predicts the DPW data at the surface was derived based on the shot profile Born modeling operator. The adjoint operator of the DPW Born modeling operator was shown to be equivalent to the frequency domain DPW RTM operator. Plane wave Green's functions were used for both the modeling and the migration processes throughout iterations, which greatly increased the efficiency of the least squares migration. An approximate Hessian matrix of the misfit function for the DPW data was derived. The diagonal matrix of the Hessian matrix was implemented as a pre-conditioner to the

gradient of the misfit function to balance the amplitude of the gradient and to improve the convergence rate.

6.2. DISCUSSION AND RECOMMENDATIONS

DPW migration methods proposed in this dissertation are flexible in that specific plane wave components can be migrated independently. Thus these DPW migration methods can be used as target-oriented imaging tool. By implementing the proposed methods, migration efficiency is improved substantially. Less computing time is required to obtain trial images and CIGs. As a result, velocity models can be refined promptly, making the methods useful for migration velocity analysis.

The frequency domain DPW RTM, which utilizes frequency plane wave Green's function for imaging, has the highest migration efficiency in 2D among three proposed DPW RTM methods. At the current stage, frequency domain plane wave Green's functions are computed via performing DFT for time domain plane wavefields, which requires the explicit time marching for wavefields. Accurate frequency domain plane wave Green's functions can be obtained more efficiently if the linear system of the Helmholtz equation can be solved promptly with little spatial dispersion.

All the methods presented in this dissertation can be implemented in 3D. And I expect that the frequency domain DPW RTM and the DPW least squares RTM methods, which greatly improve the migration efficiency in 2D, can help reduce the computation cost in 3D.

Because seismic data is compressed in the DPW domain, performing FWI using the DPW data has the potential to increase the computation efficiency. Also, given plane components can be selected to perform FWI independently, so that velocity models can

be built according to the dips of the subsurface structures. Staging over plane wave aperture might be able to achieve better starting model and to avoid local minimal. The gradient and Hessian computations proposed in the DPW least squares RTM can be implemented for FWI directly. A modeling operator that predict the DPW data at the surface without using the Born approximation should be derived to perform the forward modeling for FWI.

Appendix A: Equivalence of Equations 3.14 and 3.25, Ignoring Amplitude Filtering Terms

We rewrite equations (3.14) and (3.25) as

$$I(\mathbf{x}) = \sum_{\omega}\sum_{\mathbf{p}_s}\sum_{\mathbf{p}_r} \mathrm{Re}(\omega^2 \hat{\tilde{u}}_{\mathbf{p}_s}(\mathbf{p}_s,\mathbf{x},\omega)\hat{\tilde{v}}_{p_r}(\mathbf{p}_s,\mathbf{p}_r,\mathbf{x},\omega) \times \exp(+i\omega(\mathbf{p}_s+\mathbf{p}_r)\cdot(\mathbf{x}_h-\mathbf{x}_{ref}))), \tag{A - 1}$$

and

$$I(\mathbf{x}) = \mathrm{Re}(\int \frac{\omega^6}{c^2(\mathbf{x})}\iint f_s^*(\omega)G^*(\mathbf{p}_s,\mathbf{x},\omega)G^*(\mathbf{p}_r,\mathbf{x},\omega) \times P(\mathbf{p}_s,\mathbf{p}_r,\omega)\exp(+i\omega(\mathbf{p}_s+\mathbf{p}_r)\cdot(\mathbf{x}_h-\mathbf{x}_{ref}))d\mathbf{p}_s d\mathbf{p}_r d\omega). \tag{A - 2}$$

Taking off the summation and integration for equations A - 1 and A - 2, respectively, and ignoring the amplitude filtering terms, we can obtain

$$I(\mathbf{x},\mathbf{p}_s,\mathbf{p}_r) = \mathrm{Re}(\hat{\tilde{u}}_{\mathbf{p}_s}(\mathbf{p}_s,\mathbf{x},\omega)\hat{\tilde{v}}_{\mathbf{p}_r}(\mathbf{p}_s,\mathbf{p}_r,\mathbf{x},\omega) \times \exp(+i\omega(\mathbf{p}_s+\mathbf{p}_r)\cdot(\mathbf{x}_h-\mathbf{x}_{ref}))), \tag{A - 3}$$

and

$$I(\mathbf{x},\mathbf{p}_s,\mathbf{p}_r) = \mathrm{Re}(f_s^*(\omega)G^*(\mathbf{p}_s,\mathbf{x},\omega)G^*(\mathbf{p}_r,\mathbf{x},\omega) \times P(\mathbf{p}_s,\mathbf{p}_r,\omega)\exp(+i\omega(\mathbf{p}_s+\mathbf{p}_r)\cdot(\mathbf{x}_h-\mathbf{x}_{ref}))). \tag{A - 4}$$

In the frequency domain, the acoustic wave equation can be written as

$$\tilde{\mathbf{S}}\tilde{\mathbf{u}} = \tilde{\mathbf{f}}, \tag{A - 5}$$

where $\tilde{\mathbf{u}}$ is the frequency domain wave field, and $\tilde{\mathbf{f}}$ is the source term. $\tilde{\mathbf{S}} = (\tilde{\mathbf{K}} + i\omega\tilde{\mathbf{C}} - \omega^2\tilde{\mathbf{M}})$, where $\tilde{\mathbf{K}}$ represents the stiffness matrix, $\tilde{\mathbf{C}}$ represents the absorbing boundary condition, and $\tilde{\mathbf{M}}$ is the mass matrix. If $\tilde{\mathbf{f}}$ is defined as

$$\tilde{\mathbf{f}} = [0,0,...\delta(\mathbf{s})...0,0]^T, \tag{A - 6}$$

where $\delta(\mathbf{s})$ is the impulse source at the source location **s**, a spherical Green's function can be calculated by solving

$$\tilde{\mathbf{G}}_s = \tilde{\mathbf{S}}^{-1}\tilde{\mathbf{f}}, \tag{A - 7}$$

where $\tilde{\mathbf{S}}^{-1}$ is the inverse of the impedance matrix and $\tilde{\mathbf{G}}_s$ is the spherical Green's function $G(\mathbf{s},\mathbf{x},\omega)$ in the column vector form. If the source term $\tilde{\mathbf{f}}$ is defined as

$$\tilde{\mathbf{f}}_p = [...\delta(\mathbf{s}_1)\exp(-i\omega\mathbf{p}_s \cdot \mathbf{s}_1)...\delta(\mathbf{s}_n)\exp(-i\omega\mathbf{p}_s \cdot \mathbf{s}_n)...]^T, \tag{A - 8}$$

where *n* is the number of source location, and $\mathbf{s_1}$ … $\mathbf{s}_n$ are source locations at the surface, a plane wave Green's function can be obtained by solving

$$\tilde{\mathbf{G}}_p = \tilde{\mathbf{S}}^{-1}\tilde{\mathbf{f}}_p, \tag{A - 9}$$

where $\tilde{\mathbf{G}}_p$ is the vector form of the plane wave Green's function, and $\tilde{\mathbf{f}}_p$ denotes the plane wave source. Due to the linearity of the wave equation, the element of $\tilde{\mathbf{G}}_p$ obtained by solving equation (A - 9) can be calculated by

$$G(\mathbf{p}_s,\mathbf{x},\omega) = \int G(\mathbf{s},\mathbf{x},\omega)\exp(-i\omega\mathbf{p}_s\cdot\mathbf{s})d\mathbf{s}, \qquad \text{(A - 10)}$$

where $G(\mathbf{p}_s,\mathbf{x},\omega)$ is the plane wave Green's function. As discussed in Chapter 3, frequency domain wavefields obtained by solving the two-way wave equation (A - 5) are equivalent to time domain wavefields propagating in terms of traveltime *t*. A phase shift term should be applied on the frequency domain wavefields, so that the wavefields are equivalent to time domain wavefields propagating in terms of vertical delay time τ. Applying the phase shift term $\exp(+i\omega\mathbf{p}_s\cdot\mathbf{x}_h)$ on both side of equation (A - 10), we get

$$\hat{G}(\mathbf{p}_s,\mathbf{x},\omega) = \int G(\mathbf{s},\mathbf{x},\omega)\exp[-i\omega\mathbf{p}_s\cdot(\mathbf{s}-\mathbf{x}_h)]d\mathbf{s}, \qquad \text{(A - 11)}$$

where $\hat{G}(\mathbf{p}_s,\mathbf{x},\omega)$ is the phase shifted frequency domain plane wave Green's function for $\mathbf{p}_s$ plane wave, which can also be written as

$$\hat{G}(\mathbf{p}_s,\mathbf{x},\omega) = G(\mathbf{p}_s,\mathbf{x},\omega)\exp(+i\omega\mathbf{p}_s\cdot\mathbf{x}_h). \qquad \text{(A - 12)}$$

$\hat{G}(\mathbf{p}_s,\mathbf{x},\omega)$ is equivalent to time domain wavefield propagating in terms of τ.

If $\mathbf{s}$ and $\mathbf{p}_s$ are replaced by $\mathbf{r}$ and $\mathbf{p}_r$, respectively in equation (A - 8), the solution of equation (A - 9) can be written as

$$G(\mathbf{p}_r,\mathbf{x},\omega)=\int G(\mathbf{r},\mathbf{x},\omega)\exp(-i\omega\mathbf{p}_r\cdot\mathbf{r})d\mathbf{r}. \qquad \text{(A - 13)}$$

Similarly, we have

$$\hat{G}(\mathbf{p}_r,\mathbf{x},\omega)=\int G(\mathbf{r},\mathbf{x},\omega)\exp[-i\omega\mathbf{p}_r\cdot(\mathbf{r}-\mathbf{x}_h)]d\mathbf{r}, \qquad \text{(A - 14)}$$

and

$$\hat{G}(\mathbf{p}_r,\mathbf{x},\omega)=G(\mathbf{p}_r,\mathbf{x},\omega)\exp(+i\omega\mathbf{p}_r\cdot\mathbf{x}_h), \qquad \text{(A - 15)}$$

where $\hat{G}(\mathbf{p}_r,\mathbf{x},\omega)$ is the phase shifted frequency domain plane wave Green's function for $\mathbf{p}_r$ plane wave.

Multiplying both sides of equation (A - 12) with $f_s(\omega)$, we have

$$f_s(\omega)\hat{G}(\mathbf{p}_s,\mathbf{x},\omega)=f_s(\omega)G(\mathbf{p}_s,\mathbf{x},\omega)\exp(+i\omega\mathbf{p}_s\cdot\mathbf{x}_h). \qquad \text{(A - 16)}$$

If the source term $\tilde{\mathbf{f}}$ is defined as

$$\begin{aligned}\tilde{\mathbf{f}}_p=[&...f_s(\omega)\delta(\mathbf{s}_1)\exp(-i\omega\mathbf{p}_s\cdot\mathbf{s}_1)...\\ &...f_s(\omega)\delta(\mathbf{s}_n)\exp(-i\omega\mathbf{p}_s\cdot\mathbf{s}_n)...]^T,\end{aligned} \qquad \text{(A - 17)}$$

the forward propagated plane wavefield $\tilde{\mathbf{u}}_{\mathbf{p}_s}$ can be obtained by solving the linear system

$$\tilde{\mathbf{u}}_{\mathbf{p}_s} = \tilde{\mathbf{S}}^{-1}\tilde{\mathbf{f}}_p. \qquad \text{(A - 18)}$$

Each element of $\tilde{\mathbf{u}}_{\mathbf{p}_s}$ can be expressed as

$$\tilde{u}_{\mathbf{p}_s}(\mathbf{p}_s,\mathbf{x},\omega) = f_s(\omega)G(\mathbf{p}_s,\mathbf{x},\omega). \qquad \text{(A - 19)}$$

Substituting equation (A - 19) into equation (A - 16), we have

$$f_s(\omega)\hat{G}(\mathbf{p}_s,\mathbf{x},\omega) = \tilde{u}_{\mathbf{p}_s}(\mathbf{p}_s,\mathbf{x},\omega)\exp(+i\omega\mathbf{p}_s\cdot\mathbf{x}_h). \qquad \text{(A - 20)}$$

Substituting equation (3.12) into equation (A - 20), we get

$$f_s(\omega)\hat{G}(\mathbf{p}_s,\mathbf{x},\omega) = \hat{\tilde{u}}_{\mathbf{p}_s}(\mathbf{p}_s,\mathbf{x},\omega). \qquad \text{(A - 21)}$$

If the source term $\tilde{\mathbf{f}}$ is defined as

$$\begin{aligned}\tilde{\mathbf{f}}_p = [&...P^*(\mathbf{p}_s,\mathbf{p}_r,\omega)\delta(\mathbf{r}_1)\exp(-i\omega\mathbf{p}_r\cdot\mathbf{r}_1)...\\ &...P^*(\mathbf{p}_s,\mathbf{p}_r,\omega)\delta(\mathbf{r}_m)\exp(-i\omega\mathbf{p}_r\cdot\mathbf{r}_m)...]^T,\end{aligned} \qquad \text{(A - 22)}$$

where m is the number of receivers, $\mathbf{r}_1$ … $\mathbf{r}_m$ are receiver locations at the surface, the backward propagated plane wavefield $\tilde{\mathbf{v}}_{\mathbf{p}_r}$ can be obtained by solving the linear system

$$\tilde{\mathbf{v}}_{\mathbf{p}_r} = \tilde{\mathbf{S}}^{-1}\tilde{\mathbf{f}}_p. \qquad \text{(A - 23)}$$

Each element of $\tilde{\mathbf{v}}_{\mathbf{p}_r}$ can be expressed as

$$\tilde{v}_{\mathbf{p}_r}(\mathbf{p}_s,\mathbf{p}_r,\mathbf{x},\omega) = P^*(\mathbf{p}_s,\mathbf{p}_r,\omega)G(\mathbf{p}_r,\mathbf{x},\omega). \qquad \text{(A - 24)}$$

Applying a phase shift term $\exp(+i\omega\mathbf{p}_r\cdot\mathbf{x}_h)$ on both sides of equation (A - 24) and employing the relationships indicated by equations (3.13) and (A - 12), we have

$$\hat{\tilde{v}}_{\mathbf{p}_r}(\mathbf{p}_s,\mathbf{p}_r,\mathbf{x},\omega) = P^*(\mathbf{p}_s,\mathbf{p}_r,\omega)\hat{G}(\mathbf{p}_r,\mathbf{x},\omega). \qquad \text{(A - 25)}$$

As discussed in Chapters 1, 2 and 3, the phase shift term $\exp(+i\omega(\mathbf{p}_s+\mathbf{p}_r)\cdot(\mathbf{x}_h-\mathbf{x}_{ref}))$ needs to be applied to the backward propagated wavefield to correct the vertical delay time of the DPW data. Therefore, multiplying both sides of equation (A - 25) with $\exp(+i\omega(\mathbf{p}_s+\mathbf{p}_r)\cdot(\mathbf{x}_h-\mathbf{x}_{ref}))$, we achieve

$$\begin{aligned}&\hat{\tilde{v}}_{\mathbf{p}_r}(\mathbf{p}_s,\mathbf{p}_r,\mathbf{x},\omega)\exp(+i\omega(\mathbf{p}_s+\mathbf{p}_r)\cdot(\mathbf{x}_h-\mathbf{x}_{ref}))\\ &= P^*(\mathbf{p}_s,\mathbf{p}_r,\omega)\hat{G}(\mathbf{p}_r,\mathbf{x},\omega)\exp(+i\omega(\mathbf{p}_s+\mathbf{p}_r)\cdot(\mathbf{x}_h-\mathbf{x}_{ref})).\end{aligned} \qquad \text{(A - 26)}$$

Substituting equations (A - 21) and (A - 26) into equation (A - 3), we get

$$I(\mathbf{x}) = \mathrm{Re}(f_s(\omega)\hat{G}(\mathbf{p}_s,\mathbf{x},\omega)\hat{G}(\mathbf{p}_r,\mathbf{x},\omega) \times P^*(\mathbf{p}_s,\mathbf{p}_r,\omega)\exp(+i\omega(\mathbf{p}_s+\mathbf{p}_r)\cdot(\mathbf{x}_h-\mathbf{x}_{ref}))). \quad \text{(A - 27)}$$

Because $\hat{G}(\mathbf{p}_s,\mathbf{x},\omega)$ and $\hat{G}(\mathbf{p}_r,\mathbf{x},\omega)$ in equation (A - 27) are defined as the same as $G(\mathbf{p}_s,\mathbf{x},\omega)$ and $G(\mathbf{p}_r,\mathbf{x},\omega)$ in equation (A - 4) (cf. equations (A - 11), (A - 14), (3.23) and (3.24)), equation (A - 27) is equivalent to equation (A - 4). The above analysis can be conducted to prove the equivalence of equations (3.15) and (3.26).

Appendix B: Acronyms and Mathematical symbols

ACRONYMS

ART	Asymptotic ray theory
CIGs	Common image gathers
CMP	Common middle point
DFT	Discrete Fourier transform
DPW	Double plane wave
FWI	Full waveform inversion
Ps-Pr	DPW data transformed from source-receiver coordinates
Ps-Po	DPW data transformed from source-offset coordinates
REM	Rapid expansion method
RTM	Reverse time migration
TTI	Tilted transversely isotropic
VTI	Vertical transversely isotropic
DPW-based RTM in the time domain	Performing RTM with DPW data using adjoint state method in the time domain
DPW-based RTM in the frequency domain	Performing RTM with DPW data using adjoint state method in the frequency domain
Frequency domain DPW RTM	Performing RTM with DPW data using frequency domain plane wave Green's function

Table B. 1. Table of acronyms.

DEFINITION OF MATHEMATICAL SYMBOLS

·	Dot product
Superscript *T*	Transpose of a matrix
Superscript †	Conjugate transpose of a matrix
Superscript *	Conjugate of a complex number
Symbol ~	Frequency domain
∇^2	Laplace operator
∇	Gradient
Superscript -1	Inverse of a matrix
RE	Real part of a complex number
$\sum$	Summation
$\int$	Integration

Table B. 2. Table of mathematical symbols.

Bibliography

Aminzadeh, F., J. Brac, and T. Kunz, 1997, 3-D salt and overthrust models: SEG/EAGE 3-D Modeling Series No. 1, SEG.

Akbar, F. E., M. K. Sen, and P. L. Stoffa, 1996, Prestack plane-wave kirchhoff migration in laterally varying media: Geophysics, **61**, no. 4, 1068-1079, doi: 10.1190/1.1444028.

Baysal, E., D. D. Kosloff, and J. W. C. Sherwood, 1983, Reverse time migration: Geophysics, **48**, no. 11, 1514-1524, doi: 10.1190/1.1441434.

Bleistein, N., J. K. Cohen, and J. W. Stockwell, 2001, Mathematics of multidimensional seismic imaging, migration, and inversion. Vol. 13: Springer Science & Business Media.

Borselen, R. G. v., P. M. v. d. Berg, and J. T. Fokkema, 1992, Removal of surface - related wave phenomena in the double radon transform domain: 72nd Annual International Meeting, SEG, Expanded Abstractss, 1085-1088, doi: 10.1190/1.1821913.

Brysk, H., M. Cathriner, R. A. Goodrum, and J. L. Pennacchioni, 1987, Predictive deconvolution of cylindrical slant stacks: 57th Annual International Meeting, SEG, Expanded Abstractss, 795-797, doi: 10.1190/1.1891955.

Brysk, H., and D. W. McCowan, 1986, A slant - stack procedure for point - source data: Geophysics, **51**, no. 7, 1370-1386, doi: 10.1190/1.1442187.

Chattopadhyay, S., and G. A. McMechan, 2008, Imaging conditions for prestack reverse-time migration: Geophysics, **73**, no. 3, S81-S89, doi: 10.1190/1.2903822.

Claerbout, J. F., 1985, Imaging the Earth's Interior: Blackwell Scientific Publications, Inc.

--, 1986, Fundamentals of Geophysical Data Processing, 2nd ed. Vol. 86: Blackwell Publishing Ltd.

Clapp, R. G., 2009, Reverse time migration with random boundaries: 79th Annual International Meeting, SEG, Expanded Abstractss, 2809-2813, doi: 10.1190/1.3255432

Clayton, R. W., and R. H. Stolt, 1981, A Born-WKBJ inversion method for acoustic reflection data: Geophysics, **46**, no. 11, 1559-1567, doi: 10.1190/1.1441162.

Dai, W., and G. T. Schuster, 2013, Plane-wave least-squares reverse-time migration: Geophysics, **78**, no. 4, S165-S177, doi: 10.1190/geo2012-0377.1.

Dai, W., X. Wang, and G. T. Schuster, 2011, Least-squares migration of multisource data with a deblurring filter: Geophysics, **76**, no. 5, R135-R146, doi: 10.1190/geo2010-0159.1.

Diebold, J. B., and P. L. Stoffa, 1981, The traveltime equation, tau - p mapping, and inversion of common midpoint data: Geophysics, **46**, no. 3, 238-254, doi: 10.1190/1.1441196.

Dong, S., J. Cai, M. Guo, S. Suh, Z. Zhang, B. Wang, and Z. Li, 2012, Least-squares reverse time migration: towards true amplitude Imaging and improving the resolution: 83rd Annual International Meeting, SEG, Expanded Abstracts, 1425-1429, doi: 10.1190/segam2012-1488.1

Etgen, J. T., and S. Brandsberg - Dahl, 2009, The pseudo - analytical method: Application of pseudo - Laplacians to acoustic and acoustic anisotropic wave propagation: 79th Annual International Meeting, SEG, Expanded Abstractss, 2552-2556, doi: 10.1190/1.3255375.

Farmer, P. A., I. F. Jones, H. Zhou, R. I. Bloor, and M. C. Goodwin, 2006, Application of reverse time migration to complex imaging problems: First Break, **24**, no. 9.

Fokkema, J. T., and P. M. van den Berg, 1992, Reflector imaging: Geophysical Journal International, **110**, no. 1, 191-200, doi: 10.1111/j.1365-246X.1992.tb00721.x.

Fomel, S., L. Ying, and X. Song, 2013, Seismic wave extrapolation using lowrank symbol approximation: Geophysical Prospecting, **61**, no. 3, 526-536, doi: 10.1111/j.1365-2478.2012.01064.x.

Foster, D. J., and C. C. Mosher, 1992, Suppression of multiple reflections using the radon-transform: Geophysics, **57**, no. 3, 386-395, doi: 10.1190/1.1443253.

Hildebrand, S. T., and R. J. Carroll, 1993, Radon depth migration: Geophysical Prospecting, **41**, no. 2, 229-240, doi: 10.1111/j.1365-2478.1993.tb00867.x.

Hill, N. R., 1990, Gaussian-beam migration: Geophysics, **55**, no. 11, 1416-1428, doi: 10.1190/1.1442788.

--, 2001, Prestack Gaussian-beam depth migration: Geophysics, **66**, no. 4, 1240-1250, doi: 10.1190/1.1487071.

Hustedt, B., S. Operto, and J. Virieux, 2004, Mixed-grid and staggered-grid finite-difference methods for frequency-domain acoustic wave modelling: Geophysical Journal International, **157**, no. 3, 1269-1296, doi: 10.1111/j.1365-246X.2004.02289.x.

Kim, Y., D.-J. Min, and C. Shin, 2011, Frequency-domain reverse-time migration with source estimation: Geophysics, **76**, no. 2, S41-S49, doi: 10.1190/1.3534831.

Kosloff, D., A. Queiroz Filho, E. Tessmer, and A. Behle, 1989, Numerical solution of the acoustic and elastic wave equations by a new rapid expansion method:

Geophysical Prospecting, **37**, no. 4, 383-394, doi: 10.1111/J.1365-2478.1989.Tb02212.X.

Liu, F., D. W. Hanson, N. D. Whitmore, R. S. Day, and R. H. Stolt, 2006, Toward a unified analysis for source plane-wave migration: Geophysics, **71**, no. 4, S129-S139, doi: 10.1190/1.2213933.

Liu, F., and S. A. Morton, 2006, Hess VTI synthetic datasets, http://software.seg.org/datasets/2D/Hess_VTI/.

Liu, F., M. K. Sen, and P. L. Stoffa, 2000, Dip selective 2-D multiple attenuation in the plane - wave domain: Geophysics, **65**, no. 1, 264-274, doi: 10.1190/1.1444717.

Liu, F., R. H. Stolt, D. W. Hanson, and R. S. Day, 2002, Plane wave source composition: An accurate phase encoding scheme for prestack migration: 72nd Annual International Meeting, SEG, Expanded Abstracts, 1156-1159, doi: 10.1190/1.1816854.

Liu, F., D. N. Whitmore, D. W. Hanson, R. S. Day, and C. C. Mosher, 2004, The impact of reciprocity on prestack source plane wave migration: 74th Annual International Meeting, SEG, Expanded Abstracts, 1045-1048, doi: 10.1190/1.1839651

Liu, H., R. Ding, L. Liu, and H. Liu, 2013, Wavefield reconstruction methods for reverse time migration: Journal of Geophysics and Engineering, **10**, no. 1, 015004, doi: 10.1088/1742-2132/10/1/015004.

Marfurt, K. J., 1984, Accuracy of finite - difference and finite - element modeling of the scalar and elastic wave equations: Geophysics, **49**, no. 5, 533-549, doi: 10.1190/1.1441689.

McMechan, G. A., 1983, Migration by extrapolation of time-dependent boundary-values: Geophysical Prospecting, **31**, no. 3, 413-420, doi: 10.1111/j.1365-2478.1983.tb01060.x.

Mosher, C. C., D. J. Foster, and S. Hassanzadeh, 1996, Seismic imaging with offset plane waves: SPIE's 1996 International Symposium on Optical Science, Engineering, and Instrumentation, 52-63.

Nemeth, T., C. Wu, and G. T. Schuster, 1999, Least - squares migration of incomplete reflection data: Geophysics, **64**, no. 1, 208-221, doi: 10.1190/1.1444517.

Operto, S., J. Virieux, B. Hustedt, and F. Malfanti, 2002, Adaptive wavelet-based finite-difference modelling of sh-wave propagation: Geophysical Journal International, **148**, no. 3, 476-498, doi: 10.1046/j.1365-246x.2002.01573.x.

Operto, S., J. Virieux, A. Ribodetti, and J. E. Anderson, 2009, Finite-difference frequency-domain modeling of viscoacoustic wave propagation in 2D tilted transversely isotropic (TTI) media: Geophysics, **74**, no. 5, T75-T95, doi: 10.1190/1.3157243.

Ottolini, R., and J. F. Claerbout, 1984, The migration of common midpoint slant stacks: Geophysics, **49**, no. 3, 237-249, doi: 10.1190/1.1441656.

Pestana, R. C., and P. L. Stoffa, 2010, Time evolution of the wave equation using rapid expansion method: Geophysics, **75**, no. 4, T121-T131, doi: 10.1190/1.3449091.

Plessix, R. E., 2006, A review of the adjoint-state method for computing the gradient of a functional with geophysical applications: Geophysical Journal International, **167**, no. 2, 495-503, doi: 10.1111/j.1365-246X.2006.02978.x.

Plessix, R. E., and W. A. Mulder, 2004, Frequency-domain finite-difference amplitude-preserving migration: Geophysical Journal International, **157**, no. 3, 975-987, doi: 10.1111/j.1365-246X.2004.02282.x.

Pratt, R. G., 1999, Seismic waveform inversion in the frequency domain; part 1, theory and verification in a physical scale model: Geophysics, **64**, no. 3, 888-901, doi: 10.1190/1.1444597.

Pratt, R. G., C. Shin, and G. J. Hick, 1998, Gauss–Newton and full Newton methods in frequency–space seismic waveform inversion: Geophysical Journal International, **133**, no. 2, 341-362, doi: 10.1046/j.1365-246X.1998.00498.x.

Ren, H., H. Wang, and S. Chen, 2013, Least-squares reverse time migration in frequency domain using the adjoint-state method: Journal of Geophysics and Engineering, **10**, no. 3, 035002, doi: 10.1088/1742-2132/10/3/035002.

Romero, L. A., D. C. Ghiglia, C. C. Ober, and S. A. Morton, 2000, Phase encoding of shot records in prestack migration: Geophysics, **65**, no. 2, 426-436, doi: 10.1190/1.1444737.

Schneider, W. A., 1978, Integral formulation for migration in two and three dimensions: Geophysics, **43**, no. 1, 49-76, doi: 10.1190/1.1440828.

Schneider, W. A., K. A. Ranzinger, A. H. Balch, and C. Kruse, 1992, A dynamic programming approach to first arrival traveltime computation in media with arbitrarily distributed velocities: Geophysics, **57**, no. 1, 39-50, doi: 10.1190/1.1443187.

Schuster, G. T., 1993, Least-squares cross-well migration: 63rd Annual International Meeting, SEG, Expanded Abstracts, 110-113, doi: 10.1190/1.1822308.

Scott, A. M., and C. O. Curtis, 1998, Fastershot - record depth migrations using phase encoding: 68th Annual International Meeting, SEG, Expanded 1131-1134, 10.1190/1.1820088.

Seifoullaev, R. K., P. L. Stoffa, and M. K. Sen, 2005, Use of reciprocity in a double plane wave Kirchhoff depth migration: 9th International Congress of the Brazilian Geophysical Society, Expanded Abstractss, 1636-1640, doi: 10.1190/sbgf2005-326.

Sen, M. K., and L. N. Frazer, 1991, Multifold phase space path integral synthetic seismograms: Geophysical Journal International, **104**, no. 3, 479-487, doi: 10.1111/j.1365-246X.1991.tb05695.x.

Sen, M. K., and A. Mukherjee, 2003, τ-p analysis in transversely isotropic media: Geophysical Journal International, **154**, no. 3, 647-658, doi: 10.1046/j.1365-246X.2003.01997.x.

Sen, M. K., and A. Pal, 2009, A reflectivity method for laterally varying media: Homogeneous layers with curved interfaces: Geophysical Journal International, **178**, no. 2, 792-812, doi: 10.1111/j.1365-246X.2009.04172.x.

Shin, C., S. Jang, and D.-J. Min, 2001, Improved amplitude preservation for prestack depth migration by inverse scattering theory: Geophysical Prospecting, **49**, no. 5, 592-606, doi: 10.1046/j.1365-2478.2001.00279.x.

Sil, S., and M. K. Sen, 2009a, Seismic critical-angle anisotropy analysis in the tau-p domain: Geophysics, **74**, no. 4, A53-A57, doi: 10.1190/1.3137019.

--, 2009b, Azimuthal tau-p analysis in a weak orthorhombic medium: Journal of Seismic Exploration, **18**, no. 1, 81-91.

Stoffa, P. L., 1989, Tau - p: An alternative domain for filtering, velocity analysis, and imaging: 59th Annual International Meeting, SEG, Expanded Abstractss, 551-554, doi: 10.1190/1.1889655.

Stoffa, P. L., and P. Buhl, 1979, Two - Ship multichannel seismic experiments for deep crustal studies: Expanded spread and constant offset profiles: Journal of Geophysical Research: Solid Earth (1978–2012), **84**, no. B13, 7645-7660, doi: 10.1029/JB084iB13p07645.

Stoffa, P. L., P. Buhl, J. B. Diebold, and F. Wenzel, 1981, Direct mapping of seismic data to the domain of intercept time and ray parameter-a plane-wave decomposition: Geophysics, **46**, no. 3, 255-267, doi: 10.1190/1.1441197.

Stoffa, P. L., M. K. Sen, R. K. Seifoullaev, R. C. Pestana, and J. T. Fokkema, 2006, Plane-wave depth migration: Geophysics, **71**, no. 6, S261-S272, doi: 10.1190/1.2357832.

Stolt, R. H., and A. B. Weglein, 1985, Migration and inversion of seismic data: Geophysics, **50**, no. 12, 2458-2472, doi: 10.1190/1.1441877.

--, 2012, Seismic imaging and inversion: Volume 1: Application of linear inverse theory: Cambridge University Press.

Sun, P., S. Zhang, and F. Liu, 2002, Prestack migration of areal shot records with phase encoding: 72nd Annual International Meeting, SEG.

Symes, W. W., 2007, Reverse time migration with optimal checkpointing: Geophysics, **72**, no. 5, SM213-SM221, doi: 10.1190/1.2742686.

Tal-Ezer, H., 1986, Spectral methods in time for hyperbolic equations: SIAM Journal on Numerical Analysis, **23**, no. 1, 11-26, doi: 10.1137/0723002.

Tal-Ezer, H., D. Kosloff, and Z. Koren, 1987, An accurate scheme for seismic forward modeling: Geophysical Prospecting, **35**, no. 5, 479-490, doi: 10.1111/j.1365-2478.1987.tb00830.x.

Tan, S., and L. Huang, 2014, Reducing the computer memory requirement for 3d reverse-time migration with a boundary-wavefield extrapolation method: Geophysics, **79**, no. 5, S185-S194, doi: 10.1190/Geo2014-0075.1.

Taner, M. T., 1976, SIMPLAN: Simulated plane-wave exploration: 46th Annual International Meeting, SEG, Expanded Abstractss, 186-187.

Taner, M. T., E. Baysal, and F. Koehler, 1987, Controlled directional seismic source: 57th Annual International Meeting, SEG, Expanded Abstractss.

Tao, Y., and M. Sen, 2013, Frequency-domain full waveform inversion with plane-wave data: Geophysics, **78**, no. 1, R13-R23, doi: 10.1190/geo2012-0267.1.

Tarantola, A., 1984, Inversion of seismic reflection data in the acoustic approximation: Geophysics, **49**, no. 8, 1259-1266, doi: 10.1190/1.1441754.

Tatalovic, R., M. W. P. Dillen, and J. T. Fokkema, 1991a, Prestack imaging in the double transformed radon domain: 61th Annual International Meeting, SEG, Expanded Abstracts, 1285–1288, doi: 10.1190/1.1889124

Tatham, R. H., and D. V. Goolsbee, 1984, Separation of S - wave and P - wave reflections offshore western Florida: Geophysics, **49**, no. 5, 493-508, doi: 10.1190/1.1441685.

Vigh, D., and E. W. Starr, 2006, Comparisons of shot-profile vs. plane-wave reverse time migration: 76th International Annual Meeting, SEG, Expanded Abstracts, 2358-2361, doi: 10.1190/1.2370008

Vigh, D., and E. W. Starr, 2008, 3D prestack plane-wave, full-waveform inversion: Geophysics, **73**, no. 5, Ve135-Ve144, doi: 10.1190/1.2952623.

Virieux, J., and S. Operto, 2009, An overview of full-waveform inversion in exploration geophysics: Geophysics, **74**, no. 6, WCC1-WCC26, doi: 10.1190/1.3238367.

Whitmore, N. D., 1983, Iterative depth migration by backward time propagation: 63rd Annual International Meeting, SEG, Expanded 382-385, 10.1190/1.1893867.

--, 1995, An imaging hierarchy for common-angle plane wave seismograms: Ph. D. thesis, University of Tulsa.

Xu, K., B. Zhou, and G. A. McMechan, 2010, Implementation of prestack reverse time migration using frequency-domain extrapolation: Geophysics, **75**, no. 2, S61-S72, doi: 10.1190/1.3339386.

Xu, S., Y. Zhang, and B. Tang, 2011, 3D angle gathers from reverse time migration: Geophysics, **76**, no. 2, S77-S92, doi: 10.1190/1.3536527.

Yilmaz, O., and M. T. Taner, 1987, Semi - elastic plane - wave depth migration and velocity analysis: 67th Annual International Meeting, SEG, Expanded Abstractss, 1579-1582, doi: 10.1190/1.1885721.

Zhang, Y., and J. Sun, 2008, Practical issues of reverse time migration-true-amplitude gathers, noise removal and harmonic-source encoding: 70th Annual International Conference and Exhibition, EAGE, Extended Abstracts.

Zhang, Y., J. Sun, and S. Gray, 2007, Reverse-time migration: Amplitude and implementation issues: 77th Annual International Meeting, SEG, Expanded Abstracts, 2145-2149, doi: 10.1190/1.2792912

Zhang, Y., J. Sun, S. Gray, and J. Young, 2006, Sampling issues in delayed-shot migration and plane-wave migration: 68th Annual International Conference and Exhibition, EAGE, Extended Abstracts.

Zhang, Y., J. Sun, C. Notfors, S. Gray, L. Chernis, and J. Young, 2003, Delayed-shot 3D prestack depth migration: 73rd Annual International Meeting, SEG, Expanded Abstracts.

Zhang, Y., J. Sun, C. Notfors, S. H. Gray, L. Chernis, and J. Young, 2005, Delayed-shot 3D depth migration: Geophysics, **70**, no. 5, E21-E28, doi: 10.1190/1.2057980.

Zhang, Y., and D. Wang, 2009, Traveltime information-based wave-equation inversion: Geophysics, **74**, no. 6, WCC27-WCC36, doi: 10.1190/1.3243073.

Zhang, Y., and G. Zhang, 2009, One-step extrapolation method for reverse time migration: Geophysics, **74**, no. 4, A29-A33, doi: 10.1190/1.3123476.

Zhao, Z., M. K. Sen, and P. L. Stoffa, 2014, Double plane wave reverse time migration in the frequency domain: 84th Annual International Meeting, SEG, Expanded Abstracts, 1033-1039, doi: 10.1190/segam2014-1641.1.

--, 2015a, Plane Wave Reverse Time Migration in VTI Media using Green's Function: 85th Annual International Meeting, SEG, Expanded Abstracts, 4002-4007, doi: 10.1190/segam2015-5926023.1.

--, 2015b, Utilizing Reciprocity Principle for Double Plane Wave Dataset and Imaging: 85th Annual International Meeting, SEG, Expanded Abstracts, 4153-4157, doi: 10.1190/segam2015-5926824.1.

Zhao, Z., M. K. Sen, P. L. Stoffa, and H. Zhu, 2015, Double Plane Wave Least Squares Reverse Time Migration: 85th Annual International Meeting, SEG, Expanded Abstracts, 4170-4174, doi: 10.1190/segam2015-5924229.1.

Zhao, Z., P. L. Stoffa, and M. K. Sen, 2014, Double plane wave reverse time migration in the time domain: 84th Annual International Meeting, SEG, Expanded Abstracts, 4032-4037, doi: 10.1190/segam2014-1604.1.